Aircraft Landing Gear
Thermo-Tribomechanical Model Development

by

Laurent Heirendt

A thesis submitted in conformity with the requirements
for the degree of Doctor of Philosophy
Graduate Department of Aerospace Science and Engineering
University of Toronto

Abstract

Aircraft Landing Gear
Thermo-Tribomechanical Model Development

Laurent Heirendt
Doctor of Philosophy
Graduate Department of Aerospace Science and Engineering
University of Toronto
2015

A transient numerical model for studying the thermo-tribomechanical behavior of an aircraft landing gear is presented. The study reveals the major heat sources and heat sinks that impact the characteristic thermal behavior of the landing gear shock absorber. The severe in-service performance degradation and reported structural damage can be explained as a consequence of the heat generated by the high drag loads induced by rough runways on the bearings, and by the high sliding velocities of the piston. A conclusive model may lead to improved landing gear performance once the transient process of heat generation in a phase-changing grease-lubricated lower bearing is fundamentally understood. A novel tribotopological lubrication theory is derived in order to take into account all distinct physical phases of the non-Newtonian Bingham lubricant. The governing equations are solved using a hybrid numerical solver that is optimized for numerical efficiency and fast convergence. The proposed framework is validated against existing theories and results, and it demonstrates accurate predictions of the thermal performance of the landing gear. Strategies to passively optimize the lower bearing lubrication mechanism are further suggested in order to achieve optimal thermal performance of future aircraft landing gear.

Acknowledgements

Feeling gratitude and not expressing it is like wrapping a present and not giving it.

William Arthur Ward, critical thinker (1921 - 1994)

On this special occasion, I would like to express my deepest gratitude and appreciation to my supervisors, Prof. Hugh H.T. Liu and Phillip Wang, for their time, guidance and support. Without their commitment, knowledge and inspiring words, this project would not have been successful. Further, a particular thank you to the DEC committee members, Prof. Craig Steeves and Prof. Prasanth Nair, for their guidance and constructive suggestions.

I would like to thank David Bond who challenged me and always believed that I could succeed in this fascinating project. Additionally, I have learnt the importance of experienced executive decisions thanks to the very knowledgeable Mick White. With Bertrand Petot's explanations, I clearly understood the link between practice and theory. Thanks to Grant Minnes's and Jean-Marc Theret's expert judgment, publications have been cleared and released on time. Also, a very special thanks to René Billardon, with whom I spent a considerable amount of time discussing technicalities and modern prose.

I acknowledge and appreciate all the support from Pat Hickey, Jean-Luc Faillot, Antoine Boillot, Mike Game, Jean-François Locufier, Leszek Dacko, Claire Mercier, Joseph Lan, Kamal Chopra and Ian McCluskey. Without the help of all, this project would not have been possible to set up and organize.

This project would never have been accomplished without the brains, savoir-faire and wisdom of Dan Hetherington, James Ning, Trevor Lewin, Marin Besliu, Zlatko Auer, Marie-Laure De-Crescenzo, Olivier Noël, Andrew Thomas, Yann Bernery and Jean-Noël Mercereau, who invested numerous hours of their time in technical debate. My curiosity has been stimulated by the prudence and know-how of Branko Vukicevic who always expressed his rational and critical point of view, making me realize that a gap between theory and practice does indeed exist. George Constandinides always had the ability to recognize the industrial value of the present work, which inspired me to continue.

Moreover, I would like to deeply thank all the members of the Flight Systems and Control Group for the common activities and unforgettable moments that we spent together.

I want to express my profound gratitude towards the most important people in my life. I learnt from my father that I should never give up, no matter how bad or difficult a situation in life is. My dearest mother has spent so many hours teaching me precious wisdom about life. She has always been insisting on the importance of details. I would like to say thank you to my lovely sister Myriam for all the time and unforgettable moments that we have spent together since childhood. Especially, I would like to thank her for the number of hours that she dedicated to correcting my MSc thesis. Without them, I would never have been able to reach my goals. *Merci, dass dir 3 ëmmer fir mech do wart, an allen Momenter!*

I owe a lot to my sweet and lovely wife Jaqueline. Even though darkness sometimes looms, she has always kept looking at the bright and positive side. Her philosophical thoughts on life, tolerance, patience and dreams allowed me to endure even the most difficult moments of doubt. *Muito obrigado meu amor. Por trás de um grande homem, sempre existe uma grande mulher.*

Lastly, I want to highlight that this Ph.D. project would not have been possible without the generous financial and technical support from Messier-Dowty Inc., a wholly owned subsidiary of Messier-Bugatti-Dowty, SAFRAN Group, and additional financial support from the Natural Sciences and Engineering Research Council of Canada (NSERC).

Toronto, ON, Canada, January 2015

Laurent Heirendt

To The People Who Really Matter In My Life.

Contents

List of Figures

Nomenclature

Parameters, Scalars and Scalar Fields (Latin)

a	Integration factor, component, factor
a'	Semi-contact width [m]
A	Cross-sectional area [m^2]
b	Integration factor, component
B	Width [m]
c	Bearing lubrication profile [m]
c'	Thickness of TT space [m]
c_p	Heat capacity at constant p [J/(kg K)]
C	Center point
C_k^y	Integration factor of order k evaluated at y
e	Piston eccentricity [m]
$\breve{e}$	Specific internal energy [J/kg]
e_ϵ	Numerical error
E	Young's modulus [Pa]
f	Function/factor in TTR equation
F	Force [N]
G	Interpolation coefficient
h	Heat transfer coefficient [W/(m^2K)]
H	Analytical factor
i	Index/discretization index x
j	Index/discretization index y
k	Index/discretization index z
k_θ	Thermal conductivity [W/(mK)]
K	Orifice loss coefficient
l	TT space type
L	Length/bearing contact length [m]
m	Order of power law for τ, index
$\breve{m}$	Mobility parameter
M	Mass [kg]
n	Counter
n_i	Exponent i
N	Integer for vector/matrix size, maximum counter value
O	Origin of a reference frame
p	Pressure [Pa]
P	Internal energy rate (power) [W]
q	Heat flux [W/m^2]
Q	Heat source (power) [W]
r	Position in r-direction [m]
R	Radius [m]
s	Shock absorber stroke [m]
S	Entropy [J/K]
S^r	Sensitivity ratio
$\dot{s_s}$	Stiction speed [m/s]
t	Time [s]
u	Structural displacement [m]
u_i	Specific enthalpy of chamber i [J/kg]
U	Characteristic speed [m/s]
v	Fluid flow velocity field [m/s]
$\breve{v}$	Internal plug space velocity [m/s]
V	Volume [m^3]
$\delta\dot{V}$	Volumetric flow rate [m^3/s]
w	Hydrodynamic load [N]
W	Weight-over-gear (Main LG) [N]
x	Position in x-direction [m]
X	Aircraft runway position [m]
y	Position in y-direction [m]
Y	Response surface
z	Position in z-direction (piston) [m]
z_0	Length of thrust portion [m]
Z	Position in Z-direction (cylinder) [m]

Parameters, Scalars and Scalar Fields (Greek)

α	Angle [rad]
β	Ratio between dry and lubricated BFCs
$\dot{\gamma}$	Lubricant shear rate [1/s]
Γ	Integrated surface [m^2]
δ	Small distance [m]
ϵ	Small number, ratio
$\epsilon_{\dot{s}}$	Sign of net piston sliding speed
$\overline{\epsilon}_{\dot{s}}$	Flow coefficient
ε	Cauchy strain
ζ	Damping coefficient [Ns/m]
η	Dynamic viscosity [Pas]
$\eta_{\mathbf{D}}$	Bulk viscosity [Pas]
θ	Temperature [K]
Θ	Main LG rake angle [rad]
ι	Volumetric fraction of thickener/oil
κ	Stiffness [N/m]
κ_θ	Thermal expansion coefficient [1/K]
λ	Poisson coefficient
λ_θ	Thermal diffusivity: $k_\theta/(\rho c_p)$ [m^2/s]
Λ	Integration function
μ	Friction coefficient
$\mu^\star$	Modified BFC
ν	Kinematic viscosity [m^2/s]
ν_i	Relaxation factor
ξ	Heat flux sharing coefficient
Ξ	Algorithm parameter, multi-objective function
ϖ	Grid level index
ρ	Density [kg/m^3]
ς	Radial thrust portion increment [m]
τ	Shear stress field [Pa]
Υ	Polytropic coefficient
ϕ	Position in ϕ-direction [rad]
ω	Rotational speed [rad/s]
$\breve{\omega}$	Weight for Jacobi iterations

Vectors and Vector Fields

$\mathbf{a}$	Diagonal vector
$\mathbf{b}$	Right-hand-side vector
$\breve{\mathbf{b}}$	Body force vector
$\mathbf{e}_\epsilon$	Numerical error vector
$\mathbf{e}_i$	Unit base vector in direction i
$\mathbf{f}$	External force
$\mathbf{f_c}$	Damping force
$\mathbf{f_f}$	Friction force
$\mathbf{f_k}$	Stiffness force
$\mathbf{n}$	Normal unit vector
$\mathbf{p}$	Pressure vector
$\mathbf{r}$	Position vector
$\mathbf{r}_\epsilon$	Residual vector
$\mathbf{s}$	Shell vector
$\mathbf{u}$	Displacement vector
$\mathbf{v}$	Fluid film velocity vector
$\tilde{\mathbf{v}}$	Approximate solution vector
$\hat{\mathbf{v}}$	Numerical solution vector
$\mathbf{w}$	Material properties vector
$\mathbf{x}$	Position vector
$\mathbf{z}$	State vector
$\boldsymbol{\theta}$	Chamber temperatures vector
$\boldsymbol{\Lambda}$	Integration functions vector
$\boldsymbol{\psi}$	Source vector

Matrices, Tensors and Tensor Fields

$\mathbf{A}$	General matrix of linear system
$\mathbf{D}$	Stretching tensor
$\mathbf{E}$	Stiffness matrix
$\mathbf{I}_{n\times n}$	Identity matrix
$\mathbf{L}$	Thermal mass matrix
$\mathbf{L}_\pi$	Pressure matrix
$\mathbf{L}_\theta$	Temperature matrix
$\mathbf{M}$	Mass matrix
$\mathbf{T}$	Cauchy stress tensor
$\mathbf{T}_s$	Topology matrix
$\dot{\boldsymbol{\gamma}}$	Shear rate tensor
$\boldsymbol{\epsilon}$	Strain tensor
$\boldsymbol{\sigma}$	Stress tensor
$\boldsymbol{\Omega}$	Spin tensor

Functionals, Sets and Shells

$\mathcal{B}$	Boundary index span
$\mathcal{C}$	Bearing configuration set
$\mathcal{D}$	Domain index span
$\mathcal{F}_i$	Functional i
$\mathcal{I}$	Index span
$\mathcal{H}$	Heaviside function
$\mathcal{L}$	Modified BFC functional
$\mathcal{N}$	Viscosity functional
$\mathbb{N}$	Set of all integers
$\mathcal{R}$	Condition on the radial direction
$\mathbb{R}$	Set of all real numbers
$\mathcal{S}$	TT space
$\mathcal{Z}$	Condition on the vertical direction
Φ	Angular domain
Ω	Domain

Constants, Universal Parameters and Dimensionless Parameters

g	Gravitational constant [N/kg]
r_χ	Specific gas χ constant [J/kg/K]
Re	Reynolds number
Nu	Nusselt number
Pr	Prandtl number
π	Mathematical constant

Subscripts

$\setminus$	Diagonal
$+\|-$	Specific to the positive/negative shells of a TT space
0	Constant property
a	Surrounding air/atmosphere
A	Solid material A specific
b	Boundary b
bc	Boundary condition specific
B	Solid material B specific
c	Cylinder specific
C	Solid material C specific
d	Dry space specific
e	Extended/eccentric
ex	External
f	Fluid space specific
g	Groove specific
i	Index i, chamber i, direction i
j	Index j, direction j
k	Index k, direction k
l	Lower bearing specific
m	Index m
mp	Metering pin specific
M	Index designating solid material M
N_2	Nitrogen specific
o	Hydraulic oil specific
p	Plug space specific
P	Piston specific
Q	Heat
r	r - direction specific
R	Runway specific
s	TT space specific
st	Support tube specific
t	Taxiing specific
to	Take-off/landing specific
T	Aircraft tire specific
u	Upper bearing specific
V	Volume
x	x - direction specific
X	X - direction specific
y	y - direction specific
Y	Y - direction specific
z	z - direction specific
Z	Z - direction specific
$\dot{\gamma}$	Shear rate specific
ϕ	ϕ - direction specific

Superscripts

$'$	Equivalent/reduced/fixed, counter
0	Initial, at initial/rated conditions
$*$	Base oil specific
$\star$	Fixed, discrete, sorted
b, b''	Off-diagonal
d	Dynamic
E	Eastern node
f	Friction
H	Hertzian
(i)	Space/shell number/counter
n	Time step n
$[n]$	Iteration number, solution set
N	Northern node
or	Orifice
P	Central node
ro	Recoil orifice
s	Static
S	Southern node
t	Time specific
W	Western node

Mathematical Functions and Operators

$\cos(\cdot)$	Cosine function
$\frac{D}{Dt}$	Material derivative
$\det(\cdot)$	Determinant of a matrix
$\mathrm{diag}(\cdot)$	Diagonal matrix
$\exp(\cdot)$	Exponential function of base e
$\ln(\cdot)$	Natural logarithm
$\max(\cdot)$	Maximum function
$\min(\cdot)$	Minimum function
mod	Modulo operator
$\mathrm{tr}(\cdot)$	Trace of a matrix
$\mathrm{sgn}(\cdot)$	Signum function
$\sin(\cdot)$	Sine function
$\tan(\cdot)$	Tangent function
∂	Partial derivative operator/surface or shell
$:$	Frobenius product
$\circ$	Hadamard product
$\boldsymbol{\nabla}$	Gradient
$\boldsymbol{\nabla}^2$	Laplacian

Miscellaneous Symbols and Notations

a_i	Component of vector $\mathbf{a}$
$a_{m.j}$	Discretization of $\mathbf{a}$ at grid node (i, j, k)
$\mathbf{A}_{ij}$	Coefficient of matrix $\mathbf{A}$ at row i and column j
C^k	Set of continuous functions with continuous first k derivatives
dX	Infinitesimal part of quantity X
δf	Small incremental change/shift in f
Δx	Large incremental change/shift in x
$\Delta\mathbf{A}$	Determinant of matrix $\mathbf{A}$
$\tilde{f}$	First order integration of $f(\mathbf{x})$
$\tilde{\tilde{f}}$	Second order integration of $\tilde{f}(\mathbf{x})$
online	TEHD in the main loop
offline	TEHD outside the main loop
$\in$	'Element of'
$\notin$	'Not an element of'
$\Gamma^{(k,j)}$	Sub-boundary j of boundary k
$\leftrightarrow$	Action of swapping
$\Leftrightarrow$	'Equivalent to'
$\wedge$	Logic condition 'and'
$\vee$	Logic condition 'or'
$\times$	Cross product of sets
$\cup$	Reunion of sets
$\bigstar$	TEHD (FE/CFD) software package
$\blacksquare$	Multibody software package
$\hat{x}$	Stationary/static/maximum or normalizing value of x
$\tilde{x}$	Variable, moving $x(t)$
$\overline{x}$	Average, normalized x/Adiabatic
$\dot{x}$	Time derivative of x
$\lvert\cdot\rvert$	Absolute value, Euclidean norm
$\lvert$	'or'

Acronyms

2BC	2 Dirichlet Boundary Conditions algorithm
3SA	3-Spaces Algorithm (floating plug space)
ANSYS	Commercial FE/CFD simulation software
ASTM	American Society for Testing and Materials
BFC	Bearing Friction Coefficient
BWR	Benedict–Webb–Rubin equation
CAD	Computer Aided Design
CFD	Computational Fluid Dynamics
CIS	Commonwealth of Independent States
DOF	Degree-of-Freedom
EHD	Elastohydrodynamic(s)
FD	Finite Differences
FE	Finite Elements
FEM	Finite Element Method
FFT	Fast Fourier Transform
FLOTRAN	Deprecated thin fluid film module within ANSYS
FLUENT	Commercial CFD package, part of ANSYS
FORTRAN	Scientific computer language
FSI	Fluid-Structure Interaction
FVM	Finite Volume Method
GPU	Graphics Processing Unit
HD	Hydrodynamic(s)
HTC	Heat Transfer Coefficient
IFA	Integration Functions Algorithm
LG	Landing Gear
LU	Lower/Upper matrix decomposition
MATLAB	Commercial scientific computing software/language
MBD	Messier-Bugatti-Dowty, SAFRAN Group
MCA	Marching Cubes Algorithm
MG	Multigrid
MLG	Main Landing Gear
NLG	Nose Landing Gear
NSGA-II	Non-dominated Sorting Genetic Algorithm-II
PDE	Partial Differential Equation
SA	Shock Absorber
SI	International System of units
SSI	Structure-Structure Interaction
STP	Standard Temperature and Pressure conditions
TAA	Topology Adjustment Algorithm
TDA	Topology Detection Algorithm
TDMA	TriDiagonal Matrix Algorithm
TEHD	Thermo-Elastohydrodynamic(s)
THD	Thermo-Hydrodynamic(s)
TT	TriboTopological
TTM	Thermo-TriboMechanical
TTR	TriboTopological Reynolds equation
TTT	TriboTopological Theory
TZI	Thermal Zone of Interest
WOG	Weight-Over-Gear

Chapter 1

Introduction

> If we knew what it was we were doing, it would not be called research, would it?
>
> Albert Einstein, physicist (1879-1955)

1.1 Purpose and Motivation

In recent years, many civil airlines operating in countries known for airports that have rough runways have reported serious in-service overheating issues on commercial aircraft [4]. The aircraft manufacturer as well as the landing gear (LG) supplier have attempted to assess the reported problems, and the root-cause has been identified as the overheating of the LG shock absorber (SA) bearings. LG are especially challenged during landing, taking-off, maneuvering and taxiing on extremely rough and bumpy runways. Due to the combination of high sliding speeds of the LG piston and high drag loads induced by the rough runway on the SA bearings (see Fig 1.1), thermal issues arise leading to structural heat damage, such that the LG performance is reduced [2]. Despite this finding, a coherent and sufficient numerical model for predicting, understanding and studying the thermal behavior of the LG SA has not yet been established. The fundamentals of LG as well as its associated design process are explained in detail in [5]. Since the Maiden Flight in 1903, LG systems have been actively designed and continuously improved in production (see Fig. 1.2). For the last 40 years, Computational Fluid Dynamics (CFD) and the Finite Element Method (FEM) have been used for many different purposes beyond the application to in-service issues. The main efforts to develop a thermal model of the LG SA were focused on the lower bearing-piston interface, where the main findings, which can be classified as heat damage failure, have been reported. Nevertheless, even by simple calculations and estimations based on test results recorded from test flights on different rough-runway airports, an accurate quantification of the temperature field was not yet possible. Previous theoretical but preliminary temperature calculations either under- or overestimated the heat that must have been generated in order to lead to such heat damage.

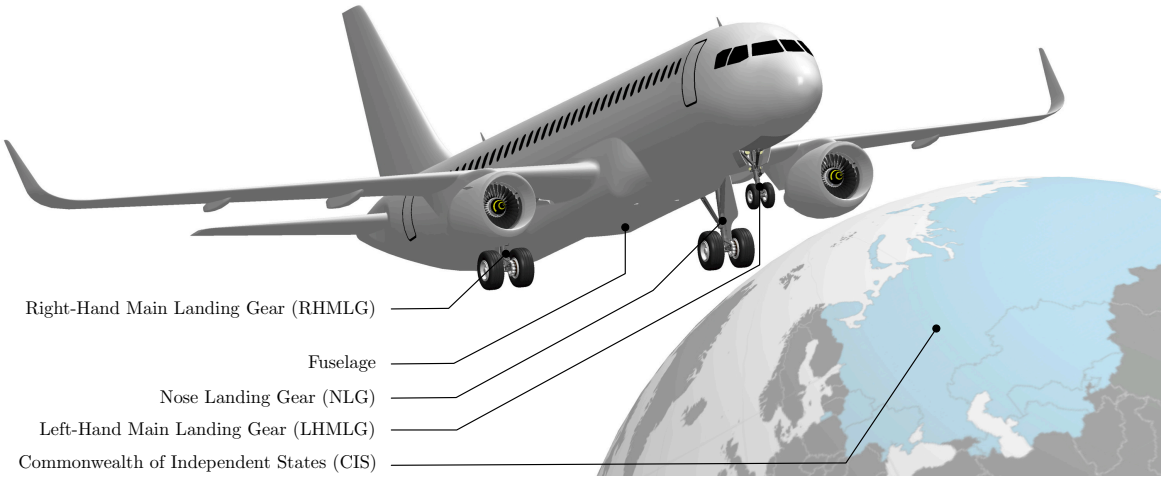

Figure 1.1: Commercial aircraft and regions reporting in-service overheating issues.[1]

Typical runways in the Commonwealth of Independent States (CIS) have a roughness with a short bump wavelength and an excessive bump amplitude, as shown in Fig. 1.3 [1]. The acceptability criterion is based on the level of vibrations on the aircraft while maneuvering and might need to be revised in order to take into account thermal aspects of the LG SA.

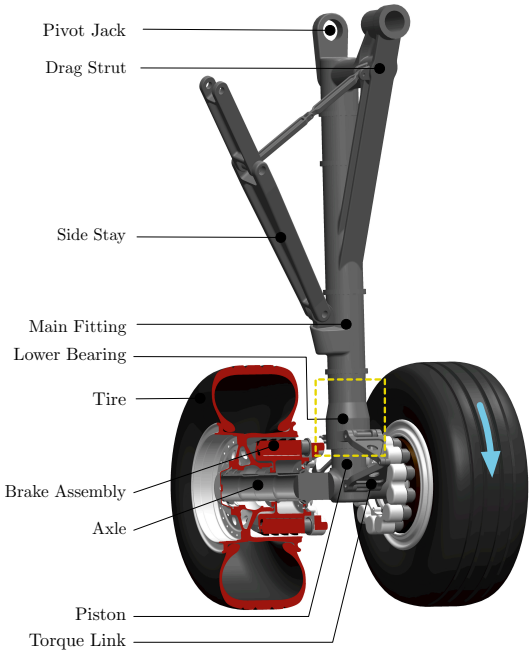

Figure 1.2: Main landing gear (MLG)[1].

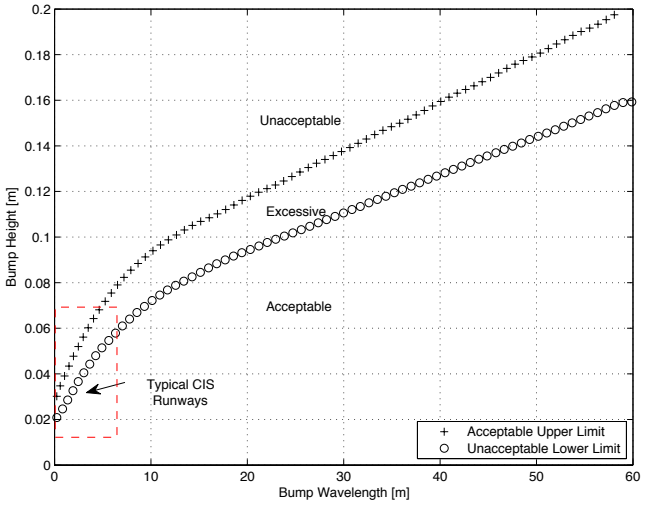

Figure 1.3: Airfield pavement roughness criterion (isothermal LG, AC150/5380-9) [1].

In order to illustrate the severity of maneuvering on a rough runway, a sample runway profile is shown in Fig. 1.4 [6]. A spectrum shown in Fig. 1.5 and calculated for this runway profile using the Fast Fourier Transform (FFT with a constant ground speed of 1m/s), reveals that a characteristic wavelength of a rough runway is small ($\overline{X_R} = 2$m). Rough runways are mostly paved with concrete slabs, which are all at a different vertical level with an average amplitude of $\overline{\hat{Z}_R} = 0.03$m (see Fig. 1.3). The excessively high loads on the LG SA combined

[1]Image based on CAD model available freely online - www.grabcad.com

with the high piston sliding velocities are easily imaginable when considering a commercial jet (weight-over-gear (WOG): $\overline{W} = 332$kN, see Fig. 1.1) maneuvering and taking-off at a typical (WOG dependent) speed of $\dot{X}_{to} = 270$km/h (with an acceleration on the runway of $\dot{X}_l/\hat{t} = 0.25$g). At the airports in the CIS, a typical ground maneuver takes approximately $\hat{t} = 30$s, and includes taxiing at $\dot{X}_t = 40$km/h (21.6kts) for $t_t = 15$s. These characteristic parameters will be used throughout the development of the aircraft LG thermo-tribomechanical (TTM) model.

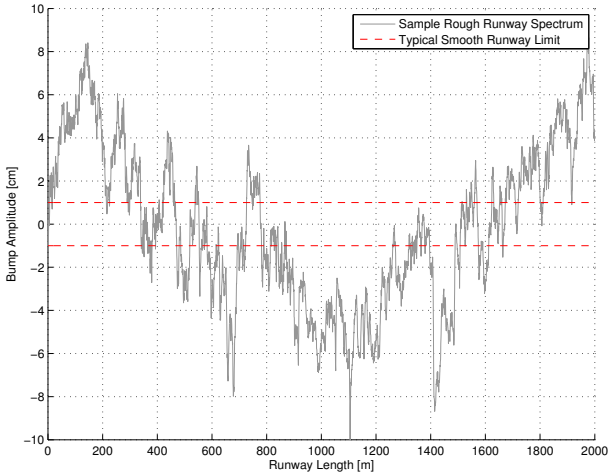

Figure 1.4: Sample rough runway profile.

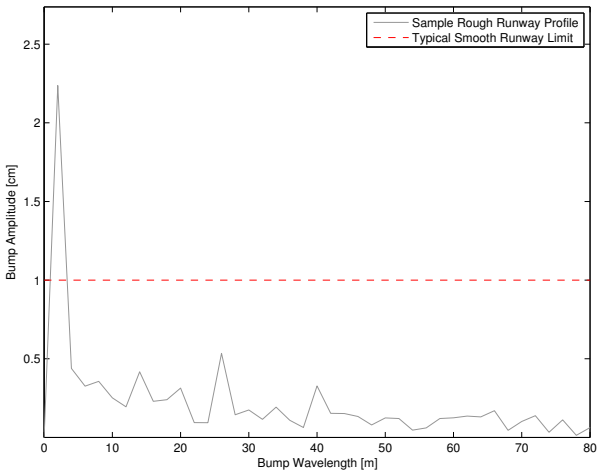

Figure 1.5: Rough runway spectrum.

In order to prevent in-service overheating issues, it might seem obvious to repave or repair runways in certain regions of the world. Some airports in the CIS are regional, and because of various factors such as low passenger traffic or restricted budgets, they may not be at the maintenance standard of heavily frequented airports in other parts of the world. The airfield roughness degrades over time, and is mainly caused by poor maintenance, uncertified construction techniques, adverse weather conditions, or failures of base or sub-base runway materials.

It is important to mention that not all aircraft operating on rough runways experience the same overheating issues. Military aircraft or very large transport aircraft are able to cope with landings on rough or unpaved runways. The LG of these aircraft are specifically designed to withstand severe operations, whereas commercial aircraft that are operating in the CIS are not. In addition, not every LG is equally affected when operating on rough runways. For instance, no overheating issues have been reported on the nose landing gear (NLG), as the loads are much lower on the NLG than on the MLG. An analogy can be drawn with an example from the automotive sector. Similarly to the commercial aircraft, a luxury car might encounter suspension damage when taken off-road or driven on rough roads.

In order to reduce ever-increasing maintenance costs and to prevent thermal issues, it is critical to investigate a different solution strategy than repaving the runway or keep continually replacing damaged LG components. Before formulating such suggestions, it is highly important to thoroughly understand the thermal behavior of a LG system and to accurately model the energy dissipated into heat. In other words, the frictional energy dissipated during taxiing and take-off needs to be accurately quantified. Before introducing the numerical LG TTM model, a summary of the state of the art in the area of LG thermo-tribomechanics is given in Section 1.2.

1.2 LG Thermo-Tribomechanics: A Review

1.2.1 Dynamic and Thermal Modeling of LG

Dynamic Modeling of the SA and LG on Rough Runways

Dynamic simulations in the systems development process should ensure that the dynamic loads on the LG components are within the design limits necessary to comply with high performance and safety requirements for operation on rough runways. A complete overview of recent developments in the area of LG dynamics is provided in [7], including a survey of the most critically needed enhancements to LG simulations; among those listed is the requirement for a comprehensive (nonisothermal) friction model for LG bearings. A relevant example of the dynamic modeling of LG is shown in [8], where the impact of repetitive and excessive bearing loads on the LG fatigue life is investigated, demonstrating the application of the general theory of multibody systems [9]. The touchdown of a helicopter LG has been modeled in [10], assuming, however, imperfect bearing lubrication, which was approximated as dry friction. Rough runways and their impact on the isothermal performance of LG have been studied previously. For instance, a Boeing 747's capabilities on rough runways have been assessed in [11], and investigations to reduce LG vibrations of runway excitations were conducted in [12]. However, all of the more advanced LG studies used constant or isothermal bearing friction. Although runway profiles have been studied and roughness criteria defined in [1], a sensitivity study that demonstrates the effect of key runway parameters (e.g., runway bump amplitude) on the thermal behavior of aircraft LG has never been performed [2]. LG related dynamic phenomena such as shimmy or gear-walk have been studied in [13], including the LG shock strut elasticity, but omitting any modeling of bearing friction forces. Brake-gear interactions have been tackled in [14], using the model of isothermal friction with free-play in a similar way as in [15]. In neither study, was the friction model extended beyond a typical, isothermal Coulomb model. The dynamics of LG have been extensively studied in [16], but only the initial landing impact with no heat transfer effects was considered. The inclusion of friction in a SA is a nonlinear phenomenon as demonstrated in [17], but the specified nonlinearity did not include thermal effects. Nevertheless, all studies mentioned to some extent the difficulties encountered with the stick-slip phenomenon, especially in transient simulations.

Despite the fact that the theory of stick-slip for the case of dry surfaces has been shown in [18], it remains a very active area of research; however, it seems as though the area of LG dynamics and the field of tribology are disconnected. In addition to the lack of knowledge of the frictional heat generation in LG dynamic simulations, little importance has been given to stick friction phenomena, as stated by Dr. W. Krüger [19]: "*Stick friction has not been covered widely in past publications. [...] The subject is of major importance for future research [...] at the main landing gears (when) taxiing.*"

Thermal Modeling of the SA

Although heat sources and sinks in a LG system have not been studied previously, heat transfer effects have been considered in the LG SA chambers during landing impact by using the bond graph methodology [20]. Bearing friction was not explicitly included, although the use of a more advanced friction model was mentioned. While there exists a clear need for nonisothermal and comprehensive friction models for LG dynamic simulations, heat generation has been taken into account in other applications.

A thermomechanically coupled study of a SA of a car is shown in [21], including a more advanced, although oil-based, friction model and dissipation of heat. A more sophisticated thermodynamic model of a SA of a car is given in [22], but explicit frictional heat generation was not taken into account. The influence of friction in the guide bearing of a suspension system has been separately investigated in [23], showing that friction might have a negligible effect for road bump amplitudes of *more* than 0.04m, but has a significant effect for smaller bump amplitudes. The trend of omitting frictional heat generation in a SA has been reversed in [24], where thermal phenomena are discussed specifically for the telescopic SAs of mountainbikes, but the proposed model is based on high-level bond graphs.

Existing Dynamic Models and Frictional Heat Generation

Despite the fact that LG dynamic simulations have mostly used isothermal friction models, research in other fields for other applications, such as published in [25], included frictional heat generation. The surface temperatures of oscillating sliding surfaces have been calculated for pin-joint assemblies (similar to LG bearings) using a frictional heat-flux, but the friction model followed the laws of Coulomb. A simplified model of stick-slip motion and two coupled masses, such as in a LG, has been shown in [26], but the contacts have been assumed to be dry and isothermal. In similar dynamic models shown in [27, 28], heat generation has been included in the dynamic behavior of sliding masses.

Although the comprehensive overview of friction models provided in [29] seems to provide a solid base for developing dynamic simulations of mechanical systems, the need for a more accurate prediction of the bearing friction coefficient (BFC) was formulated in [30]. It is a fact that the BFC changes because of thermal effects, and therefore the research area of LG thermo-tribomechanics and field of tribology have to be linked.

Nonisothermal Friction in Simulations of LG and Dynamic Systems

As illustrated previously, the trend has been to ignore the frictional heat generation in LG dynamic simulations. In recent years, however, several publications have been released in order to show the importance of thermal considerations in LG dynamic simulations [31], where a characteristic aircraft LG model including the dynamics of the SA as well as frictional heat generation have been considered. A first attempt to bridge the gap between LG dynamic simulations and tribology is shown in [32], where a high-level methodology is introduced for including a complex thermal model into existing LG dynamic simulations.

1.2.2 Tribology and Thermo-Elastohydrodynamics

Tribology, which is the science of contacting surfaces in motion, including dry and lubricated contacts, provides the fundamentals to explain the LG overheating issues. For a long time, the field of tribology has been heavily studied; it is probably one of the oldest research fields, having the obvious link to heat with prehistoric friction-based fire making. Tribology has been extended to many different research fields, including dynamic modeling of mechanical systems. For instance, a practical reference of lubrication principles is provided in [33].

Tribological Studies of Dry Friction

Although the joints in aircraft LG are lubricated, it is the dry-running of joints, including slider bearings, that is of particular interest. The frictional heat generation between dry surfaces has been considered in older studies [34, 35], but loses validity once the contacting surfaces are lubricated. Some well-known studies like [36] focused on calculating how the heat is shared between contacting surfaces, and are still very useful for comparing dry and lubricated contacts from a thermal point of view. Analytical solutions to the frictional heat energy generation and its impact on the temperature field are given in [37], but are hardly practical for modeling complex industrial systems. A thermodynamic overview of the frictional thermal energy process is shown in [38], but is only applicable to dry surfaces.

A first attempt to link the friction coefficient between contacting and lubricated surfaces and the temperature is shown in [39], where the contact temperature drives a sudden change of the physical phase of the lubricant. However, this inclusion of temperature in the BFC might not be accurate enough to fundamentally understand frictional heat generation in lubricated contacts. In addition to the effect of heat on the lubricant in lubricated contacts, the elasticity of dry contacting structural components is considered in [40], but only parallel layers and vertical thermoelastic oscillations have been studied.

Isothermal Classical Reynolds Lubrication Theory

After the derivation of the Navier-Stokes equations in the 1840s, the computational power needed to solve them was not available, and the equations were simplified by using various approximations. The most prominent simplified theory for thin films was derived by Osborne Reynolds more than a century ago, who adapted the Navier-Stokes equations to a more simple equation, namely the Reynolds equation. His equation has been used for many years, and was the only means of obtaining an acceptable solution to hydrodynamic problems with the available computational power.

Most studies in the field of hydrodynamics have focused on isothermal studies in order to design higher performance and higher efficiency bearings. While shearing the lubricant, energy is dissipated into heat, which raises the temperature within the lubrication gap, leading to a change in the viscosity (and density) of the lubricant. Numerous publications that outline the theory of lubrication in detail have been written, and this work has been summarized in [41].

For more than 30 years, lubrication studies have been extended to include temperature effects, but were mostly limited to simplified geometries in order to derive analytical solutions such as in [42]. Similarly, the patterns that exist in flow between unsteady or oscillating plates were investigated in [43]. Although analytical solutions are eventually relevant for validation purposes, they are barely applicable in real-life applications, such as in LG.

Recent research has led to the conclusion that the performance of bearings is dependent on the deformation of the contacting surfaces, and that the elasticity of lubricated contacting surfaces has to be considered [44]. Friction in mixed and elastohydrodynamic (EHD) lubrication that includes thermal effects has been discussed in [45], but the focus of the thesis was on point-contact applications.

Thermo-Elastohydrodynamic Lubrication

The field of thermo-elastohydrodynamics (TEHD) is an extension of the EHD field through the inclusion of thermal effects, and is the field within tribology that has seen the most recent developments, especially to calculate the tribological performance of complex systems. The field of TEHD is the field that is most relevant to the study of the reported overheating (thermal) problem, as the slider bearings are grease-lubricated. The governing equations for thermo-hydrodynamic (THD) behavior and a numerical scheme based on Finite Differences (FD) are shown in [46] for the application of an oil-lubricated journal bearing, but did not include the elasticity of the bearing. Slider bearings such as in [47] are rarely studied. Although the model development steps might be relevant, the focus was not on TEHD, but on a more advanced lubricant.

Similarly to the case of EHD studies, slider bearings have rarely been considered. A simplified TEHD model of a surface slider is given in [48], estimating the elastic deformations of the slider surface with a 1D elastic beam model. A validated fully-coupled and transient TEHD model similar to the one proposed for an aircraft LG has been shown in [49], but the application was for reciprocating cylinders in hydraulic machines (journal bearings), and the lubricant was oil. The methodology and fluid-structure interaction (FSI) algorithms are partially applicable to the LG SA.

To the author's current knowledge, LG SA bearings have not been considered from a TEHD point of view. In order to fill this gap in knowledge, multiple publications in connection with the TTM model have been released. For example, a 3D model with rigid LG components and an oil-lubricated lower bearing has been given recently [50], omitting, however, the elasticity of structural components. Additionally, an axisymmetric numerical concept model for the LG SA bearings has been shown in [51], demonstrating the differences of grease and oil flow and the impact on the friction coefficient.

A more common application in TEHD is for rotating machinery, and such an analysis is shown in [52] for an oil-lubricated journal bearing under severe operating conditions, outlining the importance of including thermal and elasticity aspects. The work concludes by comparing

both THD and TEHD results. Similar conclusions have been drawn in [53], where thrust bearings have been studied from a TEHD point of view.

Transient TEHD analyses are the exception, and only a few studies have focused on run-in phases of rotary machinery, on vibrations, or on oscillating machinery parts. TEHD problems can, in some distinct applications and under specific operating conditions, be formulated as quasi-static, because the inertia of the lubricant can be ignored. Longitudinal vibrations in line contacts have been considered in [54], showing that both thermal and transient effects need to be included with non-Newtonian lubricants. A new TEHD algorithm is shown in [55, 56] for dynamically-loaded connecting-rod journal bearings, showing the influence of thermal and elastic deformations and the importance of transient TEHD simulations. Depending on the thermal boundary conditions of the system, a notable conclusion is that the TEHD and THD results might not be very different, which implies that the thermal expansion of the structure is dependent not only on the heat generated between the surfaces, but also on the surrounding components and environment.

TEHD and Optimization of the Lubrication Mechanism

Other geometries such as the lemon-bore bearing have been explored in [57], where the THD performance was evaluated. An interesting conclusion is that the lubrication mechanism of the bearing can be modified according to application requirements in order to increase the THD (and consequently TEHD) performance. Compressible lubricants, such as in gas-lubricated bearings, have been considered in [58]. Although the lubricant was different than grease or oil, it is the methodology of studying different bearing shapes that is of particular interest.

EHD/TEHD and non-Newtonian Lubricants (Bingham Fluids)

Most of the previously-cited work uses Newtonian lubricants, such as mineral oil. LG slider bearings are lubricated with a high-pressure non-Newtonian lubricant, namely grease (a Bingham fluid), which has rarely been considered. An experimental investigation of the EHD behavior of grease is provided in [59], determining the limiting (or yield) shear stress τ_0 for grease.

One of the first publications involving a Bingham fluid is [60], outlining the identification of a solid (also known as *plug*) phase in grease-lubricated bearings, confirming the tendency of an increased hydrodynamic pressure with increasing τ_0. The rheology of the lubricant is explained in detail in [61], resulting in the derivation of a 2D lubrication theory based on the Herschel-Bulkley model. It is the comparison with experimental results and their good agreement that is of particular importance. In a similar way, grease-lubricated point-contacts have been considered in [62], comparing both the EHD and TEHD performance. A major and relevant finding is that for the *stiction* case, the plug fills the entire lubrication gap. A relevant study is given in [63], in which thermal effects using the THD theory are studied for a finite journal bearing, taking into account multiple plug regions. Nevertheless, the work does not refer to other phase changes, such as those caused by local disintegration or 'burning' of the lubricant. A similar study involving non-Newtonian lubricants that follow the power law (grease follows the

power law of first order) is shown in [64]. However, the focus was only on the THD performance, resulting in the conclusion that the thermal effects are generally more pronounced for shear thickening fluids.

Another relevant THD analysis with a Bingham fluid is provided in [65], demonstrating a multi-regional velocity field, together with a stationary and moving solid layer. Along these lines, a THD study involving a Bingham fluid shown in [66] demonstrates multiple cases of plug formations that can exist or co-exist, but does not consider other eventual phases, such as those caused by an increasing temperature.

A more general approach has been taken in [67] for any non-Newtonian fluid (shear thinning/thickening) in EHD lubrication, but the application was limited to line contacts. Nonetheless, the viscosity was considered to be a function of the shear rate and is included in the model as an equivalent viscosity. A similar method using an equivalent viscosity is followed in [68]; the conclusion is that thermal effects prevail over the rheological contributions in TEHD contacts.

A theory that considers TEHD effects of a Bingham fluid in an aircraft LG bearing and its application in a comprehensive model has not yet been established. The phase changing, transient character of grease is not captured in the classical Reynolds theory, and the solution times of any more advanced technique used to solve the Navier-Stokes equations, such as CFD, are not compatible with the stringent requirements of fast, transient dynamic simulations of aircraft LG.

1.2.3 Relevant Numerical Developments

Numerical Methods in Classical Lubrication and Dry Friction

Despite considerable efforts in developing analytical solutions to the heat conduction equation in solids [69] or to the Reynolds equation [70], numerical studies have emerged more frequently during the last decade. For instance, several numerical methods have been combined in [71] in order to determine a solution to the steady state and transient problem of THD lubrication for the case of journal bearings. Similarly, boundary elements and finite elements (FE) have been combined in [72] to yield a solution to the EHD problem of journal bearings, providing as well a comprehensive algorithm of the FSI simulation. An interesting analysis of not using FSI techniques, but rather solving both structural and Reynolds equations together for a simple cylindrical journal bearing is provided in [73].

The fundamentals of fluid film lubrication and the associated modeling efforts for journal bearings have been summarized in a very comprehensive way in [74]. In [75], an extensive summary of numerical methods in EHD/TEHD together with a comparison of the different methods is provided.

One of the most prominent numerical solution methods in TEHD is the Multigrid (MG) method. A practical reference detailing the MG method and the underlying algorithms is provided in [76]. A full MG implementation for a Poisson-type (elliptic) partial differential equation (PDE) is detailed in [77].

A computational study on the appropriate modeling of dry friction is shown in [78], where the sliding process was modeled and the surface roughness considered. Similarly, an FE formulation including the flash temperature in dry contacts is given in [79], and the numerical results are compared to the analytically-derived expression.

Numerical Studies in Lubrication using CFD and FSI

As shown previously, the field of EHD and TEHD lubrication based on the classical (or modified) Reynolds theory has been very active. Most notably, grease and other non-Newtonian lubricants were considered in TEHD simulations, and their rheological models were derived. As confidence was gained in the models and the computational resources became available in recent years, researchers turned away from the Reynolds theory and towards the promising features of CFD.

Advanced modeling aspects of EHD lubrication were investigated in [80], where the performance of pocketed bearings was investigated, but thermal aspects were not considered. A full 3D journal bearing is modeled using CFD in [81] using the Finite Volume (FVM) method and the tridiagonal matrix algorithm (TDMA). The work is of particular importance as the results are experimentally validated.

A relevant study dealing with the implementation of FSI and CFD algorithms that provided results for Bingham fluids in lubrication gaps was done in 2008 [82]. For different journal bearing configurations, the formation of the plug is calculated with FLUENT. The authors state that the main advantage of solving the Navier-Stokes equations using CFD would be to take into account the 3D formation of a plug, implicitly suggesting, however, a need for a Reynolds-based model. A very practical EHD study of a journal bearing involving CFD and FSI techniques is shown in [83], demonstrating the use of ANSYS and the deprecated FLOTRAN module. Nevertheless, the use of this technique is limited to oil-lubricated journal bearings.

Comparison: Navier-Stokes equations and Classical Lubrication Theory

A line contact solution is obtained in [84] using the CFD method implemented in an open-source software package. Apart from distinct cases of high viscosity, a good agreement with the classical Reynolds theory was found. A similar problem yielding the same conclusion is tackled in [85], assuming full elasticity of contacting surfaces. A study providing more details on the implementation of CFD and FSI methods for the case of a rotor-bearing system is shown in [86], concluding that CFD is a valuable tool for investigating the hydrodynamic and EHD performance of journal bearings. The CFD method gives a certain flexibility for the inclusion of other eventual study variables, but there is a high computational cost involved in obtaining similar results as with the classical lubrication theory.

The Navier-Stokes equations are the underlying governing equations of CFD methods and are commonly known to be very tedious and computationally expensive to solve numerically. Solution times for CFD-based methods are generally quoted to be several orders of magnitude longer than those for traditional Reynolds solvers.

Year	Model	Computer/Processor	Cores	Nodes/elements	N.-S.	Class.	Ref.
1995	3D Short Bearing	SPARCstation 514 MP	4	1800 F + 54000 S	5400s	180s	[81]
2007	3D Point contact	Intel Xeon 5100	32	200'000 total	3 weeks	N/A	[87]
2010	3D Short Bearing	Intel Core i5 2.67Ghz	1	7200 F + 16800 S	7440s	60s	[86]
2012	2D Sliding Line	Intel Xeon 2.27 Ghz	2	61000 F + 63000 S	600s	N/A	[85]
2014	2D Roller Bearing	N/A	N/A	23474 F + 0 S	20.21hrs.	N/A	[88]

Table 1.1: Quoted solution times for the solution of the Navier-Stokes equations (CFD) compared to the classical (Reynolds) approach.

As shown in Table 1.1, the flexibility of CFD simulations comes at a substantial computational cost. In [89], the major differences between the Navier-Stokes approach (CFD) and the Reynolds approach are discussed. Inertia effects of the lubricant, as well as the flexibility to implement complex rheological models, are cited as advantages of CFD. At the same time, the disadvantage of full CFD is emphasized. By using CFD, four equations (Navier-Stokes) have to be solved, compared to a single Reynolds equation. This negatively affects the solution times.

For the cases considered in [89], it is shown that almost no difference exists in the results obtained from the Navier-Stokes equations (CFD) or with the Reynolds approach (even by including inertia effects). In short, the CFD methods offer apparently more flexibility for cavitation or rheological models, but are obtained at a much higher computational cost. The Reynolds equation is still valid for non-Newtonian lubricants, but using the Reynolds equation for non-Newtonian and multiphase (more than two phases) lubricants in transient 3D applications (such as in a LG) has so far not been investigated.

Although the CFD method seems to be applied more and more often in the literature, the drawback of a high simulation cost puts this method out of reach when trying to simulate *transient* and *grease*-lubricated contacts. In fact, the quoted simulation times in Table 1.1 are for steady state simulations and for oil. Simulating transient runs lasting 100s or more, with time steps of the order of micro-seconds, would bring the total simulation time to months (or even years) for the application of LG.

1.3 Research Goals and Outline

As a result of the review of existing work in the area of LG thermo-tribomechanics, two major issues have crystallized. These are formulated as the following two research goals:

1. **Fundamentally understand the LG SA thermal behavior, in particular the transient heat generation process in a grease - lubricated LG SA bearing**, by developing a mathematical framework and providing accurate simulation results in suitably fast manner.

2. **Conceptualize and develop a strategy for solving** the reported overheating problem.

The logical outline of the thesis is shown in Fig. 1.6 and the aim of each chapter is specified. All the chapters are shown as parts of a hexagon. The hexagon is equivalent to the research area of LG TTM (see Fig. 1.7).

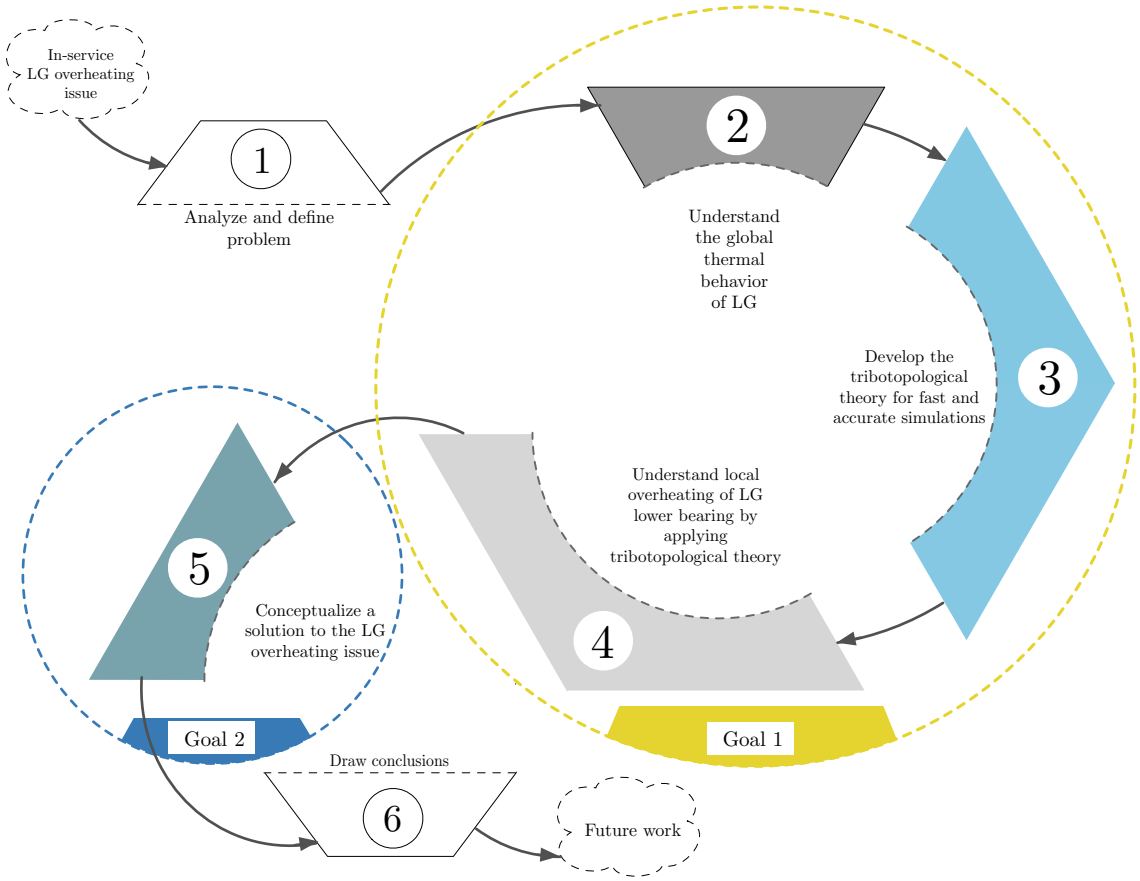

Figure 1.6: Outline of thesis and logical flow of chapters with specification of thesis goals.

The chapters are grouped into two indicated circles that correspond to the two postulated goals. Although the chapters are shown in a sequence, it is the union of Chapters 2, 3 and 4 that leads to attaining Goal 1, so that Goal 2 can be reached in Chapter 5. A brief summary of each chapter highlights its content and is given below for each of the two goals.

Goal 1: Fundamental understanding of the LG SA thermal behavior

In **Chapter 2**, the LG system is defined, the methodology and governing algorithm are outlined, and the developments leading to a characteristic LG thermal model are highlighted. A general overview of the LG system leads to the identification of three subsystems (*mechanical*, *tribological* and *thermal*) and one interface module, which are modeled with a limited complexity, and which give the name to the *thermo-tribomechanical* (TTM) model. Special emphasis is placed on the rheology of the lubricant (grease) used in LG bearings.

The root-cause of the heat damage is confirmed, and characteristic results that quantify the heat sources and sinks are provided. A sensitivity study of the effects of a change in key

parameters, such as the characteristic dimensions of the runway profile and the WOG, on the maximum temperature (proportional to the maximum frictional heat flux) in the thermal zone of interest (TZI) is performed.

In **Chapter 3**, a novel *tribotopological* theory (TTT) is presented, which takes into account non-Newtonian, multiphase lubricants, and rewrites the Reynolds equation. The theory relies on CFD principles for accuracy, but uses the advantages of the classical lubrication theory for fast simulations. Virtual topologies, namely shells and spaces, form the underlying concept of the TTT. Spaces are surrounded by shells, and are defined through a threshold value (such as maximum operating temperature or yield shear stress) of any scalar field, including electro- or magneto-rheological fields. Spaces can either be attached to a contacting surface, or can float within the lubrication gap.

The main difference between the present approach and [3, 63] is that not only is the formation of a single plug space taken into account, but also multiple spaces (physical phases) of a non-Newtonian lubricant are considered.

In **Chapter 4**, a comprehensive 3D transient TTM model that takes into account thermal and elastic structural deformations of the LG lower bearing is developed by applying the TTT. Special attention is given to the underlying algorithm of the numerical FSI framework used to efficiently solve the governing equations. The transient model, which is a sequence of steady state steps, each with different initial and boundary conditions, is validated against existing results, both for rotational and translational motion. The discretization of the governing equations and the MG implementation are shown. The newly developed hybrid Reynolds-based solver runs at an acceptable speed and provides transient results in a short time frame.

The heat generation process within the lubrication gap is fundamentally understood, and numerical results indicate significant differences in flow behavior between greased and oil-lubricated bearings. Plug and dry spaces are identified, and their transient behavior as well as their impact on the friction coefficient is studied. In addition to the THD results, the TEHD results are shown, which demonstrate that the temperature field at both contacting surfaces is different. This finding explains the reported uneven and asymmetrical heat damage.

Goal 2 : Conceptualization and development of solution strategy

In **Chapter 5**, the advantages and disadvantages of various solution strategies are discussed. The fundamental understanding of the heat generation (Goal 1) leads to conceptualizing solutions that will reduce the heat generation and avoid the local disintegration of the lubricant. An in-depth systemic analysis of LG simulations is performed, the strategy of solving the overheating problem is outlined, and design modifications are highlighted.

In addition, TEHD results show the effect and benefits of a modified lubrication mechanism. Optimization results of a novel lubrication mechanism design of the lower bearing are summarized, which show a significant and beneficial effect on the heat generation.

In **Chapter 6**, final conclusions are drawn. Design suggestions and the eventual practical steps necessary to implement the findings that may lead to an industrial solution are highlighted.

In addition, various aspects of optimizing the TEHD simulation, such as nonuniform grids, are given. An industrial solution may allow aircraft operators to reduce maintenance costs and allow aircraft LG suppliers to improve the LG system thermal performance.

1.4 Scope and Significance

The thesis contributions outlined above are significant from both academic and industrial points of view. The aim is to seamlessly link various research areas together. Specifically, this thesis defines a new area of LG TTM, which can be seen in Fig. 1.7 as a hexagonal intersection of six fields: LG SA dynamics, fluid mechanics/CFD, classical lubrication, numerical analysis, multiphysics/FSI and lubrication mechanism design.

In the area of LG dynamics, this thesis provides a more accurate friction coefficient by including thermal effects. The fields of fluid mechanics/CFD and the classical lubrication field are linked by the novel TTT, which incorporates the advantages of both fields. The novel TTT is applied during the development of the comprehensive model, as the fields of multiphysics/FSI and numerical analysis are linked by the integration of a new hybrid solver (based on the MG method) into ANSYS using advanced FSI techniques. Conventional lubrication mechanism design guidelines can be extended by implementing the results of the comprehensive TTM model in order to avoid the overheating problem in the future.

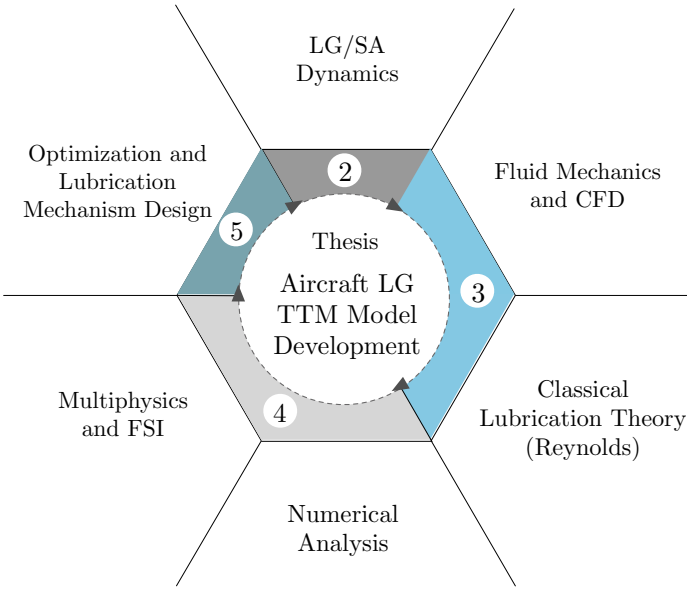

Figure 1.7: Thesis positioning at the intersection of six research fields.

This thesis is believed to be one of the first comprehensive studies in the new area of LG TTM, and the impact is believed to be significant in the larger field of LG design and engineering. It covers various aspects of TTM model development which are beneficial to the understanding of the reported overheating and to the design of future LG with a higher thermal performance.

Although the thesis takes a pioneering role in the area of LG TTM, specifically with the development of the TTT for LG bearings, it is not thought to provide the only method of solving the reported overheating problems; other strategies may also work, but entail issues or complications that are not discussed (such as changing the type of LG).

This thesis does not aim to develop specific design guidelines for future LG, as it relies solely on a theoretical framework. Although various real-life aspects, such as the roughness of bearing surfaces, existing wear, or fatigue of parts are not included, the essential physics of the LG lower

bearing overheating are captured in the numerical TTM model. The comprehensive model and the TTT are validated for simplified and theoretical cases, but may need to be validated against existing test results of LG before future model refinement steps can be taken. As the model is not yet validated against existing test results, the model results provide insight into the thermal behavior of LG, but do not give, for example, an exact quantification of the temperature at the lower bearing sliding interface.

Although the TTT is developed for translational and rotational motion, the aim of the comprehensive model is to provide results for the case of the translational motion of a slider in a specific MLG of a commercial airliner that is operating on rough runways. This thesis provides the fundamentals of LG TTM model development, and, if needed, they can be adapted to other cases, such as for LG of military aircraft or NLG.

1.5 Relevant Notations

The unit base vector of a reference frame is defined as $\mathbf{e}_i = (\ 0 \ \cdots \ 1 \ \cdots \ 0\ )^T$, with its i-th component being one. The translation vector $\mathbf{x}(t)$ in the global reference frame describes the position of the pivot jack (see Fig. 1.2) of the LG on the runway. As the aircraft is moving in a straight line (no turning) over the runway, the position vector is given by: $\mathbf{x}(t) = X(t)\ \mathbf{e}_X + Z(t)\ \mathbf{e}_Z$, where $X(t)$ is the position of the aircraft over the runway and the vertical position $Z(t)$ is given by the dynamic model. A vector $\mathbf{v}$ in the local reference frame of the lubrication gap $(O, \mathbf{e}_x, \mathbf{e}_y, \mathbf{e}_z)$ is written as: $\mathbf{v} = v_x\mathbf{e}_x + v_y\mathbf{e}_y + v_z\mathbf{e}_z$. The n^{th} spatial derivative of a scalar field θ is written as:

$$\frac{\partial^n \theta}{\partial x^n} = \theta_{,\underbrace{x \ldots x}_{n\ times}} \tag{1.1}$$

The first order partial derivative of a scalar function f with respect to x is denoted as $f_{,x}$. The temporal derivative of a vector or scalar field is defined as:

$$\dot{\theta} = \frac{\partial \theta}{\partial t} \quad , \quad \dot{\mathbf{v}} = \frac{\partial \mathbf{v}}{\partial t} \tag{1.2}$$

The material derivative (sometimes called total derivative) of a vector field $\mathbf{v}$ is written as $\frac{D\mathbf{v}}{Dt} = \dot{\mathbf{v}} + \mathbf{v} \cdot \boldsymbol{\nabla}\mathbf{v}$. The gradient of a scalar field p is given by $\boldsymbol{\nabla} p = p_{,x}\mathbf{e}_x + p_{,y}\mathbf{e}_y + p_{,z}\mathbf{e}_z$. The gradient of a vector field $\mathbf{v}$ is given by:

$$\boldsymbol{\nabla}\mathbf{v} = \frac{\partial v_j}{\partial i}\mathbf{e}_j \otimes \mathbf{e}_i \quad , \quad i, j = x, y, z \tag{1.3}$$

where $\mathbf{e}_j \otimes \mathbf{e}_i$ designates the tensor operator between two vectors $\mathbf{e}_j$ and $\mathbf{e}_i$: $\mathbf{e}_j \otimes \mathbf{e}_i = \mathbf{e}_i\mathbf{e}_j^T$, or component-wise: $(\mathbf{e}_j \otimes \mathbf{e}_i)_{kl} = e_{ik}e_{jl}$. $\boldsymbol{\nabla}\mathbf{v}$ is also known as a second-order tensor. In some cases, a quantity may yield the same analytical expression if derived in different directions in the reference frame. For instance, $p_{,x|z}$ means that $p_{,x} = \frac{\partial p}{\partial x}$ and $p_{,z} = \frac{\partial p}{\partial z}$. The notation '|' reads 'or' and is adopted in order to simplify the equations. Any other notations are highlighted in the respective model development sections. ■

Chapter 2

Landing Gear Thermo-Tribomechanics

> If you can walk away from a landing, it's a good landing. If you use the airplane the next day, it's an outstanding landing.
>
> Chuck Yeager, test pilot (1923 -)

2.1 Landing Gear System Definition

Despite being considered dead-weight during flight, the LG is one of the most critical and most complex systems of a modern aircraft. Although the LG system is composed of various subsystems, such as the wheels and brakes assembly, torque link and side stay identified in Fig. 1.2, it is the internal mechanism of the main fitting that is of particular interest to the field of LG thermo-tribomechanics. The role of each LG component, the function of the internal components and the flow of the hydraulic oil within the LG SA (chamber interactions) are key to understanding the TTM behavior while operating on a rough runway.

Definition of the LG SA Components and Functions

In Fig. 2.1, the two major components of the LG SA are the cylinder (1)[2], which is a part of the main fitting defined in Fig. 1.2, and the piston (3). The piston, which links the LG SA to the wheels and brakes assembly, is sliding inside the cylinder and is supported by two bearings, namely the upper (5) and lower bearings (2). The upper bearing is fixed on the piston, whereas the lower bearing assembly is inserted into the cylinder. The portion of the piston inside the cylinder is submerged in hydraulic oil up to a certain level, and the remaining volume of the SA is filled with nitrogen gas, which is chosen for its inert properties in consideration of the strict requirements of aircraft operating in all parts of the world. In a double-acting SA such as is

[2]The bracketed numbers correspond to the components shown in Fig. 2.1

considered in the present case, nitrogen gas fills the voids on the top inside (I) of the cylinder and the bottom of the piston below the Piccolo tube base (4). The double-action of such a SA results from the different stiffness characteristics of the two gas compartments and is designed for operating on rough runways.

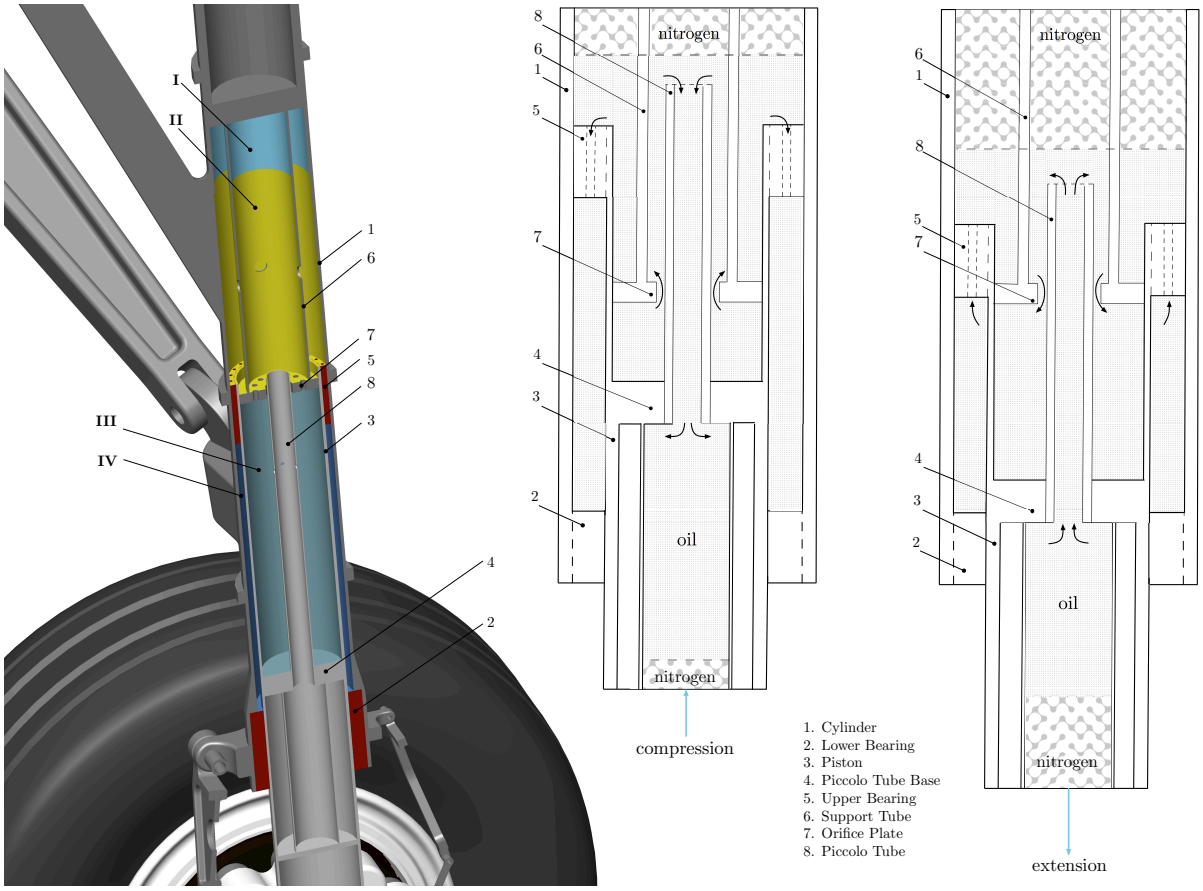

Figure 2.1: LG SA components and oil flow during compression and extension within the chambers II-IV. Chamber I is filled with nitrogen. The components (3), (4), (5) and (8) are moving and other components are stationary.

In a single-acting SA, nitrogen gas fills a single void on the top inside of the cylinder (I). The piston ends at the axle of the two wheels, as shown in Fig. 1.2, and is filled with oil as shown in Fig. 2.1. In a double-acting SA and similar to the cylinder, the piston is filled with oil and nitrogen. The nitrogen at the bottom of the piston is confined in a thermally insulated compartment. For simplification of the thermal model, the second gas compartment is omitted as explained in Section 2.6.4. The LG SA has two dynamic functions, namely a spring and a damper function. The spring function is particularly relevant to the study of the dynamics of the LG, whereas the damper function is of importance to study the dissipation of the mechanical energy within the SA. Both functions drive the dynamic input of the thermal model (see Section 2.3).

LG Spring Function The LG SA acts as a spring in order to allow the SA to rebound after touchdown. The spring function is realized by compressing and expanding nitrogen gas. The

stiffness of the SA is dependent on the pressure within the LG SA and other factors such as temperature and the mixing of the hydraulic oil and nitrogen.

LG Damper Function In modern LG SA, the dissipation of the mechanical energy during ground maneuvers, taking-off and landing is realized by forcing hydraulic oil through two orifices, which are holes designed according to the LG dynamic specifications (primary dissipation mechanism). The orifices are the most critical and expensive components within the LG SA.

An important part of the mechanical energy is dissipated through mechanical friction within the LG SA at the upper and lower bearings (secondary dissipation mechanism). The frictional heat generated at these interfaces flows to the cylinder and the piston (normal heat fluxes). As no energy is lost during operation, the dissipation of mechanical energy is equivalent to its conversion to heat energy. Both dissipation (heat generation) mechanisms are considered in the subsequent TTM model development.

The compression of the SA is governed by the flow of hydraulic oil through the primary orifice plate (7), whereas the rebound (extension) of the LG is controlled by the flow through the recoil orifice, which is part of the upper bearing assembly (5). The primary orifice plate is held in place with a support tube (6). A Piccolo tube (8) (also called metering pin) is attached to the Piccolo tube base (4), which is approximately situated in the middle of the piston, and changes the flow rate through the orifice. The components (6)-(8) are not considered in the thermal model, but contribute to the dynamic response of the LG SA. The design of the Piccolo tube is key for determining the stroke-variable damping characteristics of the LG SA, and is different for each type of LG. The cross-sectional area of the recoil orifice is also stroke-variable and often mechanically realized using a stroke-dependent flapper valve.

When operating on smooth runways, the LG SA endures only heavy loadings during the landing impact, which usually does not last longer than several milliseconds. However, when operating on rough runways, the mechanical energy is dissipated during the entire operation, which lasts several seconds, or even minutes. Consequently, the heat within the LG SA accumulates during the operation on a rough runway and the heat generation process can be considered as a repetitive process. Although the SA stroking amplitude is small, it is the relative sliding speed that is key to the mechanical energy dissipation process (proportional to the square of the relative sliding speed).

Definition of LG Chambers

In assembling the piston and the cylinder, and designing the orifices, several compartments, called *chambers*, can be defined (see Fig. 2.1). The advantage of defining chambers within the LG system is that the theory of thermodynamics can be applied. Consequently, relatively simple equations can be derived by using the First and Second Laws of thermodynamics that describe the TTM behavior of the LG SA from a macroscopic point of view. The thermodynamic laws are applied to the open hydraulic and closed gas chambers that are pressurized, by considering several assumptions that are defined in Section 2.4.

Chamber I Although for the present LG type no physical barrier exists between the hydraulic oil and the nitrogen gas, the nitrogen volume (or virtual chamber) is historically referred to as chamber I. Chamber I can be physically considered as open, as the orifice support tube (6) passes through chambers I and II. However, from a thermodynamic point of view, and as any mixing of the nitrogen gas and the hydraulic oil is ignored, chamber I is considered as a closed chamber that follows a polytropic transformation during the compression/extension of the LG SA. For the purpose of simplifying the governing equations, the nitrogen gas is considered as a perfect gas.

Chamber II The largest chamber in the LG SA that is filled with hydraulic oil and that is in contact with chamber I is defined as chamber II. Although not defined by a physical barrier at the top, the remaining borders of chamber II are the SA and piston walls. The top border of chamber II corresponds to the mean oil level inside the LG SA, and consists of an emulsion of nitrogen gas and hydraulic oil present as foam at this interface. Chamber II is an open chamber, as hydraulic oil flows in and out through both orifices, which changes the volume of chamber II. This chamber is also considered as being the exchange chamber through which the hydraulic oil from chambers III and IV flows.

Chamber III The second-largest chamber in the LG SA is denoted as chamber III. During ground maneuvers, this chamber is generally far away from the upper and lower bearings. The primary heat generation in chamber III is due to the hydraulic oil exchange with chamber II.

Chamber IV The smallest chamber in the LG SA is chamber IV, and it is closest to the Thermal Zone of Interest (TZI). Consequently, the energy dissipated at the upper and lower bearing interfaces can flow into this chamber. Although chamber IV is the smallest chamber in the LG SA, it has the largest area of the surrounding SA walls that are in contact with the surrounding air, which leads to an increased heat evacuation potential.

Definition of Chamber Interactions and LG Operation

As the geometry of both orifices is variable, the TTM behavior of the LG SA is different during compression and extension. The compression of the LG SA occurs at a relatively high compression speed, whereas the extension is relatively slow. During compression, the oil flows through the orifices as chambers I, II and III are compressed and chamber IV is extended. During extension, the process is reversed.

The difference of hydraulic pressure between chambers II-IV ensures the damping function and the conversion of the mechanical energy to heat by squeezing the flow through the orifices. When passing through the orifices, a turbulent hydraulic oil flow (or turbulent jet) is generated, in which the mechanical energy is dissipated. The heat is stored within each chamber and

partially transferred to the nonadiabatic SA walls. The difficulty of modeling the turbulent jets is overcome by applying the theory of thermodynamics to the various chambers of the LG SA.

Both the pressure and temperature of each chamber are included by considering the variation of the specific enthalpy within each chamber. The combination of the thermodynamic differential equations leads to a matrix system that reveals, together with the frictional heat energy generation, the heat sources and sinks within the LG SA and the importance of each dissipation mechanism.

The definition of the LG components reveals that multiple physics interact together and that multiple heat sources and heat sinks exist. A thermo-tribomechanical (TTM) model is defined in Section 2.3, which summarizes the functional links between the LG components and illustrates how each LG component contributes to the TTM behavior of the LG SA.

2.2 TTM Model Development Strategy

The LG system as defined in Section 2.1 is designed and engineered to allow for rapid compression and extension paired with a considerable stroking amplitude. This motion, however, occurs mostly only once per flight cycle of the aircraft. On rough runways, the LG SA undergoes a repetitive cycle of compressions and extensions, which suggests that the mechanical, the tribological as well as the thermal response of the LG SA are closely related. As has been described in Section 2.1, the thermal response of the LG cannot be neglected for maneuvers on rough runways.

In order to determine the relationships between the individual thermo-, tribo- and mechanical responses of the LG SA, the LG SA system is divided into subsystems. In other words, the mechanical response is governed by the distribution of the loads and the structural response of the SA, whereas the tribological response is determined by the rheological laws of the lubricant between the moving (piston) and the stationary (cylinder) parts of the LG SA. The thermal response of the LG SA can be seen not only as a result of the mechanical and tribological responses, but also as a feedback element of the system. More precisely, it is through the thermal response (or temperature) that the combined tribomechanical response is governed.

The model development is equivalent to the development of each of the subsystems, each with different physics. Nonetheless, it is only the combination of all that results in determining which of the three responses is dominant. Whichever subsystem dominates is dependent on the input parameters (e.g., LG configuration, physical properties of the LG components), and the runway and operating conditions.

2.3 TTM Model and Simulation Algorithm

The development of a TTM model of a LG SA which identifies the heat sinks and heat sources and determines the position and instant of the occurrence of the maximum temperature, is one of the major steps required in order to understand the global TTM behavior of a LG SA.

A system diagram of the TTM model is shown in Fig. 2.2 and is subdivided into three subsystems (thermal, tribological and mechanical) and one interface module, each including two submodels. Each LG component and chamber identified in Section 2.1 contributes in each subsystem to the overall TTM behavior of the LG SA.

The spring and damper functions of the LG SA are included in the dynamic submodel. In addition, the pressure and temperature within chamber I (denoted as p_1 and θ_1) are driven by the output of the dynamic submodel. The load vector $\mathbf{f}$ is applied to the cylinder (1) and the piston (3) to determine the bearing pressures in the lower (2) and upper (5) bearings (see Fig. 2.10). The lubricant governed by the rheology submodel is modeled between the upper and lower bearing interfaces in the EHD submodel. The temperatures and pressures of chambers II-IV are determined using the thermodynamic submodel. All LG components apart from components (6) - (8) are considered in the thermal submodel. The mathematical details together with the governing physical equations of each subsystem, including their submodels, are elaborated in the following sections. The result is a complete theoretical description of a simplified 3D, transient TTM characteristic model of a cantilevered MLG, which can be found on common commercial airplanes.

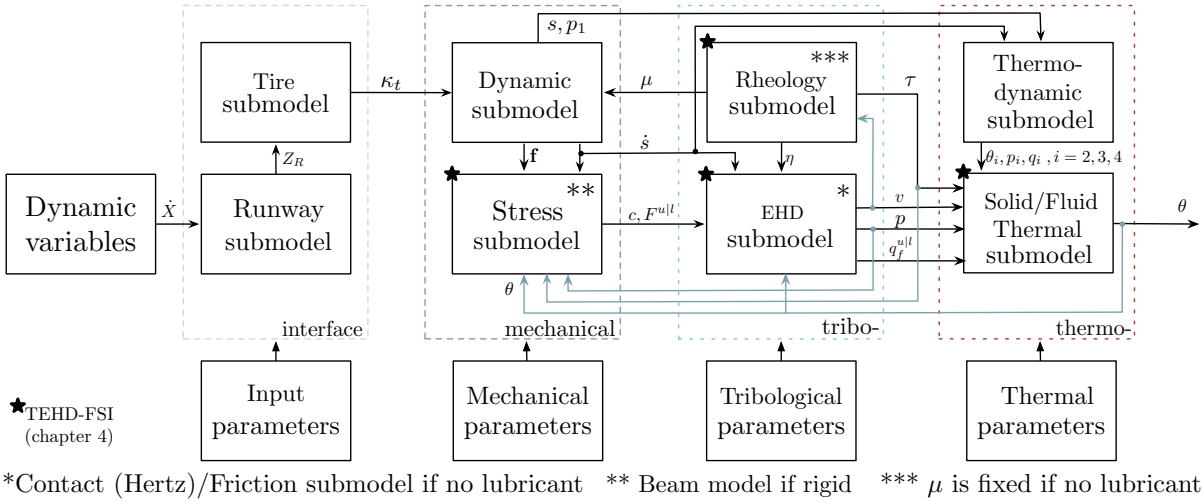

Figure 2.2: System diagram of the thermo-tribomechanical model (TTM model).

In simple terms, the thermal response θ of the LG SA depends on the dynamic input and can only be determined once the appropriate boundary conditions and heat sources/sinks are known (calculated by the governing equations of the thermo-, tribo- and mechanical subsystems).

Interface Module

The dynamic variables, such as the ground speed $\dot{X}$ of the aircraft, are input to the submodels of the input subsystem, in which the runway profile Z_R and the deformation of the tire (through stiffness κ_T) are captured. The output of the tire submodel is driven by the input of the runway submodel and is provided to the mechanical subsystem.

Mechanical Subsystem

The dynamic submodel provides the loads $\mathbf{f}$ acting on the LG SA, induced by the rough runway profile through the tire. Additionally, the relative sliding speed $\dot{s}$ and stroke s that yield the LG gas chamber pressure p_1 are calculated in the dynamic submodel. If the LG components are considered to be rigid, the forces acting on the bearings $F_{u|l}$ are calculated using a simplified beam submodel; otherwise, the stress submodel provides the structural deformations and the updated clearance c at the LG SA bearings.

Tribological Subsystem

The contact pressure p and contact area in the lower and upper bearing are calculated in a contact model (Hertz). If the lubricant is modeled using EHD principles, the hydrodynamic pressure p that is equivalent to the contact pressure p and the fluid flow velocity field v are determined in the EHD submodel. In addition to the shear stress τ at the sliding interface, the viscosity η of the lubricant is determined in the rheology submodel, which, for a simple case, equals an empirical BFC μ. In addition to the friction forces, the frictional heat fluxes $q^f_{u|l}$ are calculated.

Thermal Subsystem

Once the dynamic response of the system is known, the bulk chamber pressures p_i and temperatures θ_i in each of the three chambers of the LG SA (see Fig. 2.10) filled with the hydraulic oil ($i = 2, 3, 4$) are calculated in the thermodynamic submodel. Empirical correlations for the heat transfer coefficients (HTCs) are used to determine the convective heat fluxes q_i. The heat diffusion equation in cylindrical coordinates is solved in a commercial software package using FE. The temperature response θ is the main output of the system and is fed back to the tribological module, which in turn affects the dynamic response of the LG.

Simulation Algorithm

The underlying algorithm used to calculate the thermal response of the LG SA is given in Algorithm 1. A 'weakly' coupled simulation (sequential runs until convergence) is preferred to a strongly coupled simulation, as the thermal response of the system is much slower than its dynamic response. The thermal contribution of the repetitive impact energy dissipated into heat is studied, the effect of the various heat sources/sinks in the LG SA on the maximum temperature in the TZI are quantified, and the root-cause of the heat damage is confirmed in Section 2.8. The TZI is the region near the lower bearing-piston interface. Emphasis is placed on studying the evolution of the average temperature in the TZI while taxiing and taking-off. In addition, it is shown that, during the aircraft ground maneuvers, the SA oil acts as a heat sink and not as a heat source, leading to the conclusion that the heat energy dissipated during a single landing impact does not contribute significantly to the LG lower bearing overheating. The sensitivity of the maximum heat flux to variations of key runway parameters is studied, which reveals that the LG lower bearing overheating is affected primarily by the runway amplitude.

Algorithm 1 Simulation algorithm (weakly coupled simulation).

```
BEGIN
Read SA configuration (geometry)
Calculate runway input
Initialize pressures, temperatures, loads, velocities and displacements
Initialize heat fluxes, friction and HTCs
DO WHILE (structural temperature not converged)
    Calculate loads, BFCs and friction forces
    DO WHILE (temperature in SA not converged)
        Calculate velocities, chamber pressures and chamber temperatures
    END DO
    Calculate HTCs, convective heat fluxes and friction forces
    Calculate contact pressures and frictional heat fluxes
    Calculate structural temperature field
    IF(bearing is not dry) Calculate new viscosity
END DO
Plot results
END
```

2.4 Characteristic Assumptions

Before providing the mathematical descriptions of each submodel, a few assumptions must be given. Most of the listed assumptions are alleviated or refined in Chapter 4. The transient analysis is only performed in the case of steady acceleration of the aircraft on the runway and constant speed taxiing (highest WOG and $\dot{X}$). The ranges of the different study variables, such as the WOG or the take-off (or taxiing) speed, are chosen for a single aisle commercial aircraft. For the sake of simplicity, no vibrations or noise are considered.

Interface Module

The dynamic input variables are derived as a function of stroke and stroke velocity, and depend on the initial thermodynamic state and the SA configuration. The LG thermal behavior is studied using a simplified runway profile, which is empirically chosen to provide an oscillatory vertical force. The profile and its first spatial derivative are continuous (the runway profile is C^1), in order to avoid jerks in the LG input force. The bump height is assumed to be constant, but can be modeled as random. The tire is modeled to be constantly contacting the runway surface at only one point. Tire slip is negligible in any direction.

Mechanical Subsystem

As the cantilevered MLG is twin-wheeled, the load is equally shared between both tires. The dynamic model is a pure 2-DOF (1 vertical translation per body) model, rigidly fixed to the airframe. The aircraft is not turning, so that no side loads (not to be confused with aerodynamic side loads) contribute to the dynamic excitation of the LG system. Engine reverse thrust is zero and the total braking force is provided solely by the aircraft brakes. The aircraft center of gravity

is assumed to be above the LG and is not laterally or longitudinally shifted (same longitudinal position as the MLG). The vertical tire stiffness follows an empirical model. Additionally, the aerodynamic drag load created by the surrounding airflow is not considered.

For the purpose of studying the global behavior exclusively, the stresses generated in the structure are independent of the temperature, which allows conclusions to be drawn on the sensitivity of the maximum temperature in the TZI to a change of input variables, while not being biased by the mechanical strain. By ignoring the thermal expansion of the structural components, the governing equations are considerably simplified, which leads to a reduced computation time. In other words, the uncoupling of the mechanical stress and thermal model is equivalent to assuming that the structural components are rigid and initially stress-free (e.g., no thermal mismatch stresses are considered): $\overline{\boldsymbol{\sigma}}(\mathbf{r},\theta,t) : \boldsymbol{\nabla}\dot{\overline{\mathbf{u}}}(\mathbf{r},t) \ll 1$, where $\overline{\mathbf{u}}$ is the normalized displacement field and $\overline{\boldsymbol{\sigma}}$ the normalized stress field.

The dissipated power (friction and damping) during the motion of the piston is much higher than the power loss due to structural deformation. Strains and strain rates are assumed to be small, and the influence of the inertial contribution on the contact pressures is not considered.

Tribological Subsystem

In a simplified friction model, all the ranges of the BFC are empirically chosen. The upper and lower dynamic BFCs are assumed to be 80% of the static BFC, and the critical stiction speed is assumed to be 0.1mm/s. The BFCs are assumed to be exclusively velocity and temperature dependent. The eventual sudden 'burning' of grease, which happens at the dropping point (temperature at which the lubricating characteristics of the grease deteriorate), is modeled using a step function. The simulation for lubricated friction loses validity after the dropping point temperature. The friction model is then adapted to pure dry friction. Only lubricated metal-metal contact and no seals or visco-elastic materials are considered. The average BFC, which is derived by following the viscous Stribeck friction model, takes into account the metal-metal contact as well as the EHD lubrication that occurs when a bearing load is applied, and exists over a wide range of temperatures.

Thermodynamic/Thermal subsystem

No local fluid effects are considered within the SA chambers, and the SA stiffness and damping coefficients are derived using fundamental thermodynamics, fluid mechanics and Bernoulli's equation of the conservation energy. In order to simplify at most the governing equations, the nitrogen N_2 in the SA is modeled as a perfect gas that obeys the ideal gas laws. The mechanical energy is dissipated in a turbulent jet created by the orifices (as stated in [90]), which is, however, not modeled (the holes in the support tube are neglected). From experience of having a small thermal effect, neither the nitrogen dissolution, nor cavitation conditions of the SA hydraulic oil are considered. Although the inner chamber walls of the SA are assumed to be perfectly smooth, a coefficient taking into account nonsmooth orifice holes is implemented.

Although the cylinder and piston are moving, it is only the relative speed that is considered for advection in the moving domain (piston). The potential energy change due to gravity is neglected. The viscous damping coefficient of the SA is a function of temperature, as the density of oil is linearly dependent on temperature. The hydraulic SA oil is assumed to be incompressible, as the pressure variations are small within the stroke range and are not believed to have a significant impact on the thermal response of the LG SA.

It is assumed that both ends of the SA are far away from the TZI, such that both ends are adiabatic and initially at the temperature of the fuselage. As the heat is only diffusing slowly through the structure, the heating of the brakes is assumed to have a negligible effect on the TZI. No heat diffusion in the gas or hydraulic oil is considered, as the thermal conductivity of both fluids is low. As the temperature differential is small, no radiation from the SA to the environment is considered. The external temperature is assumed to be constant. The influence of convective cooling of the surrounding air on the TZI is studied, and is modeled using an average convective HTC. Local turbulence is not considered.

In order to simplify the model development, no side loads are considered, which results in a 3D and half-cylindrical thermal model. Only the cylinder and the piston are considered, and any other parts (such as the orifice plate) are not included, as they have a small effect on the maximum temperature in the TZI. For thermal calculations only, it is assumed that the Piccolo tube has a constant radius.

2.5 Review of Relevant Physical Properties

2.5.1 Fluid and Solid Materials

Nitrogen Gas and Surrounding Air

The heat capacity of N_2 is assumed to be temperature invariant and is equal to $c_{p_{N_2}} = 1040$ J/kg/K. The properties of the surrounding air are taken from [91] and are evaluated at STP conditions. In the range of interest of the external temperature θ_5, the thermal conductivity of air varies linearly with θ. The interpolation coefficients have been determined using the least squares method: $k_{\theta a}(\theta_5) = 7.455 \cdot 10^{-5} \cdot \theta_5 + 3.737 \cdot 10^{-3}$. The kinematic viscosity of air varies linearly with temperature. The interpolation coefficients have been determined using the least squares method: $\nu_a(\theta_5) = 8.814 \cdot 10^{-8} \cdot \theta_5 - 1.060 \cdot 10^{-5}$. The Prandtl number for the air flow around the cylinder is constant over the temperature range: $\mathrm{Pr}_a = 0.71$.

Shock Absorber Hydraulic Oil and Base Oil of the Lubricant

As the oil is considered incompressible, the specific heat capacity at constant pressure is equal to the specific heat capacity at constant volume. The physical properties for the SA oil (referenced by MIL-H-5606), which is also considered the base oil of the lubricant, are taken from [92]. The heat capacity c_{p_i} in chamber i of the SA oil depends linearly on θ: $c^*_{p_i} = c^*_p(\theta_i) = G_1\theta_i + G_2$.

The interpolation coefficients have been determined using the least squares method[3]. The data for the thermal conductivity as a function of temperature have been retrieved from [92]. The thermal conductivity of the SA oil varies linearly with temperature and can be expressed as: $k^*_{\theta i} = k_\theta(\theta_i)$. The conductivity is very low compared to the solid materials surrounding the SA oil. The properties $k^*_{\theta i}$ and $c^*_{p_i}$ do not vary significantly over the temperature range.

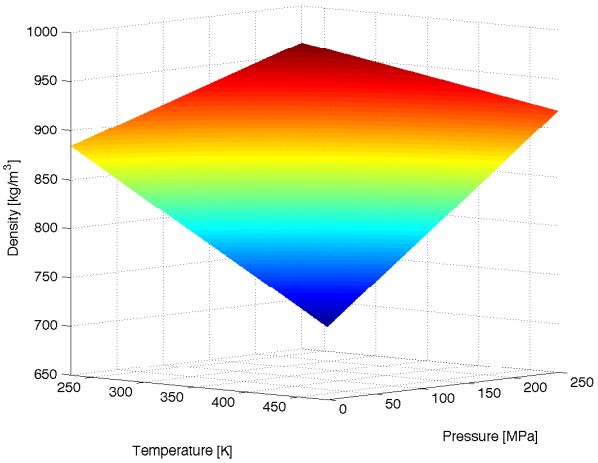

Figure 2.3: Density ρ^* of the oil.

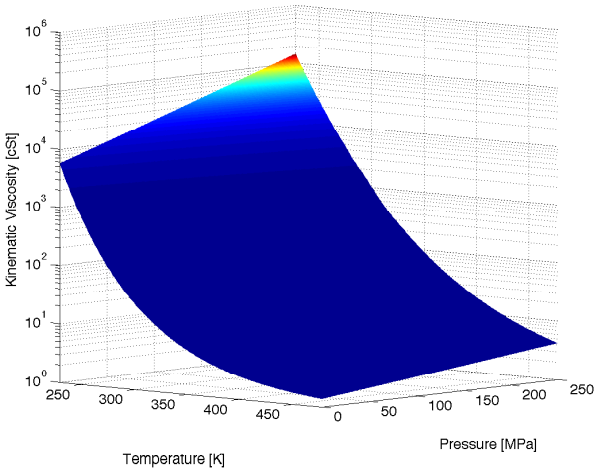

Figure 2.4: Kinematic viscosity ν^* of the oil.

The density of the hydraulic oil $\rho^*(p_i, \theta_i)$ in chamber i of the SA oil is linearly dependent on θ_i but not on p_i (see Fig. 2.3), and is expressed as $\rho^*_i = (G_3 p_i + G_4)\,\theta_i + \left(G_5 p_i^3 + G_6 p_i^2 + G_7 p_i + G_8\right)$. By following the methodology (ASTM) and the suggestions given in [93], the kinematic viscosity $\nu^*(p_i, \theta_i)$ (see Fig. 2.4, expressed in cSt) can be expressed as (in SI units): $\nu^*_i = G_{15}\left(\exp\left(\exp\left(G_9 \ln 10 - G_{10} \ln\theta_i\right)\ln 10\right) - 0.7\right) \cdot \exp\left(\left(G_{11}\theta_i^3 + G_{12}\theta_i^2 + G_{13}\theta_i + G_{14}\right) p_i\right)$.

Solid Materials

The material properties for the structural LG components are assumed to be homogeneous, linear, and temperature independent. The thermal conductivity $k_{\theta M}$, heat capacity c_M, density ρ_M, Young's modulus E_M, Poisson's coefficient λ_M, and the coefficient of thermal expansion $\kappa_{\theta M}$ are shown for the materials $M = A, B, C, D$ in Table 2.1. The chrome plating is omitted in Chapter 2, but is considered in Chapter 4.

Quantity	**Unit**	**Al alloy** (A)	**Al-Bronze** (B)	**Steel** (C)	**Chrome** (D)
$k_{\theta M}$	W/(mK)	130	78	13.8	12
$c_{p M}$	J/(kg K)	841	435	400	430
ρ_M	kg/m^3	2800	7700	8000	8730
E_M	GPa	68	110	210	200
λ_M	/	0.30	0.32	0.28	0.3
$\kappa_{\theta M}$	1/K	$2.2 \cdot 10^{-5}$	$1.8 \cdot 10^{-5}$	$1.2 \cdot 10^{-5}$	$1.2 \cdot 10^{-5}$

Table 2.1: Physical properties of solid material evaluated at 20°C [91, 94].

[3] $G_1 = 4.295$; $G_2 = 600.110$; $G_3 = 3.067 \cdot 10^{-9}$; $G_4 = -7.3525 \cdot 10^{-1}$; $G_5 = 3.369 \cdot 10^{-22}$; $G_6 = -3.688 \cdot 10^{-14}$; $G_7 = 6.286 \cdot 10^{-7}$; $G_8 = 1.071 \cdot 10^{3}$; $G_9 = 7.263$; $G_{10} = 2.889$; $G_{11} = -9.310 \cdot 10^{-15}$; $G_{12} = 9.381 \cdot 10^{-12}$; $G_{13} = -3.192 \cdot 10^{-9}$; $G_{14} = 3.845 \cdot 10^{-7}$

2.5.2 Rheology of Lubricant

The dynamic viscosity of a non-Newtonian lubricant, such as grease, is dependent on the temperature θ (following Arrhenius' law), pressure p and the shear rate $\dot{\gamma}$. An analytical function is not determined, but the viscosity data are interpolated during the simulation. The advantage of dynamic interpolation is that *any* lubricant can be used, as long as the viscosity relationship $\eta\,(p, \theta)$ is known.

The lubricant is a common aerospace lubricant, which at room temperature is in a semisolid state, and its rheological model is governed by $\mathcal{N} = \eta(p, \theta, \dot{\gamma}) = \eta_{\dot{\gamma}}(\dot{\gamma}) \cdot \eta(p, \theta)$. The dependency of the lubricant's viscosity on the shear rate can be modeled using the power law $\eta_{\dot{\gamma}}(\dot{\gamma}) = \eta_{\dot{\gamma}}^{0} \cdot \dot{\gamma}^{m-1}$, where m is the order of the lubricant, which is, in general, determined experimentally. In the application of a LG, the shear rate dependency on the viscosity does not have a decreasing effect, as shown in [95], and is omitted by considering that the order of the grease is $m = 1$ (Bingham grease): $\eta(p, \theta, \dot{\gamma}) = \eta(p, \theta)$. The particularity of grease is a discontinuous shear stress as a function of the shear rate, marked by a yield shear stress τ_0, which, for grease in LG lower bearings, is around 200Pa [61, 82]. The effect of the shear rate and the non-Newtonian behavior of grease is taken into account with the Herschel-Bulkley model [62]:

$$\tau = \tau_0 + \eta\,(p, \theta)\,|\dot{\gamma}|^{m} \tag{2.1}$$

The viscosity of grease η is given as a function of the base oil dynamic viscosity $\eta^* = \rho^* \cdot \nu^*$ (see Fig. 2.4) such that $\eta = \eta^*\,(1 + 0.25 \cdot \iota)$, where ι is the volumetric fraction of thickener and oil [62]. The typical range of ι for aircraft LG specific greases is $\iota = 0.1 - 0.12$. The dropping point of grease is the temperature at which the grease transforms from a semisolid state into a liquid state, and is around 260°C [96]. The flash point, which is the point at which the grease ignites, is lower and is around 235°C. The useful operating temperature range is considered to be from -65°C to $\hat{\theta} = 204$°C. The density of grease is $\rho = 868$ kg/m^3 (at a temperature of 15°C) and is considered to be constant, although in general, the density depends on the pressure and temperature. In the model, only the dynamic viscosity is affected by a temperature change.

2.6 Subsystem Modeling

In consideration of the characteristic assumptions highlighted in Section 2.4, the submodels of the subsystems that compose the TTM Model shown in Fig. 2.2 are detailed in the following subsections.

2.6.1 Interface Module - Global System Part I

Tire Submodel

Empirical formulas yield the deflection of a LG tire under a given vertical load. It is assumed that the tire damping is provided and dependent on the tire type. The static tire deflection is

calculated using an empirical correlation $\delta_T^0\left(F_T, B_T, p_T, p_T^0, R_T^0\right)$, given in [97] for a specific tire type of commercial aircraft, where F_T is the normal load on the tire, B_T is the width of the unloaded tire, p_T is the pressure of the tire, p_T^0 is the rated pressure, and R_T^0 is the radius of the unloaded tire. The tire deflection δ_T^0 is used to calculate the tire vertical stiffness $\kappa_T^0 = \kappa_T\left(\delta_T^0\right)$, which is considered to be constant [15] under the initial tire load $F_T^0 = \frac{g}{2}\mathrm{tr}(\mathbf{M})$. The tire model is a point model, and no effects of the tire conforming to the runway are considered. The mass matrix $\mathbf{M}$ includes the complete mass of the mechanical system (including W). The total aircraft landing mass and W are linked and can be determined as a function of the location of the center of gravity of the aircraft. As shown in Fig. 2.7, no shift of the center of gravity is considered.

Runway Submodel

The runway elevation is defined as a continuously differentiable cosine wave input ($Z_R \in C^1$), expressed with reference to the spatial period X_R. Every X_R, the LG wheel rolls over a bump. The chosen runway profile in Fig. 2.6 represents a typical runway profile and is considered to be the most representative for studying the impact of the bump spacing X_R and the bump amplitude $\hat{Z}_R$ on the TZI. However, an arbitrary and random profile could be input.

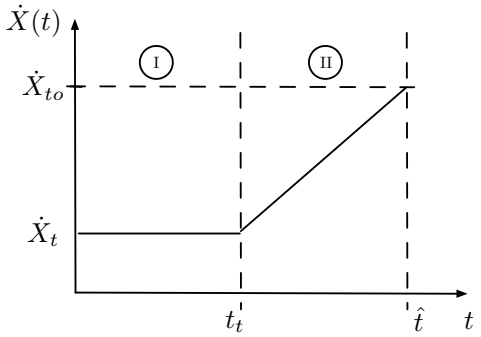

Figure 2.5: Magnitude of $\dot{X}$.

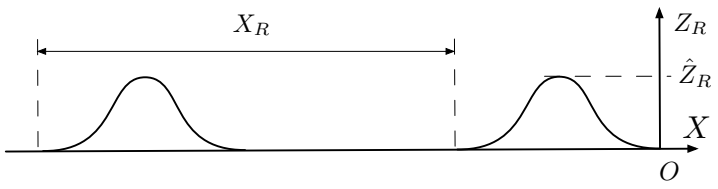

Figure 2.6: Simple runway/taxiway profile [2].

The definition of the runway elevation is given by $\left(\forall i \in \mathbb{N},\ 0 \leq i \leq \hat{X}/X_R\right)$:

$$Z_R(X) = \frac{\hat{Z}_R}{2}\begin{cases} 1 - \cos\left(\dfrac{4\pi}{X_R}X\right) & , i \leq \dfrac{-X}{X_R} \leq i + \dfrac{1}{2} \\ 0 & , i + \dfrac{1}{2} \leq \dfrac{-X}{X_R} \leq i + 1 \end{cases} \tag{2.2}$$

Common practice suggests directing the horizontal axis along the airplane toward its tail. The oncoming airflow velocity $\dot{X}$ is directed along $\mathbf{e}_X$, whereas the ground speed of the aircraft is the opposite. The ground speed $\dot{X}(t) \geq 0$ (see Fig. 2.5) is defined for the taxi and take-off phases, which are representative of an aircraft ground maneuver:

$$\dot{X}(t) = \dot{X}_t\ ,\ \ 0 \leq t \leq t_t \quad \text{and} \quad \dot{X}(t) = \frac{\dot{X}_{to} - \dot{X}_t}{\hat{t} - t_t}\left(t - t_t\right) + \dot{X}_t\ ,\ \ t_t \leq t \leq \hat{t} \tag{2.3}$$

The take-off speed $\dot{X}_{to}$ is weight dependent and is calculated as 110% of the aircraft stall speed (with a load factor of 1). The case of landing is not considered. Although an additional braking force may be present, the WOG and landing speed are lower (and consequently the stroking frequency) than at take-off, which leads to a reduced combined dissipation of heat.

The actual towing of the aircraft from and to the gate is considered as quasi-static and not having an effect on the temperature. The simulation is stopped once the end of taxiing is reached, marked by the time period $\hat{t}$. The runway position of the aircraft is the negative integral of the oncoming airflow velocity $\dot{X}$, assuming that the initial position is zero. The maximum distance, $\hat{X} = X(\hat{t})$, traveled on the runway depends on the weight of the aircraft and is determined using the governing equations of aerodynamics.

2.6.2 Mechanical Subsystem - Global System Part II

Dynamic Submodel

The dynamic submodel used to derive the piston sliding speed as a function of the runway profile and ground speed of the aircraft is a simplified nonlinear 2-DOF model, shown in Fig. 2.7.

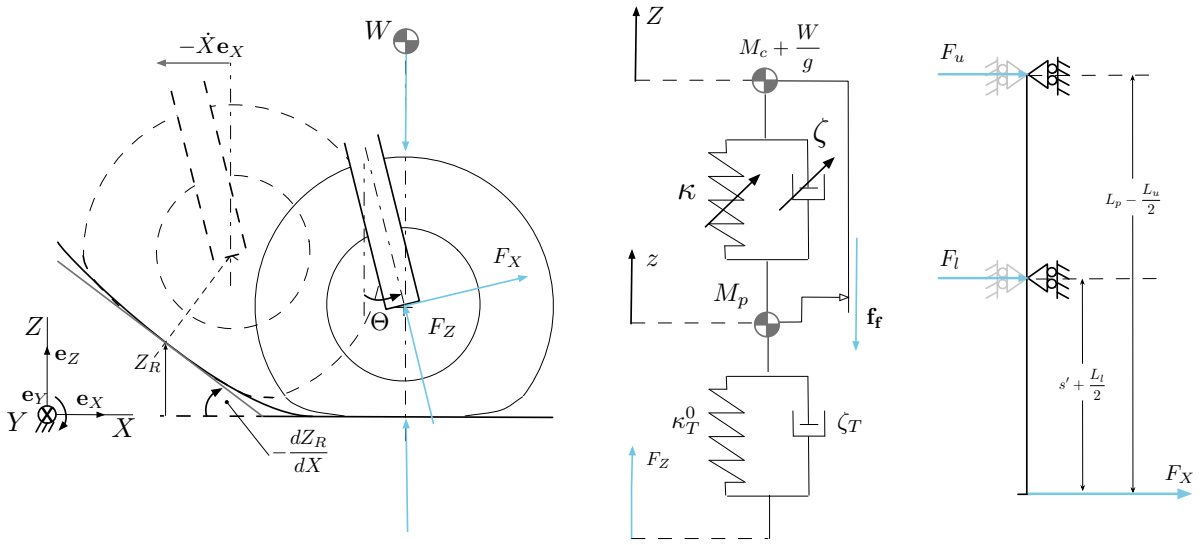

Figure 2.7: Simplified 2-DOF nonlinear dynamic model of a MLG and beam model [2].

The upper mass consists of the reduced aircraft mass (equivalent to W) and the cylinder assembly. The lower mass is the reduced equivalent mass of the piston assembly, including wheels and brakes. The dynamic ground reaction force is derived from static equilibrium as a function of the tire deflection (two tires): $F_T = 2\kappa_T^0 \left(Z_R + \delta_T^0\right) + 2\zeta_T^0 \dot{Z}_R - F_T^0$, where ζ_T^0 is the tire damping coefficient. The horizontal and vertical forces F_X, F_Z are derived using the projection of F_T in the reference frame of the SA, modified using the slope of the runway $Z_{R,X} = \frac{dZ_R}{dX}$. The horizontal and vertical forces on the SA are defined by:

$$\begin{pmatrix} F_X \\ F_Z \end{pmatrix} = F_T \cdot \cos\left(Z_{R,X}\right) \begin{bmatrix} \cos\Theta & -\sin\Theta \\ \sin\Theta & \cos\Theta \end{bmatrix} \begin{pmatrix} \mu_R + \tan\left(Z_{R,X}\right) \\ 1 \end{pmatrix} \tag{2.4}$$

where Θ is the MLG rake angle (negative for aft inclination) and μ_R an equivalent constant Coulomb friction coefficient between the tire and the runway that includes the rolling resistance and the braking of the aircraft. The nonlinear dynamic model is shown in Fig. 2.7. The vertical position states are denoted as $\mathbf{z} = \begin{pmatrix} z(t) & Z(t) \end{pmatrix}^T$. By integrating the piston sliding speed, the position (stroke) is defined as: $s(t) = z(t) - Z(t) + s^0$. The sliding speeds of the reduced aircraft and piston masses are obtained from the dynamic differential equations system of:

$$\mathbf{M}\ddot{\mathbf{z}}(t) + \mathbf{f_c}\left(\mathbf{z}, \dot{\mathbf{z}}\right) + \mathbf{f_k}\left(\mathbf{z}\right) = \mathbf{f}(t) + \mathbf{f_f}(t, \mu) \tag{2.5}$$

where the stiffness and damping forces are defined by:

$$\mathbf{f_k} = \begin{pmatrix} p_1(s)A_P + \kappa_T^0 z(t) \\ -p_1(s)A_P \end{pmatrix} \qquad \text{and} \qquad \mathbf{f_c} = \dot{s}\begin{pmatrix} \zeta(s)\left|\dot{s}\right| + \zeta_T^0 \\ -\zeta(s)\left|\dot{s}\right| \end{pmatrix} \tag{2.6}$$

The damping coefficient $\zeta = \zeta(s)$ is dependent on the stroke of the SA (hence on time). As the damping coefficient is dependent on the damping oil density (linearly dependent on the chamber temperatures), the damping coefficient is also temperature dependent $\zeta = \zeta(s, \theta)$, as shown in Eq. (2.16). The stiffness of the SA that is derived in Section 2.6.4 is dependent on the stroke: $\kappa = \kappa(s)$. As the LG structural components are assumed to be rigid, no structural damping is considered. The mass matrix is diagonal and is written as $\mathbf{M} = \mathrm{diag}\left(M_P, M_c + W/g\right)$. The sign of the relative sliding speed provides the information as to whether the SA is in compression ($\epsilon_{\dot{s}} = 1$) or extension ($\epsilon_{\dot{s}} = -1$), and is defined as $\epsilon_{\dot{s}} = \mathrm{sgn}(\dot{s}), \dot{s} \neq 0$, and $\epsilon_{\dot{s}} = 1, \dot{s} = 0$. The total friction force acting at the lower and upper bearing sliding interfaces is given by: $F^f(t) = F_u^f(t) + F_l^f(t) = \mu_u \left|F_u(t)\right| + \mu_l \left|F_l(t)\right|$. The friction force vector is defined as $\mathbf{f} = \begin{pmatrix} F_Z & 0 \end{pmatrix}^T$, and the input force vector as $\mathbf{f_f} = \epsilon_{\dot{s}} F^f \begin{pmatrix} -1 & 1 \end{pmatrix}^T$. The nitrogen pressure as a function of stroke is denoted as $p_1(s)$ and follows a polytropic transformation. The visible length of the piston is given by $s'(t) = s_e - s(t)$, where s_e is defined as the fully extended length. The initial conditions are given as $z(0) = Z(0) = 0$. The static stroke $s^0 = s(0)$ is defined from an isothermal compression ($\Upsilon = 1$):

$$s^0 = L_o - L_o \frac{p_1^0}{p_1(0)}\ ,\ p_1(0) < \overline{p}_1 \quad \text{and} \quad s^0 = L_o' - \left(L_o' - \overline{s}\right)\frac{\overline{p_1}}{p_1(0)}\ ,\ p_1(0) \geqslant \overline{p}_1 \tag{2.7}$$

where L_o' is the length of the second stage gas pressure (pure extension of chamber I, considered adiabatic at all times) and p_1^0 is the gas charge pressure (unloaded conditions). The breakout pressure for a dual-stage SA is denoted as $\overline{p_1}$. The gas pressure under static load conditions is denoted as $p_1(0) = WA_P^{-1}\cos\Theta$, where the breakout stroke $\overline{s}$ is defined by $\overline{s} = L_o\left(1 - \frac{p_1^0}{\overline{p_1}}\right)^{\frac{1}{\Upsilon}}$.

Beam Submodel

The load analysis that yields the bearing loads that are used in the Hertzian contact model is simplified by using a beam model, illustrated in Fig. 2.7. As the displacements are very small,

the forces acting on each bearing are calculated using static equilibrium with rigid LG structural components (no dynamics and no structural deformations considered):

$$F_l(t) = \frac{L_u - 2L_P}{2L_P - L_u - L_l - 2s'(t)} \cdot F_X(t) \quad , \quad F_u(t) = -F_l(t) - F_X(t) \tag{2.8}$$

It can be seen that $\forall t \in [0, \hat{t}] : \; s \leq s_e \iff s'(t) \geq 0$. The equality only holds for the situation in which no drag load is applied at the axle. In practice, however, this situation never occurs when the aircraft is maneuvering on the runway. Under these operating conditions and for all times, the load at the lower bearing is higher than the load at the upper bearing: $|F_l(t)| \geq |F_u(t)|$. As the frictional heat flux is proportional to the normal bearing load, the frictional heat flux at the lower bearing will always be higher than the frictional heat flux at the upper bearing (for these ground maneuvers). This beam model is only an approximation, and a more accurate analysis would be given by a complete stress analysis.

2.6.3 Tribological Subsystem - Global System Part III

Contact Submodel

The parabolic contact pressure profile p_l^H is derived for a convex-concave Hertzian contact [98] under a normal bearing load derived from the beam submodel, and closely follows the model outlined in [25]. The top view of the lower bearing can be seen in Fig. 2.8. For a LG rake angle Θ, the bearing loads are defined as $F_l(t) > 0$ and $F_u(t) < 0$. The semi-contact arc length $\phi'_{l|u}$ yields the area over which the frictional heat flux is input to the piston and cylinder. An equivalent radius, effective elasticity modulus, and semi-contact width are defined in Table 2.2.

Although the contact model has been derived under the assumption that no angular frictional forces are present at the contact interface, the surfaces are dry (or can be modeled with an equivalent friction coefficient), and the contact length is infinite, the Hertzian theory serves as a reasonable, but preliminary approximation of the contact stresses at the interface. As the LG structural components are considered to be rigid, the cylinder and piston do not change shape due to the temperature increase (inflation) or due to load (ovalization).

	Lower Bearing	**Upper Bearing**
Equivalent radius	$\frac{1}{R'_l} = \frac{1}{R_P - c_0} - \frac{1}{R_P}$	$\frac{1}{R'_u} = \frac{1}{R_c - B - c_0} - \frac{1}{R_c - B}$
Effective elasticity modulus	$\frac{1}{E'_l} = \frac{1-\lambda_B^2}{E_B} + \frac{1-\lambda_C^2}{E_C}$	$\frac{1}{E'_u} = \frac{1}{E'_l}$
Semi-contact width	$a'_l = \sqrt{\frac{4\lvert F_l(t)\rvert R'_l}{\pi E'_l L_l}}$	$a'_u = \sqrt{\frac{4\lvert F_u(t)\rvert R'_u}{\pi E'_u L_u}}$
Semi-contact arc length	$\phi'_l = \sin^{-1}\left(\frac{a'_l}{R_P}\right)$	$\phi'_u = \pi - \sin^{-1}\left(\frac{a'_u}{R_c - c_0}\right)$

Table 2.2: Hertzian contact model parameters.

Friction Submodel

In the ideal Hertzian contact model, the contact pressure is zero everywhere, but not within the semi-contact arc length ($0 \leq \phi \leq \pi$):

$$p^H_{l|u} = \sqrt{\frac{\left|F_{l|u}(t)\right| E'_{l|u}}{\pi L_{l|u} R'_{l|u}} \left(1 - \frac{R_P^2}{a'^2_{l|u}} \sin^2\phi\right)}, \quad \phi < \phi'_l \quad \text{or} \quad \phi > \phi'_u \tag{2.9}$$

The clearance c_0, considered constant at the upper and lower bearings, is filled with a lubricant. In order to quantify the frictional heat fluxes at the contacting surfaces without performing a TEHD analysis (see Chapter 4), it is suggested to derive an average and equivalent BFC at the bearing sliding interfaces. The friction model that yields the BFC is an odd function, such that during stiction, the absolute friction force is equal in any sliding direction.

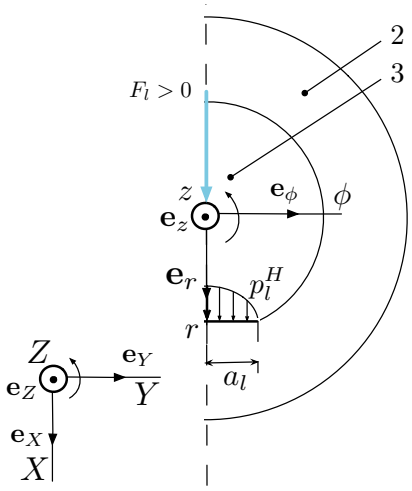

Figure 2.8: Bearing Hertzian contact pressure profile [2].

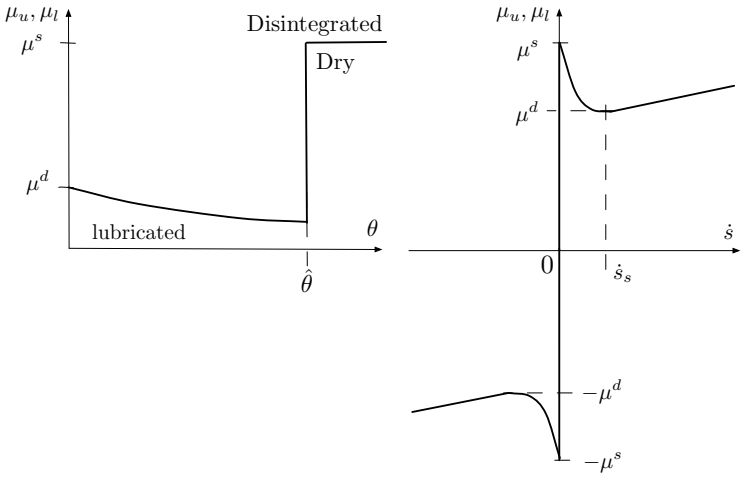

Figure 2.9: BFC as a function of relative sliding speed and temperature [2].

The upper and lower bearing friction forces $F^f_{l|u}$ follow the SWITCH Model [99] for viscous Stribeck friction, and are dependent on the configuration of the bearings and the operating conditions such that:

$$F^f_{l|u} = \begin{cases} \min\left(|F_{ex}|, \dfrac{1+\beta\mathcal{H}}{\beta+\mathcal{H}}\hat{\mu}^s \left|F_{l|u}(t)\right|\right) \cdot \operatorname{sgn}(F_{ex}) & , |\dot{s}| < \dot{s}_s \\ \epsilon_{\dot{s}} \dfrac{1+\beta\mathcal{H}}{\beta+\mathcal{H}} \left|F_{l|u}(t)\right| \left(\hat{\mu}^d + \left(\hat{\mu}^s - \hat{\mu}^d\right) e^{-\left|4\dot{s}\dot{s}_s^{-1}\right|}\right) + \epsilon_{\dot{s}} (1-\mathcal{H}) 2\pi R_{l|u} L_{l|u} \dfrac{\eta\left(\theta_{l|u}\right)|\dot{s}|}{c_0} & , |\dot{s}| \geq \dot{s}_s \end{cases} \tag{2.10}$$

where $\dot{s}_s$ is the stiction speed, η the dynamic viscosity of the lubricant, and F_{ex} is the externally applied force during stiction, derived from the conservation of momentum [16]:

$$F_{ex} = \frac{\mathbf{M}\mathbf{e}_2 \cdot \mathbf{e}_2}{\operatorname{tr}(\mathbf{M})}(\mathbf{f}\mathbf{e}_1 - \mathbf{f}_\mathbf{c}\mathbf{e}_1 - \mathbf{f}_\mathbf{k}\mathbf{e}_1) - \frac{\mathbf{M}\mathbf{e}_1 \cdot \mathbf{e}_1}{\operatorname{tr}(\mathbf{M})}(-\mathbf{f}_\mathbf{c}\mathbf{e}_2 - \mathbf{f}_\mathbf{k}\mathbf{e}_2) \tag{2.11}$$

where $\mathbf{e}_i$ are unit vectors. The radii at the lower and upper bearings are defined as $R_l = R_P$ and $R_u = R_c - c_0$. The lower and upper BFCs are calculated as $\mu_{l|u} = F^f_{l|u}(t)/F_{l|u}(t)$. The ratio between the dry and the lubricated BFCs is defined as $\beta = \hat{\mu}^d \cdot \left(\mu^d\right)^{-1} = \hat{\mu}^s \cdot \left(\mu^s\right)^{-1} = 0.8$.

The temperature dependent viscosity η yields a temperature dependent BFC. The transition between lubricated and dry friction happens at a precise instant in time, as the grease disintegrates [39], once the maximum operating temperature $\hat{\theta}$ has been reached (see Fig. 2.9). The transition is modeled with the Heaviside step function $\mathcal{H} = \mathcal{H}\left(\theta_{l|u} - \hat{\theta}\right)$, where the interface temperatures $\theta_{l|u}$ are area averaged temperatures at the lower and upper bearings.

2.6.4 Thermal Subsystem - Global System Part IV

Thermal Submodel

The aim of the thermal model shown in Fig. 2.10 is to determine a continuous and smooth temperature field $\theta : \mathbb{R}^3 \times \mathbb{R}_+ \to \mathbb{R} : (\mathbf{r}, t) \mapsto \theta(\mathbf{r}, t) \in C^2(\Omega)$ at a position $\mathbf{r}(r, \phi, z) \in \Omega$ that satisfies the applied boundary conditions in the homogeneous and isotropic domain $\Omega(t) = \tilde{\Omega}(t) \cup \hat{\Omega}$ for time invariant and temperature independent material properties. For the thermal analysis, the support tube (6), the orifice plate (7) and the Piccolo tube (8) are not considered. The stationary domain is the union of all the stationary components: $\hat{\Omega} = \bigcup_{i \in \hat{\mathcal{D}}} \Omega_i(t)$, and the moving domain is the union of all the moving components: $\tilde{\Omega}(t) = \bigcup_{i \in \tilde{\mathcal{D}}} \Omega_i(t)$. The index span $\mathcal{D} = \hat{\mathcal{D}} \cup \tilde{\mathcal{D}}$ is the union of the index spans of a stationary domain $\hat{\mathcal{D}} = \{1, 2\}$ and a moving domain $\tilde{\mathcal{D}} = \{3, 4, 5\}$. Each domain $i \in \mathcal{D}$ corresponds to a component of the SA (see Table 2.3) and is defined as: $\Omega_i(t) = \{r \in \mathbb{R}_+ : \mathcal{R}\} \times \Phi \times \{z \in \mathbb{R}_- : \mathcal{Z}\}$, where the angular domain Φ corresponds to a 3D half-cylindrical model: $\Phi = \{\phi \in \mathbb{R} : 0 \leq \phi \leq \pi\}$. The domain border $\Gamma(t) = \partial\Omega(t)$ is subdivided in different sub-boundaries, indexed by $\mathcal{B} = \{1, ..., 7\}$. The mobility parameter $\breve{m}_i$ is given by $\breve{m}_i = 1,\ i \in \tilde{\mathcal{D}}$ and $\breve{m}_i = 0,\ i \in \hat{\mathcal{D}}$, and activates the advective contribution in the transient heat diffusion equation, which is written as $\left(\forall\ (\mathbf{r}, t) \in \Omega(t) \times [0, \hat{t}],\ i \in \mathcal{D}\right)$:

$$\partial_{,t}\theta - \breve{m}_i\ \dot{s}(t)\ \theta_{,z} = \lambda_{\theta M}\ \boldsymbol{\nabla}^2\theta \tag{2.12}$$

where $\lambda_{\theta M}$ is the thermal diffusivity of material M [25].

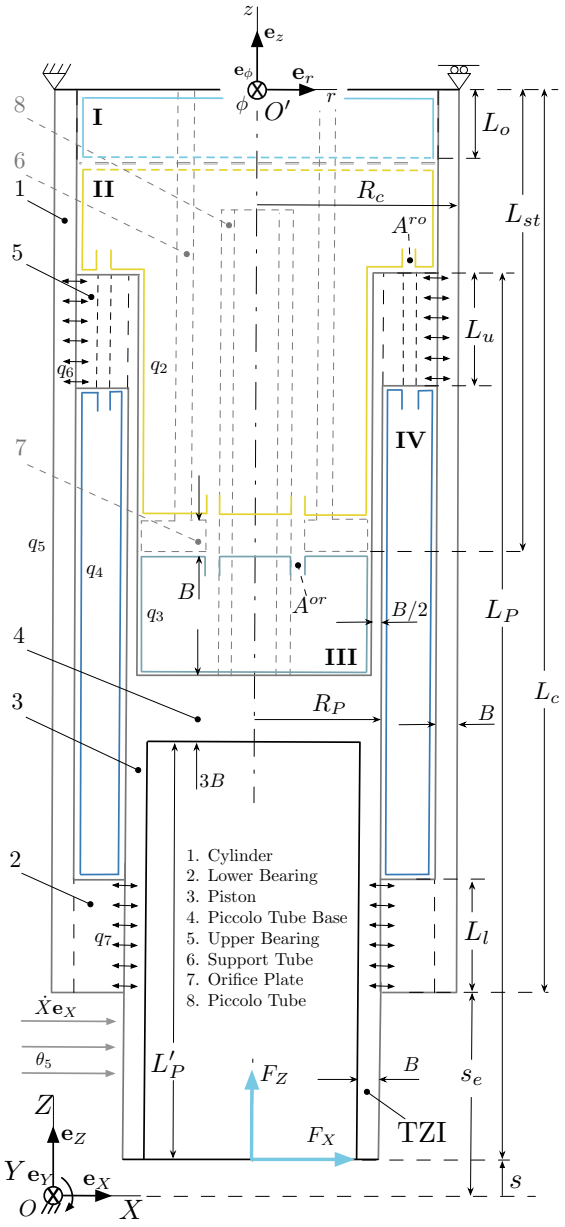

Figure 2.10: Thermodynamic chamber and geometry definitions together with the heat fluxes within the LG SA [2].

i	**Domain Name**	**Condition** $\mathcal{Z}$	**Condition** $\mathcal{R}$	**Material** M
1	**Cylinder**	$-L_c \leq z \leq 0$	$R_c - B < r < R_c$	C
2	**Lower Bearing**	$-L_c \leq z < -L_c + L_l$	$R_P \leq r \leq R_c - B$	A,B (coating)
3	**Piston**	$0 \leq z + s'(t) + L_c \leq L'_P + 3B$	$R_P - B \leq r \leq R_P$	C
		$0 \leq z + s'(t) + L_c \leq L_P$	$R_P - B/2 \leq r \leq R_P$	C
4	**Piccolo Tube Base**	$0 \leq z + s'(t) + L_c - L'_P \leq 3B$	$0 \leq r \leq R_P - c_0$	C
5	**Upper Bearing**	$-L_u \leq z + s'(t) + L_c - L_P \leq 0$	$R_P \leq r \leq R_c - B$	A,B (coating)

Table 2.3: Component list and domain conditions.

The Laplacian is expressed in the cylindrical reference frame $(O', \mathbf{e}_r, \mathbf{e}_\phi, \mathbf{e}_z)$ and the boundary conditions are defined in Section 2.6.5. The structural temperature field, initially homogeneous $(\forall \mathbf{r} \in \Omega(0) \cup \Gamma(0)) \quad \theta(\mathbf{r}, 0) = \theta^0$, is solved with ANSYS.

Thermodynamic Submodel

The First Law of thermodynamics expressed in terms of power for closed and open systems [100] is given by $P = P_Q + P_V$, where P is the total power, P_Q is the heat power supplied and P_V the instantaneous work done on the system.

Based on the First Law, the governing equations of the thermodynamic submodel yield the chamber temperatures θ_i and pressures p_i, which are used to derive the convective heat fluxes in each SA chamber i (see Fig. 2.10). Once the governing energy rate and flow rate equations are expressed, a temperature differential matrix equations system is derived. Although the model considered in the thermal submodel is for half of a SA, the equations for the thermodynamic submodel are derived for a complete SA.

The Second Law of thermodynamics [100], which states that the entropy S can only increase $(\Delta S > 0)$ and that heat flows from a hot to a cold environment, is considered to be verified at all times. The entropy of the process of compression and extension of the SA is considered to increase at all times. The process is considered as irreversible, because heat is transferred through the boundaries to neighboring chambers and the environment.

The SA chambers II-IV contain oil, whereas chamber I contains nitrogen. There is no physical barrier between chamber I and II, and heat and mass transfer can occur, although mass transfer, which happens by the mixing of the fluids (creation of foam), is not considered in this model. Chambers II and III are sealed (no leakage), but no friction is modeled at this sliding interface (piston and support tube), as the frictional heat flux is not considered to contribute significantly to the maximum temperature in the TZI.

Chambers I-IV: Volumes The chambers deform during compression/extension of the SA, but not the actual structure (rigid structural components). The inner cylinder area is given by $A'_c = \pi (R_c - B)^2$, and the inner piston area (closed) is defined as: $A'_P = \pi (R_P - B/2)^2$. The external piston area on which the axle vertical load acts is defined as: $A_P = \pi R_P^2$. The differential stroke (incremental vertical displacement) of the piston is defined as $\Delta s(t) = s(t) - s^0$. The volumes for chambers I-IV are shown in Table 2.4.

	Initial Volume $(t=0)$	**Volume** $(\forall t \in [0, \hat{t}])$
I	$V_1(0) = A'_c L_o$	$V_1(t) = V_1(0) - \epsilon_{\dot{s}} A'_c \lvert\Delta s\rvert$
II	$V_2(0) = A'_c \left(L_c + s_e - s^0 - L_P\right) - V_1(0)$ $+A'_P \left(L_{st} - B - L_c - s_e + s^0 + L_P\right)$	$V_2(t) = V_2(0) + \epsilon_{\dot{s}} A'_P \lvert\Delta s\rvert$
III	$V_3(0) = A'_P \left(L_c + s_e - s^0 - L'_P - L_{st} - 3B\right)$	$V_3(t) = V_3(0) - \epsilon_{\dot{s}} A'_P \lvert\Delta s\rvert$
IV	$V_4(0) = (A'_c - A_P) \left(L_P - s_e + s^0 - L_l - L_u\right)$	$V_4(t) = V_4(0) + \epsilon_{\dot{s}} \left(A'_c - A_P\right) \lvert\Delta s\rvert$

Table 2.4: Volumes and areas of the chambers of the LG SA.

The initial volume of oil and gas $V_1(0)$ is provided, from which the initial volumes in each chamber can be derived. The sum of the chamber volumes is given by $\sum_{i=1}^{4} V_i(t) = \sum_{i=1}^{4} V_i(0) - \epsilon_{\dot{s}} A_P \lvert\Delta s\rvert$, where $A_P \lvert\Delta s\rvert$ corresponds to the piston displacement.

Chambers I and II: Pressures The pressure in chambers I and II follows a polytropic compression of the nitrogen gas in the SA:

$$\left(\forall t \in [0, \hat{t}]\right) \quad p_1(t) V_1(t)^{\Upsilon} = p_1(t') V_1(t')^{\Upsilon} \tag{2.13}$$

where t' is a previous instant in time such that $0 \leq t' < t$ and Υ is the polytropic exponent, which is dependent on the LG SA type and correlated with experimental results. The initial nitrogen pressure is given as $p_1(0)$. In combination with Eq. (2.13), the pressure p_1 is given as:

$$\left(\forall t \in [0, \hat{t}]\right) \; p_1(t) = p_2(t) = p_1(t') \left(\frac{L_o - \Delta s(t')}{L_o - \Delta s(t)}\right)^{\Upsilon(\epsilon_{\dot{s}})} \tag{2.14}$$

For the static or quasi-static case, Υ is dependent on $\epsilon_{\dot{s}}$. For an isothermal compression ($\epsilon_{\dot{s}} = 1$), $\Upsilon = 1$ and an adiabatic extension ($\epsilon_{\dot{s}} = -1$), $\Upsilon = 1.4$. The net heat transfer is only considered during compression, as the extension is considered adiabatic (no heat transfer through the chamber boundaries). As the relative sliding speeds are relatively high, a pure adiabatic or isothermal transformation does not exist. Instead, the transformation is considered to be polytropic, with a polytropic coefficient of $\Upsilon = 1.1$.

Chambers III and IV: Pressures and Volumetric Flow Rates The damping function in a LG SA consists of oil flowing through orifices (a damping orifice and a recoil orifice) that physically separate the chambers. The primary orifice is fixed, but the rebound orifice configuration, and hence the flow rate, change during extension and compression. The geometry of both orifices is not uniform along the vertical axis, and together with viscous losses, leads to combined discharge coefficients $K'^{or}_{\epsilon_{\dot{s}}}$ and $K'^{ro}_{\epsilon_{\dot{s}}}$ that are dependent on the direction of the piston movement, and defined in Table 2.5. Although orifice viscous losses exist, they are considered to be negligible for convective heat transfer, as the length of the orifice is relatively small. The net mass flow rates through the orifices correspond to the internal chamber volume change, and are determined using Bernoulli's modified equation of the conservation of energy, such that $\delta\dot{V}^{or}_{\epsilon_{\dot{s}}} = K'^{or}_{\epsilon_{\dot{s}}} A^{or}_{\epsilon_{\dot{s}}} \sqrt{\lvert\Delta p^{or}\rvert}$ and $\delta\dot{V}^{ro}_{\epsilon_{\dot{s}}} = K'^{ro}_{\epsilon_{\dot{s}}} A^{ro}_{\epsilon_{\dot{s}}} \sqrt{\lvert\Delta p^{ro}\rvert}$. The orifice areas are considered as given.

	Symbol	Compression ($\epsilon_{\dot{s}} = 1$)	Extension($\epsilon_{\dot{s}} = -1$)
Orifice	$K'^{or}_{\epsilon_{\dot{s}}}$	$K_1^{or}\left\lvert\frac{\rho_3}{2}-\frac{\rho_2}{2}\frac{A_1^{or2}}{(A'_P-\pi R_{mp}^2)^2}\right\rvert^{-\frac{1}{2}}$	$K_{-1}^{or}\left\lvert\frac{\rho_2}{2}-\frac{\rho_3}{2}\frac{A_{-1}^{or2}}{(A'_P-\pi R_{mp}^2)^2}\right\rvert^{-\frac{1}{2}}$
Rebound orifice	$K'^{ro}_{\epsilon_{\dot{s}}}$	$K_1^{ro}\left\lvert\frac{\rho_2}{2}-\frac{\rho_4}{2}\frac{A_1^{ro2}}{(A'_c-A'_P)^2}\right\rvert^{-\frac{1}{2}}$	$K_{-1}^{ro}\left\lvert\frac{\rho_4}{2}-\frac{\rho_2}{2}\frac{A_{-1}^{ro2}}{(A'_c-A'_P)^2}\right\rvert^{-\frac{1}{2}}$

Table 2.5: Orifice characteristics and discharge coefficients.

The static pressure differentials connecting chambers II-III and chambers II-IV are given by:

$$\Delta p^{or}(\epsilon_{\dot{s}},t)=\epsilon_{\dot{s}}\dot{s}^2\left[\frac{A'_P-\pi R_{mp}^2}{K'^{or}_{\epsilon_{\dot{s}}}A^{or}_{\epsilon_{\dot{s}}}}\right]^2 \quad \text{and} \quad \Delta p^{ro}(\epsilon_{\dot{s}},t)=\epsilon_{\dot{s}}\dot{s}^2\left[\frac{A'_c-A_P}{K'^{ro}_{\epsilon_{\dot{s}}}A^{ro}_{\epsilon_{\dot{s}}}}\right]^2 \tag{2.15}$$

The pressure differentials yield the pressures in chambers III and IV such that $p_3(t)=p_1(t)+\Delta p^{or}$ and $p_4(t)=p_1(t)-\Delta p^{ro}$. In addition, the pressure differentials $\Delta p^{or|ro}\propto\epsilon_{\dot{s}}\dot{s}^2$ are used in the force equilibrium equation $F_Z-p_1A_P=\Delta p^{or}\left(A'_P-\pi R_{mp}^2\right)-\Delta p^{ro}\left(A'_c-A_P\right)=\zeta\dot{s}\left|\dot{s}\right|$ to yield the damping coefficient ζ of the SA [16]:

$$\zeta(s,\theta)=\frac{\left(A'_P-\pi R_{mp}^2\right)^3}{\left(K'^{or}_{\epsilon_{\dot{s}}}(\theta)\cdot A^{or}_{\epsilon_{\dot{s}}}(s)\right)^2}+\frac{\left(A'_c-A_P\right)^3}{\left(K'^{ro}_{\epsilon_{\dot{s}}}(\theta)\cdot A^{ro}_{\epsilon_{\dot{s}}}(s)\right)^2} \tag{2.16}$$

Chamber I: Temperature A similar law to the polytropic gas law is applicable for the temperature and yields the bulk temperature of chamber I:

$$\left(\forall t\in[0,\hat{t}]\right)\quad p_1(t)^{1-\Upsilon}\theta_1(t)^{\Upsilon}=p_1(t')^{1-\Upsilon}\theta_1(t')^{\Upsilon} \tag{2.17}$$

where t' is a previous instant in time such that $0\leq t'<t$. For higher temperatures, the Benedict-Webb-Rubin (BWR) equation can be used to represent the behavior of real gas, for which the pressure is temperature dependent. In combination with Eq. (2.14), the homogeneous bulk temperature of chamber I is given by:

$$\left(\forall t\in[0,\hat{t}]\right)\quad \theta_1(t)=\theta_1(t')\left(\frac{L_o-\Delta s(t')}{L_o-\Delta s(t)}\right)^{\Upsilon(\epsilon_{\dot{s}})-1} \tag{2.18}$$

Chambers II - IV: Temperatures A convective heat flux through the boundaries of each chamber is considered. Even though the heat flux is input as a boundary condition to the thermal model (see Section 2.6.5), the total heat source is considered as the integral of the convective heat flux over the active boundary surfaces, and is given by:

$$Q_i=2\iint\limits_{\Gamma^{(i)}}\overline{h}_i\left(\theta_i-\theta|_{\Gamma^{(i)}}\right)d\Gamma=2\overline{h}_i\Gamma_i\left(\theta_i-\overline{\theta_i}\right)\quad ,i=2,3,4 \tag{2.19}$$

where the total surface i is given by: $\Gamma_i=\iint\limits_{\Gamma^{(i)}}d\Gamma, i\in\mathcal{B}$, and the average wall temperature is given by: $\overline{\theta_i}=\dfrac{1}{\Gamma_i}\iint\limits_{\Gamma^{(i)}}\theta|_{\Gamma^{(i)}}\,d\Gamma\ ,i=2,3,4.$

Chambers II - IV Internal Energy Rate As shown in Section 2.5.1, the density of the oil (assumed to be incompressible) in chamber i is denoted as $\rho_i(p_i, \theta_i)$, and the specific heat capacity as $c_{p_i}(\theta_i)$. All physical properties are evaluated at the mean pressure and temperature values of the connecting chambers. In order to develop a thermodynamic differential matrix system, it is essential to derive an analytical expression of the material properties. The specific enthalpy in chamber i, defined as $u_i = c_{p_i}\theta_i + \rho_i^{-1}p_i$, is exchanged between chambers, and together with the work done on the chamber, leads to a change in its internal energy. As chambers II-IV are open thermodynamic systems, input and output flow from an adjacent chamber is dependent on the sign of the stroke velocity. The following definition of a binary flow coefficient is adopted:

$$\overline{\epsilon}_{\dot{s}} = \frac{1-\epsilon_{\dot{s}}}{2} = \begin{cases} 0 & \dot{s} \geq 0 \quad \text{(compression)} \\ 1 & \dot{s} < 0 \quad \text{(extension)} \end{cases} \tag{2.20}$$

The chamber internal energy rate (internal power) P_i is derived as:

$$P_i = \frac{d}{dt}\left[\rho_i c_{p_i} V_i(t)\theta_i(t)\right] = V_i\theta_i\left(\frac{d\rho_i}{dt}c_{p_i} + \rho_i\frac{dc_{p_i}}{dt}\right) + \rho_i c_{p_i}\left(\dot{V}_i\theta_i + V_i\dot{\theta}_i\right), i = 2,3,4 \tag{2.21}$$

The total derivative of the oil density within the chamber i, which can be simplified by considering the oil as incompressible and time independent ($\rho_{i,p_i} \simeq 0$), is expressed as:

$$\frac{d\rho_i}{dt} = \frac{\partial\rho_i}{\partial t} + \frac{\partial\rho_i}{\partial p_i}\frac{\partial p_i}{\partial t} + \frac{\partial\rho_i}{\partial\theta_i}\frac{\partial\theta_i}{\partial t} \simeq \frac{\partial\rho_i}{\partial\theta_i}\frac{\partial\theta_i}{\partial t} = \dot{\theta}_i\left(G_3 p_i + G_4\right) \tag{2.22}$$

Similarly, the total derivative of the heat capacity is simplified, as the heat capacity is only dependent on temperature:

$$\frac{dc_{p_i}}{dt} = \frac{\partial c_{p_i}}{\partial t} + \frac{\partial c_{p_i}}{\partial\theta_i}\frac{\partial\theta_i}{\partial t} = \frac{\partial c_{p_i}}{\partial\theta_i}\frac{\partial\theta_i}{\partial t} = G_1\dot{\theta}_i \tag{2.23}$$

Finally, the internal energy rate of chamber i is given as:

$$P_i = c_{p_i}G_3 V_i p_i\theta_i\dot{\theta}_i + \left(c_{p_i}G_4 + \rho_i G_1\right)V_i\dot{\theta}_i\theta_i + \rho_i c_{p_i}\dot{V}_i\theta_i + \rho_i c_{p_i}V_i\dot{\theta}_i \tag{2.24}$$

By considering that the absolute work done on chamber i is the same absolute work needed to increase the internal energy rate of chamber i, the internal energy rate of chamber II is given by [22]:

$$\begin{aligned} P_2 = {} & \left(1-\overline{\epsilon}_{\dot{s}}\right)\rho_3\delta\dot{V}_1^{or}u_3 - \left(1-\overline{\epsilon}_{\dot{s}}\right)\rho_2\delta\dot{V}_1^{ro}u_2 + \overline{\epsilon}_{\dot{s}}\rho_4\delta\dot{V}_{-1}^{ro}u_4 - \overline{\epsilon}_{\dot{s}}\rho_2\delta\dot{V}_{-1}^{or}u_2 \\ & -Q_2 + Q_0 + p_1(t)\left(A_c' - A_P - A_P' + \pi R_{mp}^2\right)\dot{s}(t) \end{aligned} \tag{2.25}$$

The total heat released per unit of time by chamber I and transferred to chamber II is denoted as Q_0 and approximated using a polytropic transformation with a constant polytropic coefficient Υ for dynamic conditions such that:

$$Q_0(t) = -\frac{p_1(0)V_1(0)}{r_{N_2}\theta_1(0)}\frac{\left(c_{p_{N_2}} - r_{N_2}\right)\Upsilon - c_{p_{N_2}}}{\Upsilon - 1}\dot{\theta}_1(t) \tag{2.26}$$

where the material properties for nitrogen are defined in Section 2.5.1 and:

$$\dot{\theta}_1(t) = (1-\Upsilon)\frac{\theta_1(0)}{V_1(0)^{1-\Upsilon}}\frac{\dot{V}_1}{V_1^{\Upsilon}} \tag{2.27}$$

By combining Eq. (2.26) and Eq. (2.27):

$$Q_0(t) = \left(\left(c_{p_{N_2}} - r_{N_2}\right)\Upsilon - c_{p_{N_2}}\right)\frac{p_1(0)}{r_{N_2}}\left(\frac{V_1(0)}{V_1(t)}\right)^{\Upsilon}\dot{V}_1(t) \tag{2.28}$$

Similarly as for chamber II, the internal energy rate (or power) in chambers III and IV are given by:

$$\begin{aligned} P_3 &= \overline{\epsilon}_{\dot{s}}\rho_2\delta\dot{V}_{-1}^{or}u_2 - (1-\overline{\epsilon}_{\dot{s}})\,\rho_3\delta\dot{V}_1^{or}u_3 - Q_3 + p_3(t)\left(A'_P - \pi R_{mp}^2\right)\dot{s}(t) \\ P_4 &= (1-\overline{\epsilon}_{\dot{s}})\,\rho_2\delta\dot{V}_1^{ro}u_2 - \overline{\epsilon}_{\dot{s}}\rho_4\delta\dot{V}_{-1}^{ro}u_4 - Q_4 - p_4(t)\left(A'_c - A_P\right)\dot{s}(t) \end{aligned} \tag{2.29}$$

Temperature Differential Equations Matrix System

The outlined governing thermodynamic equations used to determine the chamber bulk temperatures θ_i can be written as a nonlinear matrix system which is given by:

$$\mathbf{L}(\boldsymbol{\theta},\mathbf{p})\,\dot{\boldsymbol{\theta}}(t) + \mathbf{L}_\theta(t)\,\boldsymbol{\theta}(t) = \mathbf{L}_\pi(t)\,\mathbf{p}(t) + \boldsymbol{\psi}(t) \tag{2.30}$$

where $\boldsymbol{\theta} = \begin{pmatrix} \theta_2 & \theta_3 & \theta_4 \end{pmatrix}^T$ is the unknown temperature state vector, $\mathbf{p} = \begin{pmatrix} p_1 & p_3 & p_4 \end{pmatrix}^T$ is the pressure input vector, and $\boldsymbol{\psi} = \begin{pmatrix} \psi_2 & \psi_3 & \psi_4 \end{pmatrix}^T$ is the source vector that links the chambers to the structure. The temperature and pressure matrices are defined by:

$$\mathbf{L}_\theta(t) = \begin{bmatrix} L_{\theta 11} & L_{\theta 12} & L_{\theta 13} \\ L_{\theta 21} & L_{\theta 22} & 0 \\ L_{\theta 31} & 0 & L_{\theta 33} \end{bmatrix} \quad , \quad \mathbf{L}_\pi(t) = \begin{bmatrix} L_{\pi 11} & L_{\pi 12} & L_{\pi 13} \\ L_{\pi 21} & L_{\pi 22} & 0 \\ L_{\pi 31} & 0 & L_{\pi 33} \end{bmatrix} \tag{2.31}$$

Some matrix coefficients of $\mathbf{L}_\theta$ and $\mathbf{L}_\pi$ are zero for the case of chambers III and IV, as no physical link (no heat or mass transfer) exists between both chambers. The corresponding coefficients are given in Table 2.6. The normalized thermal mass matrix is defined as $\mathbf{L}(\boldsymbol{\theta},\mathbf{p}) = \mathbf{I}_{3\times 3} + \mathrm{diag}\left(\mathbf{w}(\boldsymbol{\theta},\mathbf{p}) \circ \boldsymbol{\theta}\right)$. It can be seen that the internal chamber bulk temperatures depend on other chamber temperatures (through $\mathbf{L}_\theta$), on the adjacent chamber pressures (through $\mathbf{L}_\pi$), and on the average structural boundary temperatures (through $\boldsymbol{\psi}$). The vector $\boldsymbol{\theta}$ is the unknown vector (states) of the chamber temperatures, $\mathbf{p}$ is the chamber pressure vector, and $\boldsymbol{\psi}$ is the source vector. The oil properties are temperature dependent, making the differential system nonlinear, and are taken into account in $\mathbf{w}(\boldsymbol{\theta},\mathbf{p})$, making use of the Hadamard product defined as $\left(\mathbf{w}(\boldsymbol{\theta},\mathbf{p}) \circ \boldsymbol{\theta}\right)_i = w(\boldsymbol{\theta},\mathbf{p})_i \cdot \theta_i$:

$$\mathbf{w}(\boldsymbol{\theta},\mathbf{p}) = G_3 \begin{pmatrix} \rho_2^{-1} \\ \rho_3^{-1} \\ \rho_4^{-1} \end{pmatrix} \circ \mathbf{p} + \begin{pmatrix} G_4\rho_2^{-1} + G_1 c_2^{-1} \\ G_4\rho_3^{-1} + G_1 c_3^{-1} \\ G_4\rho_4^{-1} + G_1 c_4^{-1} \end{pmatrix} \tag{2.32}$$

$\mathbf{L}_\theta$ coefficients	$\mathbf{L}_\pi$ coefficients
$L_{\theta 11} = \frac{(1-\overline{\epsilon}_{\dot{s}})\delta\dot{V}_1^{ro}}{V_2} + \frac{\overline{\epsilon}_{\dot{s}}\delta\dot{V}_{-1}^{or}}{V_2} + \frac{2\overline{h_2}\Gamma_2}{\rho_2 c_2 V_2} + \frac{\dot{V}_2}{V_2}$	$L_{\pi 11} = \frac{\left(A_c' - A_P - A_P' + \pi R_{mp}^2\right)\dot{s}}{\rho_2 c_2 V_2} - \frac{(1-\overline{\epsilon}_{\dot{s}})\delta\dot{V}_1^{ro}}{\rho_2 c_2 V_2} - \frac{\overline{\epsilon}_{\dot{s}}\delta\dot{V}_{-1}^{or}}{\rho_2 c_2 V_2}$
$L_{\theta 12} = -\frac{(1-\overline{\epsilon}_{\dot{s}})\rho_3\delta\dot{V}_1^{or}c_3}{\rho_2 c_2 V_2}$	$L_{\pi 12} = \frac{(1-\overline{\epsilon}_{\dot{s}})\delta\dot{V}_1^{or}}{\rho_2 c_2 V_2}$
$L_{\theta 13} = -\frac{\overline{\epsilon}_{\dot{s}}\rho_4\delta\dot{V}_{-1}^{ro}c_4}{\rho_2 c_2 V_2}$	$L_{\pi 13} = \frac{\overline{\epsilon}_{\dot{s}}\delta\dot{V}_{-1}^{ro}}{\rho_2 c_2 V_2}$
$L_{\theta 21} = -\frac{\overline{\epsilon}_{\dot{s}}\rho_2\delta\dot{V}_{-1}^{or}c_2}{\rho_3 c_3 V_3}$	$L_{\pi 21} = \frac{\overline{\epsilon}_{\dot{s}}\delta\dot{V}_{-1}^{or}}{\rho_3 c_3 V_3}$
$L_{\theta 22} = \frac{(1-\overline{\epsilon}_{\dot{s}})\delta\dot{V}_1^{or}}{V_3} + \frac{2\overline{h_3}\Gamma_3}{\rho_3 c_3 V_3} + \frac{\dot{V}_3}{V_3}$	$L_{\pi 22} = \frac{\left(A_P' - \pi R_{mp}^2\right)\dot{s}}{\rho_3 c_3 V_3} - \frac{(1-\overline{\epsilon}_{\dot{s}})\delta\dot{V}_1^{or}}{\rho_3 c_3 V_3}$
$L_{\theta 31} = -\frac{(1-\overline{\epsilon}_{\dot{s}})\rho_2\delta\dot{V}_1^{ro}c_2}{\rho_4 c_4 V_4}$	$L_{\pi 31} = \frac{(1-\overline{\epsilon}_{\dot{s}})\delta\dot{V}_1^{ro}}{\rho_4 c_4 V_4}$
$L_{\theta 33} = \frac{\overline{\epsilon}_{\dot{s}}\delta\dot{V}_{-1}^{ro}}{V_4} + \frac{2\overline{h_4}\Gamma_4}{\rho_4 c_4 V_4} + \frac{\dot{V}_4}{V_4}$	$L_{\pi 33} = \frac{-\overline{\epsilon}_{\dot{s}}\delta\dot{V}_{-1}^{ro}}{\rho_4 c_4 V_4} - \frac{(A_c' - A_P)\dot{s}}{\rho_4 c_4 V_4}$

Table 2.6: Matrix coefficients of $\mathbf{L}_\theta$ and $\mathbf{L}_\pi$.

The source vector $\boldsymbol{\psi}$ links the temperature of the structure to the thermodynamic model, and its components are defined by:

$$\psi_i = \frac{2\overline{h}_i}{\rho_i c_{p_i} V_i}\overline{\theta}_i\Gamma_i + \frac{(i-3)(i-4)}{2}\frac{Q_0}{\rho_i c_{p_i} V_i} \quad , i = 2,3,4 \tag{2.33}$$

2.6.5 Boundary Conditions

In order to simplify the notations, the thermally active (nonadiabatic) boundaries are defined mathematically. A partial boundary j of a segmented boundary k is denoted as $\Gamma^{(k,j)}$, which results in $\Gamma^{(k)}(t) = \underset{j=1,2,3}{\cup}\Gamma^{(k,j)},\ k = 2,3,5$, and $\Gamma^{(4)} = \underset{j=1,2,3,4}{\cup}\Gamma^{(4,j)}$. For nonsegmented boundaries ($k = 1,6,7$), the boundary is written as $\Gamma^{(k)}(t)$. At any boundary $\Gamma^{(k)}(t)$, either a frictional heat flux q_k or a convective heat flux with an average empirical HTC $\overline{h_k}$ (and a fluid temperature θ_k) is defined in the normal direction $\mathbf{n}$ to the surface $\Gamma^{(k)}(t)$ $\quad (h_k = 0, k = 6,7;\ q_k = 0, k \neq 6,7)$:

$$\left(\forall \mathbf{r} \in \Gamma(t)\times[0,\hat{t}],\ i \in D,\ k \in \mathcal{B}\right) \qquad k_\theta^{(k)}{}_M\, \boldsymbol{\nabla}\theta|_{\Gamma^{(k)}} \cdot \mathbf{n} + \overline{h_k}\left(\theta|_{\Gamma^{(k)}} - \theta_k\right) = q_k(\mathbf{r},t) \tag{2.34}$$

Convective Boundary Conditions ($i = k = 2,3,4$ and $k = 5$)

The average HTCs $\overline{h_k}$ are derived using empirical correlations that are adopted from [91] for the case of laminar and turbulent flow in tubes and around cylinders. The average convective HTC used in Eq. (2.34) is defined for the external surface ($k = 5$) as $\frac{1}{2}k_{\theta a}\overline{R_5}^{-1}\cdot\overline{\mathrm{Nu}_5}$, and for the internal chamber walls ($i = 2,3,4$) as $\frac{1}{2}k_{\theta i}\overline{R_i}^{-1}\overline{\mathrm{Nu}_i}$, where $k_{\theta a}$ is the thermal conductivity of air, and $k_{\theta i} = k_\theta(\theta_i)$ is the thermal conductivity of oil evaluated at the chamber temperature θ_i. As only the average HTCs are studied, an average external radius $\overline{R_5} = \frac{1}{2}(R_c + R_P)$ is defined.

External Surface ($k = 5$) The Reynolds number $\overline{\mathrm{Re}_5} = 2\dot{X}(t)\overline{R_5}\nu_a^{-1}$ is not uniform around the cylinder and the piston, and is also time dependent. The average temperature of the free stream and the solid wall temperature at which the Reynolds number $\overline{\mathrm{Re}_5}$ is evaluated is $\overline{\theta_5}$. The HTC around the cylinder is calculated using the empirical Churchill - Bernstein correlation given in [91]:

$$\overline{\mathrm{Nu}_5} = 0.3 + \frac{0.62\overline{\mathrm{Re}_5}^{1/2}\mathrm{Pr}_a^{1/3}}{\left(1+(0.4/\mathrm{Pr}_a)^{2/3}\right)^{1/4}}\left[1+\left(\frac{\overline{\mathrm{Re}_5}}{282000}\right)^{n_1}\right]^{n_2} \tag{2.35}$$

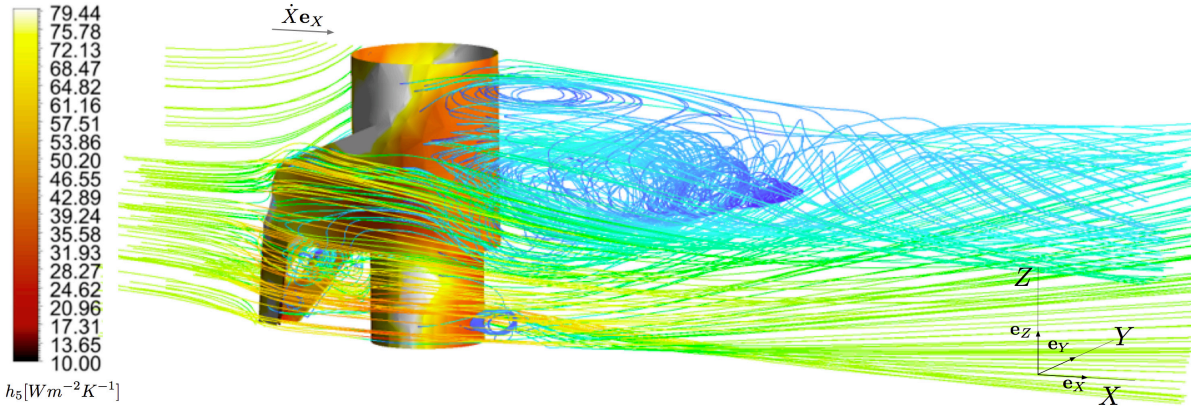

Figure 2.11: Illustration of external air flow and wall HTC ($\dot{X} = 20$ m/s).

According to [91], the exponents are $n_1 = 5/8$ and $n_2 = 4/5$ when $\overline{\mathrm{Re}_5}\mathrm{Pr} > 0.2$, and when $2 \cdot 10^4 < \overline{\mathrm{Re}_5} < 4 \cdot 10^5$, $n_1 = 1/2$ and $n_2 = 1$. An illustration of the turbulent airflow around the SA, calculated using a standard k-ϵ turbulent model in ANSYS/CFX, is shown in Fig. 2.11. For the forced convection of air, the average HTC is generally in the range of $\overline{h_5} = 25 \sim 250$ W/(m^{2}K). For free convection, the average HTC is in the range of $\overline{h_5} = 2 \sim 25$ W/(m^{2}K). The estimated range of the $\overline{\mathrm{Re}_5}$ numbers for the speed range of the aircraft (maximum 80 m/s), an average cylinder radius of 0.1m, and a kinematic viscosity of dry air $\nu_a = 1.475 \cdot 10^{-5}$ m^2/s evaluated at a temperature $\theta_5 = 290$K yields $\max(\overline{\mathrm{Re}_5}) \simeq 10^6$. For an aircraft ground speed of 0.5 m/s, and for the same geometry and airflow conditions, $\min(\overline{\mathrm{Re}_5}) \simeq 6 \cdot 10^3$. With the thermal conductivity of air of $k_{\theta a} = 0.0263$ W/(mK), and for the maximum Reynolds number, the maximum average heat transfer coefficient is approximately 160 W/(m^{2}K). For very slow speeds (of around 0.5 m/s), the average HTC is approximately 5.5 W/(m^{2}K). During towing to the gate, the convection around the cylinder is neglected (free convection, $\overline{h_5} = 2 \sim 25$ W/(m^{2}K)), and the external walls are considered to be isothermal and at a temperature θ_5 such that $\theta|_{\Gamma(5)} = \theta_5$, $\dot{X} \leq \dot{X}_t$.

Internal Walls: Chambers II-IV ($i = k = 2, 3, 4$) The convection correlations used for internal tube flow determine the average HTCs at the internal chamber walls. The $\overline{\mathrm{Re}_i}$ numbers are based on the orifice outflow/inflow rates and the average chamber diameter, and are given in Table 2.7.

Chamber i	**Average radius** $\overline{R_i}$	**Reynolds number** $\overline{\mathrm{Re}_i}$
2	$\dfrac{R_c + R_P - 3B/2}{2}$	$\dfrac{2\overline{R}_2}{\nu_2}\dfrac{\lvert\dot{s}\rvert A'_c + \delta\dot{V}^{or}_{\epsilon_{\dot{s}}} + \delta\dot{V}^{ro}_{\epsilon_{\dot{s}}}}{3A'_c}$
3	$R_P - B/2$	$\dfrac{2\overline{R}_3}{\nu_3}\dfrac{\lvert\dot{s}\rvert A'_P + \delta\dot{V}^{or}_{\epsilon_{\dot{s}}}}{2A'_P}$
4	$\dfrac{R_c + R_P - B}{2}$	$\dfrac{2\overline{R}_4}{\nu_4}\dfrac{\lvert\dot{s}\rvert + \delta\dot{V}^{ro}_{\epsilon_{\dot{s}}}\left(A'_c - A_P\right)^{-1}}{2}$

Table 2.7: Average radii and Reynolds numbers for different SA chambers.

Depending on $\overline{\mathrm{Re}_i}$, various relations for the average Nusselt number $\overline{\mathrm{Nu}_i}$ are used within chamber i; for laminar flow:

$$\overline{\mathrm{Nu}_i} = 3.66 + \frac{0.065\overline{\mathrm{Re}_i}\mathrm{Pr}_i \cdot 2\pi\overline{R_i}^3 \cdot V_i^{-1}(t)}{1 + 0.04\left[\overline{\mathrm{Re}_i}\mathrm{Pr}_i \cdot 2\pi\overline{R_i}^3 \cdot V_i^{-1}(t)\right]^{2/3}} \ , \overline{\mathrm{Re}_i} \leq 3 \cdot 10^3 \ , \ i = 2,3,4 \tag{2.36}$$

where the average chamber radius $\overline{R_i}$ is given in Table 2.7 and the chamber volume $V_i(t)$ is defined in Table 2.4. In a turbulent regime, the chamber entrance region can be considered to be equivalent to fully developed flow, as the lengths of the turbulent entry regions are small. The Gnielinski equation is used for higher accuracy (based on the second Pethukov equation) [91]:

$$\overline{\mathrm{Nu}_i} = \frac{(\mu_i^f/8)(\overline{\mathrm{Re}_i} - 1000)\mathrm{Pr}_i}{1 + 12.7(\mu_i^f/8)^{0.5}\left(\mathrm{Pr}_i^{2/3} - 1\right)} \ , 3 \cdot 10^3 < \overline{\mathrm{Re}_i} < 5 \cdot 10^6 \ , \ b = 2,3,4 \tag{2.37}$$

where μ_i^f is the fluid friction factor given by the first Pethukov equation for $i = 2,3,4$: $\mu_i^f = \left(0.790\ln\overline{\mathrm{Re}_i} - 1.64\right)^{-2}$. The properties of the hydraulic oil are evaluated at the average temperature $\overline{\theta_i}$ of the free stream within chamber i and the solid wall temperature.

Frictional Heat Flux Conditions ($k = 6,7$)

In a first approximation, the temperature at the bearing surface is the same as at the piston surface, which leads to the definition of an average gap temperature : $\theta_u = \overline{\theta_6}$, $\theta_l = \overline{\theta_7}$. The frictional heat flux generated at the lower and upper bearings is shared between the piston and the cylinder, and is dependent on the heat capacities of both materials [36]. The sharing coefficients $\xi_6 = c_{pA}\left(c_{pA} + c_{pB}\right)^{-1}$ and $\xi_7 = c_{pB}\left(c_{pB} + c_{pC}\right)^{-1}$ are dependent on the material properties, such that the heat is flowing naturally to the softer material (upper bearing $k = u = 6$; lower bearing $k = l = 7$):

$$q_{kc}(\mathbf{r},t) = \xi_k\mu_k(t,\theta_k)\left|\dot{s}(t)\right|p_k^H \ , \ q_{kP}(\mathbf{r},t) = \frac{1-\xi_k}{\xi_k}q_{kc}(\mathbf{r},t) \tag{2.38}$$

The frictional heat flux q_k is positive when directed inward, and is defined as (for $k = 6,7$): $q_k(\mathbf{r},t) = q_{kc}(\mathbf{r},t) + q_{kP}(\mathbf{r},t)$. The total frictional heat flux is proportional to the absolute value of the relative sliding speed, linearly dependent on the contact pressure, and dependent on μ_l and μ_u, which are defined in Section 2.6.3.

Symmetry, Adiabatic and Isothermal Boundary Conditions

Not all of the boundaries, such as at the top and bottom of the SA, are thermally active (nonadiabatic). The entire adiabatic boundary (including the symmetry boundary) is defined as: $\overline{\Gamma} = \Gamma \setminus \left\{ \underset{k\in\mathcal{B}}{\cup} \Gamma^{(k)}(t) \right\}$, such that the net heat flux vanishes on $\overline{\Gamma}$: $\boldsymbol{\nabla}\theta|_{\overline{\Gamma}} \cdot \mathbf{n} = 0$. During fast extension/compression of the SA, the polytropic transformation is considered to be isothermal, such that the wall boundaries are at the same temperature as the enclosed gas: $\theta|_{\Gamma^{(1)}} = \theta_1$.

2.7 Model Verification, Validation and Limitations

Before yielding results for the characteristic thermal behavior of the LG SA, the model is verified and validated. As the results shown are confidential, all quantities are normalized by the maximum value such that for quantity Y: $\overline{Y} = Y/\max(Y)$. The maximum value is proprietary and not available for publication.

The tire deflection curve is shown in Fig. 2.12. The data provided by the tire manufacturer and the implemented tire model from [97] correlate well. In addition to the tire stiffness, an additional damping coefficient of the tire is introduced and set as $\zeta_T^0 = 2$ kNs/m for each tire [101]. The power equivalence shown in Fig. 2.13 ($\hat{t} = 1$s) is used to verify the mechanical model. The input power is split into the spring force power and the dissipated power such that $P_{in} + P_{diss} + P_{spring} = 0$. During compression, the frictional loss at the SA bearings is the highest, as the sliding speeds are the highest and the SA damping coefficient the smallest. During extension, the frictional loss is almost equal to the damping loss. The gas spring curve for a common 2-stage SA is shown in Fig. 2.14, which validates the model against the provided data. The small errors between the curves are due to the fact that the provided data have been calculated using laws for real gas, whereas the model only considers perfect gas conditions. The static spring curves have been calculated for the case of isothermal compression ($\Upsilon = 1$) and adiabatic extension ($\Upsilon = 1.4$). The dynamic curves have been calculated for a constant polytropic coefficient $\Upsilon = 1.1$.

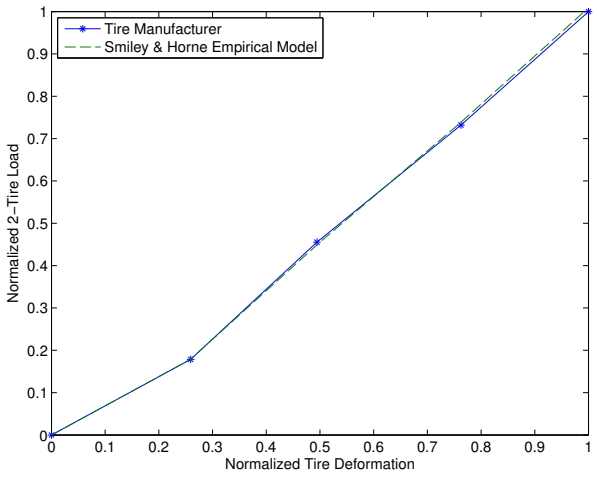

Figure 2.12: Tire deflection curve.

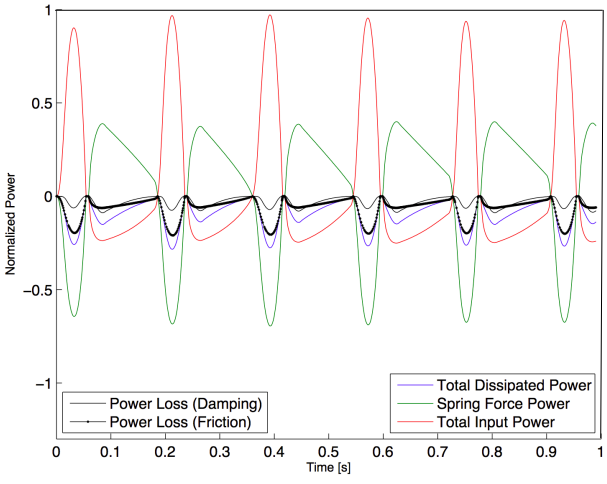

Figure 2.13: Normalized power equivalence [2].

The gas spring curve is used to calculate the stiffness (or spring force) of the dynamic model. In addition, the static stroke is determined from this curve, as the gas pressure under static conditions is known. The SA damping coefficient, similar to a step function, can be seen in Fig. 2.15 as a function of the SA stroke.

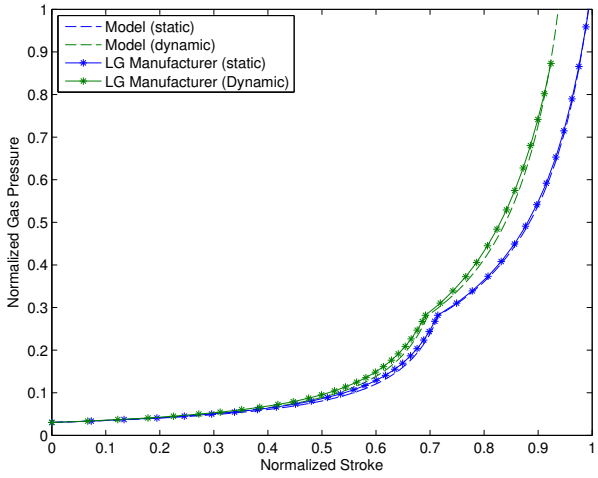

Figure 2.14: Normalized spring curve of double-acting SA.

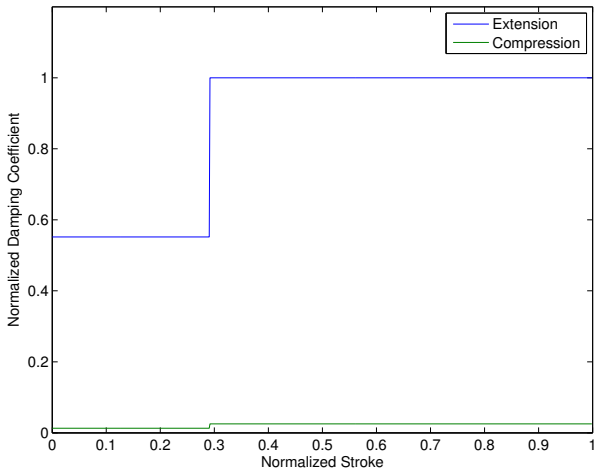

Figure 2.15: Normalized damping coefficient.

The characteristic damping curve is specific to this specific SA, whereas modern LG damping characteristics are nonlinear. The damping force is highest during extension (recoil) and lowest during compression. The aim of the model is to study the trend of the thermal behavior of a LG SA and to identify its heat sources/sinks. It is not intended to be highly accurate in capturing the details in lubricated contacts. The model is limited, as lubrication was not explicitly modeled. If a lubricating layer had been present, heat would have been generated by viscous dissipation due to pure sliding (shearing of the semisolid lubricant film). The temperature field is calculated using commercial software that has been validated and verified. The consistency of the thermal response is verified, and input errors are unlikely. The other submodels such as the dynamic submodel, the tire submodel or the thermodynamic submodel, are validated against real LG data, which are proprietary and not available for publication.

2.8 Characteristic Results

The temperature field was calculated for a ground maneuver of an aircraft equipped with cantilevered MLG on a rough runway ($\mu_R = 0.5$). A total time of $\hat{t} = 30$s (15s constant taxi speed on the taxiway, 15s constant aircraft acceleration on the runway) is considered. The static dry BFC is fixed as 0.3. The take-off speed of 74.75m/s is weight dependent, and the taxi speed is set at $\dot{X}_{to} = 11.11$m/s. The mesh shown in Fig. 2.16, used in order to calculate the temperature field, is kept as coarse as possible for the regions not of interest. The mesh is refined in the TZI, and is completely swept over the structure. The mesh used to compute the thermal response consists of SOLID226 elements (20-node 3D bricks with DOF UX, UY, UZ, T). In total, 24,962 elements are used with 38,029 nodes.

All the simulations are performed on a dual 6-core machine at 3.46 GHz with 48GB of memory. Global convergence is achieved after 3 global iterations and a total computation time of 33.32 hours. This relatively long simulation time can essentially be attributed to slow inputs/outputs between the two software systems and tight local convergence criteria.

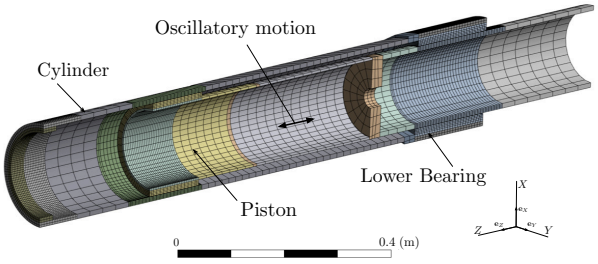

Figure 2.16: Mesh used for the temperature field calculation.

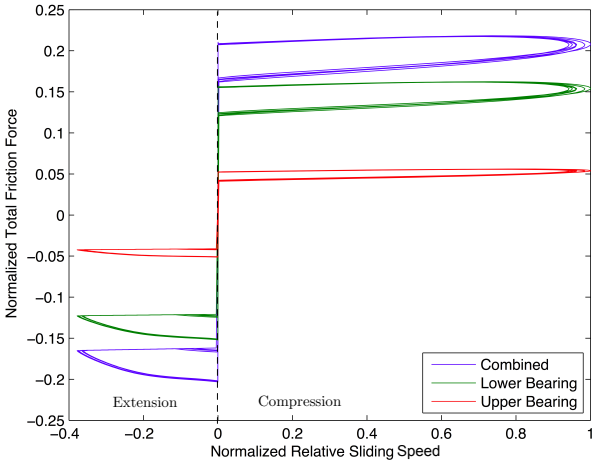

Figure 2.17: Friction forces as a function of the sliding speed [2].

A corresponding plot of the friction forces as a function of time is shown in Fig. 2.18 (minimum constant lubrication clearance of $c_0 = 10^{-6}$m), from which the friction forces shown in Fig. 2.17 as a function of the relative sliding speed are derived. As the friction forces are normalized by the maximum combined friction force, it must be noted that this normalization is not equivalent to the BFC. The friction force at the lower bearing is roughly 75% of the total friction force, demonstrating that much of the drag load applied at the axle is taken by the lower bearing under rough runway conditions.

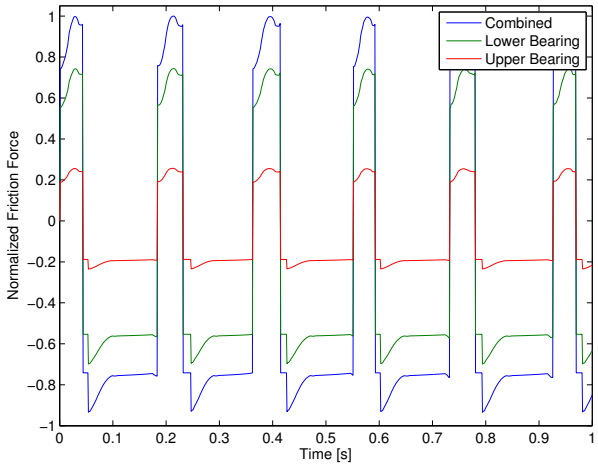

Figure 2.18: Evolution of friction forces.

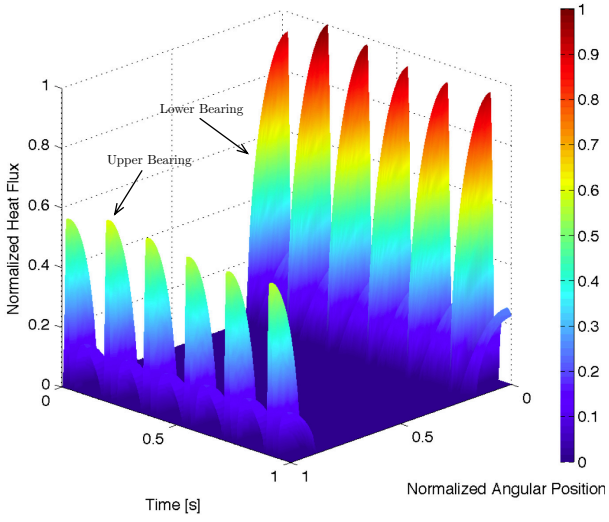

Figure 2.19: Normalized heat flux [2].

As the load is much higher at the lower bearing than at the upper bearing, the frictional heat flux (proportional to the temperature at the sliding interface) is much higher at the lower

than at the upper bearing. For the sake of clarity, the heat flux at both bearings is plotted on Fig. 2.19, revealing the characteristic evolution of the half-parabolic shape. The frictional heat flux is applied in the normal (radial) direction of the contacting surfaces. The heat flux vanishes completely for the case of stiction. The normalized heat flux is highest at the lower bearing interface and oscillates as the contact angle changes as a function of time. The maximum heat flux occurs at the aft position of the lower bearing, as no horizontal drag load was applied for the idealized conditions. The heat flux is zero for all angles for which no contact pressure is defined.

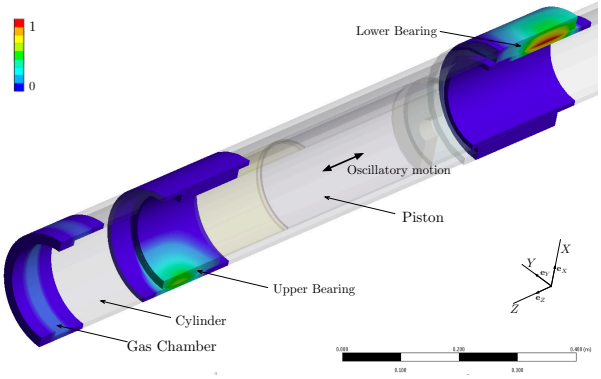

Figure 2.20: Normalized temperature field in the LG SA [2].

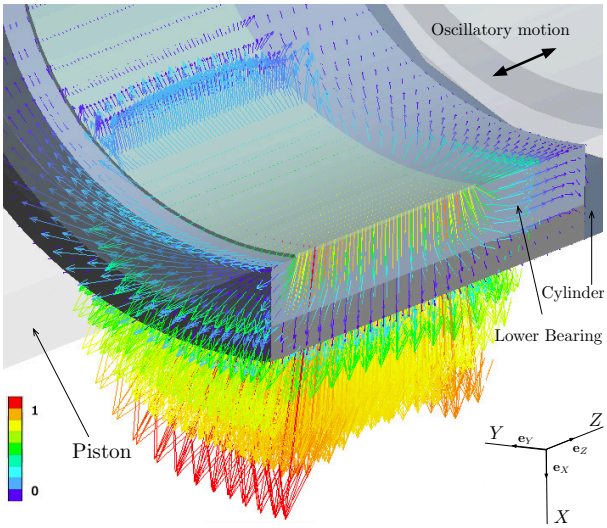

Figure 2.21: Normalized heat flux vector field at the lower bearing ($t = 30$s) [2].

The maximum temperature at the upper bearing will always be at the fore position. If ovalization is considered and the cylinder and piston deform, a reduction of the peaks and an irregular shaped surface of the heat flux are expected instead of a flat surface for angles greater than the theoretical angles predicted by Hertz's theory. A comprehensive model is shown in Chapter 4, which is used to determine the heat flux surface more accurately. The normalized temperature field in the LG SA is shown in Fig. 2.20, demonstrating that the reported overheating is a very localized phenomenon, with thermal gradients that are very high in the TZI. Although the temperature field provides insight to the thermal behavior in the TZI, the thermal behavior of the lubricant film is not captured with the present simplified model. In the circumferential direction, the temperature variation vanishes quickly. The heat flux vector field is shown in Fig. 2.21. Shortly after a compression phase ($t = 30$s), the SA extends. In the direction of movement, the heat flux at the leading edge of the stationary component is highest, as advection occurs in the stationary body and the heat is advected by the moving component (piston). The heat flux is higher on the cylinder side, which confirms the tendency of the heat to flow into the softer base material (as stated in [37]), which in turn suggests that modeling a soft coating on the piston would not alter the results. It must be noted that, although the heat flows naturally to the lower bearing, it has been reported that the high temperature reached caused asymmetric damage to the piston and the lower bearing, which is explained in Chapter 4.

The temperature increase at the end of a typical rough runway maneuver of 30s is shown in Fig. 2.22, confirming that the lower bearing is at the highest risk of heat damage, as the maximum average temperature in the TZI occurs at the lower bearing sliding interface; this suggests that the focus of the comprehensive model should lie on developing a more accurate model for the lower bearing assembly.

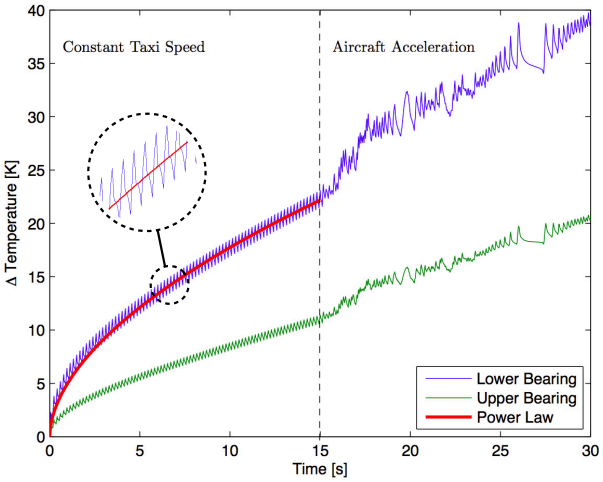

Figure 2.22: Evolution of increase of average bearing temperatures [2].

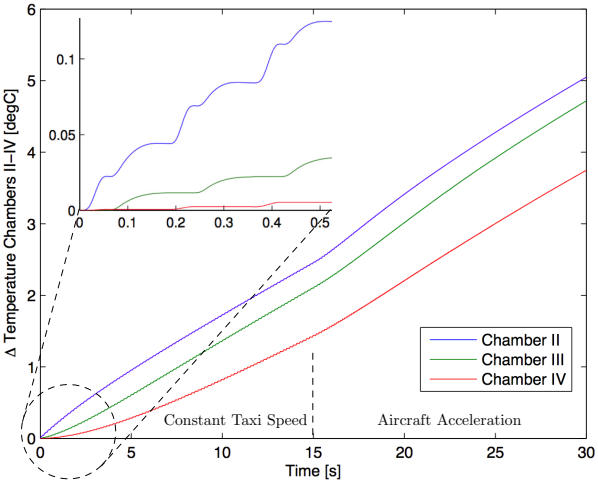

Figure 2.23: Evolution of increase of chamber temperatures [2].

During the ground maneuver, a steady state is not reached and the average temperature constantly increases. The oscillations in the temperature profile are due to the fact that the hot region is periodically brought into contact with colder oil or air. The average temperature constantly increases during taxiing at a constant speed, but follows an irregular pattern during aircraft acceleration. By performing a regression analysis, a power law is determined that yields the lower bearing average temperature during taxiing as a function of time: $(\forall t \leq t_t)\ \Delta\overline{\theta} = a \cdot t^b$.

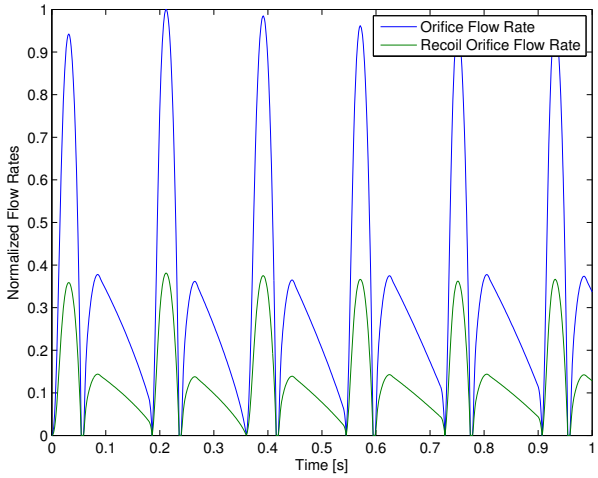

Figure 2.24: Normalized orifice flow rates.

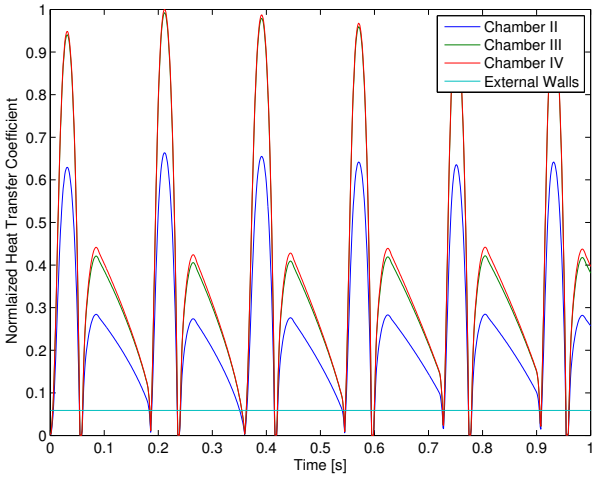

Figure 2.25: Normalized HTCs.

For this case, the parameters are determined as $a = 5$ and $b = 0.55$, and depend on the chosen LG, the runway profile and the operating conditions. The average internal chamber temperature

increase (see Fig. 2.23) is found to be small compared to the temperature increase at the lower bearing. The temperature rates are variable as the inflow and outflow of each chamber are not constant. The average temperature rate for chamber II is the highest because the work input to chamber II is highest and additional heat is transferred from chamber I to chamber II. During taxiing, the average temperature rate is almost constant, but the instantaneous temperature increases at different rates at all times because the compression and extension speeds of the SA are different. The temperature increase in chamber IV is the smallest, as the work done on chamber IV is the smallest. As the recoil orifice is much smaller than the primary orifice, the flow rates are lower for the recoil orifice, as shown in Fig. 2.24.

The normalized average HTCs for chambers II-IV are shown in Fig. 2.25. The HTC at the external walls is much lower than the internal HTCs. This suggests that the external heat removal is not as efficient as the internal heat removal. The ambient air is not as efficient a heat sink as the hydraulic oil in the chambers. The Reynolds numbers in the chambers are much higher than the Reynolds number of the external air flow, and the thermal conductivity of the oil is also higher than the thermal conductivity of the surrounding air. The HTC is proportional to the Nusselt number, and the thermal conductivity of the fluid, and consequently the internal HTCs, are higher.

2.9 Sensitivity Study

In order to study the effect of the WOG on the heat flux at the lower bearing, the relative sliding speed and the maximum Hertzian contact pressure are plotted in Fig. 2.26 and Fig. 2.27 respectively, for only a short time of 0.2s, during which only one bump is encountered. As all the bumps encountered are the same, this time period is chosen for illustration purposes. It is found that for an increasing WOG, the maximum normalized relative sliding speed decreases. In addition with an increasing WOG, the maximum Hertzian contact pressure increases.

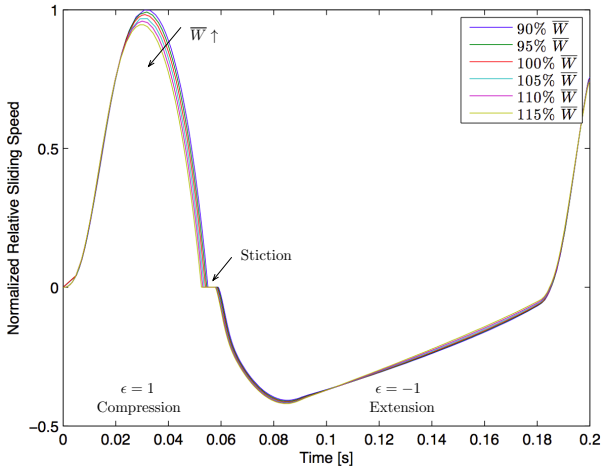

Figure 2.26: Relative sliding speed under change of $\overline{W}$ [2].

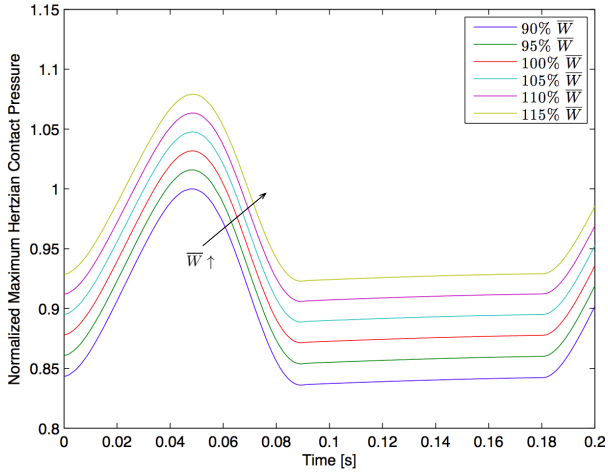

Figure 2.27: Maximum Hertzian contact pressure under change of $\overline{W}$.

As stated in [37], the interface temperature is proportional to the frictional heat flux. As the maximum temperature occurs at the lower bearing sliding interface, it is sufficient to study the sensitivity of the maximum heat flux over one bump instead of the maximum temperature at the lower bearing. The sensitivity ratios depend on the values of the fixed parameters (characteristic for a rough runway and determined by analyzing measured runway profiles). The local sensitivities are calculated using the approach outlined in [102] and are normalized in order to remove the effects of different units:

$$S_{k,i}^{r} = \frac{\partial Y^{(k)}}{\partial X_i} \cdot \frac{X_i}{Y_i} \tag{2.39}$$

where $Y^{(k)} = Y^{(k)}(X_i, \overline{X_j}),\ j = 1,2,3,\ j \neq i$, where k is the number of the output variable, and $Y^{(k)}$ is the k^{th} response surface. The local sensitivity ratios, calculated using the FD method, are determined for the nominal values $\overline{\hat{Z}_R} = 0.03\text{m}$, $\overline{X_R} = 2\text{m}$, $\overline{W} = 332\text{kN}$, $t_t = 15\text{s}$, $\hat{t} = 30\text{s}$, and are shown in Fig. 2.28. The nominal values are fictitious, but are compatible to a certain rough runway. The input variables $X_1 = \hat{Z}_R \in [0; 0.05]$, $X_2 = X_R \in [1, 15]$, and $X_3 = \overline{W}$ are varied for the following output variables: $Y^{(1)} = \max(q_l)$, $Y^{(2)} = \max(\dot{s})$, $Y^{(3)} = \max(s)$, and $Y^{(4)} = \max\left(p_l^H\right)$. The response surface is built using 11 different runway amplitudes and 15 different runway wavelengths (165 samples in total). The interpolated piecewise linear response surface $Y^{(1)} = Y^{(1)}\left(\hat{Z}_R, X_R, \overline{W}\right)$ of the maximum heat flux is shown in Fig. 2.29. The highly nonlinear relationship between the runway input and the frictional heat flux can be seen.

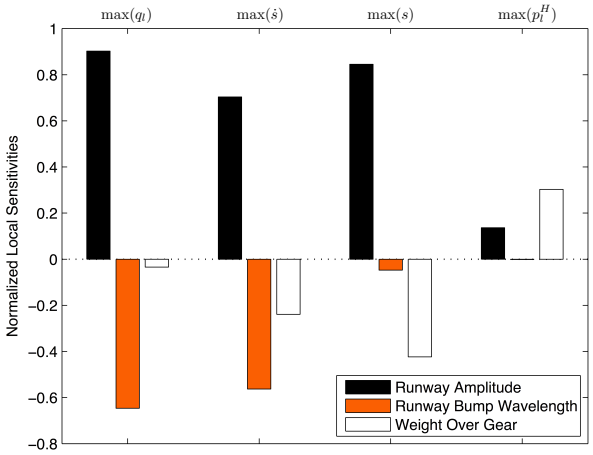

Figure 2.28: Local sensitivity ratios of output variables [2].

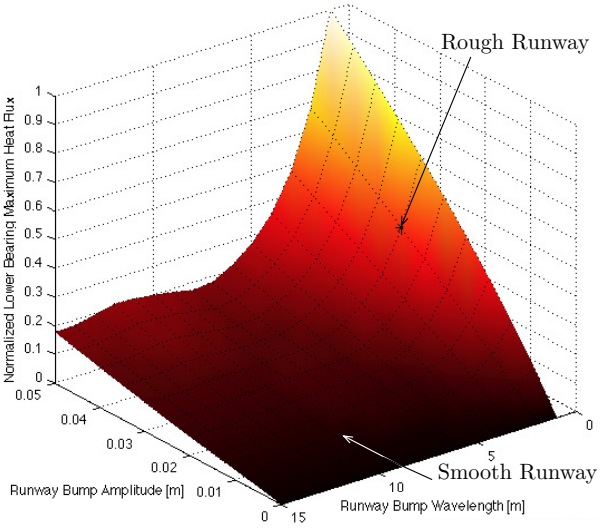

Figure 2.29: Response surface $Y^{(1)} = Y^{(1)}\left(\hat{Z}_R, X_R, \overline{W}\right)$ [2].

2.10 Summary and Conclusions

A model was developed to highlight the characteristic thermal behavior of and identify the heat sources and sinks within the LG system from a macroscopic, or global, point of view when

maneuvering on a rough runway. After outlining the characteristic model assumptions, the TTM model is defined and subdivided into three parts, all using simplified, but representative equations. Emphasis is placed on developing a methodological framework and studying the evolution of the average temperature in the TZI while taxiing and taking-off.

It is found that the zone of highest temperature is at the lower bearing, as the main heat source is proven to be at this interface. The complete system must be considered as transient, as the boundary conditions of the thermal model are closely related to the dynamic model. Contrary to common belief, it is shown that the dynamic and thermal responses of the system are closely related, despite the fact that the frequencies of both responses are different. Additionally, it is possible to identify the key parameter, the runway amplitude, which has the highest impact on the thermal response. Two statements are presented below regarding the characteristics of the LG system.

Statement 1: The maximum heat flux at the lower bearing is not sensitive to a change in WOG under the given runway and operating conditions. If the WOG is increased, the maximum contact pressure increases. At the same time, the dynamic system becomes stiffer (the stiffness of the SA and the friction force increase), yielding a smaller relative sliding speed: $S^r_{4,3} > 0 \ \wedge S^r_{2,3} < 0 \Rightarrow \left|S^r_{1,3}\right| \ll 1$.

Statement 2: The heat flux at the lower bearing is most sensitive to the runway amplitude. If the runway amplitude increases, the vertical axle force is increased, yielding a higher system excitation: $\left|S^r_{1,1}\right| > \left|S^r_{1,2}\right| \gg \left|S^r_{1,3}\right| > 0$.

In order to generate a high frictional heat flux, it is necessary to have high loads *and* high relative sliding speeds. However, the heat generation is not very sensitive to a load change. It is confirmed that the heat flows naturally to the softer material (as stated in [37]) and towards chamber IV (see Fig. 2.10). The external heat sink (air) is not as efficient as the internal heat sink (hydraulic oil). As heat is flowing to chamber IV, the lower bottom of the connecting chamber must be included. The temperature in the chambers are not very high: the oil is acting as a heat sink, not as a heat source.

The characteristic model shows that in order to find a solution to the reported overheating issues, a more detailed and validated TEHD model of the lower bearing assembly is required. Subsequent model refinements will focus on understanding and quantifying the heat generation at the lower bearing interface by rejecting limiting assumptions, and will also take into account local effects such as viscous heating of the lubricant.

Under load, the cylinder deforms and the lubricated film is squeezed out of the way, so that peaks of temperature are reached locally, which need to be calculated accurately in order to explain the reported uneven heat damage. A reduction of the heat flux peaks in Fig. 2.19 and an irregularly shaped surface of the heat flux as a function of time and angle would likely be the consequence of the ovalization of the piston and cylinder. Once the interface temperature as a function of the bearing configuration and operating conditions is known, a modified BFC can be

derived that can be used in existing aircraft LG dynamic simulations (see Chapter 5).

In order to develop a comprehensive model of the lubricating layer, several aspects must be considered. The lubricant, a non-Newtonian fluid, may change phase over time because of the generated heat, and the transient nature of the phase change must be accurately captured in order to draw conclusions on the local and sudden 'burning' of the lubricant. As noted in Chapter 1, the evolution of multiple phases must be calculated at a reasonable speed, as design/optimization studies need to be run. These specifications, combined with the requirement for a more comprehensive model of the lower bearing, lead to a novel tribotopological theory (TTT), derived in Chapter 3.

■

Chapter 3

Novel Tribotopological Theory

> A mathematical theory is not to be considered complete until you have made it so clear that you can explain it to the first man whom you meet on the street.
>
> David Hilbert, mathematician (1862-1943)

3.1 Derivation Strategy

As stated in Section 2.10 and in order to develop a more comprehensive model of the lubricant at the sliding interface of the lower bearing that provides results of the multiphasic behavior of the lubricant, a novel theory is derived in this chapter. This theory can be seen as an extension of the classical lubrication theory to include multiphasic lubricants.

Starting from the fundamental laws of conservation of fluid mechanics, assumptions are formulated that lead to the simplification of these laws. This simplification closely follows previous derivations such as shown in [41]. The benefit and the novelty of the theory, however, lie in the definition of tribotopologies, which are virtual spaces within the lubricant that are englobed with shells and that contain each a distinct phase of the lubricant. As shown in [82], the plug phase of the lubricant is distinct and separated from other phases. Similarly, the shell that englobes the disintegrated lubricant can be seen as distinct, despite the eventual possibility of bubbles or other highly-complex fluid patterns. In each of the tribotopological (TT) spaces, a different velocity field of the lubricant is defined. It is the definition and identification of the velocity profile within each TT space that are key to the novel theory.

The governing equations are integrated while taking into account the velocity profile in each TT space. This integration leads to the derivation of one governing equation, namely the general tribotopological (TTR) equation, which gives the pressure field within the lubricant that drives the velocity field. The square of the components of the gradient of the velocity field is proportional to the heat generation, which is the cause of the reported damage. A demonstration of the extension of the existing classical lubrication theory and validation is provided. The theory is kept as general as possible, and can be applied to other applications with similar multiphasic and transient system characteristics.

3.2 Fundamental Conservation Laws

Conservation of Mass

As shown in [103], the transient conservation of mass equation for a compressible lubricant is: $\mathbf{v}\cdot\boldsymbol{\nabla}\rho+\rho\boldsymbol{\nabla}\cdot\mathbf{v}=-\partial_{,t}\rho$. For an incompressible lubricant, the conservation of mass simplifies to: $\boldsymbol{\nabla}\cdot\mathbf{v}=0$ ($\boldsymbol{\nabla}\rho=0$ and $\partial_{,t}\rho=0$). The divergence of the velocity field $\boldsymbol{\nabla}\cdot\mathbf{v}$ is derived in the local Frenet-Serret reference frame (x,y,z). Commonly, a Frenet-Serret reference frame is chosen in order to capture the local phenomena of TEHD lubrication. According to the assumptions adopted in the field of TEHD lubrication (see Section 3.3), the radial component of the velocity gradient is ignored, such that $v_{y,y}=0$.

Conservation of Momentum

The definitions of the stretching and spin tensors follow [41]. The gradient of the velocity field in the domain of the lubricant is given by $\boldsymbol{\nabla}\mathbf{v}=\mathbf{D}+\boldsymbol{\Omega}$, where $\boldsymbol{\Omega}$ is the anti-symmetric spin tensor. The symmetric stretching tensor $\mathbf{D}$ is given explicitly as:

$$\mathbf{D}=\frac{1}{2}\left(\boldsymbol{\nabla}\mathbf{v}+(\boldsymbol{\nabla}\mathbf{v})^{T}\right)=\frac{1}{2}\begin{bmatrix}2v_{x,x} & v_{x,y}+v_{y,x} & v_{x,z}+v_{z,x}\\ v_{x,y}+v_{y,x} & 2v_{y,y} & v_{y,z}+v_{z,y}\\ v_{x,z}+v_{z,x} & v_{y,z}+v_{z,y} & 2v_{z,z}\end{bmatrix} \tag{3.1}$$

The shear rate tensor $\dot{\boldsymbol{\gamma}}$ is defined as $\dot{\boldsymbol{\gamma}}=\boldsymbol{\nabla}\mathbf{v}+(\boldsymbol{\nabla}\mathbf{v})^{T}=2\mathbf{D}$, and its norm is defined as:

$$\dot{\gamma}=\sqrt{2\mathbf{D}:\mathbf{D}}=\sqrt{2\mathrm{tr}\left(\mathbf{D}^{T}\mathbf{D}\right)} \tag{3.2}$$

where the inner product (Frobenius inner product) of two tensors $\mathbf{T}$ and $\mathbf{D}$ is defined as $\mathbf{T}:\mathbf{D}=\mathrm{tr}\left(\mathbf{T}^{T}\mathbf{D}\right)$. The general Cauchy stress tensor $\mathbf{T}$ for a compressible, non-Newtonian fluid is given in [103] as:

$$\mathbf{T}=\left(-p+\eta_{\mathbf{D}}\ \mathrm{tr}\mathbf{D}\right)\mathbf{I}+2\eta\mathbf{D} \tag{3.3}$$

where p is the hydrodynamic pressure and $\eta_{\mathbf{D}}$ the bulk viscosity. The general Navier-Stokes equations are given by:

$$\rho\frac{D\mathbf{v}}{Dt}=\boldsymbol{\nabla}\cdot\mathbf{T}+\rho\breve{\mathbf{b}} \tag{3.4}$$

where $\breve{\mathbf{b}}$ is the body force vector and $\frac{D\mathbf{v}}{Dt}$ is the material derivative of $\mathbf{v}$ as explained in Section 1.5. By deriving Eq. (3.3), the gradient of the stress within the incompressible lubricant is given by ($\eta_{\mathbf{D}}=0$):

$$\boldsymbol{\nabla}\cdot\mathbf{T}=-\boldsymbol{\nabla}p+\eta\boldsymbol{\nabla}^{\mathbf{2}}\mathbf{v}+2\mathbf{D}\boldsymbol{\nabla}\eta \tag{3.5}$$

By ignoring all inertia effects of the lubricant as well as the body forces ($\breve{\mathbf{b}}=0$), the Navier-Stokes equations for an incompressible non-Newtonian lubricant reduce to $\boldsymbol{\nabla}\cdot\mathbf{T}=0$. The flow within the lubrication gap is laminar, and the pressure gradient is given by:

$$\boldsymbol{\nabla}p=\eta\boldsymbol{\nabla}^{\mathbf{2}}\mathbf{v}+2\mathbf{D}\boldsymbol{\nabla}\eta \tag{3.6}$$

The shear rate variation across the film is zero: $\dot{\gamma}_{,y} = 0$. The viscosity derivatives are expressed as $\eta_{,x} = \eta_{,p}p_{,x} + \eta_{,\theta}\theta_{,x} + \eta_{,\dot{\gamma}}\dot{\gamma}_{,x}$ and $\eta_{,y} = \eta_{,p}p_{,y} + \eta_{,\theta}\theta_{,y} + \eta_{,\dot{\gamma}}\dot{\gamma}_{,y}$. The Laplacian of the vector field $\mathbf{v}$ is given by $\boldsymbol{\nabla} \cdot \boldsymbol{\nabla}\mathbf{v}$, and the angular, radial and vertical pressure gradient components are given respectively by:

$$\begin{aligned} p_{,x} &= \eta v_{x,xx} + \eta v_{x,yy} + \eta v_{x,zz} + 2\eta_{,x}v_{x,x} + \eta_{,y}v_{x,y} + \eta_{,y}v_{y,x} + \eta_{,z}v_{x,z} + \eta_{,z}v_{z,x} \\ p_{,y} &= \eta v_{y,xx} + \eta v_{y,yy} + \eta v_{y,zz} + \eta_{,x}v_{x,y} + \eta_{,x}v_{y,x} + 2\eta_{,y}v_{y,y} + \eta_{,z}v_{y,z} + \eta_{,z}v_{z,y} \\ p_{,z} &= \eta v_{z,xx} + \eta v_{z,yy} + \eta v_{z,zz} + \eta_{,x}v_{x,z} + \eta_{,x}v_{z,x} + \eta_{,y}v_{y,z} + \eta_{,y}v_{z,y} + 2\eta_{,z}v_{z,z} \end{aligned} \tag{3.7}$$

Conservation of Energy

The general conservation of energy within a fluid is given in [103]:

$$\rho\frac{D\breve{e}}{Dt} = \lambda_\theta \boldsymbol{\nabla}^2\theta + \mathbf{T} : \mathbf{D} \tag{3.8}$$

where $\breve{e}$ denotes the lubricant's specific internal energy, θ the temperature field and λ_θ the lubricant's isotropic thermal conductivity, which is constant within the temperature range ($\lambda_{\theta,\theta} \sim 0$). In consideration of the classical assumptions in the field of TEHD lubrication (see Section 3.3), Eq. (3.8) can be written as:

$$\rho\left(\dot{\breve{e}} + \mathbf{v} \cdot \boldsymbol{\nabla}\breve{e}\right) = \lambda_\theta \boldsymbol{\nabla}^2\theta - \rho p \mathbf{v} \cdot \boldsymbol{\nabla}\left(\rho^{-1}\right) + 2\eta \mathrm{tr}\left(\mathbf{D}^T\mathbf{D}\right) \tag{3.9}$$

It is assumed that the lubrication gap is very long in the directions x and z compared to the radial direction y, which implies that the temperature derivatives in these directions can be ignored. The same holds for the velocity gradient. The components of the velocity gradient are not of the same order, such that $v_{x,z} \ll v_{z,y}$ and $v_{z,x} \ll v_{z,y}$. For an incompressible lubricant, the tensor product of the stretching tensor with itself is defined as $\mathbf{D} : \mathbf{D} = \dot{\gamma}^2/2$. The square of the shear rate is given as:

$$\dot{\gamma}^2 = 8\left(v_{x,x}^2 + v_{y,y}^2 + v_{z,z}^2\right) + \left(v_{x,y} + v_{y,x}\right)^2 + \left(v_{x,z} + v_{z,x}\right)^2 + \left(v_{z,y} + v_{y,z}\right)^2 \tag{3.10}$$

By ignoring second order velocity derivatives and under the given assumptions, the shear rate $\dot{\gamma}$ simplifies to $\dot{\gamma}^2 = v_{x,y}^2 + v_{z,y}^2$. The transient energy equation is given by:

$$\rho\dot{\breve{e}} + \rho\mathbf{v} \cdot \boldsymbol{\nabla}\breve{e} + \rho p \mathbf{v} \cdot \boldsymbol{\nabla}\left(\rho^{-1}\right) = \lambda_\theta \theta_{,yy} + \eta\dot{\gamma}^2 \tag{3.11}$$

By following [104], the energy differential can be expressed as a function of known quantities such that $\partial\breve{e} = c_p\partial\theta - \theta\left(\rho^{-1}\right)_{,\theta}\partial p - p\partial\left(\rho^{-1}\right)$, which takes a simplified form for the case of constant density: $\partial\breve{e} = c_p\partial\theta$. It has been shown in [104] that convective cooling in a hydrodynamic bearing is not as important as conduction cooling (thermal gradient along the lubrication gap in x and z directions is not considered in the heat source). Within the lubricant film, the transient temperature field is governed by:

$$\rho c_p\dot{\theta} - k_\theta\theta\dot{p} = \lambda_\theta\theta_{,yy} + k_\theta v_x p_{,x}\theta + k_\theta v_z p_{,z}\theta + \eta\left(v_{x,y}^2 + v_{z,y}^2\right) \tag{3.12}$$

where the coefficient of thermal expansion κ_θ is defined by $\kappa_\theta = \rho\left(\rho^{-1}\right)_{,\theta}$.

The Dirichlet boundary conditions for the pressure field are provided by the pressure of the connecting oil chambers in the LG SA and the atmosphere. For this application, the lubricant is considered incompressible (volume change due to varying pressure), but the compression of the lubricant is considered to contribute to the temperature field (large temperature range). The coefficient of thermal expansion of grease is $k_\theta = 8.2 \cdot 10^{-4}\ \mathrm{C}^{-1}$ [92].

On the left-hand-side of Eq. (3.12), the rate of temperature can be distinguished, whereas on the right-hand-side, a diffusion term proportional to $\theta_{,yy}$ as well as compressive heating terms can be seen. The key term that links the velocity field to the temperature is given by $\eta\left(v_{x,y}^2 + v_{z,y}^2\right)$, which is the dissipation of energy through shearing of the lubricant. A key observation is that the heat generation term is proportional to the square of the components of the velocity gradient, or shear stress.

3.3 Thermo-Elastohydrodynamic Lubrication

In order to evaluate the importance of each term in Eq. (3.7), an order of magnitude analysis is performed as shown in [41]. For this purpose, normalized quantities are defined such that: $\epsilon = \frac{L_y}{L_{xz}} \ll 1$, where L_{xz} is the *length scale* of the bearing in the (x, z) plane and $L_y = \varsigma$ is the length scale of the domain of the lubricant film across the lubrication gap. The slider bearing contains a primary thrust portion located at z_0 and at an angle of α_0 and is governed by: $\varsigma = z_0 \cdot \tan\alpha_0$. The coordinates can be normalized as $x = L_{xz}\overline{x} = 2\pi R_c\overline{x}$ (Note: $R_c \simeq R_P$), $y = \epsilon L_{xz}\overline{y} = \varsigma\overline{y}$, and $z = L_{xz}\overline{z} = L\overline{z}$. The velocity and viscosity are normalized as $\eta = \eta_0\overline{\eta}$, $v_y = \epsilon\tilde{U}\overline{v}_{\overline{y}}$, $v_x = \tilde{U}\overline{v}_{\overline{x}}$, and $v_z = \tilde{U}\overline{v}_{\overline{z}}$, where $\tilde{U}$ is the nominal characteristic velocity. The pressure is normalized by $p = \eta_0\tilde{U}L\varsigma^{-2}\overline{p}$. By using the normalized quantities, the normalized pressure gradient components along the circumference are given by:

$$\begin{aligned}
\overline{p}_{,\overline{x}} &= \epsilon^2\overline{\eta}\overline{v}_{\overline{x},\overline{x}\overline{x}} + \overline{\eta}\overline{v}_{\overline{x},\overline{y}\overline{y}} + \epsilon^2\overline{\eta}\overline{v}_{\overline{x},\overline{z}\overline{z}} + 2\epsilon^2\overline{\eta}_{,\overline{x}}\overline{v}_{\overline{x},\overline{x}} + \overline{\eta}_{,\overline{y}}\overline{v}_{\overline{x},\overline{y}} + \epsilon^2\overline{\eta}_{,\overline{y}}\overline{v}_{\overline{y},\overline{x}} + \epsilon^2\overline{\eta}_{,\overline{z}}\overline{v}_{\overline{x},\overline{z}} + \epsilon^2\overline{\eta}_{,\overline{z}}\overline{v}_{\overline{z},\overline{x}} \\
\epsilon^{-2}\overline{p}_{,\overline{y}} &= \epsilon^2\overline{\eta}\overline{v}_{\overline{y},\overline{x}\overline{x}} + \overline{\eta}\overline{v}_{\overline{y},\overline{y}\overline{y}} + \epsilon^2\overline{\eta}\overline{v}_{\overline{y},\overline{z}\overline{z}} + \overline{\eta}_{,\overline{x}}\overline{v}_{\overline{x},\overline{y}} + \overline{\eta}_{,\overline{x}}\overline{v}_{\overline{y},\overline{x}} + 2\overline{\eta}_{,y}\overline{v}_{\overline{y},\overline{y}} + \epsilon^2\overline{\eta}_{,\overline{z}}\overline{v}_{\overline{y},\overline{z}} + \overline{\eta}_{,\overline{z}}\overline{v}_{\overline{z},\overline{y}} \\
\overline{p}_{,\overline{z}} &= \epsilon^2\overline{\eta}\overline{v}_{\overline{z},\overline{x}\overline{x}} + \overline{\eta}\overline{v}_{\overline{z},\overline{y}\overline{y}} + \epsilon^2\overline{\eta}\overline{v}_{\overline{z},\overline{z}\overline{z}} + \epsilon^2\overline{\eta}_{,\overline{x}}\overline{v}_{\overline{x},\overline{z}} + \epsilon^2\overline{\eta}_{,\overline{x}}\overline{v}_{\overline{z},\overline{x}} + \epsilon^2\overline{\eta}_{,\overline{y}}\overline{v}_{\overline{y},\overline{z}} + \overline{\eta}_{,\overline{y}}\overline{v}_{\overline{z},\overline{y}} + 2\epsilon^2\overline{\eta}_{,\overline{z}}\overline{v}_{\overline{z},\overline{z}}
\end{aligned} \tag{3.13}$$

All components of the velocity field are of first order, and the pressure gradient components along z and x are not of the same order as the pressure gradient across the lubrication gap. By ignoring higher order velocity and derivative terms $\overline{\eta}_{,\overline{y}}\overline{v}_{\overline{y},\overline{x}} \gg \overline{v}_{\overline{x},\overline{x}\overline{x}}$, as well as the eventual contribution of a significant viscosity increase under high pressures (small pressure variations) as explained in [105], the pressure gradient is finally given by:

$$\boldsymbol{\nabla}p = \left(\eta v_{x,y}\right)_{,y}\mathbf{e}_x + 0\ \mathbf{e}_y + \left(\eta v_{z,y}\right)_{,y}\mathbf{e}_z \tag{3.14}$$

The pressure gradient $\boldsymbol{\nabla}p$ reveals some significant characteristics of the fluid flow in the lubrication gap. In each direction x and z, the pressure gradient $p_{,x|z}$ (driving force of the fluid flow) is proportional to the variation of the respective shear stress component. As the shear stress is dependent on the yield shear stress τ_0 for a non-Newtonian lubricant such as grease, the pressure gradient, and consequently the fluid flow, are impacted as the lubrication gap is locally narrowed.

3.4 Definition of Tribotopologies

The behavior of grease in small lubrication gaps is dependent not only on the shear rate $\dot{\gamma}$ and the pressure p, but also on the temperature θ. The underlying principle of the TTT in the lubrication gap is that multiple but deformable spaces stacked across the clearance can exist and co-exist within the lubrication gap. These phases in Ω are delimited by distinct isosurfaces, which are called *shells*. The englobed region is called a *space*. Within that space, no threshold value (if applicable) of a state variable (such as temperature θ or shear stress τ) is reached. An illustrative configuration of multiple spaces and shells is shown in Fig. 3.1. In the lubrication gap, $N_s + 1$ shells of N_s spaces can be distinguished ($N_s > 1$). A space $\mathcal{S}^{(n)}$ can either be a fluid space $\mathcal{S}_f$ (similar to oil, flowing grease), a dry space $\mathcal{S}_d$ (grease residual after $\hat{\theta}$ has been reached) or a plug flow space $\mathcal{S}_p$ (grease that is not sheared beyond τ_0). The type of each TT space is defined such that:

$$l^{(n)} = \begin{cases} 0 & \text{if } \mathcal{S}^{(n)} = \mathcal{S}_d^{(n)} \quad \text{(Dry)} \\ 1 & \text{if } \mathcal{S}^{(n)} = \mathcal{S}_p^{(n)} \quad \text{(Plug)} \\ 2 & \text{if } \mathcal{S}^{(n)} = \mathcal{S}_f^{(n)} \quad \text{(Fluid)} \end{cases} \tag{3.15}$$

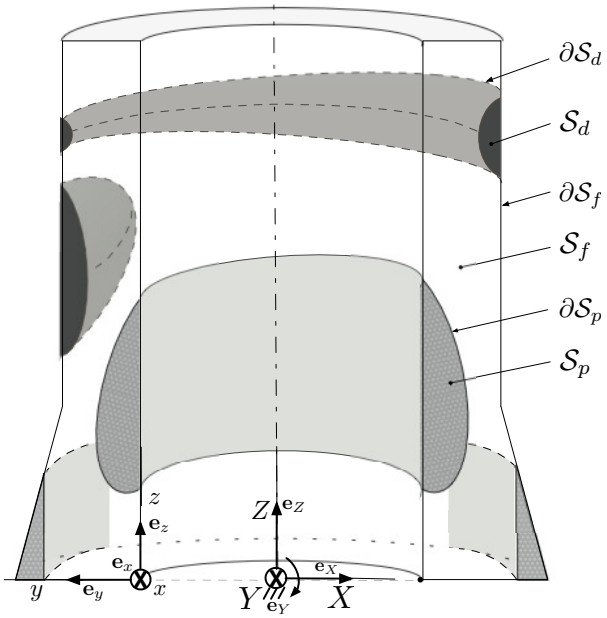

Figure 3.1: Illustration of TT spaces in Ω.

In order to determine the lubricant's behavior, the velocity profile must be determined in multiple TT spaces. In each space $\mathcal{S}^{(n)}$, a different threshold criterion is satisfied. The velocity profile is continuous and derivable (continuous shear stress) at the shells $\partial\mathcal{S}^{(n)}$, such that for a space $\mathcal{S}^{(n)}$ in between the space $\mathcal{S}^{(n-1)}$ and $\mathcal{S}^{(n+1)}$, the velocity is given by $\mathbf{v}|_{\partial\mathcal{S}^{(n)}} = \mathbf{v}|_{\partial\mathcal{S}^{(n-1)}}$ and $\boldsymbol{\nabla}\mathbf{v}|_{\partial\mathcal{S}^{(n)}} = \boldsymbol{\nabla}\mathbf{v}|_{\partial\mathcal{S}^{(n-1)}}$ (derivability condition not enforced for stiction cases 2.3-2.5).

Tribotopological Dry Space $\mathcal{S}^{(n)} = \mathcal{S}_d^{(n)}$ $(l^{(n)} = 0)$

The TT dry space $\mathcal{S}_d^{(n)}$ consists of the volume occupied by grease residuals that are left after the maximum operating temperature $\hat{\theta}$ of grease has been reached. This type of space is the last stage after the continuous and repetitive shear motion (translational or rotational) of both contacting surfaces. The main hypothesis is that no lubricant is physically lost, either through leakage, or through 'burning' of the lubricant. The lubricant can only physically disintegrate and change its lubricating properties. The dry space $\mathcal{S}_d^{(n)}$ is defined by:

$$\mathcal{S}_d^{(n)} = \left\{ \mathbf{x} \in \Omega \;\middle|\; \theta \geq \hat{\theta} \right\} \tag{3.16}$$

The shell $\partial\mathcal{S}_d^{(n)}$ is defined by $\partial\mathcal{S}_d^{(n)} = \left\{ \mathbf{x} \in \Omega \;\middle|\; \theta = \hat{\theta} \right\}$. In the dry space $\mathcal{S}_d^{(n)}$, no lubricating fluid is present, such that $\mathbf{v}|_{\mathcal{S}_d^{(n)}} = 0$. The velocity of the adjacent fluid film vanishes at $\partial\mathcal{S}_d^{(n)}$,

such that $\mathbf{v}|_{\partial\mathcal{S}_d^{(n)}} = 0$. As a fluid is not present *per se* in the dry space, the pressure gradient is zero, such that $\boldsymbol{\nabla} p|_{\mathcal{S}_d^{(n)}} = 0$. From an energy point of view, it is considered that no heat generation occurs in the dry space.

Tribotopological Plug Space $\mathcal{S}^{(n)} = \mathcal{S}_p^{(n)}$ ($l^{(n)} = 1$)

As stated in [61, 62], grease differs from oil flow in small lubrication gaps by the existence of a plug phase. The TT plug space $\mathcal{S}_p^{(n)}$ consists of the volume occupied by a semisolid phase of the grease, which is not sheared beyond a yield shear stress τ_0 in order to flow. The plug space can only exist for a grease-like lubricant or any non-Newtonian fluid, such as a shear thinning/thickening lubricant. The plug space $\mathcal{S}_p^{(n)}$ is defined such that:

$$\mathcal{S}_p^{(n)} = \{\mathbf{x} \in \Omega \mid \tau \leq \tau_0\} \tag{3.17}$$

The shell $\partial\mathcal{S}_p^{(n)}$ is defined as $\partial\mathcal{S}_p^{(n)} = \{\mathbf{x} \in \Omega \mid \tau = \tau_0\}$. A special case must be considered when the semisolid space is floating and moving at a constant velocity determined by the velocity of its shells, such that $\mathbf{v}|_{\mathcal{S}_p^{(n)}} = \mathbf{v}|_{\partial\mathcal{S}_p^{(n)}}$. The velocity gradient of the fluid film is zero within the space $\mathcal{S}_p^{(n)}$, such that $\boldsymbol{\nabla}\mathbf{v}|_{\mathcal{S}_p^{(n)}} = 0$. Similar to the dry space, a proper fluid is not present in the plug space, which implies that the pressure gradient is zero, such that $\boldsymbol{\nabla} p|_{\mathcal{S}_p^{(n)}} = 0$. From an energy point of view, no heat generation occurs within a plug space.

Tribotopological Fluid Space $\mathcal{S}^{(n)} = \mathcal{S}_f^{(n)}$ ($l^{(n)} = 2$)

The TT fluid space $\mathcal{S}_f^{(n)}$ is the only space in the lubrication gap in which an actual fluid flow can develop. The space is occupied by the part of the grease that is sheared enough to flow like oil and at a temperature below the maximum operating temperature. The fluid space is defined in the lubrication gap as $\mathcal{S}_f^{(n)} = \Omega \setminus \bigcup_{n=1}^{N_s} \mathcal{S}_d^{(n)} \setminus \bigcup_{n=1}^{N_s} \mathcal{S}_p^{(n)}$. The velocity field in $\mathcal{S}_f^{(n)}$ is governed by the pressure gradient obtained from the tribotopological Reynolds equation (TTR, see Section 3.6).

3.5 Tribotopological Velocity Profile

The TT velocity profile in the lubrication gap consists of several distinct and connected spaces $\mathcal{S}^{(n)}$ and is defined as:

$$\mathbf{v}|_{\mathcal{S}^{(n)}} = \begin{cases} (v_x^{(n)} \quad 0 \quad v_z^{(n)})^T & \text{if } l^{(n)} = 2 \\ (\breve{v}_x^{(n)} \quad 0 \quad \breve{v}_z^{(n)})^T & \text{if } l^{(n)} = 1 \\ (\ 0 \quad 0 \quad 0\ )^T & \text{if } l^{(n)} = 0 \end{cases} \tag{3.18}$$

where $\breve{v}_x^{(n)} = \breve{v}_x^{(n)}(x, y, z, t)$ and $\breve{v}_z^{(n)} = \breve{v}_z^{(n)}(x, y, z, t)$ are the constant velocities within the plug space $\mathcal{S}_p^{(n)}$. The dynamic viscosity of the lubricant is variable, which is taken into account by defining the integral factors $\tilde{C}_k^y$ and $\tilde{\tilde{C}}_k^y$ by:

$$\tilde{C}_k^y = \int_0^y \frac{\upsilon^k}{\eta} d\upsilon \quad , \quad \tilde{\tilde{C}}_k^y = \int_0^y \tilde{C}_k^\upsilon d\upsilon \tag{3.19}$$

The shells of any space $\mathcal{S}^{(n)}$ are defined by:

$$c_-^{(n)} = \delta c^{(n)} + \frac{c - c'^{(n)}}{2} \ , \ c_+^{(n)} = \delta c^{(n)} + \frac{c + c'^{(n)}}{2} \tag{3.20}$$

where $\delta c^{(n)}$ is the radial shift of any space $\mathcal{S}^{(n)}$ from the center line of the lubrication gap. Both shells are linked by the radial thickness $c'^{(n)} = c_+^{(n)} - c_-^{(n)}$ of the space $\mathcal{S}^{(n)}$ such that $c_+^{(n)} = c_-^{(n)} + c'^{(n)}$. By continuity of the domain Ω, the shells of adjacent spaces are equal such that $c_-^{(n)} = c_+^{(n-1)}$ and $c_+^{(n)} = c_-^{(n+1)}$. The velocity profile in the space $\mathcal{S}^{(n)}$ is determined from the conservation of momentum by directly integrating the pressure gradient in Eq. (3.14) over the entire space $\mathcal{S}^{(n)}$. The circumferential velocity $v_x^{(n)}$ and the vertical velocity $v_z^{(n)}$ in the space $\mathcal{S}^{(n)}$ are defined as a parabolic velocity profile, which is driven by a hydrodynamic pressure gradient:

$$\forall \mathbf{x} \in \mathcal{S}^{(n)} \ : \ v_{x|z}^{(n)}(x,y,z,t) = \Lambda''^{(n)}_{x|z}\tilde{C}_1^y + \Lambda'^{(n)}_{x|z}\tilde{C}_0^y + \Lambda_{x|z}^{(n)} \tag{3.21}$$

where $\Lambda'^{(n)}_{x|z}$ and $\Lambda_{x|z}^{(n)}$ are integration functions. As the fluid flow of the lubricant in space $\mathcal{S}^{(n)}$ resembles the flow of oil in small lubrication gaps under pressure (Poiseuille flow), the integration functions can be expressed as linear functions of the governing pressure gradient such that:

$$\Lambda_{x|z}^{(n)} = a_{x|z}^{(n)} p_{,x|z} + b_{x|z}^{(n)} \quad , \quad \Lambda'^{(n)}_{x|z} = a'^{(n)}_{x|z} p_{,x|z} + b'^{(n)}_{x|z} \quad , \quad \Lambda''^{(n)}_{x|z} = a''^{(n)}_{x|z} p_{,x|z} + b''^{(n)}_{x|z} \tag{3.22}$$

Once the velocity integration functions are known, the entire velocity profile within the lubrication gap can be determined. The definition of the integration functions as being linear functions of the governing pressure gradient is critical for the derivation of the governing TTR equation. The factors of the integration functions a, a', b, b' and a'', b'' are dependent on position (x, y, z) and time t. For each space $\mathcal{S}^{(n)}$, the velocity field at the shells is given by the type of the adjacent space. The TTT is based on the assumption that adjacent spaces of the same kind merge into one space such that $\mathcal{S}_{f|p|d}^{(n)} \Big| \mathcal{S}_{f|p|d}^{(n-1)} \rightarrow \mathcal{S}_{f|p|d}^{(n)}$ and $N_s \leftarrow N_s - 1$.

	Piston surface	**Bearing surface**
Circumferential velocity	$v_x\big\|_{y=0} = \dot{\phi} = R_P\omega_P$	$v_x\big\|_{y=c} = R'_c\omega_c$
Vertical velocity	$v_z\big\|_{y=0} = \dot{z}$	$v_z\big\|_{y=c} = \dot{Z}$

Table 3.1: Boundary conditions of the velocity field.

A space with an overall thickness below the mesh size ($c'^{(n)} < \Delta y$) is considered a zero-thickness space, or globally flat space. Locally flat spaces are commonly found when local disintegration of grease occurs. The velocity field at the contacting surfaces (lubricated surfaces) is given in Table 3.1.

Integration Functions Algorithm (IFA)

The Integration Functions Algorithm (IFA) is a core algorithm (see Algorithm 2) of the TTT, and is used to determine the integration functions $\Lambda'^{(n)}_{x|z}$ and $\Lambda_{x|z}^{(n)}$. The IFA relies on the type vector $\mathbf{l}$, which is determined using the Topology Detection Algorithm (TDA) that is explained

in Section 4.4.5. The boundary detection algorithm detects the shells $c_+^{(n)}$ and $c_-^{(n)}$ of each space $\mathcal{S}^{(n)}$. In order to determine the boundary conditions to the velocity profile in the TT spaces, the velocity profile for the space with the lowest type vector $\mathbf{l}$ is calculated first. The type vector is sorted in ascending order. For example, the type vector could read $\mathbf{l} = (2\ 1\ 0\ 1\ 2)^T$ for a dry space embedded between a plug and fluid space. In this case, the sorted type vector would read $\mathbf{l}^\star = (0\ 1\ 1\ 2\ 2)^T$. Similarly, a fluid space connected to the inner side of a plug space is characterized by a type vector $\mathbf{l} = (2\ 1)^T$. The second order integration function $\Lambda''^{(n)}_{x|z}$ is nonzero for a fluid space (and vanishes for any other type), and is dependent on the fluid pressure gradient such that:

$$\Lambda''^{(n)}_{x|z} = \begin{cases} 0 & \text{if } l^{(n)} = 0, 1 \\ p_{,x|z} & \text{if } l^{(n)} = 2 \end{cases} \tag{3.23}$$

Consequently, for any fluid space ($l^{(n)} = 2$), the factors of the integration functions are given by $a''^{(n)}_{x|z} = 1$ and $b''^{(n)}_{x|z} = 0$. In addition to the second order factor, the first and zero-th order integration functions $\Lambda'^{(n)}_{x|z}$ and $\Lambda^{(n)}_{x|z}$ must be determined for fluid spaces ($l^{(n)} = 2$) using the IFA. For plug and dry spaces ($l^{(n)} = 0, 1$), the first integration function is zero. Additionally, for a dry shell ($l^{(n)} = 0$), the zero-th order integration function is zero. For the special case of one or more plug spaces in the lubrication gap, several cases have to be distinguished. The listed cases are only for the special cases of plug spaces that are floating or surrounded by other spaces. For constellations not involving plug spaces, such as the case of fluid-dry-fluid, the 2BC algorithm is used.

CASE 1: Plug space floating between fluid spaces (3-Spaces Algorithm - 3SA)

When a plug space is floating between two fluid spaces, the 3-Spaces Algorithm (3SA) with a constant plug flow velocity is used to determine the velocity field in the fluid spaces $\mathcal{S}_f^{(n-1)}$ and $\mathcal{S}_f^{(n+1)}$, and the constant plug flow velocity in the plug space $\mathcal{S}_p^{(n)}$.

CASE 1 : Plug is floating between 2 fluid shells

1.1	fluid	plug	fluid	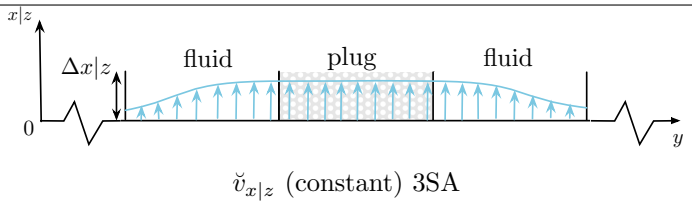

Table 3.2: Possible velocity profile configuration - Case 1.

For given shells $c_+^{(n)}$ and $c_-^{(n)}$, a pressure gradient $p_{,x|z}$ and shell velocities $v_{x|z}\big|_{c_-^{(n+1)}}$ and $v_{x|z}\big|_{c_-^{(n-1)}}$, the uniform plug flow velocity $\breve{v}^{(n)}_{x|z}$ and the integration functions $\Lambda'^{(n\pm1)}_{x|z}$ and $\Lambda^{(n\pm1)}_{x|z}$ can be determined. At the shells of the plug space, the velocity field is continuous such that $v^{(n)}_{x|z}\big|_{c_\pm^{(n)}} = v^{(n\pm1)}_{x|z}\big|_{c_\mp^{(n)}} = \Lambda^{(n)}_{x|z} = \breve{v}^{(n)}_{x|z}$. The integration factors are given by $a'^{(n)}_{x|z} = a''^{(n)}_{x|z} = b'^{(n)}_{x|z} = b''^{(n)}_{x|z} = 0$ and $b^{(n)}_{x|z} = \breve{v}_{x|z}$. The velocities at the shells from the adjacent space are denoted as $v^{(n)}_{x|z}\big|_{c_-^{(n-1)}} = \tilde{V}'_{x|z}$ and $v^{(n)}_{x|z}\big|_{c_+^{(n+1)}} = \tilde{V}_{x|z}$, where $\tilde{V}_{x|z}$ and $\tilde{V}'_{x|z}$ are linear dummy velocities which

depend on the neighboring spaces. The velocity continuity conditions lead to a linear system $\mathbf{T}_s^{(n)}\mathbf{\Lambda}^{(n)} = \mathbf{s}^{(n)}$, where $\mathbf{T}_s^{(n)}$ is the topology matrix, $\mathbf{\Lambda}^{(n)}$ the integration functions vector, and $\mathbf{s}^{(n)}$ the shell vector:

$$\underbrace{\begin{bmatrix} \tilde{C}_0^{c_-^{(n-1)}} & 1 & 0 & 0 \\ \tilde{C}_0^{c_-^{(n)}} & 1 & 0 & 0 \\ 0 & 0 & \tilde{C}_0^{c_+^{(n+1)}} & 1 \\ 0 & 0 & \tilde{C}_0^{c_+^{(n)}} & 1 \end{bmatrix}}_{\mathbf{T}_s^{(n)}} \underbrace{\begin{bmatrix} \Lambda'^{(n-1)}_{x|z} \\ \Lambda^{(n-1)}_{x|z} \\ \Lambda'^{(n+1)}_{x|z} \\ \Lambda^{(n+1)}_{x|z} \end{bmatrix}}_{\mathbf{\Lambda}^{(n)}} = \underbrace{\begin{bmatrix} \tilde{V}'_{x|z} - \tilde{C}_1^{c_-^{(n-1)}} \; p_{,x|z} \\ \breve{v}^{(n)}_{x|z} \\ \tilde{V}_{x|z} - \tilde{C}_1^{c_+^{(n+1)}} \; p_{,x|z} \\ \breve{v}^{(n)}_{x|z} \end{bmatrix}}_{\mathbf{s}^{(n)}} \tag{3.24}$$

Algorithm 2 Integration Functions Algorithm (IFA)

BEGIN
Allocate and initialize all variables and the shell counter n = 1
Determine the type vector $\mathbf{l}$ and its size N_s
Sort the type vector $\mathbf{l}$ and save as $\mathbf{l}^\star$. Save sorted index table $n \leftrightarrow n^\star$
Define the velocities at the boundaries $y = \{0, c\}$
DO WHILE ($i \leq N_x + 2$ & $k \leq N_z + 2$)
  DO WHILE ($n^\star \leq N_s$)
    Current shell: $l^{\star(n^\star)} \leftrightarrow l^{(n)}$, $n \leftrightarrow n^\star$
    Determine the adjacent shell types $l^{(n-1)}$ and $l^{(n+1)}$ (neighbors)
    Extract the boundaries $c_+^{(n)}$ and $c_-^{(n)}$ and the corresponding indices along y
    IF (shell is locally flat)
      Skip space n
    END IF
    IF ($l^{(n)} = 1$ & $l^{(n-1)} = 2$ & $l^{(n+1)} = 2$) $\sim$ 1.1 - 3SA -Floating Plug Space
      $\Lambda''^{(n)}_{x|z}$ =$\Lambda'^{(n)}_{x|z}$=0 and 3SA calculation for $\Lambda'^{(n\pm1)}_{x|z}$, $\Lambda^{(n\pm1)}_{x|z}$ and $\Lambda^{(n)}_{x|z}$ (plug velocity)
      Skip the spaces $n \pm 1$ (neighbors)
    END IF
    IF (shell is not skipped)
      IF ($l^{(n)} = 0$) $\sim$ Dry Space
        $\Lambda''^{(n)}_{x|z}$ =$\Lambda'^{(n)}_{x|z}$=$\Lambda^{(n)}_{x|z} = 0$
      ELSE IF ($l^{(n)} = 1$) $\sim$ Sticking Plug Space
        $\Lambda''^{(n)}_{x|z}$ =$\Lambda'^{(n)}_{x|z}$=0
        IF ($n = 1$ & $l^{(2)} = 2$) | ($n = N_s$ & $l^{(N_s-1)} = 2$) $\sim$ 2.1- 2.2
          $a^{(n)}_{x|z} = 0$ and $b^{(n)}_{x|z}\Big|_{y=\{0,c\}} = v_{x|z}\Big|_{y=\{0,c\}}$
        ELSE IF ($N_s = 1$) | ($n = 1$ & $l^{(2)} = 1$) | ($n = N_s$ & $l^{(N_s-1)} = 1$) $\sim$ 2.3- 2.5
          2BC0 calculation for $\Lambda'^{(n)}_{x|z}$ and $\Lambda^{(n)}_{x|z}$
        END IF
      ELSE $\sim$ Fluid Space
        2BC1 calculation for $\Lambda'^{(n)}_{x|z}$ and $\Lambda^{(n)}_{x|z}$
      END IF
    END IF
  $n^\star = n^\star + 1$
  END DO
  Increment counters i and k
END DO
END

The topology matrix $\mathbf{T}_s^{(n)}$ is generally nonsymmetric. The linear system shown in Eq. (3.24) is solved analytically to determine the integration functions in $\mathbf{\Lambda}^{(n)}$ and the unknown plug flow core velocity $\breve{v}_{x|z}^{(n)}$. The determinant of the topology matrix $\mathbf{T}_s^{(n)}$ is given by: $\Delta\mathbf{T}_s^{(n)} = \det\left(\mathbf{T}_s^{(n)}\right) = \tilde{\Lambda}_0^+ \cdot \tilde{\Lambda}_0^-$, where $\tilde{\Lambda}_0^- = \tilde{C}_0^{c_-^{(n)}} - \tilde{C}_0^{c_-^{(n-1)}}$ and $\tilde{\Lambda}_0^+ = \tilde{C}_0^{c_+^{(n)}} - \tilde{C}_0^{c_+^{(n+1)}}$. Similarly, the factors $\tilde{\Lambda}_1^- = \tilde{C}_1^{c_-^{(n)}} - \tilde{C}_1^{c_-^{(n-1)}}$ and $\tilde{\Lambda}_1^+ = \tilde{C}_1^{c_+^{(n)}} - \tilde{C}_1^{c_+^{(n+1)}}$ are defined. The integration factors are calculated such that:

$$a'^{(n-1)}_{x|z} = \frac{-\tilde{\Lambda}_1^-}{\tilde{\Lambda}_0^-} \quad , \quad a'^{(n+1)}_{x|z} = \frac{-\tilde{\Lambda}_1^+}{\tilde{\Lambda}_0^+} \quad , \quad b'^{(n-1)}_{x|z} = \frac{\breve{v}_{x|z} - \tilde{V}'_{x|z}}{\tilde{\Lambda}_0^-} \quad , \quad b'^{(n+1)}_{x|z} = \frac{\breve{v}_{x|z} - \tilde{V}_{x|z}}{\tilde{\Lambda}_0^+} \tag{3.25}$$

In a similar manner, the remaining integration factors are given by

$$\begin{aligned} a_{x|z}^{(n-1)} &= \frac{\tilde{C}_0^{c_-^{(n-1)}}\tilde{C}_1^{c_-^{(n)}} - \tilde{C}_0^{c_-^{(n)}}\tilde{C}_1^{c_-^{(n-1)}}}{\tilde{\Lambda}_0^-} \quad , \quad b_{x|z}^{(n-1)} = \frac{\tilde{C}_0^{c_-^{(n)}}\tilde{V}'_{x|z} - \tilde{C}_0^{c_-^{(n-1)}}\breve{v}_{x|z}}{\tilde{\Lambda}_0^-} \\ a_{x|z}^{(n+1)} &= \frac{\tilde{C}_0^{c_+^{(n+1)}}\tilde{C}_1^{c_+^{(n)}} - \tilde{C}_0^{c_+^{(n)}}\tilde{C}_1^{c_+^{(n+1)}}}{\tilde{\Lambda}_0^+} \quad , \quad b_{x|z}^{(n+1)} = \frac{\tilde{C}_0^{c_+^{(n)}}\tilde{V}_{x|z} - \tilde{C}_0^{c_+^{(n+1)}}\breve{v}_{x|z}}{\tilde{\Lambda}_0^+} \end{aligned} \tag{3.26}$$

The shear stress at the shell of the adjacent space must be continuous such that $\eta v_{x|z,y}^{(n)}\Big|_{c_\pm^{(n)}} = \eta v_{x|z,y}^{(n\pm1)}\Big|_{c_\mp^{(n)}}$, which determines the plug flow core velocity along the vertical and circumferential directions:

$$\breve{v}_{x|z}^{(n)} = \frac{\Delta\mathbf{T}_s^{(n)}}{\tilde{\Lambda}_0^- - \tilde{\Lambda}_0^+}\left(\frac{\tilde{\Lambda}_1^+ p_{,x|z} + \tilde{V}_{x|z}}{\tilde{\Lambda}_0^+} - \frac{\tilde{\Lambda}_1^- p_{,x|z} + \tilde{V}'_{x|z}}{\tilde{\Lambda}_0^-} + \left(c_-^{(n)} - c_+^{(n)}\right) p_{,x|z}\right) \tag{3.27}$$

CASE 2: Plug space sticking on a wall

CASES 2.1 and 2.2: Wall | Plug | Fluid or Fluid | Plug | Wall In this case, the plug space sticks on a wall on one side and contacts a fluid space on the other side. The plug space can be considered as an 'extension' of the wall, and the velocity within the space is dependent on the velocity of the wall. The coefficients of the integration functions are given by $a_{x|z}^{(n)} = 0$ and $b_{x|z}^{(n)}\Big|_{y=c} = v_{x|z}\big|_{y=c}$. Similarly, $b_{x|z}^{(n)}\Big|_{y=0} = v_{x|z}\big|_{y=0}$.

CASES 2.3, 2.4 and 2.5: Wall | Plug | Wall or Wall | Plug | Dry or Dry | Plug | Wall The plug space either sticks on both walls or contacts a wall and a dry space. If the plug space sticks in-between and contacts both walls, the lubricant is not sheared enough such that it would allow any other space to co-exist. This case is only likely to occur if both contacting walls have a near-zero velocity, leaving the plug almost entirely intact. This case is most commonly described as the near zero-velocity case or the *stiction* case. The velocity profile within the plug shell is given by a linear distribution, not governed by a pressure gradient. An eventual pressure that is calculated by the TTR equation is not applicable for nonflowing or solid phases of lubricants. The stiction case with grease can be considered as a solid-like wax that is confined between two moving surfaces.

CASE 2 : Plug is sticking on a wall

2.1	wall	plug	fluid	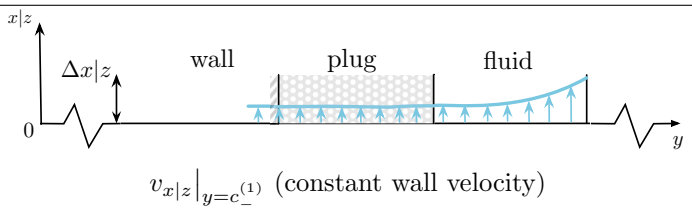 $v_{x\|z}\big\|_{y=c_-^{(1)}}$ (constant wall velocity)
2.2	fluid	plug	wall	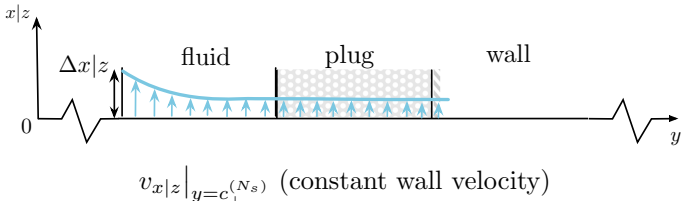 $v_{x\|z}\big\|_{y=c_+^{(Ns)}}$ (constant wall velocity)
2.3	wall	plug	wall	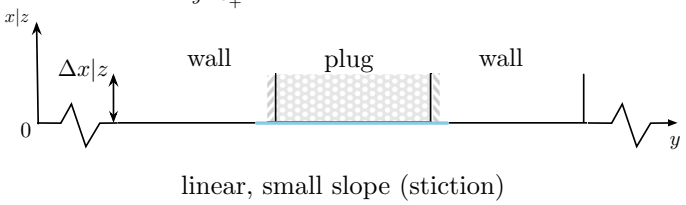 linear, small slope (stiction)
2.4	wall	plug	dry	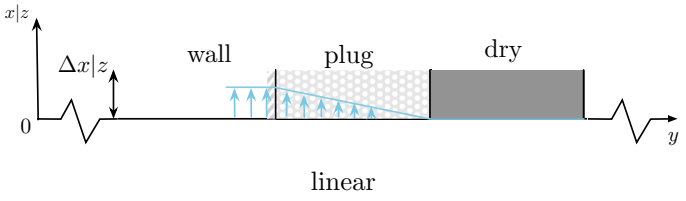 linear
2.5	dry	plug	wall	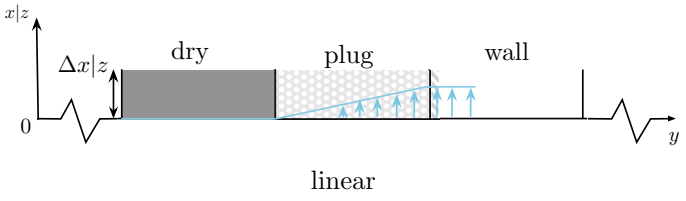 linear

CASE 3 : Plug is contacting a dry shell, but not a wall

3.1	dry	plug	dry	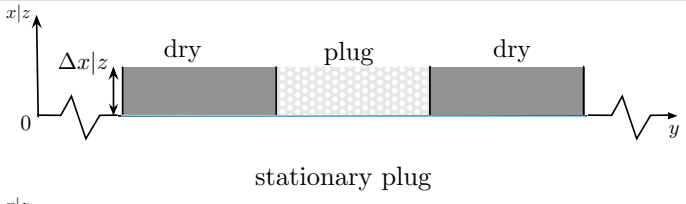 stationary plug
3.2	dry	plug	fluid	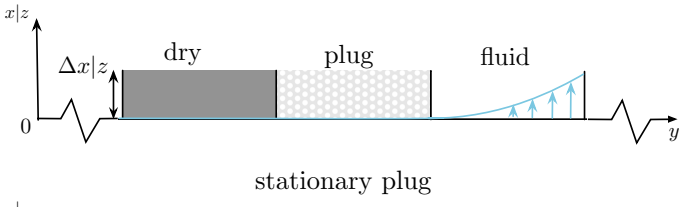 stationary plug
3.3	fluid	plug	dry	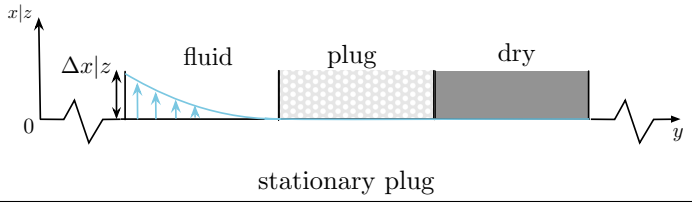 stationary plug

Table 3.3: Possible velocity profile configuration - Cases 2 and 3.

Within the plug space, the velocity profile is derived from the reduced Navier-Stokes equations:

$$\left(\eta v_{x,y}\right)_{,y} = 0 \quad , \quad \left(\eta v_{z,y}\right)_{,y} = 0 \tag{3.28}$$

Double integration of Eq (3.28) together with the boundary velocities $v^{(n)}_{x|z}\Big|_{y=c^{(n)}_{+}} = \tilde{V}'_{x|z}$ and $v^{(n)}_{x|z}\Big|_{y=c^{(n)}_{-}} = \tilde{V}_{x|z}$, where $\tilde{V}_{x|z}$ and $\tilde{V}'_{x|z}$ are linear dummy boundary velocities, leads to calculating the velocity profile using the 2BCχ algorithm (with $\chi = 0$, no pressure gradient).

CASE 3: Plug space contacting a dry space but not a wall (Dry | Plug | Dry or Dry | Plug | Fluid or Fluid | Plug | Dry)

In this case, the plug space contacts a dry space, and the velocity profile within both spaces is zero. Cases 3.1-3.3 shown in Table 3.3 can be considered in a very similar way to Cases 2.1 and 2.2, for which the plug space is sticking on a wall. As the wall is not moving, the integration factors are given by: $a^{(n)}_{x|z} = b^{(n)}_{x|z} = 0$.

Velocity Dirichlet Boundary Conditions (2BCχ)

By imposing Dirichlet boundary conditions on the velocity field of the lubricant within a fluid space $\mathcal{S}^{(n)}_f$, the integration functions can be determined in a manner similar to using the 3SA. The velocity boundary conditions are imposed as $v^{(n)}_{x|z}\Big|_{c^{(n)}_{-}} = \tilde{V}'_{x|z}$ and $v^{(n)}_{x|z}\Big|_{c^{(n)}_{+}} = \tilde{V}_{x|z}$, where $\tilde{V}_{x|z}$ and $\tilde{V}'_{x|z}$ are linear dummy boundary velocities. The continuity condition of the velocity field at the boundaries $c^{(n)}_{-}$ and $c^{(n)}_{+}$ yields the integration factors given by:

$$\underbrace{\begin{bmatrix} \tilde{C}_0^{c^{(n)}_{-}} & 1 \\ \tilde{C}_0^{c^{(n)}_{+}} & 1 \end{bmatrix}}_{\mathbf{T}^{(n)}_s} \underbrace{\begin{bmatrix} \Lambda'^{(n)}_{x|z} \\ \Lambda^{(n)}_{x|z} \end{bmatrix}}_{\mathbf{\Lambda}^{(n)}} = \underbrace{\begin{bmatrix} \tilde{V}'_{x|z} - \chi \tilde{C}_1^{c^{(n)}_{-}}\, p_{,x|z} \\ \tilde{V}_{x|z} - \chi \tilde{C}_1^{c^{(n)}_{+}}\, p_{,x|z} \end{bmatrix}}_{\mathbf{s}^{(n)}(\chi)} \tag{3.29}$$

The determinant of the topology matrix $\mathbf{T}^{(n)}_s$ is given by $\Delta\mathbf{T}^{(n)}_s = \det\left(\mathbf{T}^{(n)}_s\right) = \tilde{C}_0^{c^{(n)}_{-}} - \tilde{C}_0^{c^{(n)}_{+}}$. For a locally nonflat space, the determinant $\Delta\mathbf{T}^{(n)}_s \neq 0$. The linear system shown in Eq. (3.29) yields the integration factors for the fluid space $\mathcal{S}^{(n)}_f$:

$$\begin{aligned} a'^{(n)}_{x|z} &= \frac{\chi}{\Delta\mathbf{T}^{(n)}_s}\left(\tilde{C}_1^{c^{(n)}_{+}} - \tilde{C}_1^{c^{(n)}_{-}}\right) & b'^{(n)}_{x|z} &= \frac{1}{\Delta\mathbf{T}^{(n)}_s}\left(\tilde{V}' - \tilde{V}\right) \\ a^{(n)}_{x|z} &= \frac{\chi}{\Delta\mathbf{T}^{(n)}_s}\left(\tilde{C}_0^{c^{(n)}_{+}}\tilde{C}_1^{c^{(n)}_{-}} - \tilde{C}_0^{c^{(n)}_{-}}\tilde{C}_1^{c^{(n)}_{+}}\right) & b^{(n)}_{x|z} &= \frac{1}{\Delta\mathbf{T}^{(n)}_s}\left(\tilde{C}_0^{c^{(n)}_{-}}\tilde{V} - \tilde{C}_0^{c^{(n)}_{+}}\tilde{V}'\right) \end{aligned} \tag{3.30}$$

3.6 General Tribotopological Reynolds Equation

The general tribotopological Reynolds (TTR) equation is the governing equation of the TTT, is a novel equation and is derived from the continuity equation (conservation of mass) by integration of the velocity profile across multiple spaces. By making use of the velocity definition

in Eq. (3.21) and by transforming the original integration using the Leibniz integral rule, an integrated continuity equation across the film is given by $-\dot{c} = I_x + I_z$, where:

$$I_{x|z} = \sum_{n=1}^{N_s} \int_{c_-^{(n)}}^{c_+^{(n)}} \left(\Lambda''^{(n)}_{x|z} \tilde{C}_1^y + \Lambda'^{(n)}_{x|z} \tilde{C}_0^y + \Lambda^{(n)}_{x|z} \right)_{,x|z} dy \tag{3.31}$$

The integration components of the continuity equation are further simplified by using the linearity of the integration functions and by applying the product rule of differentiation:

$$\begin{aligned} I_{x|z} = &\sum_{n=1}^{N_s} \left(\Lambda''^{(n)}_{x|z} \right)_{,x|z} \tilde{\tilde{\Gamma}}_1^{(n)}{}_{x|z} + \sum_{n=1}^{N_s} \Lambda''^{(n)}_{x|z} \tilde{\tilde{\Gamma}}_1^{(n)}{}_{x|z,x|z} + \sum_{n=1}^{N_s} \Lambda''^{(n)}_{x|z} \tilde{\Gamma}_1^{(n)}{}_{x|z} \\ &+ \sum_{n=1}^{N_s} \left(\Lambda'^{(n)}_{x|z} \right)_{,x|z} \tilde{\tilde{\Gamma}}_0^{(n)}{}_{x|z} + \sum_{n=1}^{N_s} \Lambda'^{(n)}_{x|z} \tilde{\tilde{\Gamma}}_0^{(n)}{}_{x|z,x|z} + \sum_{n=1}^{N_s} \Lambda'^{(n)}_{x|z} \tilde{\Gamma}_0^{(n)}{}_{x|z} + \sum_{n=1}^{N_s} \left(\Lambda^{(n)}_{x|z} \right)_{,x|z} c'^{(n)} \end{aligned} \tag{3.32}$$

where $c'^{(n)} = c_+^{(n)} - c_-^{(n)}$ and:

$$\begin{aligned} \tilde{\tilde{\Gamma}}_1^{(n)}{}_{x|z} &= \tilde{\tilde{C}}_1^{c_+^{(n)}} - \tilde{\tilde{C}}_1^{c_-^{(n)}} & \tilde{\tilde{\Gamma}}_0^{(n)}{}_{x|z} &= \tilde{\tilde{C}}_0^{c_+^{(n)}} - \tilde{\tilde{C}}_0^{c_-^{(n)}} \\ \tilde{\Gamma}_1^{(n)}{}_{x|z} &= \tilde{C}_1^{c_-^{(n)}} c_-^{(n)}{}_{,x|z} - \tilde{C}_1^{c_+^{(n)}} c_+^{(n)}{}_{,x|z} & \tilde{\Gamma}_0^{(n)}{}_{x|z} &= \tilde{C}_0^{c_-^{(n)}} c_-^{(n)}{}_{,x|z} - \tilde{C}_0^{c_+^{(n)}} c_+^{(n)}{}_{,x|z} \end{aligned} \tag{3.33}$$

By using Eq. (3.22), the derivatives of the integration functions are given by

$$\begin{aligned} \left(\Lambda^{(n)}_{x|z} \right)_{,x|z} &= a^{(n)}_{x|z,x|z} p_{,x|z} + a^{(n)}_{x|z} p_{,xx|zz} + b^{(n)}_{x|z,x|z} \\ \left(\Lambda'^{(n)}_{x|z} \right)_{,x|z} &= a'^{(n)}_{x|z,x|z} p_{,x|z} + a'^{(n)}_{x|z} p_{,xx|zz} + b'^{(n)}_{x|z,x|z} \\ \left(\Lambda''^{(n)}_{x|z} \right)_{,x|z} &= a''^{(n)}_{x|z} p_{,xx|zz} \end{aligned} \tag{3.34}$$

By using Eq. (3.34), the integration components of Eq. (3.32) can be further simplified to:

$$\begin{aligned} I_{x|z} = &\sum_{n=1}^{N_s} a''^{(n)}_{x|z} \tilde{\tilde{\Gamma}}_1^{(n)} p_{,xx|zz} + a''^{(n)}_{x|z} \tilde{\tilde{\Gamma}}_1^{(n)}{}_{,x|z} p_{,x|z} + a''^{(n)}_{x|z} \tilde{\Gamma}_1^{(n)} p_{,x|z} + a'^{(n)}_{x|z,x|z} \tilde{\tilde{\Gamma}}_0^{(n)} p_{,x|z} \\ &+ a'^{(n)}_{x|z} \tilde{\tilde{\Gamma}}_0^{(n)} p_{,xx|zz} + b'^{(n)}_{x|z,x|z} \tilde{\tilde{\Gamma}}_0^{(n)}{}_{,x|z} + a'^{(n)}_{x|z} \tilde{\tilde{\Gamma}}_0^{(n)}{}_{x|z,x|z} p_{,x|z} + b'^{(n)}_{x|z} \tilde{\tilde{\Gamma}}_0^{(n)}{}_{x|z,x|z} \\ &+ a'^{(n)}_{x|z} \tilde{\Gamma}_0^{(n)} p_{,x|z} + b'^{(n)}_{x|z} \tilde{\Gamma}_0^{(n)} + a^{(n)}_{x|z,x|z} c'^{(n)} p_{,x|z} + a^{(n)}_{x|z} c'^{(n)} p_{,xx|zz} + b^{(n)}_{x|z,x|z} c'^{(n)} \end{aligned} \tag{3.35}$$

In order to reduce the integrals and identify the dominant pressure derivatives, Eq. (3.35) can be rewritten such that $I_{x|z} = \tilde{\tilde{f}}_{x|z} p_{,xx|zz} + \tilde{f}_{x|z} p_{,x|z} + f_{x|z}$, where:

$$\begin{aligned} \tilde{\tilde{f}}_{x|z} &= \sum_{n=1}^{N_s} a''^{(n)}_{x|z} \tilde{\tilde{\Gamma}}_1^{(n)}{}_{x|z} + \sum_{n=1}^{N_s} a'^{(n)}_{x|z} \tilde{\tilde{\Gamma}}_0^{(n)}{}_{x|z} + \sum_{n=1}^{N_s} a^{(n)}_{x|z} c'^{(n)} \\ \tilde{f}_{x|z} &= \sum_{n=1}^{N_s} a''^{(n)}_{x|z} \tilde{\tilde{\Gamma}}_1^{(n)}{}_{,x|z} + \sum_{n=1}^{N_s} a''^{(n)}_{x|z} \tilde{\Gamma}_1^{(n)}{}_{x|z} + \sum_{n=1}^{N_s} \left(a'^{(n)}_{x|z} \tilde{\tilde{\Gamma}}_0^{(n)}{}_{x|z} \right)_{,x|z} \\ &\qquad + \sum_{n=1}^{N_s} a'^{(n)}_{x|z} \tilde{\Gamma}_0^{(n)}{}_{x|z} + \sum_{n=1}^{N_s} a^{(n)}_{x|z,x|z} c'^{(n)} \\ f_{x|z} &= \sum_{n=1}^{N_s} \left(b'^{(n)}_{x|z} \tilde{\tilde{\Gamma}}_0^{(n)}{}_{x|z} \right)_{,x|z} + \sum_{n=1}^{N_s} b'^{(n)}_{x|z} \tilde{\Gamma}_0^{(n)}{}_{x|z} + \sum_{n=1}^{N_s} b^{(n)}_{x|z,x|z} c'^{(n)} \end{aligned} \tag{3.36}$$

The variable coefficients shown in Eq. (3.36) contain the factors of the velocity integration functions within each TT space. The sum of these factors are redefined as $f_{x|z}, \tilde{f}_{x|z}$ and $\tilde{\tilde{f}}_{x|z}$, which physically represent an assembly of tribotopological spaces. For any non-Newtonian fluid that is behaving in a nonhomogeneous, multiphasic manner, the general transient tribotopological Reynolds (TTR) equation is finally given as:

$$\tilde{\tilde{f}}_x \, p_{,xx} + \tilde{\tilde{f}}_z \, p_{,zz} + \tilde{f}_x \, p_{,x} + \tilde{f}_z \, p_{,z} = -\partial_{,t} c - f_x - f_z \tag{3.37}$$

The TTR equation shown in Eq. (3.37) is the core of the TTT and gives the pressure field within the lubricant. This transient second-order PDE is a global equation that is valid within the entire lubrication domain. In combination with the velocity profile determined in Section 3.5 and the temperature field resulting from Eq. (3.12), the physical behavior of the lubricant is fully defined.

3.7 Validation of the TTT

The TTT is validated for several simplified cases and is demonstrated to be an extension of the existing Newtonian uniphasic lubrication theory. In addition to the validation of the Reynolds equation, the temperature field, calculated with the energy equation, is validated. The validation of the theory is performed under the assumption of rigid contacting surfaces. The detailed convergence procedure of the shells is shown for a grease-lubricated bearing in Section 3.7.2. In addition, an analytical formula of the shell between a plug and a fluid space is given.

3.7.1 Special Case I: Oil-lubricated Bearing

Linear Motion (Vertical Translation)

For the case of a single ($N_s = 1$) fluid space $\mathcal{S}_f^{(1)}$, the fluid film velocity is calculated by using the 2BCχ ($\chi = 1$) algorithm. The boundary velocities are set as $v_z|_{y=c} = 0$ and $v_z|_{y=0} = \tilde{U}$. In order to generate a noncavitating hydrodynamic pressure, one of the contacting surfaces must be moving in the direction of the converging thrust portion. For a purely linear motion (nonrotating piston), the boundary circumferential velocities are given by $v_x|_{y=\{0,c\}} = 0$. The shells of the single fluid space are given as $c_-^{(1)} = 0$ and $c_+^{(1)} = c$. The thickness of the fluid space is given by $c'^{(1)} = c$. The determinant of the topology matrix $\mathbf{T}_s^{(1)}$ is given by $\Delta\mathbf{T}_s^{(1)} = \det\left(\mathbf{T}_s^{(1)}\right) = -\tilde{C}_0^c$. As the flow within the fluid space is governed everywhere by the same hydrodynamic pressure gradient, the integration factor of the pressure gradient is given by $a''^{(1)}_{x|z} = 1$. The integration functions of the fluid film velocity are simplified to

$$a'^{(1)}_{x|z} = -\frac{\tilde{C}_1^c}{\tilde{C}_0^c} \quad , \quad b'^{(1)}_{z} = \frac{\tilde{U}}{\tilde{C}_0^c} \quad , \quad a^{(1)}_{x|z} = b^{(1)}_{x|z} = b'^{(1)}_{x} = 0 \tag{3.38}$$

The velocity field components for a nonisoviscous lubricant in the circumferential direction

x and in the vertical direction z are given by ($\forall \mathbf{x} \in \mathcal{S}_f^{(1)}$):

$$v_x^{(1)} = \left(\tilde{C}_1^y - \frac{\tilde{C}_1^c \tilde{C}_0^y}{\tilde{C}_0^c} \right) p_{,x} \quad , \quad v_z^{(1)} = \left(\tilde{C}_1^y - \frac{\tilde{C}_1^c \tilde{C}_0^y}{\tilde{C}_0^c} \right) p_{,z} + \left(1 - \frac{\tilde{C}_0^y}{\tilde{C}_0^c} \right) \tilde{U} \tag{3.39}$$

Furthermore, Eq. (3.33) simplifies to:

$$\tilde{\tilde{\Gamma}}_0^{(1)}{}_{,x|z} = \tilde{\tilde{C}}_0^c \quad , \quad \tilde{\Gamma}_0^{(1)}{}_{,x|z} = -\tilde{C}_0^c c_{,x|z} \quad , \quad \tilde{\tilde{\Gamma}}_1^{(1)}{}_{,x|z} = \tilde{\tilde{C}}_1^c \quad , \quad \tilde{\Gamma}_1^{(1)}{}_{,x|z} = -\tilde{C}_1^c c_{,x|z} \tag{3.40}$$

Finally, the TTR equation given by Eq. (3.37) is written as:

$$\left(\tilde{\tilde{f}}_x p_{,x} \right)_{,x} + \left(\tilde{\tilde{f}}_z p_{,z} \right)_{,z} = -\dot{c} - f_x - f_z \tag{3.41}$$

By realizing that $\tilde{f}_{x|z} = \tilde{\tilde{f}}_{x|z,x|z}$, the integration functions are given by:

$$\tilde{\tilde{f}}_{x|z} = \tilde{\tilde{C}}_1^c - \frac{\tilde{C}_1^c}{\tilde{C}_0^c} \tilde{\tilde{C}}_0^c \quad , \quad f_z = -\tilde{U} \left(\frac{\tilde{\tilde{C}}_0^c}{\tilde{C}_0^c} - c \right)_{,z} \quad , \quad f_x = 0 \tag{3.42}$$

For isoviscous oil ($\eta = \eta_0$), the velocity profile is given by ($\forall \mathbf{x} \in \mathcal{S}_f^{(1)}$):

$$v_x^{(1)} = \frac{p_{,x}}{2\eta_0} \left(y^2 - cy \right) \quad , \quad v_z^{(1)} = \frac{p_{,z}}{2\eta_0} \left(y^2 - cy \right) + \left(1 - \frac{y}{c} \right) \tilde{U} \tag{3.43}$$

In this particular case, the integration functions are further simplified to yield:

$$\tilde{\tilde{f}}_{x|z} = -\frac{c^3}{12\eta_0} \quad , \quad f_z = \left(\tilde{U} \frac{c}{2} \right)_{,z} \quad , \quad f_x = 0 \tag{3.44}$$

In this particular case, the TTR equation is written in the well-known form:

$$\left(\frac{c^3}{12\eta_0} p_{,x} \right)_{,x} + \left(\frac{c^3}{12\eta_0} p_{,z} \right)_{,z} = \partial_{,t} c + \frac{1}{2} \left(\tilde{U} c \right)_{,z} \tag{3.45}$$

In [41], the governing Reynolds equation for a typical slider bearing configuration with a perfectly concentric arrangement ($e = 0$) is given as $\left(\frac{c^3}{12\eta_0} p_{,z} \right)_{,z} = \frac{U_0}{2} c_{,z} + V_0$, where the velocities are defined as $U_0 = U_1 - U_2$ and the radial velocity V_0 is given by $V_0 = V_2 - V_1$, where the indices 1 and 2 refer to the surfaces 1 (cylinder) and 2 (piston) respectively (see Fig. 3.2). By analogy, the velocities are given as $U_2 = \tilde{U},\ U_1 = 0$ and $V_0 = \partial_{,t} c$, which validates the TTT as an extension of the classical lubrication theory.

Rotational Motion

The case of the rotational motion of a journal bearing is provided only for the validation of the numerical code (provided in Chapter 4), as for a LG slider bearing, the rotation of the piston is neglected. The governing equations are similar to the linear motion of an oil-lubricated slider bearing and are derived for isoviscous oil. The boundary velocities, are set as $v_x|_{y=c} = 0$ and $v_x|_{y=0} = \tilde{U}$, where $\tilde{U}$ is a dummy boundary velocity. There is only one fluid space present, such

that within $\mathcal{S}_f^{(1)}$:

$$v_x^{(1)} = \frac{p_{,x}}{2\eta_0}\left(y^2 - cy\right) + \left(1 - \frac{y}{c}\right)\tilde{U} \quad , \quad v_z^{(1)} = \frac{p_{,z}}{2\eta_0}\left(y^2 - cy\right) \tag{3.46}$$

The integration functions are derived from the velocity profile of Eq. (3.46) to yield the factors of the TTR equation:

$$\tilde{\tilde{f}}_{x|z} = -\frac{c^3}{12\eta_0} \quad , \quad f_z = 0 \quad , \quad f_x = \left(\tilde{U}\frac{c}{2}\right)_{,x} \tag{3.47}$$

Temperature Field

Without considering the impact of the compressive heating on the temperature field, the energy equation given in Eq (3.12) is simplified to $\lambda_\theta \theta_{,yy} = -\eta_0\left(v_{x,y}^2 + v_{z,y}^2\right)$. For the case of constant viscosity ($\eta = \eta_0$), the components of the velocity gradient (see Eq. (3.43)) are given by:

$$v_{x,y} = \frac{p_{,x}}{2\eta_0}\left(2y - c\right) \quad , \quad v_{z,y} = \frac{p_{,z}}{2\eta_0}\left(2y - c\right) - \frac{\tilde{U}}{c} \tag{3.48}$$

By using Eq. (3.48), the second-order derivative of the temperature field is given by a quadratic polynomial $\theta_{,yy} = H_4(x,z)y^2 + H_3(x,z)y + H_2(x,z)$, where:

$$H_2 = \frac{c^2 H_4}{4} - \frac{\tilde{U}p_{,z}}{\lambda_\theta} - \frac{\tilde{U}^2\eta_0}{c^2\lambda_\theta} \quad , \quad H_3 = -cH_4 + \frac{2\tilde{U}p_{,z}}{c\lambda_\theta} \quad , \quad H_4 = -\frac{1}{\eta_0\lambda_\theta}\left(p_{,x}^2 + p_{,z}^2\right) \tag{3.49}$$

The double integration of the quadratic polynomial yields:

$$\theta(x,y,z) = \frac{H_4(x,z)}{12}y^4 + \frac{H_3(x,z)}{6}y^3 + \frac{H_2(x,z)}{2}y^2 + H_1(x,z)y + H_0(x,z) \tag{3.50}$$

where the coefficient functions H_0 and H_1 are given by:

$$H_0 = \theta|_{y=0} \quad , \quad H_1 = \frac{\theta|_{y=c} - \theta|_{y=0}}{c} - \frac{H_4}{12}c^3 + \frac{H_3}{6}c^2 + \frac{H_2}{2}c \tag{3.51}$$

The analytical temperature field is used in Chapter 4 to validate the temperature field, which is calculated numerically. A revelation is that the temperature within the lubrication gap is of 4th order across the lubrication gap for adiabatic boundaries, which indicates that there could, in theory, be more than one dry space across the lubrication gap. These dry spaces might not be located on the same contacting surface, which suggests eventual local 'burning' of the lubricant on both contacting surfaces. This finding is confirmed in Chapter 4.

3.7.2 Special Case II: Grease-lubricated Bearing

Single Sticking Plug Space ($\eta = \eta_0$)

The validation of the TTT for a grease-lubricated bearing relies on iteratively detecting multiple spaces within the lubrication gap. The analytical derivation at each iteration step leads to the

analytical formula for the thickness of a single plug space. For illustration purposes only, the iteration procedure is shown below for an isoviscous ($\eta = \eta_0$) and isothermal grease, which has only two distinct phases (configuration of $\mathcal{S}^{(1)} = \mathcal{S}_f^{(1)}$ and $\mathcal{S}^{(2)} = \mathcal{S}_p^{(2)}$). The case of an eventual floating plug space is not considered. The same boundary conditions are considered as for the pure linear motion of an oil-lubricated bearing. The convergence procedure is illustrated for a 2D case, or in other words, a concentric arrangement ($e = 0$, $p_{,x} = 0$).

Isoviscous oil: 0-th iteration ($\mathcal{S}^{(1)} = \mathcal{S}_f^{(1)}$) At $x = z = 0$, the velocity component v_z across the lubrication gap is given by:

$$v_z^{[0]} = \frac{p_{,z}}{2\eta_0} y^2 + a^{[0]} y + b^{[0]} \tag{3.52}$$

Given the boundary conditions, the integration factors are determined as $a^{[0]} = -\frac{\tilde{U}}{c} - \frac{p_{,z}c}{2\eta_0}$ and $b^{[0]} = \tilde{U}$. The shear stress τ is given as $\tau^{[0]} = \eta_0 \left| v_{z,y}^{[0]} \right| = \left| p_{,z} y + \eta_0 a^{[0]} \right|$. For this example, the numerical value of the yield stress τ_0 is chosen such that only one distinct root of $\tau \pm \tau_0 = 0$ exists. At the 0-th iteration, and in order to determine a possible plug shell, the region (space) where $\tau^{[0]} < \tau_0$ is delimited by the shell given by $y_-^{[0]}$, calculated from $\tau^{[0]} = \pm\tau_0$ as:

$$y_-^{[0]} = \frac{\pm\tau_0}{p_{,z}} + \frac{\eta_0 \tilde{U}}{c p_{,z}} + \frac{c}{2} \tag{3.53}$$

The shell positions are denoted as y_- until convergence and until the types of the respective spaces are determined. The value of $+\tau_0$ is used when $p_{,z} > 0$, otherwise $-\tau_0$ is used. Consequently, the ratio $\frac{\pm\tau_0}{p_{,z}}$ is written as $\frac{\tau_0}{|p_{,z}|}$. The type of the shell is determined using the inequality $\tau > \tau_0$, and is only determined at the 0-th iteration.

Detection of the plug space: 1-st iteration ($\mathcal{S}^{(1)} = \mathcal{S}_f^{(1)}$ and $\mathcal{S}^{(2)} = \mathcal{S}_p^{(2)}$) The second iteration of the boundary can be determined by assuming that a pressure gradient governs the entire lubrication gap until convergence, even in non-fluid spaces. For the case of two spaces (determined as plug and fluid spaces) and with a plug space attached to the stationary surface, the velocity profile is calculated in two spaces such that $v_z^{[1]}\Big|_{y=c} = 0$ and $v_z^{[1]}\Big|_{y=0} = \tilde{U}$. The types and the arrangement of the two spaces determine that $v_z^{[1]}\Big|_{y=y_-^{[0]}} = 0$. Under the assumptions of a governing pressure gradient in the lubrication gap, the shear stress $\tau^{[1]} - \tau_0$ within $\mathcal{S}_f^{(1)}$ is given by ($0 < y < y_-^{[0]}$):

$$\tau^{[1]} - \tau_0 = \begin{cases} p_{,z} y_-^{[1]} - \frac{p_{,z}}{2} y_-^{[0]} - \frac{\tilde{U}\eta_0}{y_-^{[0]}} = 0 & y_-^{[1]} < y_-^{[0]} \\ p_{,z} y_-^{[1]} - \frac{p_{,z}}{2} y_-^{[0]} - \frac{p_{,z}}{2} c = 0 & y_-^{[1]} > y_-^{[0]} \end{cases} \tag{3.54}$$

The equation system leads to the conclusion that $y_-^{[1]} > y_-^{[0]}$, or more precisely: $y_-^{[1]} = \frac{c + y_-^{[0]}}{2}$. The shear stress within the plug space is independent of the pressure gradient, which leads to the conclusion that the shell $y_-^{[1]}$ is the average of both plug space boundaries.

Convergence of the shells of the plug space: n-th iteration In general terms, and for a 2D case ($e = 0$), the boundary at iteration n is given by:

$$y_{-}^{[n]} = \frac{\eta_0 \tilde{U}}{y_{-}^{[n-1]} |p_{,z}|} + \frac{y_{-}^{[n-1]}}{2} \tag{3.55}$$

The boundary at iteration n is given as a nonlinear sequence of the previous boundaries, which converges to a final value at iteration N such that $y_{-}^{[N]} - y_{-}^{[N-1]} \ll 1$, or $y_{-}^{[N]} \approx y_{-}^{[N-1]}$, which is given by:

$$y_{-}^{[N]} = c_{-}^{(2)} = c_{+}^{(1)} = \sqrt{\frac{2\eta_0 \tilde{U}}{|p_{,z}|}} \tag{3.56}$$

An observation is that the final value of the nonlinear convergence sequence does not depend on the initial position of the boundary $y_{-}^{[0]}$. Instead of calculating the shell boundaries using an initial boundary determined by $\tau^{[0]} = \pm\tau_0$, the initial point can be determined using $\tau^{[0]} = 0$. The series converges to the same value, but the convergence speed might be faster, as subsequent iterations use the same condition. The only difference between both initial conditions is that the type of the shells cannot be determined. The type of each shell must be determined using the condition $\tau^{[0]} = \pm\tau_0$. From [62], it is known that, for this particular case, $y_{-}^{[N]}$ is given by $y_{-}^{[N]} = \frac{2\tau_0}{|p_{,z}|}$. By calculating the shear stress at the shell $y_{-}^{[N]}$, it is a given fact that:

$$\tau = \pm\tau_0 =\Leftrightarrow p_{,z} y_{-}^{[N]} + \eta_0 a^{[N]} = 0 \tag{3.57}$$

where $a^{[N]} = -\frac{\tilde{U}}{y_{-}^{[N]}} - \frac{p_{,z}}{2\eta_0} y_{-}^{[N]}$. Consequently, $\pm\tau_0 = \frac{1}{2} p_{,z} y_{-}^{[N]} = \frac{\eta_0 \tilde{U}}{y_{-}^{[N]}}$. The equivalence is achieved when $\tau_0 = \frac{1}{2} y_{-}^{[N]} p_{,z}$ or $\tau_0 = \frac{\eta_0 \tilde{U}}{y_{-}^{[N]}}$. The nonlinear sequence converges to the same final value, which validates the iteration procedure.

Convergence of the boundary (3D case) With a similar reasoning as for the 2D case, the converged value of the shell for the 3D case can be calculated from:

$$\tau_0 = \left| \frac{1}{2} p_{,x} y_{-}^{[N]} \right| \quad \text{and} \quad \tau_0 = \left| \frac{y_{-}^{n}}{2} p_{,z} - \frac{\eta \tilde{U}}{y_{-}^{n}} \right| \tag{3.58}$$

After the subtraction of both equations and further rearrangement, the theoretical final shell $y_{-}^{[N]}$ is given by:

$$y_{-}^{[N]} = c_{-}^{(2)} = c_{+}^{(1)} = \sqrt{\frac{2\eta_0 \tilde{U}}{|p_{,x}| + |p_{,z}|}} \tag{3.59}$$

For the case of a single plug space sticking on the bearing surface, the film thickness c' is given by $c'(x, y) = c(x, y) - y_{-}^{[N]}$.

Single Floating Plug Space ($\eta = \eta_0$, $\mathcal{S}^{(1)} = \mathcal{S}_f^{(1)}$, $\mathcal{S}^{(2)} = \mathcal{S}_p^{(2)}$, $\mathcal{S}^{(3)} = \mathcal{S}_f^{(3)}$)

For the special case of a single grease plug space floating in oil, the 3SA is used to determine the integration factors. This special case has been studied in detail in [51]. Three spaces

($N_s = 3$) are present in the lubrication gap, and the surface velocities are given by $v_z|_{y=c} = 0$ and $v_z|_{y=0} = \tilde{U}$. For pure vertical sliding and for the case of a nonrotating piston, $v_x|_{y=\{0,c\}} = 0$. It must be noted that compared to [51], the moving and stationary surfaces are swapped (y is inverse). For simplification purposes, the shells of the plug space are denoted as y_- and y_+ and consequently, $c_-^{(1)} = 0$, $c_+^{(1)} = c_-^{(2)} = y_-$, $c_+^{(2)} = c_-^{(3)} = y_+$ and $c_+^{(3)} = c$.

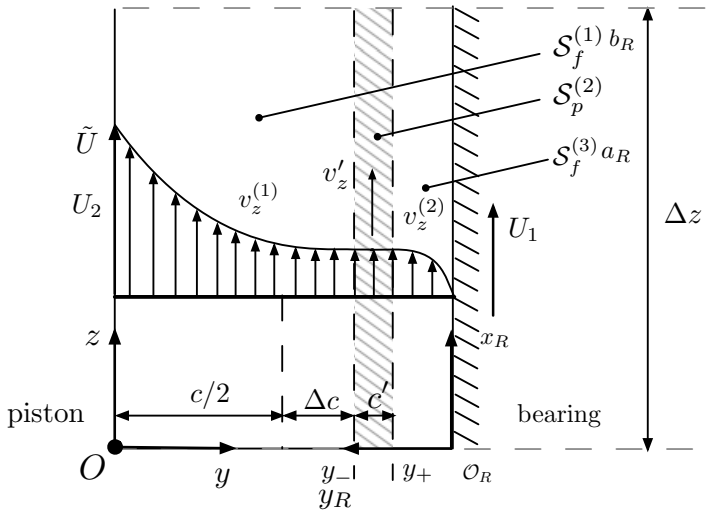

Figure 3.2: Velocity profile of grease flow in the infinitesimal part of the lubrication gap. Reference frame R is from [3].

The type vector is given by $\mathbf{l} = (2\ 1\ 2)^T$, and the corresponding sorted type vector is given as $\mathbf{l}^\star = (1\ 2\ 2)^T$. The determinant of the topology matrix $\mathbf{T}_s^{(2)}$ is given by: $\Delta\mathbf{T}_s^{(2)} = \det\left(\mathbf{T}_s^{(2)}\right) = \tilde{\Lambda}_0^+ \cdot \tilde{\Lambda}_0^-$, where $\tilde{\Lambda}_0^- = \tilde{C}_0^{y-}$ and $\tilde{\Lambda}_0^+ = \tilde{C}_0^{y+} - \tilde{C}_0^c$. Similarly, the factors $\tilde{\Lambda}_1^- = \tilde{C}_1^{y-}$ and $\tilde{\Lambda}_1^+ = \tilde{C}_1^{y+} - \tilde{C}_1^c$ are defined. Within the plug space, the integration factors are given by $a_{x|z}^{(2)} = a'^{(2)}_{x|z} = a''^{(2)}_{x|z} = b'^{(2)}_{x|z} = b''^{(2)}_{x|z} = 0$ and $b_{x|z}^{(2)} = \breve{v}_{x|z}$. The thicknesses of the 3 spaces are given by $c'^{(1)} = y_-$, $c'^{(2)} = y_+ - y_-$ and $c'^{(3)} = c - y_+$. The integration factors are given by:

$$\begin{array}{lllllllll} a'^{(1)}_{x|z} & = & -\dfrac{\tilde{C}_1^{y-}}{\tilde{C}_0^{y-}} & a'^{(3)}_{x|z} & = & -\dfrac{\tilde{C}_1^{y+} - \tilde{C}_1^c}{\tilde{C}_0^{y+} - \tilde{C}_0^c} & b'^{(3)}_{z} & = & \dfrac{\breve{v}_z}{\tilde{C}_0^{y+} - \tilde{C}_0^c} \\ b'^{(1)}_{x} & = & \dfrac{\breve{v}_x}{\tilde{C}_0^{y-}} & b'^{(3)}_{x} & = & \dfrac{\breve{v}_x}{\tilde{C}_0^{y+} - \tilde{C}_0^c} & b_x^{(3)} & = & -\tilde{C}_0^c b'^{(3)}_x \end{array} \tag{3.60}$$

The remaining integration factors are given by $a_{x|z}^{(1)} = 0$, $b_x^{(1)} = 0, b_z^{(1)} = \tilde{U}$, and:

$$a_{x|z}^{(3)} = \frac{\tilde{C}_0^c \tilde{C}_1^{y+} - \tilde{C}_0^{y+} \tilde{C}_1^c}{\tilde{C}_0^{y+} - \tilde{C}_0^c} \ , \ b_z^{(3)} = -\frac{\tilde{C}_0^c \breve{v}_z}{\tilde{C}_0^{y+} - \tilde{C}_0^c} \ , \ b'^{(1)}_z = \frac{\breve{v}_z - \tilde{U}}{\tilde{C}_0^{y-}} \tag{3.61}$$

The remaining integration components for the present case are given as:

$$\begin{array}{lll} \tilde{\tilde{\Gamma}}^{(1)}_{1\ x|z} = \tilde{\tilde{C}}_1^{y-} & \tilde{\tilde{\Gamma}}^{(2)}_{1\ x|z} = \tilde{\tilde{C}}_1^{y+} - \tilde{\tilde{C}}_1^{y-} & \tilde{\tilde{\Gamma}}^{(3)}_{1\ x|z} = \tilde{\tilde{C}}_1^{c} - \tilde{\tilde{C}}_1^{y+} \\ \tilde{\Gamma}^{(1)}_{1\ x|z} = -\tilde{C}_1^{y-} y_{-,x|z} & \tilde{\Gamma}^{(2)}_{1\ x|z} = \tilde{C}_1^{y-} y_{-,x|z} - \tilde{C}_1^{y+} y_{+,x|z} & \tilde{\Gamma}^{(3)}_{1\ x|z} = \tilde{C}_1^{y+} y_{+,x|z} - \tilde{C}_1^{c} c_{,x|z} \\ \tilde{\tilde{\Gamma}}^{(1)}_{0\ x|z} = \tilde{\tilde{C}}_0^{y-} & \tilde{\tilde{\Gamma}}^{(2)}_{0\ x|z} = \tilde{\tilde{C}}_0^{y+} - \tilde{\tilde{C}}_0^{y-} & \tilde{\tilde{\Gamma}}^{(3)}_{0\ x|z} = \tilde{\tilde{C}}_0^{c} - \tilde{\tilde{C}}_0^{y+} \\ \tilde{\Gamma}^{(1)}_{0\ x|z} = -\tilde{C}_0^{y-} y_{-,x|z} & \tilde{\Gamma}^{(2)}_{0\ x|z} = \tilde{C}_0^{y-} y_{-,x|z} - \tilde{C}_0^{y+} y_{+,x|z} & \tilde{\Gamma}^{(3)}_{0\ x|z} = \tilde{C}_0^{y+} y_{+,x|z} - \tilde{C}_0^{c} c_{,x|z} \end{array} \tag{3.62}$$

The nonisoviscous velocity profile for the 3-space configuration ($\forall \mathbf{x} \in \mathbf{\Omega}$) is given by:

$$\begin{aligned}
v_x^{(1)} &= p_{,x}\tilde{C}_1^y + \left(\frac{\breve{v}_x}{\tilde{C}_0^{y-}} - \frac{\tilde{C}_1^{y-}}{\tilde{C}_0^{y-}}\right)\tilde{C}_0^y \\
v_z^{(1)} &= p_{,z}\tilde{C}_1^y + \left(\frac{\breve{v}_z - \tilde{U}}{\tilde{C}_0^{y-}} - \frac{\tilde{C}_1^{y-}}{\tilde{C}_0^{y-}}\right)\tilde{C}_0^y + \tilde{U} \\
v_x^{(2)} &= \breve{v}_x = \frac{\tilde{C}_0^{y-}\left(\tilde{C}_0^{y+} - \tilde{C}_0^c\right)}{\tilde{C}_0^{y-} - \tilde{C}_0^{y+} + \tilde{C}_0^c}\left(\frac{\left(\tilde{C}_1^{y+} - \tilde{C}_1^c\right)p_{,x}}{\tilde{C}_0^{y+} - \tilde{C}_0^c} - \frac{\tilde{C}_1^{y-}p_{,x}}{\tilde{C}_0^{y-}} + (y_+ - y_-)\,p_{,x}\right) \\
v_z^{(2)} &= \breve{v}_z = \frac{\tilde{C}_0^{y-}\left(\tilde{C}_0^{y+} - \tilde{C}_0^c\right)}{\tilde{C}_0^{y-} - \tilde{C}_0^{y+} + \tilde{C}_0^c}\left(\frac{\left(\tilde{C}_1^{y+} - \tilde{C}_1^c\right)p_{,z}}{\tilde{C}_0^{y+} - \tilde{C}_0^c} - \frac{\tilde{C}_1^{y-}p_{,z} + \tilde{U}}{\tilde{C}_0^{y-}} + (y_+ - y_-)\,p_{,z}\right) \\
v_{x|z}^{(3)} &= p_{,x|z}\tilde{C}_1^y + \frac{\breve{v}_{x|z} - \tilde{C}_1^{y+}p_{,x|z} + \tilde{C}_1^c p_{,x|z}}{\tilde{C}_0^{y+} - \tilde{C}_0^c}\tilde{C}_0^y - \frac{\breve{v}_{x|z}\tilde{C}_0^c}{\tilde{C}_0^{y+} - \tilde{C}_0^c} + \frac{\tilde{C}_0^c\tilde{C}_1^{y+} - \tilde{C}_0^{y+}\tilde{C}_1^c}{\tilde{C}_0^{y+} - \tilde{C}_0^c}p_{,x|z}
\end{aligned} \tag{3.63}$$

The isoviscous velocity profile ($y_+ \neq y_-$ and $y_+ \neq c$) is given by:

$$\begin{aligned}
v_x^{(1)} &= \frac{p_{,x}}{2\eta_0}y^2 + \left(\frac{\breve{v}_x}{y_-} - \frac{p_{,x}y_-}{2\eta_0}\right)y \\
v_z^{(1)} &= \frac{p_{,z}}{2\eta_0}y^2 + \left(\frac{\breve{v}_z - \tilde{U}}{y_-} - \frac{p_{,z}y_-}{2\eta_0}\right)y + \tilde{U} \\
v_x^{(2)} &= \breve{v}_x = (y_+ - c)\,\frac{p_{,x}y_-}{2\eta_0} \\
v_z^{(2)} &= \breve{v}_z = \frac{y_+ - c}{y_+ - y_- - c}\tilde{U} + (y_+ - c)\,\frac{p_{,z}y_-}{2\eta_0} \\
v_{x|z}^{(3)} &= \frac{p_{,x|z}}{2\eta_0}y^2 + \left(\frac{\breve{v}_{x|z}}{y_+ - c} - \frac{y_+ + c}{2\eta_0}p_{,x|z}\right)y + \frac{cy_+p_{,x|z}}{2\eta_0} - \frac{c\breve{v}_{x|z}}{y_+ - c}
\end{aligned} \tag{3.64}$$

It can be seen that the plug velocities $\breve{v}_{x|z}$ are constant across the lubrication gap. For the nonisoviscous case, the second order factors of the TTR equation are given by:

$$\tilde{\tilde{f}}_{x|z} = \tilde{\tilde{C}}_1^{y-} + \tilde{\tilde{C}}_1^c - \tilde{\tilde{C}}_1^{y+} - \frac{\tilde{C}_1^{y-}\tilde{\tilde{C}}_0^{y-}}{\tilde{C}_0^{y-}} - \frac{\tilde{C}_1^{y+} - \tilde{C}_1^c}{\tilde{C}_0^{y+} - \tilde{C}_0^c}\left(\tilde{\tilde{C}}_0^c - \tilde{\tilde{C}}_0^{y+}\right) + \frac{\tilde{C}_0^c\tilde{C}_1^{y+} - \tilde{C}_0^{y+}\tilde{C}_1^c}{\tilde{C}_0^{y+} - \tilde{C}_0^c}\,(c - y_+) \tag{3.65}$$

The transformation of the integration functions shows that $\tilde{f}_{x|z} = \tilde{\tilde{f}}_{x|z,x|z}$. After differentiation:

$$\begin{aligned}
f_x = \Bigg(\breve{v}_x\frac{\tilde{\tilde{C}}_0^{y-}}{\tilde{C}_0^{y-}} + \breve{v}_x\frac{\tilde{\tilde{C}}_0^c - \tilde{\tilde{C}}_0^{y+}}{\tilde{C}_0^{y+} - \tilde{C}_0^c}\Bigg)_{,x} &- \breve{v}_x y_{-,x} + \breve{v}_{x,x}\,(y_+ - y_-) \\
&- (c - y_+)\left(\frac{\breve{v}_x\tilde{C}_0^c}{\tilde{C}_0^{y+} - \tilde{C}_0^c}\right)_{,x} + \breve{v}_x\frac{\tilde{C}_0^{y+}y_{+,x} - \tilde{C}_0^c c_{,x}}{\tilde{C}_0^{y+} - \tilde{C}_0^c}
\end{aligned} \tag{3.66}$$

$$\begin{aligned}
f_z = \Bigg(\left(\breve{v}_z - \tilde{U}\right)\frac{\tilde{\tilde{C}}_0^{y-}}{\tilde{C}_0^{y-}} + \breve{v}_z\frac{\tilde{\tilde{C}}_0^c - \tilde{\tilde{C}}_0^{y+}}{\tilde{C}_0^{y+} - \tilde{C}_0^c}\Bigg)_{,z} &- \left(\breve{v}_z - \tilde{U}\right)y_{-,z} \\
+ \breve{v}_{z,z}\,(y_+ - y_-) - (c - y_+)\left(\frac{\breve{v}_z\tilde{C}_0^c}{\tilde{C}_0^{y+} - \tilde{C}_0^c}\right)_{,z} &+ \breve{v}_z\frac{\tilde{C}_0^{y+}y_{+,z} - \tilde{C}_0^c c_{,z}}{\tilde{C}_0^{y+} - \tilde{C}_0^c}
\end{aligned} \tag{3.67}$$

For the isoviscous case ($\eta = \eta_0$), the integration functions are:

$$\begin{gathered}\tilde{\tilde{f}}_{x|z} = -\frac{c^3 + 3cy_+^2 - 3y_+c^2 + y_-^3 - y_+^3}{12\eta_0} \\ f_x = \left(\frac{\breve{v}_x}{2}\left(c + y_+ - y_-\right)\right)_{,x} \quad , \quad f_z = \left(\breve{v}_z\frac{c + y_+ - y_-}{2} + \tilde{U}\frac{y_-}{2}\right)_{,z}\end{gathered} \tag{3.68}$$

The integration functions shown in Eq. (3.68) correspond exactly to the integration functions derived in [51].

Reference for validation In [3], the Reynolds equation that takes into account the formation of a 'core' (or plug space) is derived. The subscripts H and L designate the upper and lower boundaries of the regions[4], and the reference configuration with reference frame $(\mathcal{O}_R, x_R, y_R)$ is shown in Fig. 3.2. The coefficients F that take into account variable viscosity effects are defined as:

$$\overline{F}_0^j = \int_{c_L^j}^{c_H^j}\frac{1}{\eta}d\upsilon \quad , \quad \overline{F}_1^j = \int_{c_L^j}^{c_H^j}\frac{\upsilon}{\eta}d\upsilon \quad , \quad \overline{F}_2^j = \int_{c_L^j}^{c_H^j}\frac{\upsilon}{\eta}\left(\upsilon - \frac{\overline{F}_1^j}{\overline{F}_0^j}\right)d\upsilon \tag{3.69}$$

For a 1D case, the Reynolds equation taking into account a floating plug is given in [3] as:

$$\left(\left(\overline{F}_2^{a_R} + \overline{F}_2^{b_R}\right)p_{,x_R}\right)_{,x_R} = -\left(\left(U_H^{a_R} - U_L^{a_R}\right)\frac{\overline{F}_1^{a_R}}{\overline{F}_0^{a_R}} + \left(U_H^{b_R} - U_L^{b_R}\right)\frac{\overline{F}_1^{b_R}}{\overline{F}_0^{b_R}}\right)_{,x_R} + \partial_{,t}c \tag{3.70}$$

By developing the integral factors for the isoviscous case $\eta = \eta_0$, Eq. (3.70) can be rewritten as:

$$\overline{F}_2^{a_R} = \frac{c^3 - 3c^2y_+ + 3cy_+^2 - y_+^3}{12\eta_0} \quad , \quad \overline{F}_2^{b_R} = \frac{y_-^3}{12\eta_0} \tag{3.71}$$

Clearly, the sum of both factors $\overline{F}_2^{a_R}$ and $\overline{F}_2^{b_R}$ yields $\tilde{\tilde{f}}_x$, which is exactly the factor shown in Eq. (3.68) and developed in [51] (sign is different as y_R and y are opposite). The boundary velocities are given by $U_H^{a_R} = 0$, $U_L^{a_R} = U_H^{b_R} = \breve{v}_{x_R}$, and $U_L^{b_R} = \tilde{U}$. The right-hand side of the TTR equation is $\left(\breve{v}_{x_R}\frac{c+y_+-y_-}{2} + \tilde{U}\frac{y_-}{2}\right)_{,x_R} + \partial_{,t}c$, which corresponds exactly to the factor given in Eq. (3.68). In [3], the core (or plug space) velocity is derived for the special configuration of a typical slider bearing. It must be noted that for the special case when $U_L^{a_R} = 0$ and $U_H^{b_R} = \tilde{U}$, the regions a_R and b_R are the $\mathcal{S}_f^{(3)}$ and $\mathcal{S}_f^{(1)}$ spaces respectively. The plug space velocity is given in [3] as:

$$\breve{v}_{x_R} = \frac{\overline{F}_0^{a_R}\overline{F}_0^{b_R}}{\overline{F}_0^{a_R} + \overline{F}_0^{b_R}}\left(\frac{\tilde{U}}{\overline{F}_0^{b_R}} + p_{,x}\left(\frac{\overline{F}_1^{a_R}}{\overline{F}_0^{a_R}} - \frac{\overline{F}_1^{b_R}}{\overline{F}_0^{a_R}}\right)\right) \tag{3.72}$$

which is equivalent to $v_z^{(2)}$ shown in Eq. (3.63). The velocity profile in the spaces a_R and b_R is

[4]The notation is adopted from [3] and is only applicable for this validation.

verified using:

$$v^{a_R|b_R} = \frac{U_H^{a_R|b_R} - U_L^{a]b_R}}{\overline{F}_0^{a_R|b_R}} \int_{c_L^{a_R|b_R}}^{y} \frac{1}{\eta} d\upsilon + p_{,z} \left(\int_{c_L^{a_R|b_R}}^{y} \frac{\upsilon}{\eta} d\upsilon - \frac{\overline{F}_1^{a_R|b_R}}{\overline{F}_0^{a_R|b_R}} \int_{c_L^{a_R|b_R}}^{y} \frac{1}{\eta} d\upsilon \right) + U_L^{a_R|b_R} \quad (3.73)$$

which yields the same velocity components as shown in Eq. (3.63). The demonstrated theoretical equivalence clearly validates the TTT as an extension of existing work.

3.8 Summary and Conclusions

A tribotopological theory (TTT) that includes multiple phases of a non-Newtonian lubricant, such as grease, has been developed. The governing equations are derived from the fundamental conservation principles. A unique equation of the pressure gradient, proportional to the variation of the shear stress, is the result of the adapted Navier-Stokes equations, and is integrated over the entire lubrication gap to yield the TTR equation.

The theory relies on tribotopologies, which are defined as spaces englobed by shells. These TT spaces form the basis for deriving the governing equations, taking into account multiple physical phases. Within a TT space, the parabolic velocity profile is governed by the pressure gradient and the linear (vertical or rotational) motion of the contacting surfaces. Contrary to full CFD, the velocity profile is not calculated from a governing equation, but instead, several velocity profile cases are distinguished by the types of the spaces.

An analogy to the TTT can be drawn as a busy, and very long, multi-lane highway. The focus of any traffic information source (equivalent to the *TTR equation*) is on how well the traffic *flows* (equivalent to the *pressure gradient*), thereby providing the information on the overall behavior, and on providing a bird's-eye view of the traffic. Key to this information is the barriers (equivalent to the *shells* detected by the Topology Detection Algorithm (TDA) shown in Chapter 4) around the zones of construction work or traffic accidents (equivalent to the *spaces*). The detailed pattern of the traffic flow (equivalent to the *velocity field*) is dependent on the type of the zone (i.e., construction or accident). For example, a moving construction zone has a different impact on the traffic flow than a stationary accident.

The major benefit and novelty of the TTT is that transient simulations of multiphasic, non-Newtonian lubricants are possible with acceptably short calculation times. This is due to the fact that the radial variation of the shear stress within the lubricant is directly linked to the pressure gradient, as shown in Eq. (3.14). As explained in Section 1.2.3, full CFD simulations provide similar results, but cannot compete from a computational speed point of view. Major highlights of the theory include:

Highlight 1: The theory is comprehensive, takes into account various physical phases of a non-Newtonian lubricant, such as dry, plug and fluid phases, and can be extended to take

into account any other physical phase (e.g., derived from electrical or magnetic properties) by adapting the classical Reynolds equation and deriving the TTR equation. Of particular interest to the LG overheating issue is the inclusion of dry spaces.

Highlight 2: The theory is demonstrated to be an extension of existing theories in 3D lubrication. In addition, the thickness of the plug space for the common case of one fluid and one plug space has been determined analytically. The theory is also validated against other existing studies for an oil- and grease-lubricated bearing, for both linear and rotational motion.

The theory can be viewed as a link between the classical Reynolds theory and the Navier-Stokes equations solved with the CFD method. The concepts of the classical Reynolds theory are used (e.g., long and thin lubrication gap), and the feature of multiple phases in a transient regime, which is an advantage of CFD, is included.

The theory is applied in Chapter 4 to the overheating of LG bearings. The theory can, however, be applied to any other lubricant that exhibits multiple phases in other applications (e.g., the bearings of the SAs of cars or other LG joints). ■

Chapter 4

Comprehensive Model and Validation

We think in generalities, but we live in detail.

Alfred North Whitehead, mathematician (1861 - 1947)

4.1 Comprehensive Model Development Strategy

The TTT has been derived in Chapter 3, but it is only its application to the LG SA lower bearing that truly reveals its significant benefits. As explained in Section 2.10, a major step in the TTM model development is an understanding of the local phenomenon of the overheating of the LG lower bearing. This chapter presents the application of the TTT and the related numerical developments for the 3D fluid film analysis of oil- and grease-lubricated flexible aircraft LG (slider) bearings.

Only the components within the TZI and in the vicinity of the lower bearing interface are of interest. In other words, it is only the interaction of the piston and cylinder assembly at the grease-lubricated sliding interface (composed of a layer of chrome and the lower bearing itself) that are of interest to the development of the comprehensive model. In addition to the application of the TTT, a major focus is the numerical implementation of the TTT and the interaction between the lubricant and the structure (fluid-structure interaction, FSI).

The governing equations, derived from First Principles and shown in Chapter 3, are discretized and solved using a hybrid solver that is based on the MG method. In addition, key numerical algorithms such as the Topology Detection Algorithm (TDA) and the method behind the FSI mapping are shown. The validation of the numerical model against existing theoretical and experimental results is given.

4.2 Model Definition and Assumptions

The comprehensive model is a 3D transient numerical model shown in Fig. 4.1. The depicted lower bearing assembly is a detailed view of the LG system shown in Fig. 2.10. The sliding interface between the cylinder (1)[5] and the piston (3) is detailed, and the lubrication profile of the lower bearing (2) is shown. Grease (10) is used for lubrication between the chrome layer (9) that protects the piston and the lower bearing inset. In order to clearly show the eccentricity of the piston, the model is not depicted to scale. In addition to the geometry and applied loads, convective heat fluxes (around the assembly) and within the assembly (chamber IV) are shown. The sliding and rotational velocities of both the piston (3) and the cylinder (1) are shown, together with the external heat flux q_5 as well as the internal chamber pressure p_4. In Detail A, a cross-section of the assembly is shown and the boundaries of the sliding interface are defined. The lubrication mechanism (bearing profile) with the primary thrust portion of angle γ_s and length z_0 is shown, which defines its radial dimension as ς.

Thermal and 3D flow effects are taken into account, and the model is solved using FE and CFD methods in a customized version of ANSYS. The underlying principle of the development of the transient model is that for thin lubrication films, the transient performance can be evaluated using a sequence of steady state simulations, each with different initial and boundary conditions. This assimilation has been mathematically demonstrated in Chapter 3, due to the omission of the lubricant's inertia. As a consequence, the development steps are shown for a steady state case, which explain the heat generation mechanism in the LG lower bearing. The transient performance of an aircraft maneuvering on a rough runway may be derived from its steady state performance. Transient results are highlighted, but do not add significantly to an understanding of the formation of TT spaces. In order to fundamentally understand the non-Newtonian fluid behavior within the lubrication gap, it is instructive to analyze a cross-section of the assembly, which is equivalent to assuming perfect circumferential symmetry (zero eccentricity, see Detail A in Fig. 4.1). The thermo-mechanical analysis of the structure is performed using FE in ANSYS, whereas the governing equations of fluid flow in the lubrication gap of the lower bearing are from the TTT and solved using a customized in-house hybrid solver. Heat and load transfer between the fluid and the solids occurs at the FSI boundaries, and the exchange and application of physical quantities is based on FSI interpolation methods for irregular and nonconforming meshes. The governing thermo-mechanical structural equations are strongly coupled whereas the governing fluid equations (TTR and energy equation) are weakly coupled. The fluid and structural equations converge in a staggered manner at each time step (referred to as instantaneous steady state).

Once the lubricant is locally disintegrated, the heat is generated as for dry friction, and the mechanism of dry frictional heat generation is adopted from Chapter 2 and [31]. As explained in Chapter 1, full CFD provides very high accuracy that is not necessary for lubricated contacts in the slider bearings of aircraft LG, and therefore the proposed hybrid methodology combines

[5]The bracketed numbers correspond to the components shown in Fig. 4.1

the assumptions of the classical theory and the basics of CFD. The proposed numerical hybrid solver obtains nearly-exact solutions in a very fast manner, allows for the freedom of using different rheological models, and integrates well into an existing industrial model framework for simulating aircraft LG performance.

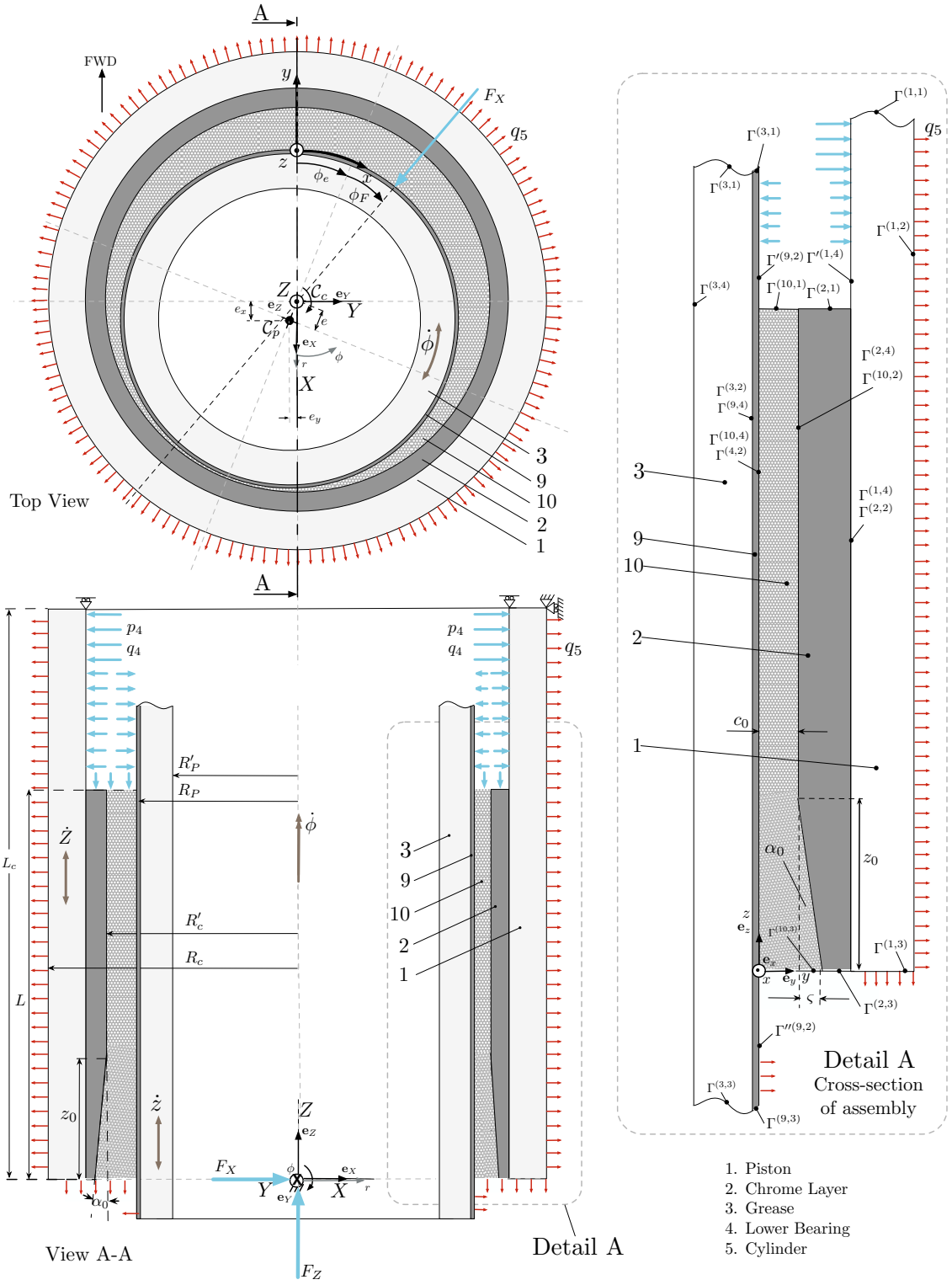

Figure 4.1: Model definition showing a top and cross-sectional view of the lower bearing assembly. The boundaries Γ are highlighted.

The main model assumptions are given in Section 2.4, but the assumptions related to the tribological submodel are refined and follow the classical Reynolds lubrication theory as explained in Section 3.3 and detailed in [51]. In addition, and throughout the present analysis, a line contact with no side leakage is assumed. The contacting surfaces are smooth, the viscosity of grease (which follows the rheology model shown in Section 2.5.2) is dependent only on pressure and temperature, and the lubricant is assumed to be entirely incompressible ($\rho_{,p} = 0$ and $\rho_{,\theta} = 0$). In compliance with the TTT, all the body forces and surface tension forces, as well as the inertia forces, are omitted. The structural components surrounding the lubrication gap are linear and isotropic. Contrary to the characteristic model shown in Chapter 2, the thermal expansion of the structural components is considered, as well as a chrome layer of 100μm on the piston. The temperature of the SA oil and surrounding air is constant, and in order to have a negligible boundary effect, the upper and lower boundaries are considered to be far away from the TZI. In order to primarily study the impact of the heat generation on the structure, a constant heat transfer coefficient of $\overline{h_5} = 50$ W/(m^2 K) is assumed and local effects of the airflow around the structure are considered. In addition, as the thermal performance is evaluated for steady state only, the application of external loads is omitted in order to understand the structural deformation due to hydrodynamic thermal and mechanical effects only.

4.3 Application Related Considerations

4.3.1 Governing Structural Equations

The provided governing structural equations follow [106]. With respect to the current assumptions, the body forces are neglected such that the structural equilibrium is given as $\rho^{(i)}\ddot{\mathbf{d}}^{(i)} = \boldsymbol{\nabla}\boldsymbol{\sigma}^{(i)}$. The infinitesimal strain tensor in domain i (including thermal expansion) is given as $\boldsymbol{\epsilon}^{(i)} = \frac{1}{2}\left(\boldsymbol{\nabla}\mathbf{u}^{(i)} + (\boldsymbol{\nabla}\mathbf{u}^{(i)})^T\right) + \kappa_\theta^{(i)}\mathbf{I}_{3\times3}$. The fundamental stress-strain relationship in domain i is $\boldsymbol{\sigma}^{(i)} = \mathbf{E}^{(i)}\boldsymbol{\epsilon}^{(i)}$, where $\mathbf{E}^{(i)}$ is the symmetric stiffness matrix (stress-strain matrix). The governing transient temperature diffusion equation for constant $\lambda_\theta^{(i)}$ is reduced to $\boldsymbol{\nabla}^2\theta^{(i)} = 0$, with transient boundary conditions.

4.3.2 Film Thickness (Clearance) Equation

The vertical contribution of the undeformed film thickness for a simple slider bearing is given by $c_z(z) = c_0 + \varsigma\left(1 - z_0^{-1}z\right)$ for $0 < z \leq z_0$, and $c_z(z) = c_0$ for $z_0 < z < L$, where $\varsigma = z_0 \cdot \tan\alpha_0$ (see Fig. 4.1). The clearance c between the piston (chrome layer) and the bearing surface is given by:

$$c(x,z) = c_z(z) + e \cdot \cos\left(\phi + \phi_e\right) \tag{4.1}$$

where $\phi = R_P^{-1}x$ (see Fig. 4.1). In the reference frame $(\mathbf{e}_X, \mathbf{e}_Y, \mathbf{e}_Z)$, the center of the cylinder is given as $C_c\,(0,0,0)$, and the center of the piston is given as $C_P\,(e_x, e_y, 0)$. The eccentricity angle is defined as $\phi_e = \frac{\pi}{2} - \tan^{-1}\left(\frac{e_y}{e_x}\right)$, and the eccentricity is defined as $e = \left(e_x^2 + e_y^2\right)^{1/2}$.

The film thickness (clearance) is a driving parameter in the TEHD solution. The clearance is updated during the solution process at each equilibrium iteration using the displacement field $\mathbf{u}$, calculated by and retrieved from ANSYS.

4.3.3 Boundary Conditions and Cavitation

The relative hydrodynamic pressure at both ends of the lubricated region is imposed by $\overline{p}|_{x,z=\{0,L\}} = 0$. The reference pressure is the atmospheric pressure. The Dirichlet boundary conditions for the pressure field are provided by the pressure of the connecting oil chambers in the LG SA. The boundary conditions at $z = \{0, L\}$ of the temperature field are continuous Dirichlet boundary conditions and depend on position (x, y) and time t. The temperature of the medium connecting to the convective boundary is denoted as $\theta^{(i')}$. The condition for a convective heat flux at the shared boundary k is given by:

$$\boldsymbol{\nabla}\theta^{(i)} \cdot \mathbf{n}^{(k)} = -\frac{h_k}{\lambda_\theta^{(i)}} \left(\theta^{(i)} - \theta^{(i')}\right) \tag{4.2}$$

For an adiabatic boundary k, the heat transfer coefficient is zero: $h_k = 0$. A summary of the applied external boundary conditions is provided in Table 4.1. The motion of the structural components is given by $v_z|_{y=c} = \dot{z}$, $v_x|_{y=c} = R_c\dot{\phi}_c$. Similarly, $v_x|_{y=0} = R_P\dot{\phi}_P$ and $v_z|_{y=c} = \dot{Z}$. For a LG lower bearing, only the vertical sliding motion is considered, such that $\dot{\phi}_c = \dot{\phi}_P = 0$.

Boundary	**Structure**	**Thermal**	**Fluid**
$\Gamma^{31} = \Gamma^{91} = \Gamma^{11}$	constrained	isothermal	
$\Gamma^{32} = \Gamma^{94} = \Gamma^{22} = \Gamma^{14}$	ssi	ssi	ssi
$\Gamma^{33} = \Gamma^{93}$	loaded	isothermal	
Γ^{34}	free	adiabatic	
$\Gamma^{92} = \Gamma^{102} = \Gamma^{104} = \Gamma^{24}$	fsi	fsi	fsi
$\Gamma'^{92} = \Gamma^{21} = \Gamma'^{14}$		convection	pressure
$\Gamma''^{92} = \Gamma^{23} = \Gamma^{22} = \Gamma^{13}$	free	convection	
$\Gamma^{101} = \Gamma^{103}$		isothermal	pressure

Table 4.1: Summary of boundary conditions (ssi: structure-structure interaction, fsi: fluid-structure interaction).

As the LG slider bearing is a long bearing, cavitation of the lubricant is unlikely. Nevertheless, as the bearing surfaces deform, cavitation might occur. The eventual cavitation of the lubricant is taken into account using the Swift-Steiber condition that sets $\overline{p} = 0$ for $\overline{p} \leq 0$.

4.3.4 Hydrodynamic Loads and Friction Coefficient

The hydrodynamic pressure field is integrated over the lubrication gap in order to yield the total load that is generated as the structural components are moving. The magnitude of the radial load $\mathbf{w}_y$ is given by integration of the pressure field on the contacting surfaces:

$$w_y = \int_0^{2\pi R_P} \int_0^{L} p \; dz \; dx \tag{4.3}$$

The load components in $(\mathbf{e}_X, \mathbf{e}_Y, \mathbf{e}_Z)$ are given as:

$$\mathbf{w}_y \cdot \mathbf{e}_Y = \int_0^{2\pi R_P} \int_0^{L} p \; \sin\phi \; dz \; dx \quad , \quad \mathbf{w}_y \cdot \mathbf{e}_X = \int_0^{2\pi R_P} \int_0^{L} p \; \cos\phi \; dz \; dx \tag{4.4}$$

where $\phi = xR_P^{-1}$. The tangential load is given by integration of the pressure field projected on the gradient of the clearance surface c:

$$\left(w_x|_{y=c} \; , \; w_z|_{y=c} \right)^T = \int_0^{2\pi R_P} \int_0^{L} p \; \boldsymbol{\nabla} c \; dzdx \tag{4.5}$$

where $\boldsymbol{\nabla} c = (c_{,x} \;\; c_{,z})^T$. The shear loads on both contacting surfaces located at $y = \{0, c\}$ are given by

$$w'_z|_{y=\{0,c\}} = \int_0^{2\pi R_P} \int_0^{L} \tau|_{y=\{0,c\}} \; dz \; dx \tag{4.6}$$

A zero tangential load does not imply that the shear load is zero. The key parameter that is calculated by the TEHD code is the friction coefficient, which is the ratio of the sum of the tangential and shear loads, and the radial load:

$$\mu = \frac{w'_z|_{y=c} + w_z|_{y=c}}{w_y} = -\frac{w'_z|_{y=0}}{w_y} \tag{4.7}$$

For the case of a LG slider bearing, the static equilibrium of the generated forces at the sliding interfaces is: $w'_z|_{y=0} + w'_z|_{y=c} + w_z|_{y=c} = 0$.

4.4 Numerical Model Development

4.4.1 Governing Simulation Algorithm

The model is a multiphysics model, and the fluid and structural fields are linked through FSI boundaries. Although the governing equations in the lubricant film are solved using in-house FORTRAN code, the code is tightly integrated into the convergence process of ANSYS. The FORTRAN code is compiled together with the existing ANSYS mechanical code in order to yield a customized and user-compiled version of ANSYS. The considerable advantage of integrating the in-house code into ANSYS is that, contrary to a co-simulation where multiple software packages are run concurrently or sequentially, the memory is shared between ANSYS and the in-house FORTRAN code. Sharing the memory in a multiphysics analysis is rarely done as it requires hard coding the interface between two software packages, but the gain in shorter solution times is considerable. The underlying algorithm is shown in Algorithm 3.

Algorithm 3 Algorithm for the strongly coupled TEHD - FSI simulation.

BEGIN
Allocate memory (local and global variables)
Read geometry, U, $\mathbf{f}$, $\mathbf{u}^0$, $\boldsymbol{\sigma}^0$
Read $\mathcal{C}$, p^0, $\mathbf{v}^0$, $\mathbf{q}^0$, θ^0,τ^0 and lubricant properties
DO WHILE (final time has not been reached)
  Determine contact elements and retrieve fluid film thickness c from ANSYS
  Read $\mathbf{u}$, p, θ, η, $\boldsymbol{\tau}$, $\boldsymbol{\sigma}$ (FSI)
  Generate/update deformed mesh
  DO WHILE (structural solution - $\mathbf{u}$, $\boldsymbol{\sigma}$,θ - has globally not converged)
    DO WHILE (p and θ have globally not converged)
      $\sim$ Fluid - Multigrid for p $\sim$
      Reduction of grid to lower spatial dimension (xz plane)
      DO WHILE (p has locally not converged)
        Multigrid for TTR equation
      END DO
      Extension of grid to higher spatial dimension (xyz space)
      IF (first iteration)
        Calculation of $\mathbf{v}$ (IFA - oil)
        Calculation of shells $c_+^{(n)}$, $c_-^{(n)}$ and spaces and define types of TT spaces (TDA)
      ELSE
        Load shells from memory
      END IF
      Combine dry and plug spaces and remove globally flat spaces
      DO WHILE (tribotopologies have not converged)
        Calculation of τ and $\dot{\gamma}$
        Adjustment of shells $c_+^{(n)}$, $c_-^{(n)}$ (TAA)
        Calculation of $\mathbf{v}$ (IFA - oil/grease)
      END DO
      $\sim$ Fluid - Multigrid for θ $\sim$
      Read boundary conditions $\theta|_{y=\{0,c\}}$
      DO WHILE (θ has locally not converged)
        1D Multigrid for energy equation
      END DO
      Calculation of $\mathbf{q}$ and η
      Update TTR equation factors
    END DO
  Read and apply p, τ and $\mathbf{q}|_{y=\{0,c\}}$ (FSI)
  Solve for $\mathbf{u}$, $\boldsymbol{\sigma}$ and θ (ANSYS)
  Partial deallocation of memory (fluid)
  END DO
Save $\mathbf{u}$, p, θ, η, $\boldsymbol{\tau}$, $\boldsymbol{\sigma}$, c, and calculate μ
END DO
Output analysis summary and deallocate memory (local and global variables)
END

The domain of the lubricant is physically located around the lower bearing. By unwrapping the domain of the lubricant film as shown in Fig. 4.2, a 2D plane xz is defined. At each position within the 2D plane, a 1D radial domain is defined to form the domain of the 3D lubrication film. This is a very convenient way to represent field variables and is used throughout the thesis.

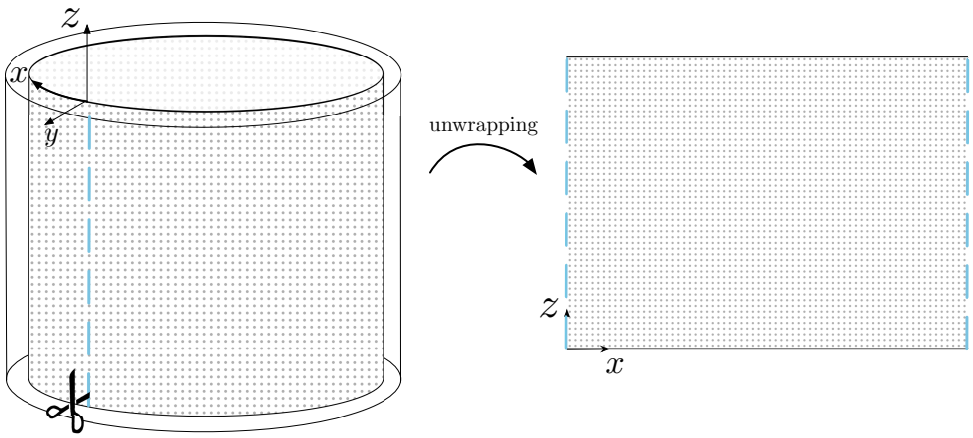

Figure 4.2: Unwrapping of the fluid film domain and mapping to the xz plane (2D).

The pressure field is constant across the lubrication gap (and variable along x and z), which reduces the numerical problem to finding the solution of a Poisson-type PDE with variable coefficients on a 2D grid with a high number of grid points. The diffusion term in the energy equation is only significant across the lubrication gap (along y). The energy equation can be reduced to a 1D numerical problem which needs to be solved repetitively along x and z. Consequently, the dimension of both governing equations is different, which yields a hybrid numerical problem that converges in a staggered manner. As long as global convergence of the pressure and temperature field has not been reached, the pressure field is obtained on a 2D grid (xz plane) before the grid is extended to a 3D grid (xyz space). On this extended 3D grid, a heat source term is calculated, which is used in the 1D temperature diffusion equation solved on the y-line while iterating over the 2D grid (xz plane).

The 2D pressure field is obtained using the 2D-MG method, whereas the energy equation is solved using the 1D-MG method. The hybrid solver is based on the MG method and has been developed in order to significantly speed up the solution of the governing equations, solved on a fine mesh. The MG method is preferred for the solution of the governing equations, as the discretized matrices are generally nonsymmetric and very large. The high number of grid points is necessary to ensure an accurate determination of the tribotopologies, which is required by the governing equations of the TTT. Instead of solving a tightly coupled TTM system, a staggered solution approach for convergence is more efficient, as iterative solvers such as the MG solver converge within a few iterations once the initial solution guess is close to the solution. Global convergence is consequently accelerated during the solution process. The staggered approach is guaranteed to converge once the TT shells and the MG iterations converge. No additional relaxation parameters other than for the MG loops have been introduced to accelerate or force convergence.

4.4.2 Computational Mesh of the Fluid and the FD Method

The finite difference (FD) method is chosen as a numerical discretization scheme in order to discretize the governing equations of the TTT. The transient governing equations are both discretized in space and time. As the partial differential equations contain highly nonlinear

coefficients, a backward differencing numerical discretization scheme for the time derivatives is used in order to ensure unconditional numerical stability of the discretization scheme. All of the physical quantities are evaluated on a regular mesh with $N_x + 2$, $N_y + 2$ and $N_z + 2$ grid points in the x, y, z directions respectively (see Fig. 4.3). The interior grid spacing is denoted as Δx, Δy and Δz. The spatial discretization scheme is a centered FD scheme. The running indices along x, y, z are denoted respectively as i, j, k, where $1 \leq i \leq N_x, 1 \leq j \leq N_y$ and $1 \leq k \leq N_z$. Before highlighting the discretization scheme, a set of interior boundary nodes is defined as:

$$\mathcal{B} = \{m \,|1 \leq i \leq N_x \text{ and } m \bmod N_x = 0 \text{ and } m \bmod N_x = 1 \text{ and } (N_z - 1)N_x + 1 \leq i \leq N\} \tag{4.8}$$

The set of $N_x \cdot N_z$ interior nodes is defined by $\mathcal{I} = \{i \,| i \notin \mathcal{B}\}$. As the pressure is obtained on a 2D grid (see Fig. 4.4), and in order to simplify the notations, an index m is defined as $m = (k-1)N_x + i,\ i \in \mathcal{I}$. The exterior edges of the computational domain (see Fig. 4.4) are the actual physical boundaries. The left and right walls are equal, as the computational domain is periodic.

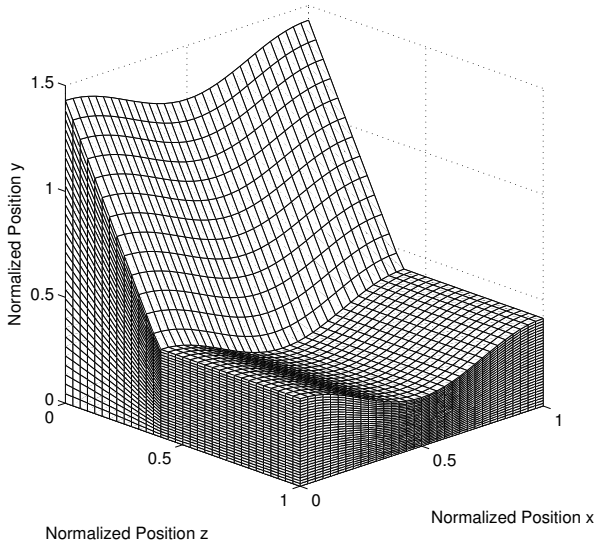

Figure 4.3: Example of a regular computational mesh ($\phi_e = 0, e/c0 = 0.286$).

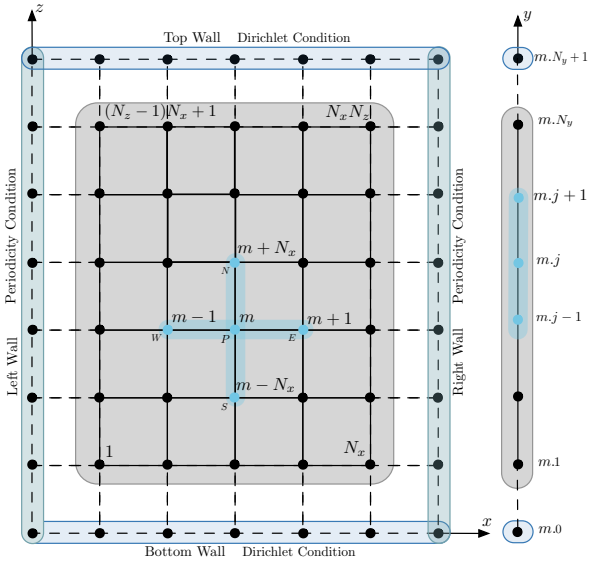

Figure 4.4: Grid stencil (2D and 1D) with N, E, S, W nodes around the center node P.

Dirichlet boundary conditions for field variables are input at the bottom and top walls. The discretization of the boundaries is shown in Section 4.4.3. The stencil around node m is shown in Fig. 4.4. The derivative of a scalar function f in directions x and z evaluated at node m is:

$$f_{,x}|_m \simeq \frac{f_{m+1} - f_{m-1}}{\Delta x} \quad , \quad f_{,z}|_m \simeq \frac{f_{m+N_x} - f_{m-N_x}}{\Delta z} \tag{4.9}$$

Similarly, the second order derivative of f in direction x is:

$$f_{,xx}|_m \simeq \frac{f_{m+1} - 2f_m + f_{m-1}}{\Delta x^2} \quad , \quad f_{,zz}|_m \simeq \frac{f_{m+N_x} - 2f_m + f_{m-N_x}}{\Delta z^2} \tag{4.10}$$

The FD discretization in time is a backward Euler scheme with N_t timesteps of duration Δt:

$$f_{,t}|_n \simeq \frac{f^n - f^{n-1}}{\Delta t} \tag{4.11}$$

4.4.3 Numerical Discretization of Tribotopological Equations

Discretization of the Tribotopological Reynolds Equation

The TTR equation (Eq. 3.37) is discretized at node m and at time step n:

$$a^n_{m+1}p^n_{m+1} + a^n_m p^n_m + a^n_{m-1}p^n_{m-1} + a^n_{m+N_x}p^n_{m+N_x} + a^n_{m-N_x}p^n_{m-N_x} = b^n_m \tag{4.12}$$

The discretization factors read:

$$\begin{array}{lllllllllll} a^n_m & = & a_m^{P\,n} & = & -\dfrac{2\tilde{\tilde{f}}_{x\,m}^{\;n}}{\Delta x^2} - \dfrac{2\tilde{\tilde{f}}_{z\,m}^{\;n}}{\Delta z^2} & , & a^n_{m-1} & = & a_m^{W\,n} & = & \dfrac{\tilde{\tilde{f}}_{x\,m}^{\;n}}{\Delta x^2} - \dfrac{\tilde{f}_{x\,m}^{\;n}}{2\Delta x} \\ a^n_{m+N_x} & = & a_m^{N\,n} & = & \dfrac{\tilde{\tilde{f}}_{z\,m}^{\;n}}{\Delta z^2} + \dfrac{\tilde{f}_{z\,m}^{\;n}}{2\Delta z} & , & a^n_{m-N_x} & = & a_m^{S\,n} & = & \dfrac{\tilde{\tilde{f}}_{z\,m}^{\;n}}{\Delta z^2} - \dfrac{\tilde{f}_{z\,m}^{\;n}}{2\Delta z} \end{array} \tag{4.13}$$

At timestep n, the matrix equation is consequently formulated as:

$$\begin{bmatrix} a^P_{N_x+2} & a^E_{N_x+2} & 0 & a^N_{N_x+2} & 0 & & \cdots & & 0 \\ a^W_{N_x+3} & \ddots & \ddots & \ddots & \ddots & \ddots & & & \\ 0 & \ddots & \ddots & \ddots & \ddots & \ddots & \ddots & & \vdots \\ a^S_{2N_x+2} & \ddots & \ddots & \ddots & \ddots & \ddots & \ddots & \ddots & \\ 0 & a^S_m & \ddots & a^W_m & a^P_m & a^E_m & \ddots & a^{N'}_m & 0 \\ & \ddots & \ddots & \ddots & \ddots & \ddots & \ddots & \ddots & a^N_{N''} \\ \vdots & & \ddots & \ddots & \ddots & \ddots & \ddots & \ddots & 0 \\ & & & \ddots & \ddots & \ddots & \ddots & \ddots & a^E_{N'-1} \\ 0 & & \cdots & & 0 & a^S_{N'} & 0 & a^W_{N'} & a^P_{N'} \end{bmatrix}^n \begin{bmatrix} p_{N_x+2} \\ \vdots \\ p_m \\ \\ \vdots \\ p_{N'} \end{bmatrix}^n = \begin{bmatrix} b_{N_x+2} \\ \vdots \\ b_m \\ \\ \vdots \\ b_{N'} \end{bmatrix}^n \tag{4.14}$$

where $N' = (N_z - 1)N_x - 1$ and $N'' = (N_z - 2)N_x - 1$. As the structural deformation is not strongly coupled to the hydrodynamic pressure, the film thickness is not calculated simultaneously at time t^n under the hydrodynamic pressure at time t^n. However, as low structural accelerations across the fluid film gap exist, it is assumed that the structural deformation velocity is similar:

$$\frac{c^n - 2c^{n-1} + c^{n-2}}{\Delta t} \simeq 0 \Leftrightarrow c^{n-1} - c^{n-2} \simeq c^n - c^{n-1} \tag{4.15}$$

Finally, the right-hand-side components of the discretized TTR equation are given by:

$$b^n_m = -\frac{c^{n-1}_m - c^{n-2}_m}{\Delta t} - f_{x\,m}^{\;n} - f_{z\,m}^{\;n} \tag{4.16}$$

For a steady state, all the factors of the TTR equation are the same, except for the right-hand-side vector components, which simplify to $b^n_m = -f_{x\,m}^{\;n} - f_{z\,m}^{\;n}$.

Discretized Boundary Conditions (Hydrodynamic Pressure)

Bottom Wall ($\overline{z} = 0$) and Top Wall ($\overline{z} = 1$) At the bottom and top walls, a Dirichlet pressure boundary condition is imposed, which results in a boundary charge for all nodes m

that are located on the top and bottom boundaries:

$$\forall\, 1 \leq m \leq N_x \;:\; p^n_{m-N_x} = {p_a}^n_m \quad \text{and} \quad \forall\, (N_z-1)N_x + 1 \leq m \leq N_x N_z \;:\; p^n_{m+N_x} = {p_b}^n_m \tag{4.17}$$

Left and Right Boundaries ($\overline{x}=0$ and $\overline{x}=1$) The condition of continuity and derivability at the common boundary of $\overline{x}=0$ and $\overline{x}=1$ is implemented using a common *ghost point*. The pressure value calculated at the ghost point is determined as the average of both boundary values.

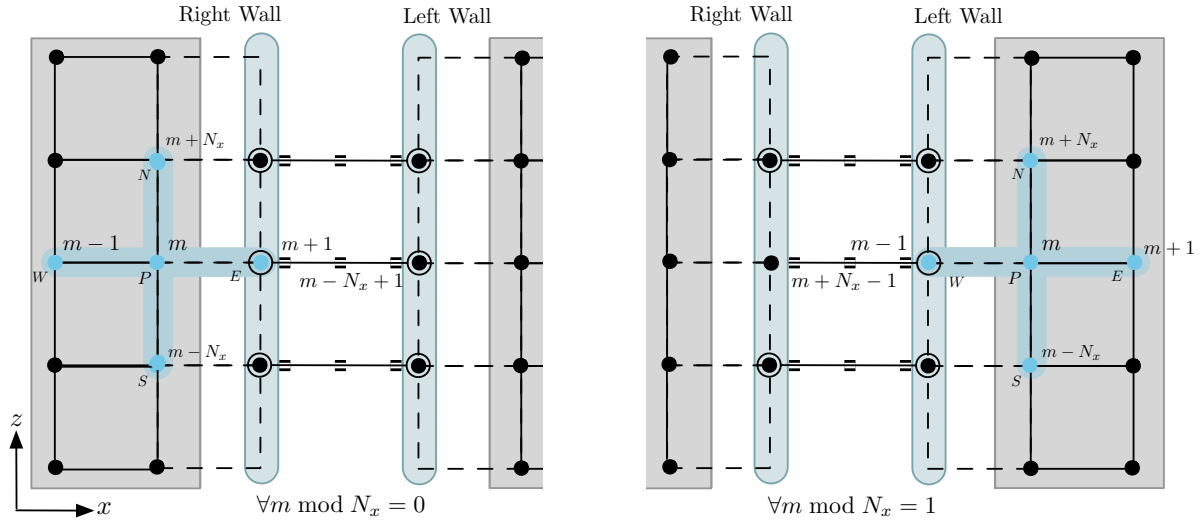

Figure 4.5: Periodicity boundary conditions of 2D grid.

The discretization of the left and right walls, which are shown in Fig. 4.5, translates at the left wall into:

$$\forall m \bmod N_x = 0 \;:\; p^{n+1}_{m+1} = \frac{1}{2}\left(p^{n+1}_m + p^{n+1}_{m-N_x+1}\right) \tag{4.18}$$

Similarly, at the right wall:

$$\forall m \bmod N_x = 1 \;:\; p^{n+1}_{m+1} = \frac{1}{2}\left(p^{n+1}_m + p^{n+1}_{m+N_x-1}\right) \tag{4.19}$$

Discretization of the Energy Equation

At time step n, the pressure vector $\mathbf{p}^n$, the derivative vectors $\mathbf{p}^n_{,x}$ and $\mathbf{p}^n_{,z}$, as well as the shear rate vector components $v^n_{x|z,y}$, are calculated before the matrix system of the discretized energy equation is solved. The discretized temperature at grid node $(i,j,k)=(m,j)$ is denoted as $\theta_{m.j}$. The transient energy equation (see Eq. (3.12)) is discretized across the lubrication gap (along y, index j) on a 1D line, which is situated above the 2D grid at node m, such that:

$$\begin{aligned}\left(\frac{\rho c_p}{\lambda_\theta}\right)_m \frac{\theta^n_{m.j} - \theta^{n-1}_{m.j}}{\Delta t} - \left(\frac{\kappa_\theta}{\lambda_\theta}\right)_m \frac{p^n_m - p^{n-1}_m}{\Delta t}\theta^n_{m.j} = \frac{\theta^n_{m.j+1} - 2\theta^n_{m.j} + \theta^n_{m.j-1}}{\Delta y^2} \\ + \left(\frac{\kappa_\theta}{\lambda_\theta}\right)_m {v_x}^n_{m.j} {p_{,x}}^n_m \theta^n_{m.j} + \left(\frac{\kappa_\theta}{\lambda_\theta}\right)_m {v_z}^n_{m.j} {p_{,z}}^n_m \theta^n_{m.j} + \left(\frac{\eta^{n-1}}{\lambda_\theta}\right)_m \left(v^2_{x,y} + v^2_{z,y}\right)^n_{m.j}\end{aligned} \tag{4.20}$$

which can be written in a compact form as:

$$a^n_{m.j+1}\theta^n_{m.j+1} + a^n_{m.j}\theta^n_{m.j} + a^n_{m.j-1}\theta^n_{m.j-1} = b^n_{m.j} \tag{4.21}$$

In addition to the obvious identification of $a^n_{m.j+1} = \frac{-1}{\Delta y^2}$ and $a^n_{m.j-1} = \frac{-1}{\Delta y^2}$, the discretization factors are given as:

$$\begin{aligned} a^n_{m.j} &= \frac{2}{\Delta y^2} - \left(\frac{\kappa_\theta}{\lambda_\theta}\right)_m {v_x}^n_{m.j} {p_{,x}}^n_m - \left(\frac{\kappa_\theta}{\lambda_\theta}\right)_m {v_z}^n_{m.j} {p_{,z}}^n_m - \left(\frac{\kappa_\theta}{\lambda_\theta}\right)_m \frac{p^n_m - p^{n-1}_m}{\Delta t} + \frac{1}{\Delta t}\left(\frac{\rho c_p}{\lambda_\theta}\right)_m \\ b^n_{m.j} &= \left(\frac{\eta^{n-1}}{\lambda_\theta}\right)_m \left(v^2_{x,y} + v^2_{z,y}\right)^n_{m.j} + \frac{\theta^{n-1}_{m.j}}{\Delta t}\left(\frac{\rho c_p}{\lambda_\theta}\right)_m \end{aligned} \tag{4.22}$$

An important fact to consider is that the lubricant's physical properties, such as the viscosity η at timestep n, are not updated with the temperature at timestep n. Instead, the viscosity at timestep $n-1$ is used, such that $\eta^n \simeq \eta^{n-1}$. The discretized Eq. (4.21) at the 2D grid position m is written in a tridiagonal matrix system ($0 \leq j \leq N_y$):

$$\text{tridiag}\left[a_{m.j-1}\ ,\ a_{m.j}\ ,\ a_{m.j+1}\right]^n_{N_y \times N_y} \left[\theta_{m.j}\right]^n_{N_y} = \left[b_{m.j}\right]^n_{N_y} \tag{4.23}$$

For a steady state, some discretization factors of the energy equation are simplified such that:

$$\begin{aligned} a^n_{m.j} &= \frac{2}{\Delta y^2} - \left(\frac{\kappa_\theta}{\lambda_\theta}\right)_m {v_x}^n_{m.j} {p_{,x}}^n_m - \left(\frac{\kappa_\theta}{\lambda_\theta}\right)_m {v_z}^n_{m.j} {p_{,z}}^n_m \\ b^n_{m.j} &= \left(\frac{\eta^{n-1}}{\lambda_\theta}\right)_m \left(v^2_{x,y} + v^2_{z,y}\right)^n_{m.j} \end{aligned} \tag{4.24}$$

The remaining discretization factors of the steady state energy equation are the same as for the transient energy equation.

Discretized Boundary Conditions (Temperature Field)

The boundary conditions of the temperature field are defined as Dirichlet boundary conditions (fixed temperatures). Similar to the hydrodynamic pressure, the boundaries for the temperature field are discretized as:

$$\forall m.0\ :\ \theta^n_{m.0} = {\theta_a}^n_m \quad \text{and} \quad \forall m.Ny+1\ :\ \theta^n_{m.Ny+1} = {\theta_b}^n_m \tag{4.25}$$

4.4.4 Hybrid Multigrid-based Numerical Solver

Both the energy and the generalized TTR equations are classified as elliptic Poisson-type PDEs with variable coefficients. As shown in Section 4.4.3, the PDE is discretized using the FD method, which yields a linear system of the form $\mathbf{A}\hat{\mathbf{v}} = \mathbf{b}$, where $\hat{\mathbf{v}}$ is either the pressure vector $\mathbf{p}$ or the temperature vector $\boldsymbol{\theta}$. For variable coefficients, the matrix $\mathbf{A}$ is sparse, but not necessarily symmetric. For the TTR equation with periodic boundary conditions, $\mathbf{A}$ is generally 7-diagonal, whereas for the energy equation, $\mathbf{A}$ is 3-diagonal. As the same solver is used to solve matrix systems of different dimensions, the solver is classified as *hybrid*.

In order to save on computation time and storage, the matrix coefficients of the 7-diagonal (or 3-diagonal for the energy equation) matrix $\mathbf{A}$ are stored in 7 (respectively in 3) vectors. The

7-diagonal matrix is written as $\mathbf{A} = \text{diag}\left(\mathbf{a}^S, \mathbf{a}^{b'}, \mathbf{a}^W, \mathbf{a}^P, \mathbf{a}^E, \mathbf{a}^{b''}, \mathbf{a}^N\right)$, where the vectors $\mathbf{a}^{b'}$ and $\mathbf{a}^{b''}$ are non-zero for the nodes close to the left and right walls (periodic boundaries) of the 2D grid. The linear system can be solved using direct methods (such as Gaussian elimination or LU decomposition) or indirect methods (such as Gauss-Seidel) to calculate an approximate solution $\tilde{\mathbf{v}}$. The direct methods are reportedly slow for high numbers of nodes. The disadvantage of indirect methods (not MG) is that their convergence is slow once the residual error between convergence iterations becomes small and smooth on a given grid. Various numerical methods have been investigated but have failed to provide fast converging results for the problem at hand.

The reason behind investigating higher performing and faster converging numerical methods is that many iterations are needed for optimization studies and transient simulations, especially for a very high number of grid points. One of the fastest numerical algorithms known today is the MG method (with a linear logarithmic convergence rate of $O(N)$), which is explained in a very illustrative way in [107]. In order to solve the governing equations of the TTT, the MG method is implemented in an in-house hybrid solver, such that the governing TTR equation is solved on a 2D grid and the governing energy equation on a 1D-grid using MG.

As demonstrated in [108], the idea behind the MG method is to take advantage of a fast iterative scheme, but to also represent the residual $\mathbf{r}_\epsilon = \mathbf{b} - \mathbf{A}\tilde{\mathbf{v}}$ on a coarser grid once the error is smooth enough. The advantage is that a smooth error $\mathbf{e}_\epsilon = \hat{\mathbf{v}} - \tilde{\mathbf{v}}$ is eliminated faster on a coarser grid than on a finer grid. The convergence procedure shown in Fig. 4.6 starts with an initial guess $\tilde{\mathbf{v}}$, which is obtained on the fine grid. Once the error $\mathbf{e}_\epsilon$ is smooth enough, the residual $\mathbf{r}_\epsilon$ is transferred onto a coarser grid (restriction) and the residual error is computed from $\mathbf{A}\mathbf{e}_\epsilon = \mathbf{r}_\epsilon$. The iteration procedure continues until the error is smoothed out on the coarsest grid. Then, a correction is applied to each approximation of the solution until the fine grid is reached (prolongation). Such a convergence cycle of restriction and prolongation steps can be seen as a V-cycle.

The restriction of the residual error from a finer grid level to a coarser grid level is performed by averaging the value at the neighboring nodes. As can be seen in Fig. 4.6, the mesh is coarsened during the restriction, whereas during the prolongation, the mesh is refined at every step. For an interior node (i, k) on the coarse grid:

$$\begin{aligned} e_{\epsilon_{(i,k)}}^{\text{coarse}} \quad = \quad & \frac{1}{16}\Big(e_{\epsilon_{(2i-1,2k-1)}}^{\text{fine}} + e_{\epsilon_{(2i-1,2k+1)}}^{\text{fine}} + e_{\epsilon_{(2i+1,2k-1)}}^{\text{fine}} + e_{\epsilon_{(2i+1,2k+1)}}^{\text{fine}} \\ & +2\left(e_{\epsilon_{(2i,2k-1)}}^{\text{fine}} + e_{\epsilon_{(2i,2k+1)}}^{\text{fine}} + e_{\epsilon_{(2i-1,2k)}}^{\text{fine}} + e_{\epsilon_{(2i+1,2k)}}^{\text{fine}}\right) + 4e_{\epsilon_{(2i,2k)}}^{\text{fine}}\Big) \end{aligned} \tag{4.26}$$

where ${e_\epsilon}^{\text{coarse}}$ is the restricted residual error on the coarse grid, and ${e_\epsilon}^{\text{fine}}$ the residual error on the finer grid. Similarly as for the restriction, the prolongation from a coarser to a finer grid level for an interior node (i, k) is given by:

$$e_{\epsilon_{(i,k)}}^{\text{fine}} = \frac{1}{4}\left(e_{\epsilon_{(i,k)}}^{\text{coarse}} + e_{\epsilon_{(i+1,k)}}^{\text{coarse}} + e_{\epsilon_{(i,k+1)}}^{\text{coarse}} + e_{\epsilon_{(i+1,k+1)}}^{\text{coarse}}\right) \tag{4.27}$$

In order to guarantee proper restriction and prolongation of the grids in the MG algorithm, the grid is considered uniform and the number of nodes is an exponential of base 2 in each direction x and z, such that $N_{x|z} = 2^{\varpi} - 1$, where ϖ is the grid level index. The number of coarser grids in the MG algorithm is $\varpi - 1$.

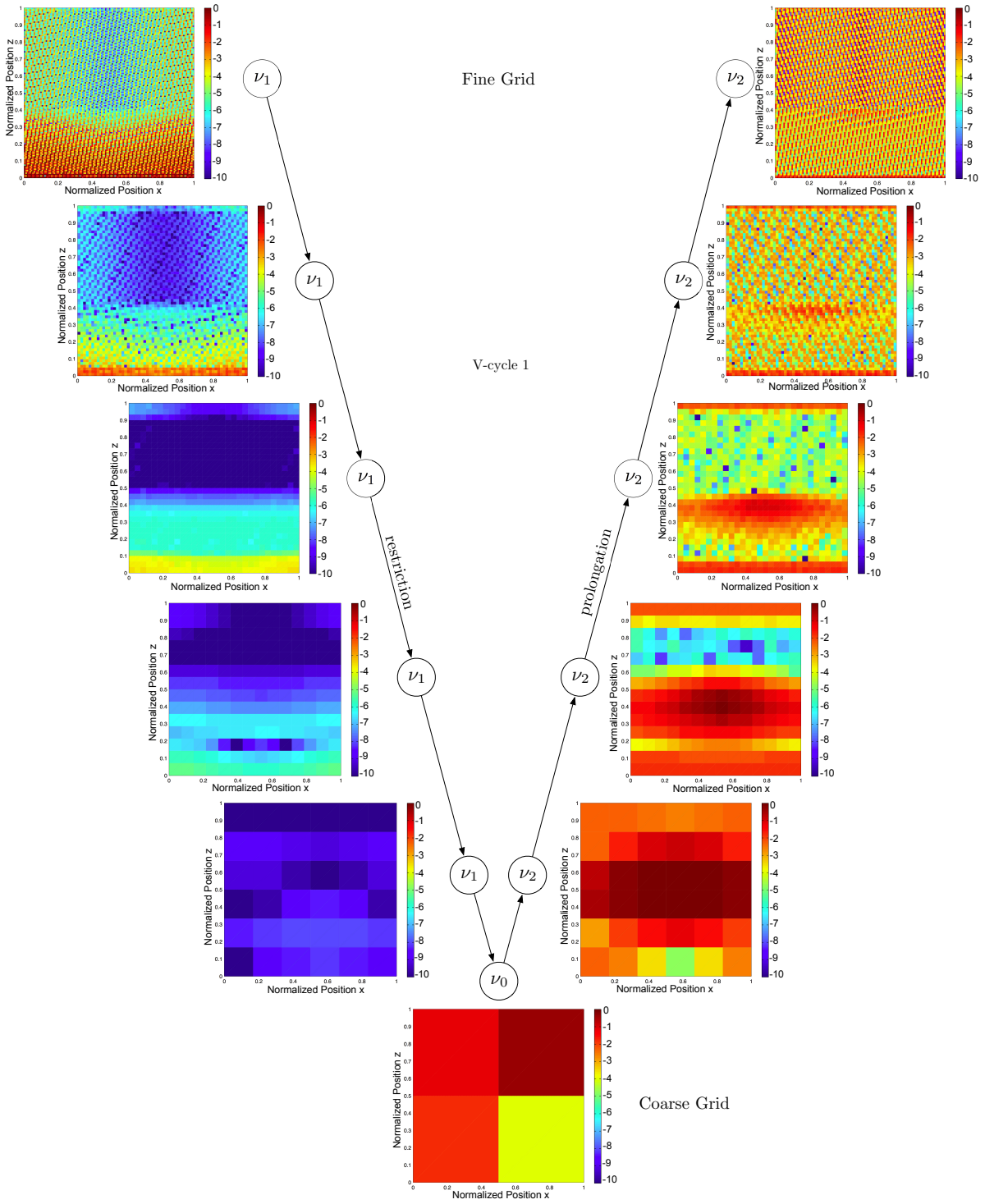

Figure 4.6: Typical first V-cycle restriction/prolongation cycle of the error $\mathbf{e}_\epsilon$ (logarithmic scale).

The convergence of the 2D-MG solver is illustrated for an oil-lubricated, isothermal, steady state slider bearing, in which case the coefficients of the TTR equation (see Eq. (3.37)) are given in Eq. (3.47). The convergence sequence of the TTR equation residual on the fine grid (end of each V-cycle) is shown in Fig. 4.7. The random initialization of the solution p, generated with the random number generator explained in [109], is shown in sub-figure A.

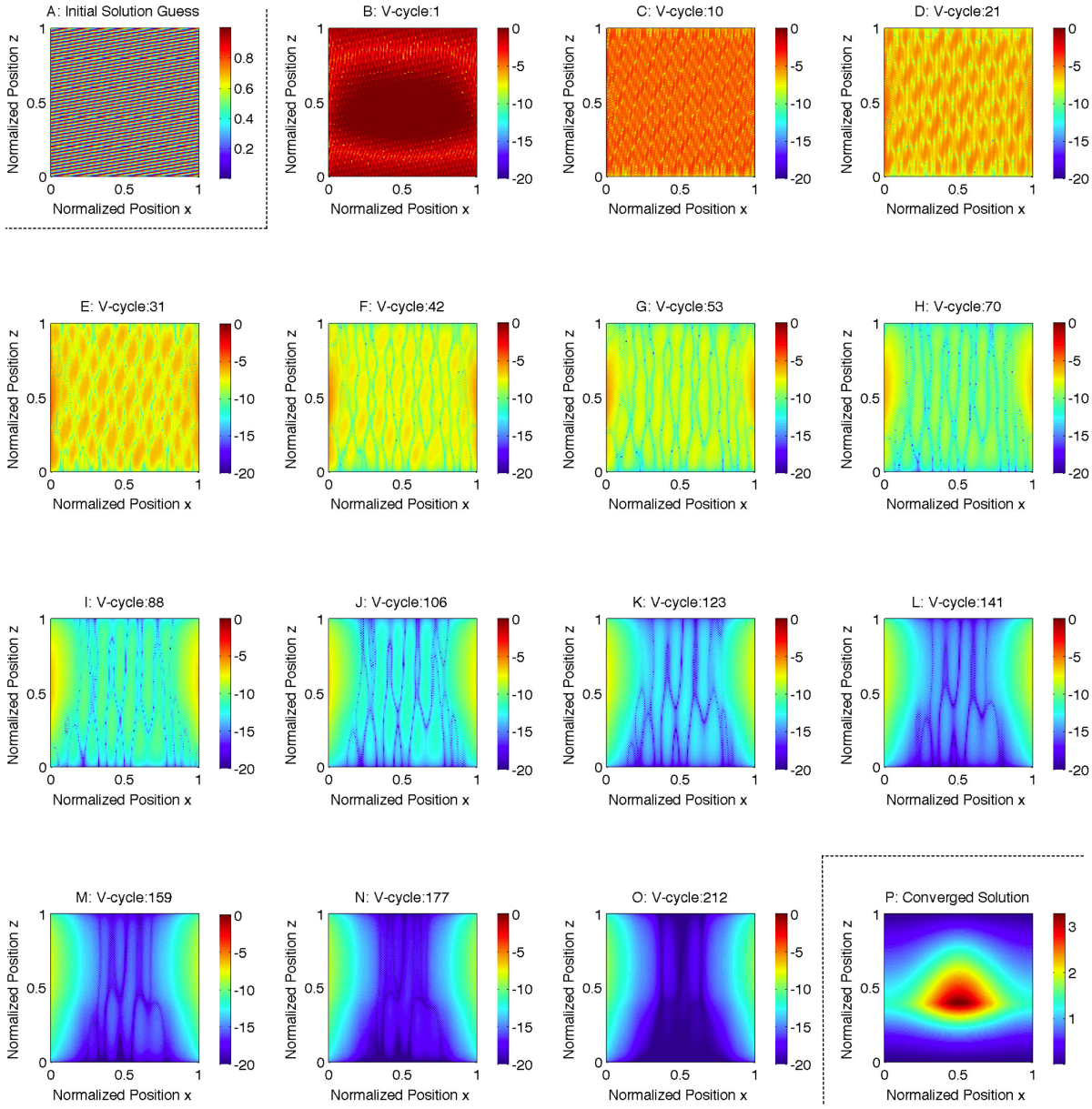

Figure 4.7: Convergence sequence of the 2D-MG algorithm (A: Initial solution guess; B-O: Logarithm of error $\mathbf{e}_\epsilon$; P: Converged solution).

For an oil-lubricated slider bearing, the solution is obtained after 212 V-cycles for 127x127 nodes (without boundaries), and the natural logarithm of the residual error on the fine grid is shown for several V-cycles in the sub-figures B-O. The residual error, although high in the first V-cycles, dissipates fairly quickly during the V-cycle iterations. An interesting observation

is that the residual numerical error dissipates in the circumferential direction (with Neumann boundary conditions at $\overline{x} = \{0, 1\}$), while the vertical edges at $\overline{z} = \{0, 1\}$ are fixed with Dirichlet boundary conditions. The converged solution of the normalized pressure field is shown in sub-figure P. The implemented MG method follows a V-cycle with relaxation factors chosen by trial and error, with $\nu_1 = 2$ error relaxations per restriction step and $\nu_2 = 1$ error relaxation per prolongation step. The criterion for global convergence is chosen as $|\mathbf{e}_\epsilon| < 10^{-7}$ for the pressure and temperature fields. The restricted matrices on the coarser grids are solved using the iterative weighted Jacobi algorithm, as the linear system for variable material properties and deformable surfaces is generally nonsymmetric.

The weighted Jacobi method is similar to the Gauss-Seidel method, but in the Jacobi method, the matrix $\mathbf{A}$ is decomposed into a diagonal matrix $\mathbf{A}_\backslash = \mathrm{diag}\left(\mathbf{a}^P\right)$ and an off-diagonal matrix $\mathbf{A}'_\backslash = \mathbf{A} - \mathbf{A}_\backslash$. The numerical error at iteration $k+1$ is given by $\mathbf{e}_\epsilon^{(k+1)} = (1 - \breve{\omega})\,\mathbf{e}_\epsilon^{(k)} + \breve{\omega}\mathbf{A}_\backslash^{-1}\left(\mathbf{b} - \mathbf{A}'_\backslash \mathbf{e}_\epsilon^{(k)}\right)$. The weight $\breve{\omega}$ of the weighted Jacobi method is initially 0.99 (aggressive). However, if the logarithm of the residual in the first iterations is greater than zero, the weight is gradually reduced in order to guarantee convergence. In total, $\nu_0 = 30$ weighted Jacobi iterations are performed at the coarsest grid level. With the storage of the matrix $\mathbf{A}$ as 7 vectors, the matrix products are equivalent to vector multiplications, with trivial multiplications being avoided.

4.4.5 Topology Detection Algorithm (TDA)

The Topology Detection Algorithm (TDA, shown in Algorithm 4) is used to determine the shells (virtual boundaries) of the TT spaces within the lubrication gap. The TT shells are isosurfaces determined from a scalar field f. The TDA is consequently an isosurface extraction algorithm, which determines the shells and the types of each enclosed TT space. In order to reduce the complexity of the numerical model and generate nonintersecting and bijective surfaces, the TDA relies on root detection techniques [110]. Any other sophisticated isosurface detection/extraction algorithm that is based on the Marching Cubes method might not necessarily guarantee bijective shells and splitting into bijective surface parts might be required, which may increase robustness at the cost of an increased computation time.

The underlying method of the TDA is the Van Wijngaarden–Dekker–Brent root-finding method [111] for a 1D scalar function $f'(y) - f_0$, which is defined across the lubrication gap as the restriction of a scalar field $f(x, y, z)$ along y for a given position $(\overline{x}, \overline{z})$. This method has been chosen as the ideal method for the problem at hand, as it is specifically meant to converge at an acceptable speed for functions that might have a discontinuous second order derivative. As explained in [111], this method is also particularly suitable for finding roots of functions where the derivatives are not available, which are generally required for Newton-based root-finding algorithms. The restricted scalar function $f'(y) - f_0$ is discretely defined on all grid points. In order to use root-finding techniques, the restricted scalar function $f'(y) - f_0$ is interpolated along the radial direction y. The interpolation of the restricted function is performed using a cubic spline interpolation technique [111].

Algorithm 4 Topology Detection Algorithm (TDA)

BEGIN
DO WHILE ($i \leq N_x + 2$ & $k \leq N_z + 2$)
Extract a restriction f' of the function f (either τ or θ)
Interpolate the extracted restriction f' using a cubic spline interpolation technique
Split the radial domain $[0, c(i,k)]$ into N_i intervals.
DO WHILE ($m < N_i + 1$)
Find root c_m of $f' - f_0$ within $[(m-1) \cdot N_i, m \cdot N_i]$
IF (c_m found)
Determine which shell is most appropriate based on previous roots
IF (jump detected and no existing shell fits)
Initialize a new shell and update the shell type vector
Store the root in the newly created shell and initialize existing shells
ELSE
Store the root in the appropriate shell
END IF
ELSE
Adjust existing shells depending on their position
Continue with the next interval: $m = m + 1$
END IF
END DO
END DO
Remove globally flat spaces
Determine the type vector and the type of each TT space
END

The scalar field $f(x, y, z)$ for the TT plug space is the norm of the shear stress τ, and the corresponding isovalue is τ_0. For the TT dry space, $f = \theta$ and the isovalue is $\hat{\theta}$. The shell is hence determined as the root $c^{(n)}_{+|-}$ that satisfies $f'\left(c^{(n)}_{+|-}\right) - f_0 = 0$. The TDA, however, is not only a root-finding algorithm, but is also the algorithm used for detecting nonintersecting shells, especially for multiple types of TT spaces. The TDA is also used to remove globally flat shells that appear during the convergence iterations.

4.4.6 Topology Adjustment Algorithm (TAA)

The Topology Adjustment Algorithm (TAA) is called during the iteration procedure of the TEHD - FSI simulation (see Algorithm 3). Once the tribotopologies are detected using the TDA, the velocity field is updated and a new shear stress field is calculated. The TAA relies on the principle of the existence of at least one position across the lubrication gap where the shear stress is minimum. If a shell exists as determined by the TDA, the shear stress across the lubrication gap (along y) within the fluid space is linear, as the velocity field is a quadratic polynomial as postulated in the TTT. Consequently, the shell is located at the minimum shear stress of the grease, or, in other words, where $v_{x|z,y} = 0$. Across the lubrication gap, the values of the shear stress exist at discrete nodes, as shown in Fig. 4.8.

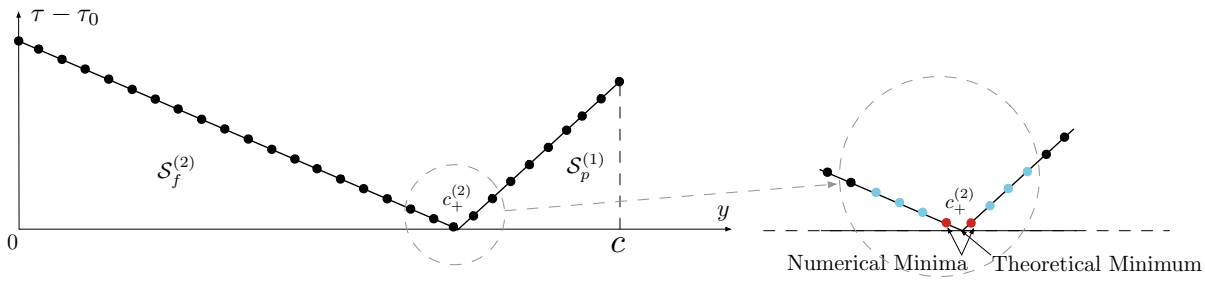

Figure 4.8: Illustration of the Topology Adjustment Algorithm (TAA).

At the minimum, the relative shear stress is, in theory, zero. However, for discretely defined values, there is one (or more) minimum(a) of the shear stress, because the shear stress is a derived and numerically calculated field. In order to determine the theoretical minimum, the shell $c_+^{(2)}$ is adjusted using linear extrapolation of the neighboring nodes.

Algorithm 5 Topology Adjustment Algorithm (TAA)

BEGIN
DO WHILE ($i \leq N_x + 2$ & $k \leq N_z + 2$)
  DO WHILE ($m < N_s$)
    Determine the grid index of the existing shell boundaries of space m
    Find the numerical minimum of the shear stress field
    IF(numerical minimum is close to either contact surface)
      Move minimum to the contact surface
    ELSE
      Calculate the theoretical value of the minimum and adjust the minimum value
    END IF
  END DO
END DO
END

4.4.7 Fluid-structure Interaction (FSI)

The fluid-structure interaction mapping (FSI mapping) of the physical quantities between the structure and the fluid is implemented in the TEHD module, which is integrated in ANSYS in order to profit from the shared memory. The FSI boundaries (shown in Fig. 4.1) are the boundaries at which the hydrodynamic pressure p, the shear stress $\tau_{x|z}$, and the heat flux q_y calculated within the lubricant, are applied. The clearance c and the boundary temperatures $\theta_{y=\{0,c\}}$ are retrieved from ANSYS and input to the TEHD module. As explained in [112], the in-house code relies on the partitioned FSI approach, where the behavior of the structure is solved on two independent meshes. The displacement (or clearance) between the two physical domains i, i' and a shared boundary k is compatible, which is ensured by $\mathbf{u}^{(i)}\big|_{\Gamma^{(k)}} = \mathbf{u}^{(i')}\Big|_{\Gamma^{(k)}}$. In addition, the shear stress at the FSI interface is equal, such that the traction equilibrium at the interface is given by $\boldsymbol{\sigma}^{(i)}\mathbf{n}^{(k)} = -\boldsymbol{\sigma}^{(i')}\mathbf{n}^{(k')} = \boldsymbol{\sigma}^{(i')}\mathbf{n}^{(k)}$. The heat flux at the interface is conserved by $\lambda_\theta^{(i)}\boldsymbol{\nabla}\theta^{(i)} \cdot \mathbf{n}^{(k)} = -\lambda_\theta^{(i')}\boldsymbol{\nabla}\theta^{(i')} \cdot \mathbf{n}^{(k)}$.

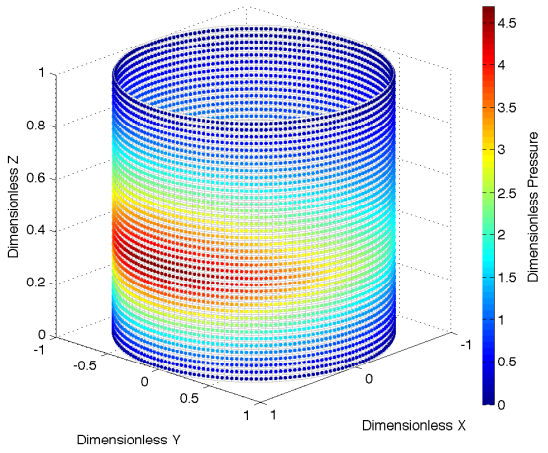

Figure 4.9: FSI mapping of $\overline{p}$ (grease).

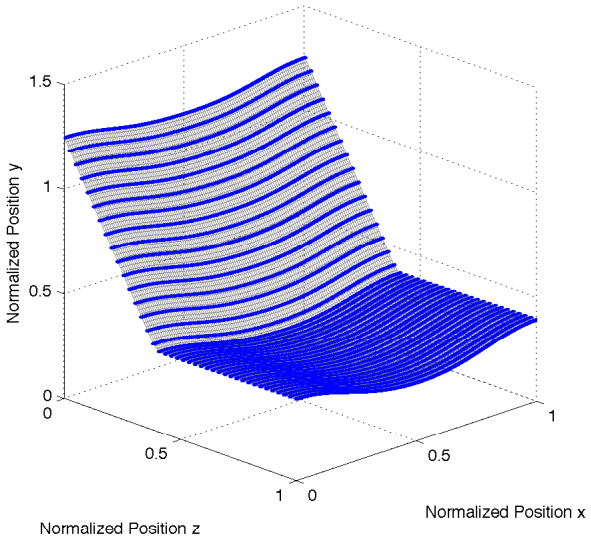

Figure 4.10: Interpolated clearance $\overline{c}$.

The temperature field between the two domains i and i' is continuous at the boundary: $\theta^{(i)}\big|_{\Gamma(k)} = \theta^{(i')}\Big|_{\Gamma(k)}$. The applied hydrodynamic pressure is applied at the FSI interface and balanced by structural reaction forces (see Fig. 4.9). The values retrieved from ANSYS are irregularly distributed, as they are retrieved on the integration points of the structural contact elements, which are averaged on the structural element (see Fig. 4.10). The values retrieved need to be on a structured grid for the TEHD module, and are interpolated using the method of bivariate interpolation shown in [113].

4.4.8 Computational Mesh of the Structure

The structural components of the comprehensive model are meshed in ANSYS. In order to allow optimal for contact detection and mapping of the physical fluid quantities onto the structure, the mesh is a structured and swept mesh on all the structural components.

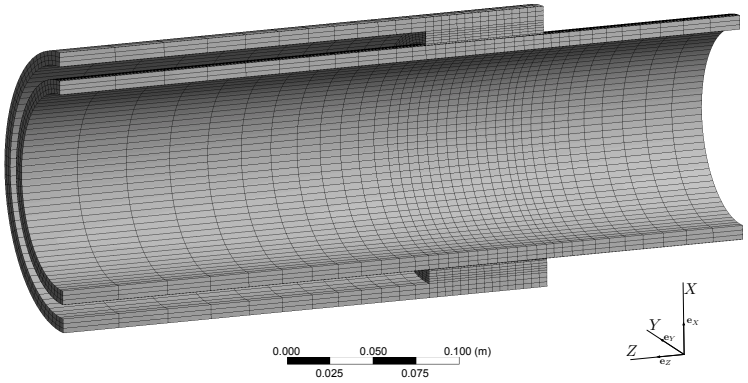

Figure 4.11: Structural mesh (assembly).

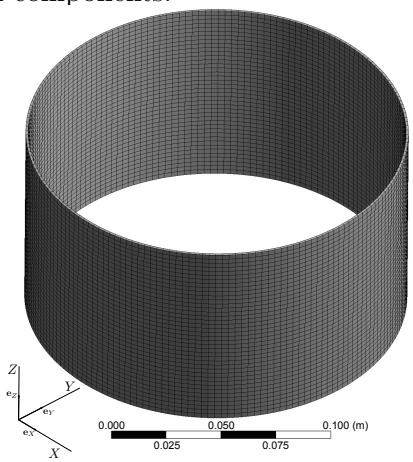

Figure 4.12: Structural mesh (lower bearing).

The structural mesh of the assembly is shown in Fig. 4.11. The mesh is similar to the structural mesh of the characteristic model shown in Fig. 2.16, but different types of elements are used and the mesh is refined in the TZI. It is of particular importance to adequately mesh the

lower bearing interface (shown in Fig. 4.12), as the FSI boundaries are mapped at this interface. There are 180 circumferential divisions at the lower bearing interface, and the remaining structural components have 90 circumferential divisions. The number of circumferential divisions at the lower bearing interface and on the piston are identical, in order to guarantee proper detection of the contact. In addition, each component is divided radially three times in order to allow the calculation of a radial temperature gradient. A summary of all the elements is provided in Table 4.2.

Type	**Element Count**	**Purpose**
SOLID226	42480	Calculate structural deformation and temperature
CONTA174	65340	Contact elements on the bearing surface
TARGE170	65340	Target elements on the piston surface
SURF154	N/A	Apply hydrodynamic pressure and shear stress
SURF152	N/A	Apply heat fluxes and boundary temperatures
TOTAL	107820	248220 nodes

Table 4.2: Summary of the structural elements.

4.5 Numerical Performance Analysis

Before the comprehensive model validation is given, a numerical convergence and mesh independence study is performed. The mesh independence study guarantees that the solution of the governing equations is obtained on an optimal mesh. As the numerical code is intended to be used for diverse LG bearing applications and lubricants, the numerical performance is studied for several cases shown in Table 4.3 and for various mesh sizes shown in Table 4.4. For these cases, a rigid and isothermal structure is assumed (no structural deformation considered), in order to analyze the performance of the TEHD code and, in particular, the performance of the hybrid numerical solver based on the MG method.

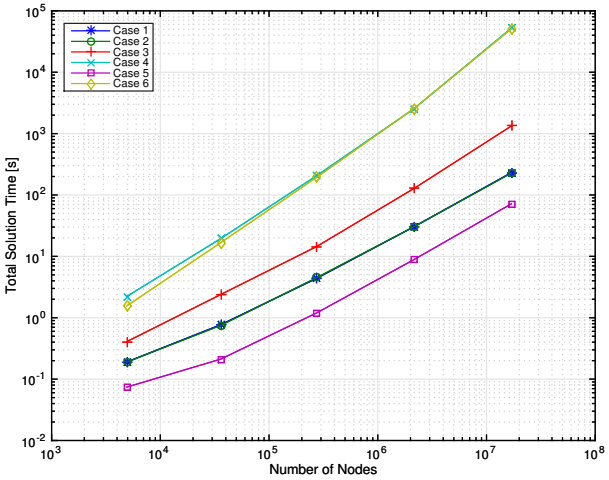

Figure 4.13: Total solution time.

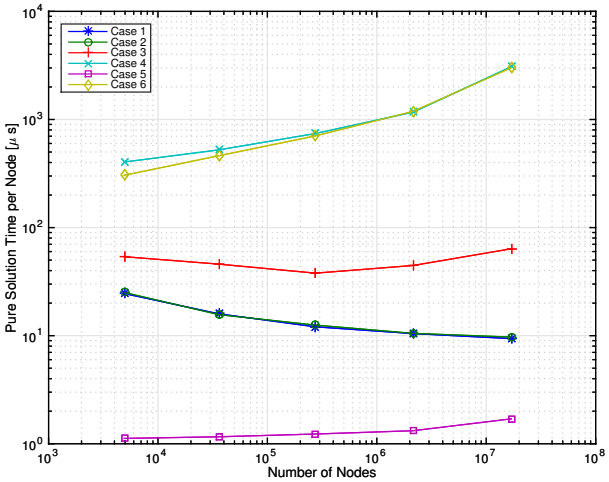

Figure 4.14: True solution time per node.

The convergence criterion for the field f (either pressure $f = p$ or temperature $f = \theta$) at the global iteration n is $\left(f^{[n]} - f^{[n-1]}\right)/f^{[n-1]} < 10^{-7}$. The grids shown are structured grids and have an equal grid spacing in all the directions x, y, z. The numerical performance analysis cases were run on a UNIX-based computer with 2.7GHz Intel quad-core i7 processors and 16GB of RAM. The total solution times for each case as a function of N are shown in Fig. 4.13, where N is the dimension of the square system matrix on the fine grid that is solved. The solution times for the cases with grease are higher than for oil, and increase (almost) linearly with higher node numbers, in particular for Case 3. The linear trend of the solution time as a function of N is due to the MG solver, which scales as $O(N)$. The total solution time does not exactly follow a linear trend for the cases with grease, and this is primarily due to the fact that the TDA does not scale as $O(N)$. In order to evaluate the hardware-independent numerical performance of the hybrid solver, the true solution time per node as a function of N is shown in Fig. 4.14. The total number of operations is obtained by multiplying the true solution time by the clock rate of the computer. For the cases with oil, the solution times per node are constant and even slightly decrease for higher node numbers. This observation is in agreement with the expected behavior of a MG-based solver. Nevertheless, for higher N and the cases with grease, the solution times per node are not only higher, but also increase with N.

Case	**Lubricant**	e/c_0	**Isothermal**	$\eta = \eta_0$
1	oil	0.0	no	yes
2	oil	0.286	no	yes
3	oil	0.0	no	no
4	grease	0.0	no	yes
5	oil	0.286	yes	yes
6	grease	0.286	yes	yes

Table 4.3: Analysis cases.

Grid	ϖ	$N_{x\|y\|z}$	N
1	4	17	4913
2	5	33	35937
3	6	65	274625
4	7	129	2146689
5	8	257	16974593

Table 4.4: Computational grids.

This fact is an indication of a need for parallelizing the numerical code, especially for the cases with grease. The numerical algorithm can be parallelized, and the necessary steps are discussed in Chapter 6. Of particular interest is the numerical performance of the 2D-MG solver for the TTR equation. As the residual error of a parabolic PDE is mostly reduced at the first global iterations (see Fig. 4.7), the number of V-cycles necessary for the convergence of the first two global iterations is shown in Fig. 4.15. An interesting observation is that for all cases, the number of V-cycles is reduced after the first global iteration. For increasing N, the number of V-cycles increases almost quadratically, which demonstrates the performance and applicability of the MG method to the TTR equation. The optimal grid for solving any of the given cases is chosen by comparing the maximum hydrodynamic pressure to the maximum hydrodynamic pressure calculated on the finest grid ($\varpi = 8$), as shown in Fig. 4.16. The acceptable error for the maximum pressure is restricted to 2%. In order to satisfy this upper limit, and based on the accuracy obtained and the respective solution times, Grid 4 ($\varpi = 7$) is chosen for consecutive simulations. Grid 5 ($\varpi = 8$) is used for validation purposes only.

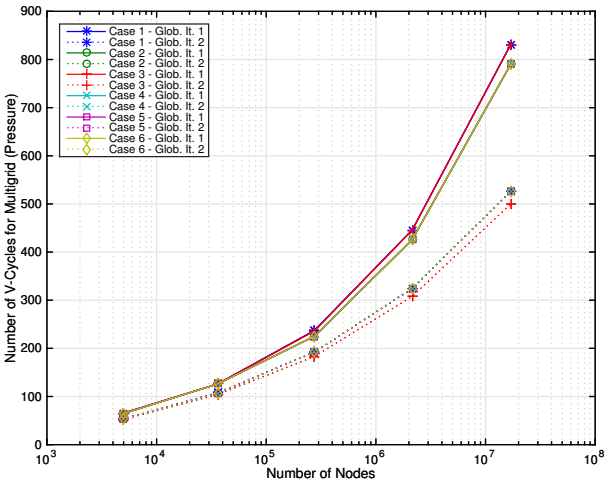

Figure 4.15: Number of V-cycles for the first 2 global iterations as a function of N.

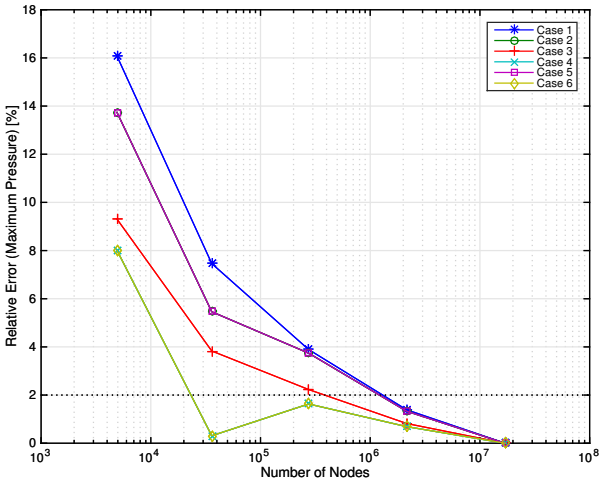

Figure 4.16: Relative error of maximum hydrodynamic pressure as a function of N.

4.6 Validation of the Comprehensive Model

4.6.1 Methodology and Limitations

The comprehensive model is validated by considering two specific cases. First, the case of a quasi-isothermal, oil-lubricated inclined slider bearing, for which an analytical solution exists, is considered. The hydrodynamic pressure, the temperature field, the velocity field and the hydrodynamic loads generated are validated with analytical formulas. Second, the comprehensive model is validated using the experimental data of the hydrodynamic pressure field available in the literature for the case of an oil-lubricated bearing and rotational motion. Although the model is validated against some experimental data, the validation of the comprehensive model is limited, as no experimental data for a LG slider bearing are available.

Solution Quantity	**Vertical Motion**	**Rotational Motion**
Number of nodes	16974593	16974593
Number of global iterations	2	4
Weight $\breve{\omega}$ of MG solver (Press. Iter. 1)	0.99	0.07
Number of V-Cycles (Press. Iter. 1)	1259	10243
Average number of V-Cycles (Temp. Iter. 1)	7	N/A
Total solution time [s]	163.85	526.04
True solution time per node [μs]	6.44	2.24

Table 4.5: Validation solution summary.

In addition, the validation is only performed for a steady state case, and no transient effects are included. Nevertheless, as the transient behavior is considered as a sequence of instantaneous steady states (see Section 4.7.5), the comprehensive model is considered to be validated. For both validation cases shown in Table 4.5, the numerical performance is notably fast, as the solution times are very low for a high number of grid points. Although it is not required to solve

the governing equations on a structured mesh with such a high number of grid points to reach convergence, as demonstrated in Section 4.5, the high number of grid points has been chosen to demonstrate the performance of the numerical code and to obtain numerical errors within a 1% limit.

4.6.2 Analytical Validation - Vertical Motion

As the available validation data are limited for slider bearings, the numerical model is validated using a quasi-isothermal, steady state reference case provided in [114] and the parameters $\tilde{U} = 1.0$ m/s, $\eta_0 = 0.032$ Pas, $\frac{c_0}{\varsigma} = 0.127$, and is validated for an inclined bearing surface with a noneccentric piston ($e = 0, z_0/L = 1$) and isoviscous oil. The TTR equation shown in Eq. (3.37) reduces to $\left(c^3 p_{,z}\right)_{,z} = 6\eta_0 \tilde{U} c_{,z}$, which, after full integration, leads to:

$$p_{,x} = 0 \quad \text{and} \quad p(z) = \begin{cases} -\dfrac{\eta_0 H}{c \cdot c_{,z}} - \dfrac{\eta_0 H_1}{2\rho c^2 c_{,z}} + H_2 & \text{if } c_{,z} \neq 0 \\ H_3 z + H_4 & \text{if } c_{,z} = 0 \end{cases} \tag{4.28}$$

where $H = 6\tilde{U}$. The application of the boundary conditions $p|_{z=0} = p|_{z=L} = 0$, combined with the conditions for continuity $p|_{z=z_0^-} = p|_{z=z_0^+}$ and $p_{,y}|_{z=z_0^-} = p_{,z}|_{z=z_0^+}$, leads to the following coefficients of Eq. (4.28):

$$H_1 = -2H\rho c_0 \frac{c_0 - \varsigma + \varsigma z_0^{-1} L - c_0^2 \left(c_0 + \varsigma\right)^{-1}}{c_0 - 2\varsigma + 2\varsigma z_0^{-1} L - c_0^3 \left(c_0 + \varsigma\right)^{-2}} \tag{4.29}$$

$$H_2 = -\frac{\eta_0 H z_0}{\left(c_0 + \varsigma\right)\varsigma} - \frac{\eta_0 H_1 z_0}{2\rho \left(c_0 + \varsigma\right)^2 \varsigma} \quad , \quad H_3 = \frac{A\eta_0}{c_0^2} + \frac{\eta_0 H_1}{\rho c_0^3} \quad , \quad H_4 = -H_3 L \tag{4.30}$$

The analytical velocity field for a moving slider is given in Eq. (3.43). The pressure and velocity fields (normalized by $\hat{p} = \varsigma^2 \eta^{-1} \tilde{U}^{-1} L^{-1}$ and $\tilde{U}$ respectively) are shown in Fig. 4.17. The recirculation zone can clearly be distinguished and the pressure profile matches the analytical solution. The temperature field is normalized as $\overline{\theta} = \frac{\varsigma^2 \rho_0 c_p}{\eta_0 \cdot \dot{s}^2 t''} \theta$, where t'' is a characteristic time, chosen as 1s. The normalization value of the temperature field corresponds to the temperature raise from the reference temperature in 1s for characteristic frictional energy generated through shear motion at a velocity $\dot{s}$. For constant lubricant properties, and by ignoring compressive heating, the steady state energy equation in the lubricant film domain is given in Eq. (3.50). The analytical and numerical solutions of the temperature field are shown in Fig. 4.18. Although the pressure, velocity and temperature fields are validated, it is only through the comparison of the hydrodynamically generated loads that the numerical model is truly validated. By defining $\overline{c_0} = c_0/\varsigma$, the analytical normalized radial load $\overline{w_y}$ and the tangential load component are given in [114] as:

$$\overline{w_y} \cdot \frac{\hat{p}}{L} = 6\ln\left(\frac{1 + \overline{c_0}}{\overline{c_0}}\right) - \frac{12}{1 + 2\overline{c_0}} \quad , \quad \overline{w_z}|_{y=c} \cdot \frac{\hat{p}}{\varsigma} = \overline{w_y} \cdot \frac{\hat{p}}{L} \tag{4.31}$$

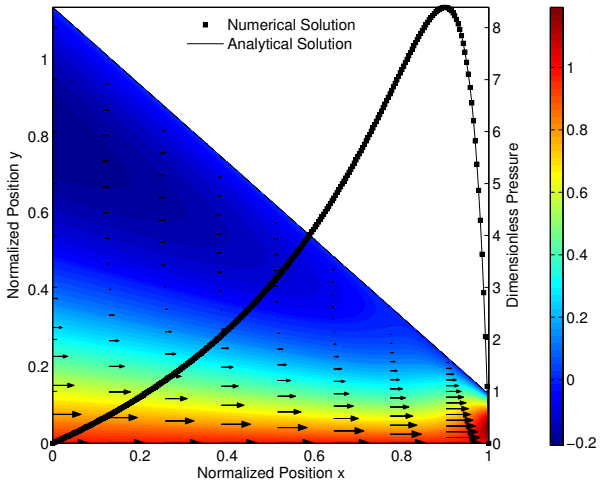

Figure 4.17: Normalized pressure and velocity fields (numerical and analytical solutions).

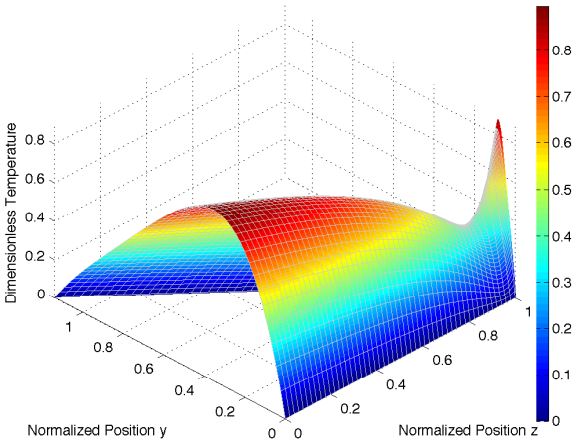

Figure 4.18: Normalized temperature field. Numerical solution (mesh) and analytical solution (surface).

The shear forces on the slider and on the bearing are given in [114] as:

$$\overline{w_z'}\big|_{y=0} \cdot \frac{\hat{p}}{\varsigma} = 4\ln\left(\frac{\overline{c_0}}{1+\overline{c_0}}\right) + \frac{6}{1+2\overline{c_0}} \quad , \quad \overline{w_z'}\big|_{y=c} \cdot \frac{\hat{p}}{\varsigma} = 2\ln\left(\frac{\overline{c_0}}{1+\overline{c_0}}\right) + \frac{6}{1+2\overline{c_0}} \tag{4.32}$$

The friction coefficient is the ratio of the tangential and shear forces over the applied radial load and is given analytically in [114] as:

$$\mu = \frac{2\varsigma \ln\overline{c_0} - 2\varsigma \ln\left(1+\overline{c_0}\right) + 3\varsigma\left(1+2\overline{c_0}\right)^{-1}}{3L\ln\overline{c_0} - 3L\ln\left(1+\overline{c_0}\right) + 6L\left(1+2\overline{c_0}\right)^{-1}} \tag{4.33}$$

The normalized forces as well as the friction coefficient are shown in Table 4.6, validating the numerical code.

Quantity	**Symbol**	**Code**	**Theory**	**Absolute Error**
Normalized radial load	$\overline{w_y}\big\|_{y=0}$	3.538	3.540	0.06%
Normalized tangential load	$\overline{w_z}\big\|_{y=0}$	3.566	3.538	0.79%
Normalized slider shear force	$\overline{w_z'}\big\|_{y=0}$	-3.923	-3.956	0.84%
Friction coefficient	$\mu \cdot 1/1000$	5.877	5.851	0.47%

Table 4.6: Normalized hydrodynamic loads and absolute error.

4.6.3 Experimental Validation - Rotational Motion

In addition to the analytical validation, an experimental validation is performed. For the application of a LG slider bearing, no data exist that can be used for validation. Instead, the numerical code is validated against experimental data available in the literature for isothermal oil-lubricated bearings in rotational motion.

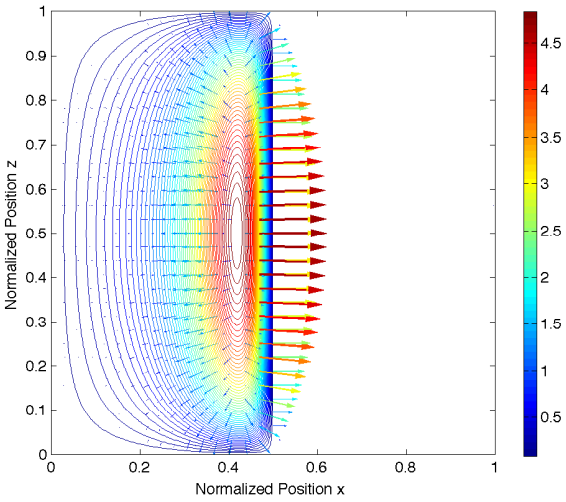

Figure 4.19: Hydrodynamic pressure profile (oil, $e/c_0 = 0.7$).

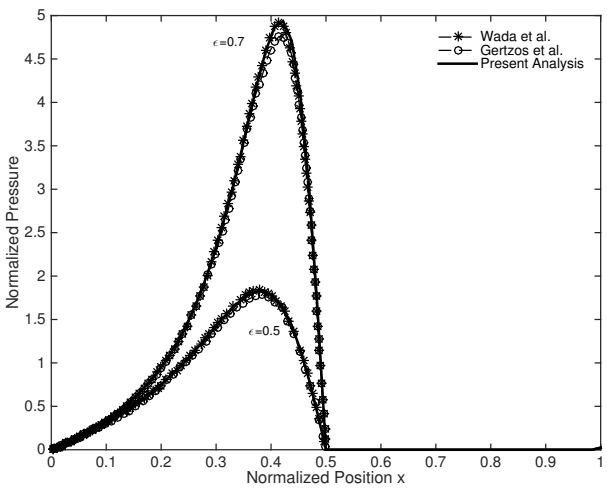

Figure 4.20: Hydrodynamic pressure at the center line of the bearing (oil, $\overline{z} = 0.5$) [60, 82].

The generated hydrodynamic pressure, normalized with $\hat{p} = \frac{c_0^2}{\eta_0 \omega_c R_c^2}$, is shown in Fig 4.19. Clearly, the lubricant cavitates for $\overline{x} \geq 0.5$. By ignoring side effects, the pressure profile at $\overline{z} = 0.5$ is shown in Fig. 4.20 and compared to existing data from [60, 82]. A very close match is found, validating the numerical code.

4.7 Comprehensive Results

The results of the comprehensive model include the structural deformation, structural temperature and fluid quantities such as the hydrodynamic pressure, the shear stress and the temperature within the lubrication gap. All the coupled simulations were performed on a dual 6-core computer (12x3.47GHz, 48GB RAM), but only a single core has been used to perform the numerical iterations to solve the governing equations of the TTT, and 8 cores (and a GPU) were used for the iterations to reach structural equilibrium. The nonstructural simulations have been obtained using a quad-core machine (4x2.7GHz) with 16GB of RAM. All the results are obtained on Grid 4 ($\varpi = 7$), as explained in Section 4.5. Although no external load is applied ($\mathbf{f} = 0$), the case of an eccentric piston is studied for both rigid and flexible structural components. The eccentricity is such that $e_x/\varsigma = 0.09$ and $e_y/\varsigma = 0$, yielding an eccentricity angle $\phi_e = \pi$. The ratio governing the normalization of the lubrication gap is given as $c_0/\varsigma = 0.3165$. The relative thrust portion is located at $z_0/L = 0.4$. The reference temperature is fixed at $\theta_0 = 273.15$K and, for the rigid and isothermal structure case, the boundary temperature is set as $\theta_{bc} = 293.15$K. The rigid and isothermal cases are of major importance to the understanding of the lubrication mechanism and the fundamental differences between oil- and grease-lubricated slider bearings.

4.7.1 Numerical Details of Results

The convergence graphs of the last iteration of the two coupled simulations for oil- and grease-lubricated LG slider bearings are shown in Fig. 4.21 and Fig. 4.22. As shown in Fig. 4.21, global

convergence of the governing equations for oil is reached after 3 global iterations, whereas for grease, global convergence is only achieved after 9 iterations. For both cases, the characteristic linear convergence of the 2D-MG solver can be seen. In addition, convergence accelerates over the course of the iteration procedure, as fewer and fewer V-cycles are necessary in order to obtain convergence.

For oil, the global error is reduced quickly, once the 2D-MG solver has converged once. However, for grease, the global error increases after the first iteration. This is primarily due to the fact that after the detection of the TT spaces, the factors of the TTR equation are updated, hence modifying the PDE. The global error is not reduced linearly, but reduces only slowly until close to the final solution, when the error suddenly drops below the convergence threshold. This behavior is typical for the numerical model. The details of the key numerical simulations (solution Sets 1-12) performed are shown in Table 4.7.

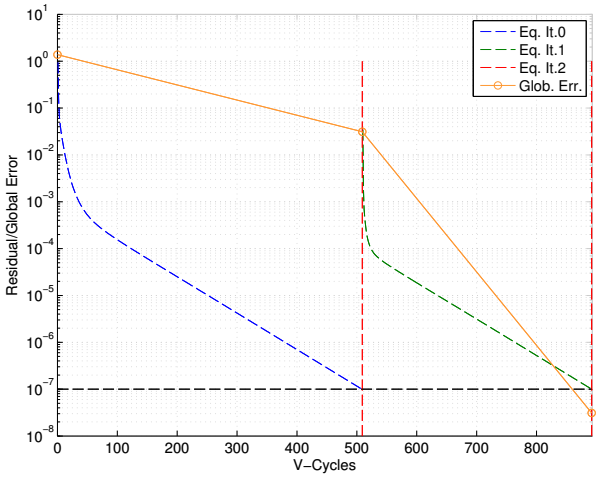

Figure 4.21: Structural iteration 3/3 - convergence history (oil, Set 3).

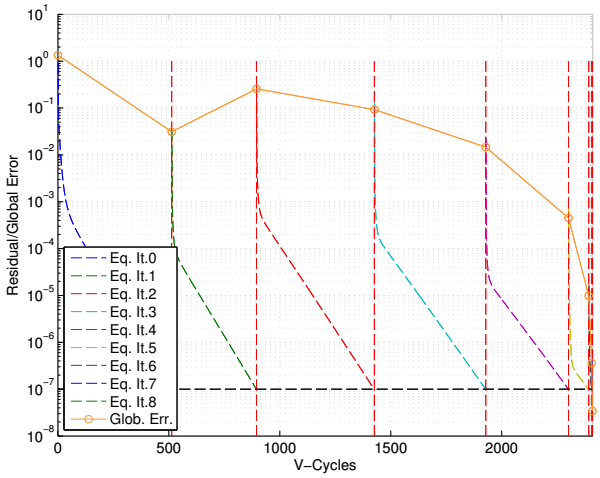

Figure 4.22: Structural iteration 3/3 - convergence history (grease, Set 4).

As indicated in Section 4.5, the total solution times for simulations with grease are higher than for oil. In addition, the solution time is much longer due to the taking into account of the structural behavior (FSI). The increased solution times are an indication of the structural simulation being a bottleneck for slider bearing simulations. As the structural solver and the fluid solver share the same memory, the difference in solution time is essentially due to the different scaling of the solvers for the structural and fluid equations. For all 12 solution sets, the number of V-cycles is similar at the first iterations for both pressure and temperature fields.

It has been found, however, that the coupled FSI simulations show a slightly higher number of V-cycles for the first iterations, as the mapping of the FSI quantities modifies the coefficients of the TTR equation. It is remarkable that the friction coefficient is similar for both oil and grease under isothermal and isoviscous conditions (solution Sets 1-4 and 9-12). This is primarily due to the fact that during the (instantaneous) steady state, the temperature increase does not have a significant effect on the viscosity, and consequently on the friction coefficient. Nevertheless, the friction coefficient is very different for oil- and grease-lubricated bearings, which is due to

the presence of a plug space. It is remarkable that the plug space, which reduces the clearance, has such a high impact on the friction coefficient[3]. The results of the friction coefficients shown in Table 4.7 demonstrate that the TTT is essential for capturing the nonhomogeneous behavior of grease.

Set	Lubricant	FSI	$\eta = \eta_0$	$\theta = \theta_0$	# Glob. Iter.*	Solut. Time [s]	$\mu \cdot 1/1000$ **
1	oil	no	yes	no	3	31.29	6.43
2	grease	no	yes	no	15	2532.10	11.97
3	oil	yes	yes	no	3+3+3	1339.00	6.94
4	grease	yes	yes	no	9+9+9	7209.00	10.32
5	oil	no	no	no	4	123.58	6.38
6	grease	no	no	no	20	3961.14	11.97
7	oil	yes	no	no	4+4+5	1726.00	6.95
8	grease	yes	no	no	20+20+20	13755.00	10.42
9	oil	no	yes	yes	3	8.84	6.42
10	grease	no	yes	yes	15	2552.80	11.97
11	oil	yes	yes	yes	2+2	690.00	7.00
12	grease	yes	yes	yes	10+15	5135.00	14.33

Table 4.7: Solution summary for select solution sets ($\varpi = 7$). * Number of fluid iterations at each structural iteration. ** Last structural iteration.

The simulations for an isothermal and nonisoviscous lubricant are not shown, as the effect of increased pressure on the viscosity is not of particular interest to the study at hand. The set that best simulates the actual situation of an aircraft LG slider bearing is Set 8, but the solution time is long. This is essentially due to a stagnation of the residual global error for very tight convergence criteria.

4.7.2 Rigid and Isothermal Structure (Oil and Grease)

Isoviscous Oil-lubricated Bearing (Set 1)

As the hydrodynamic behavior of grease is derived from the behavior of the base oil, the isoviscous behavior of oil is of major interest to the understanding of the flow patterns that are guided by the hydrodynamic pressure field shown in Fig. 4.23. The pressure isolines are perpendicular to the streamlines, which demonstrates that oil is escaping the high pressure zone while lift is generated through the motion of the piston surface. The pressure peak is located at the relative position of the thrust portion z_0 and shifted by the eccentricity angle $\phi_e/(2\pi)$ along the circumference. The norm of the pressure gradient, which is a measure of the driving force behind the fluid flow and which indicates the concentration of the pressure force, is shown in Fig. 4.24. In addition, the pressure force varies most for $\overline{z} < \overline{z_0}$, which is an indication of a different flow behavior at the thrust portion. The norm of the velocity field for the case of a piston sliding in vertical motion only is shown in Fig. 4.25. The stationary (bearing) and sliding (piston) contacting surfaces are visible.

[3]Seemingly different data for the friction coefficient have been reported in [51] in the context of a noneccentric piston.

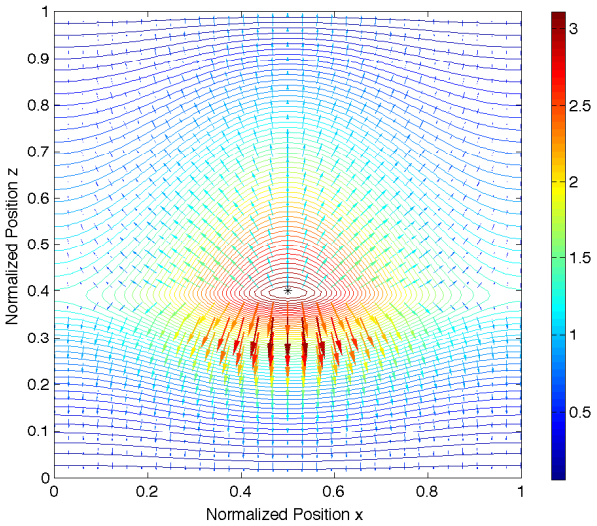

Figure 4.23: Hydrodynamic fluid pressure $\overline{p}$.

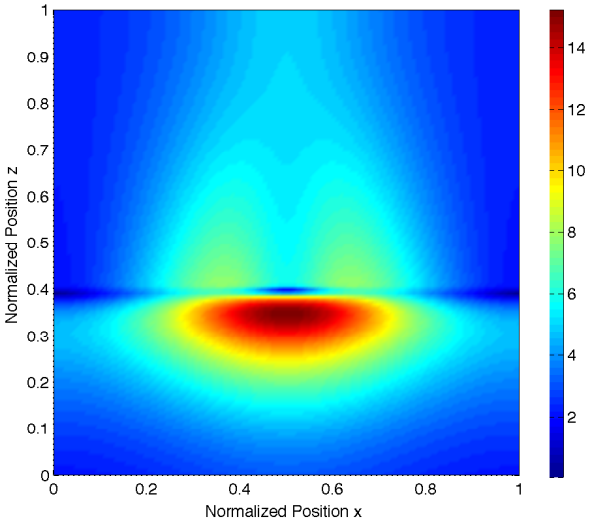

Figure 4.24: Pressure gradient norm $|\boldsymbol{\nabla}\overline{p}|$.

The velocity at the thrust portion is low (and even drops to zero), and a recirculation zone can be distinguished. The shear stress field, normalized by $\overline{\tau} = \frac{c_0\tau}{\eta_0\tilde{U}}$, is shown in Fig. 4.26, and the cross-sections across the lubrication gap are shown in the sub-figures A-I. The shear stress, which can be understood as proportional to the frictional heat generation term, is highest at the moving surface (piston) for $\overline{z} < \overline{z_0}$ and highest at the stationary bearing surface for $\overline{z} > \overline{z_0}$. Sub-figures E-I indicate a notable observation (region for $y > 0.5c$): the shear stress is very low in this region and the formation of a plug space (for grease) is likely. In order to understand the fluid flow behavior and the cause of the shear stress variations, it is instructive to analyze the normalized components of the velocity gradient.

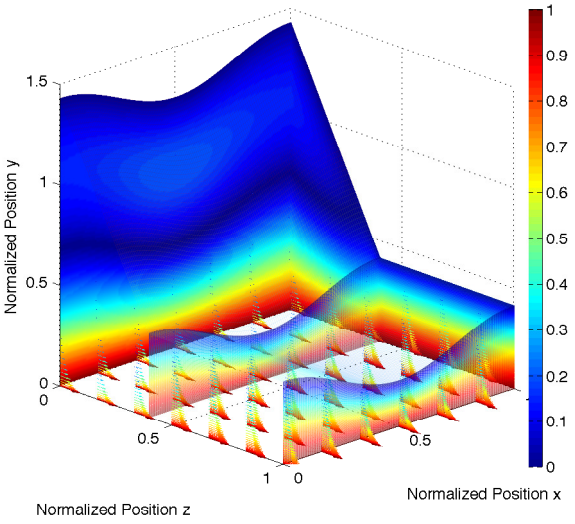

Figure 4.25: Fluid film velocity field $\overline{\mathbf{v}}$ (oil).

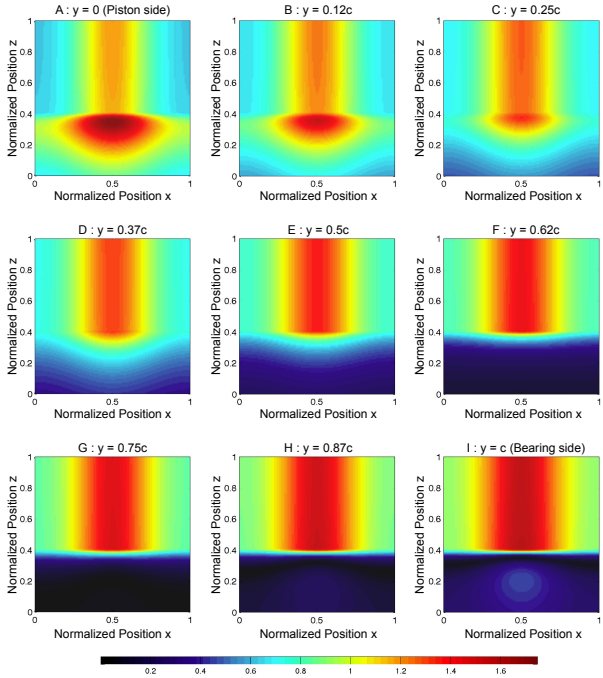

Figure 4.26: Shear stress field $\overline{\tau}$ across the lubrication gap (oil).

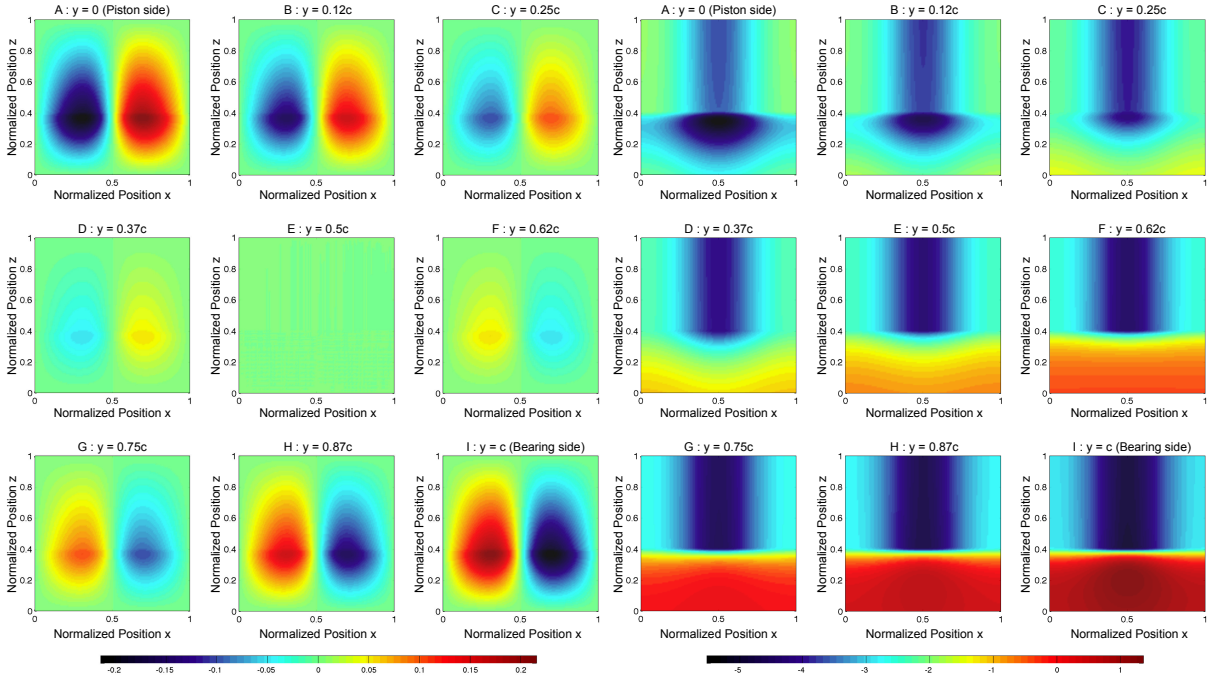

Figure 4.27: Normalized circumferential component of velocity gradient $\overline{v}_{\overline{x},\overline{y}}$.

Figure 4.28: Normalized vertical component of velocity gradient $\overline{v}_{\overline{z},\overline{y}}$.

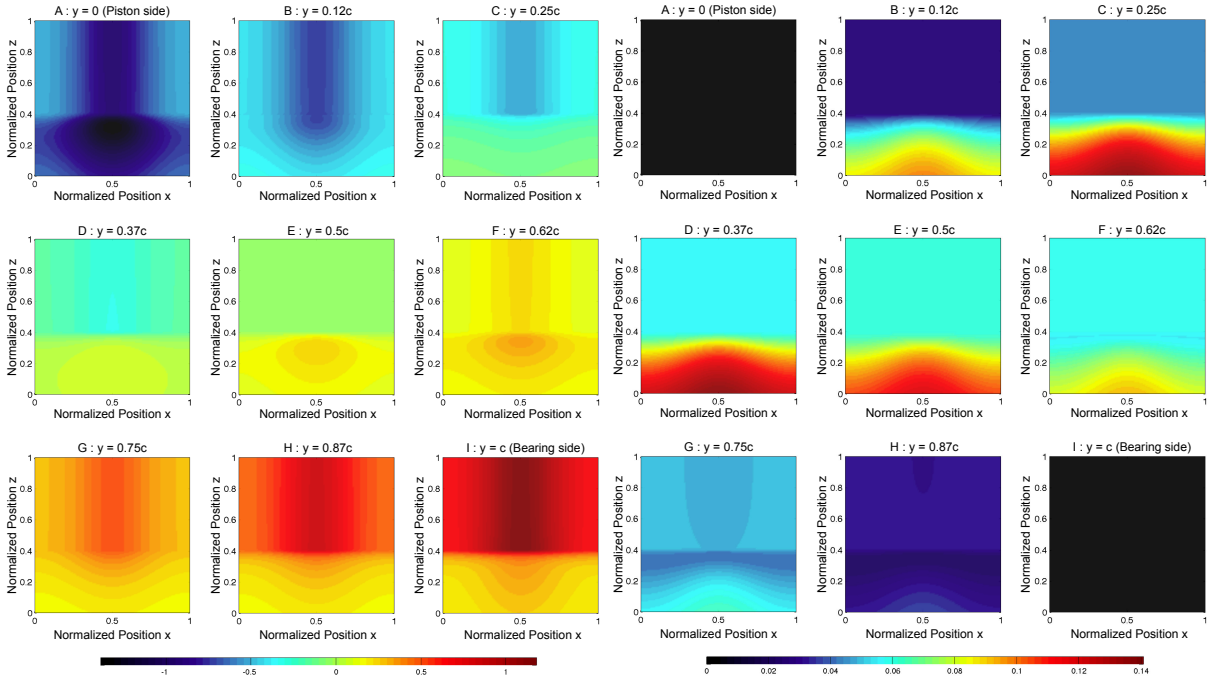

Figure 4.29: $\overline{q}_{\overline{y}}$ across the lubrication gap.

Figure 4.30: $\overline{\theta}$ across the lubrication gap.

At the thrust portion, the shear stress field is practically constant along the circumference of the bearing, which is the result of the vertical motion of the piston (see Fig. 4.28). The circumferential variations of the shear stress are due to the shearing of the lubricant caused by the lubricant escaping from the area of highest pressure, as shown in Fig. 4.27. An interesting observation is that on the piston side, the velocity variation is opposite to the velocity variation

on the bearing side, which suggests that a shell (for grease) might exist. The formation a plug space is most likely (for grease) at the thrust portion where the dominant component $\overline{v}_{\overline{z},\overline{y}}$ is zero.

The normalized temperature field $\overline{\theta}$ is shown in Fig. 4.30. At the piston and bearing surfaces, the temperature is uniform and fixed at $\overline{\theta} = 0$. The highest temperature does not occur at the mid-plane of the lubrication gap; rather the temperature is almost uniform along the circumference of the bearing, which is due to the sliding motion of the piston (no significant heat generated along x). It must be noted that the amount of heat generated and the incremental temperature for the case of a rigid and isothermal structure are not very high. This is due to the fact that the temperature at the contacting surfaces is fixed. The case of isothermal contacting surfaces is of interest especially for an FSI case (nonisothermal and flexible structure), as the temperature values from the contacting surfaces are input to the TEHD code. The heat flux is normalized by $q = q_0\overline{q}$, where q_0 is given by $q_0 = \lambda_{\theta 0}\varsigma^{-1}\left(\theta_{bc} - \theta^0\right)$. The predominant component of the heat flux vector field is across the lubrication gap $q_y = -\lambda_\theta \theta_{,y}$, and is shown in Fig. 4.29. The heat flux field is almost symmetric across the lubrication gap. At the piston surface, the heat flux is negative, whereas on the bearing side, the heat flux is positive. The magnitude of the heat flux at both contacting surfaces is not equal (higher at the piston surface) [51]. At the mid-plane of the lubrication gap, the heat flux does not vanish, which is an indication that the maximum temperature, contrary to common belief, does not occur at the mid-plane.

Isoviscous Grease-lubricated Bearing (Set 2)

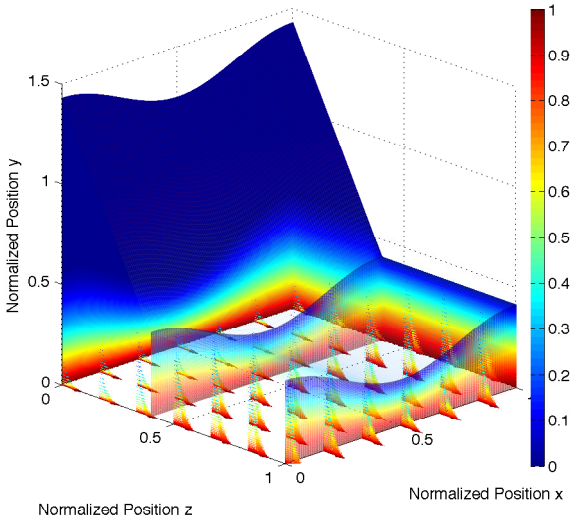

Figure 4.31: Fluid film velocity field $\overline{\mathbf{v}}$ (grease).

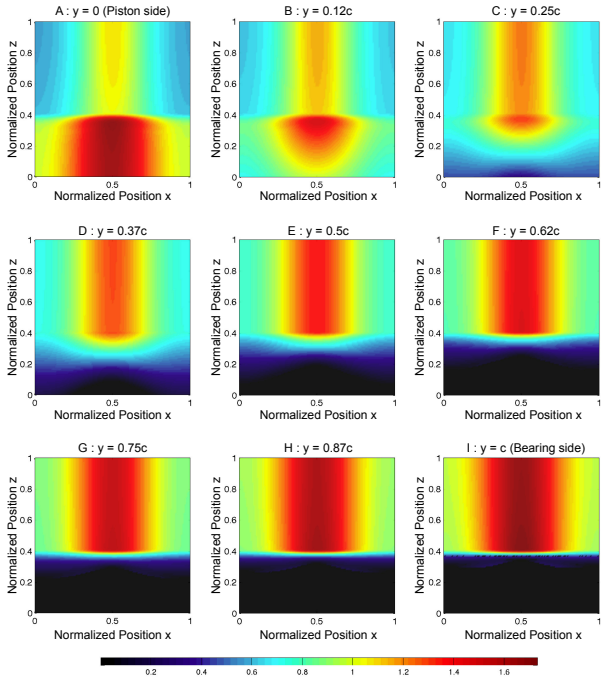

Figure 4.32: Shear stress field $\overline{\tau}$ across the lubrication gap (grease).

Although the peak pressure is higher for the case of grease than for oil, the hydrodynamic pressure field is not shown for the present case, because the shape of the pressure field is similar

to that in Fig. 4.23. The hydrodynamic pressure fields for both oil and grease are compared in Section 4.7.4. The velocity profile for isoviscous grease is shown in Fig. 4.31. At the thrust portion, a plug space is formed, as postulated by the results for oil shown in Section 4.7.2. Within the plug space, the velocity field is zero, as the semisolid plug sticks to the stationary wall (bearing). The shear stress τ is a function of the gradient of the velocity field. The normalized components of $\boldsymbol{\nabla}\overline{\mathbf{v}}$ are shown in Fig. 4.33 and Fig. 4.34.

The normalized relative shear stress $\overline{\tau} = \frac{c_0(\tau-\tau_0)}{\eta_0 \tilde{U}}$ is shown in Fig. 4.32. At the thrust portion, the relative shear stress is zero, indicating the presence of a plug space. The heat generation term of the energy equation can also be written as $\eta\dot{\gamma}^2 = \eta^{-1}(\tau-\tau_0)^2$, which indicates that the heat generation can be seen as proportional to the square of the relative shear stress. The plug and the fluid spaces within the lubrication gap are shown in Fig. 4.35, delimited by their respective shells. There are no dry spaces present, as the temperature is not high enough.

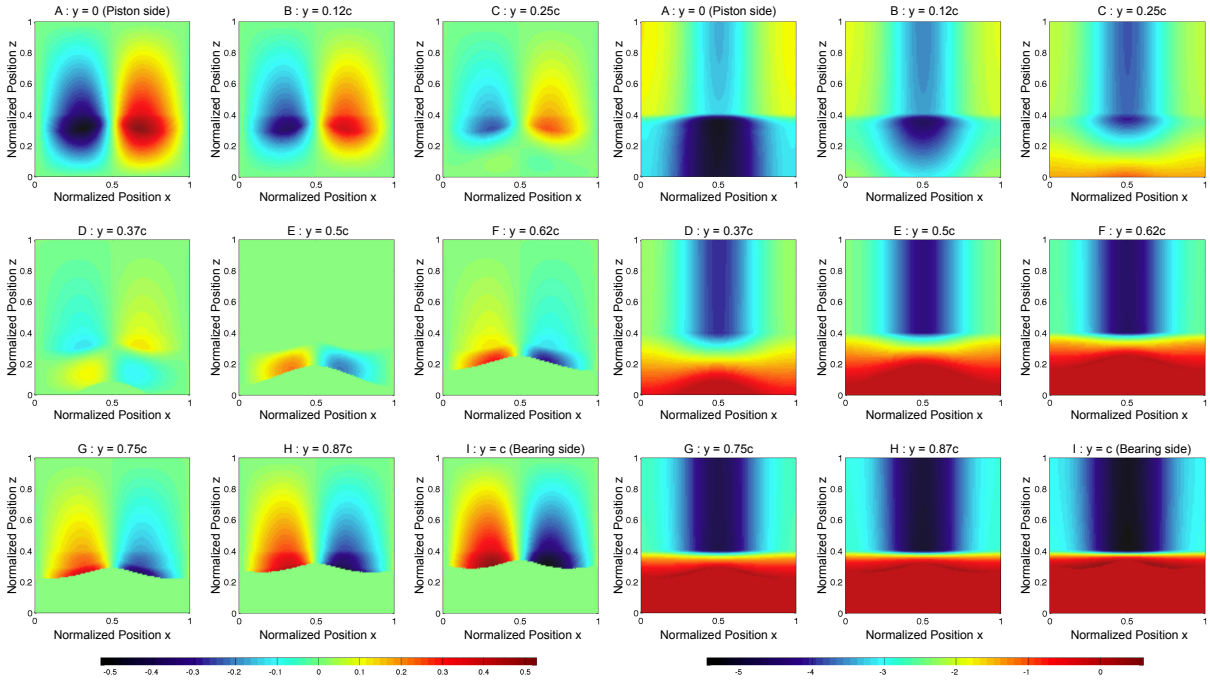

Figure 4.33: Normalized circumferential component of velocity gradient $\overline{v}_{\overline{x},\overline{y}}$.

Figure 4.34: Normalized vertical component of velocity gradient $\overline{v}_{\overline{z},\overline{y}}$.

The thicknesses of the spaces $\mathcal{S}_p^{(1)}$ and $\mathcal{S}_f^{(2)}$ are shown in Fig. 4.36. In addition, the theoretical thickness of the plug space is shown, and a very close match can be observed. In order to illustrate the plug and the fluid spaces within the lubrication gap, a cross-section at $\overline{x} = 0.5$ is shown in Fig. 4.37. The plug space is shown and the calculated shells coincide very well with the predictions of the theory. As a plug space is present, it is of interest to understand the (radial) heat flux, which is shown in Fig. 4.38. The heat is conducted through $\mathcal{S}_p^{(1)}$, despite the fact that no heat is generated within $\mathcal{S}_p^{(1)}$. The heat flux is not uniform along the lubrication gap (contrary to the theory for dry friction). The highest heat flux is at the aft portion of the slider, and almost no heat is input at the location of $\mathcal{S}_p^{(1)}$, which acts as an insulator. For the isothermal case, the maximum heat flux is at the slider, although the highest share of the

heat flows into the bearing surface. The locus of the maximum temperature is highlighted in Fig. 4.38, which confirms that the maximum temperature along the thrust portion of the bearing is not at the center line of the lubrication gap (contrary to the theory for dry friction).

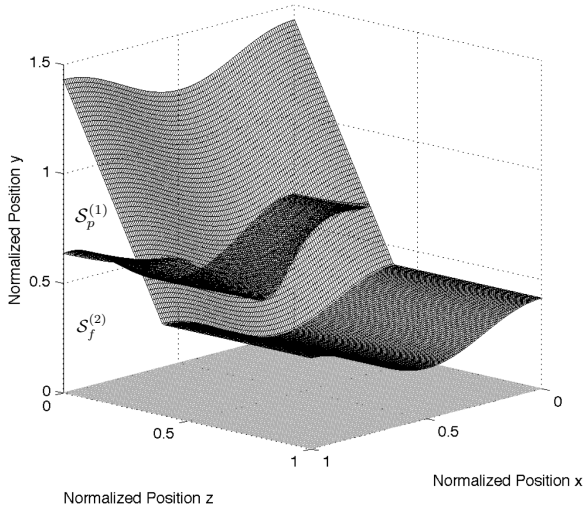

Figure 4.35: Combined shells.

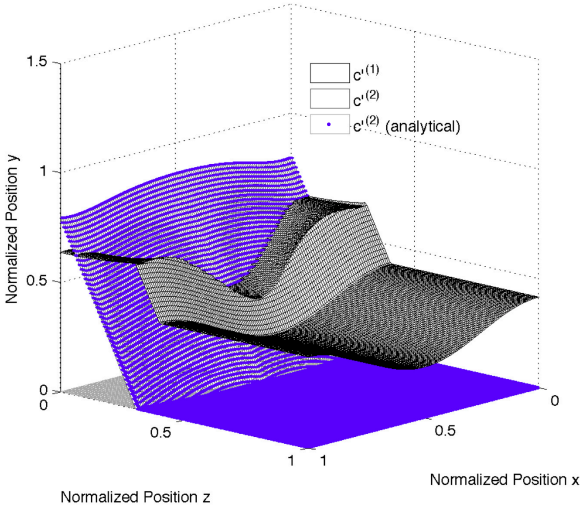

Figure 4.36: Thicknesses of the spaces.

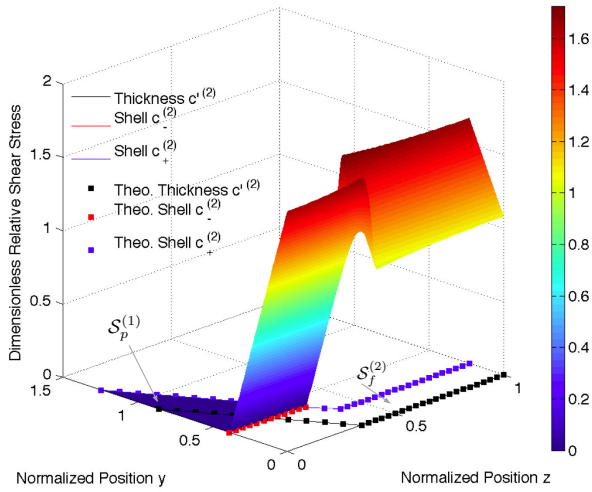

Figure 4.37: $\overline{\tau}$ and cross-sections of shells ($\overline{x} = \overline{x_e}$).

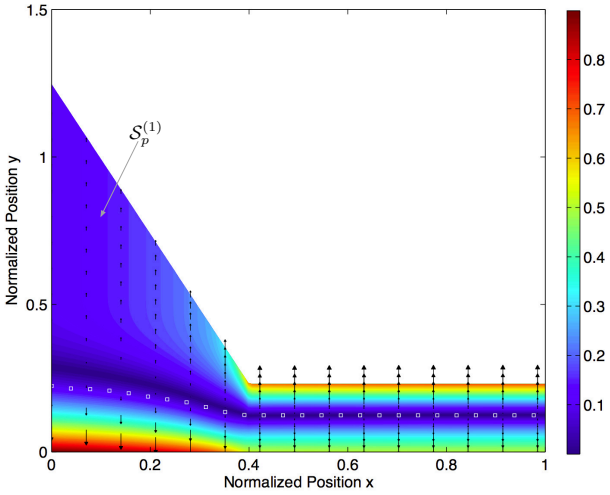

Figure 4.38: $\overline{q}_{\overline{y}}$ and maximum temperature locus ($\overline{x} = \overline{x_e}$).

4.7.3 Flexible, Nonisothermal Structure (Grease, Set 4)

For a LG lower bearing, the structure is not isothermal and the lubricant is not isoviscous, as heat leaves the fluid film and diffuses through the adjacent structure. It is critical to consider full FSI and to take into account the behavior of the fluid and the structure, as the deformation of the lubrication gap yields different pressure and temperature fields. As the structural behavior is similar for oil- and grease- lubricated bearings (see Section 4.7.4), the results for a grease-lubricated bearing only are highlighted. The normalized radial heat flux field is shown in Fig. 4.39. The shape of the heat flux across the lubrication gap is similar, which indicates

that the temperature is almost linearly (asymmetrically) distributed across the lubrication gap. Nevertheless, the heat flux is higher in the region of the highest hydrodynamic pressure, and it is lowest at the thrust portion. This behavior is due to the presence of the plug space as postulated in Section 4.7.2. The normalized temperature field across the lubrication gap is depicted in Fig. 4.40. One important fact is that the temperature is highest on the piston side, and lowest on the bearing side. The temperature is highest around ϕ_e across the lubrication gap. This temperature profile is characteristic for the LG lower slider bearing, as the inner side of the piston is adiabatic, whereas the structure on the bearing side is surrounded by external air, and the heat is removed by convection ($\overline{h_5} = 50\text{W}/(\text{m}^2\text{K})$). On the piston side, the heat that is input stagnates, and diffuses slowly along the circumference (wide temperature band).

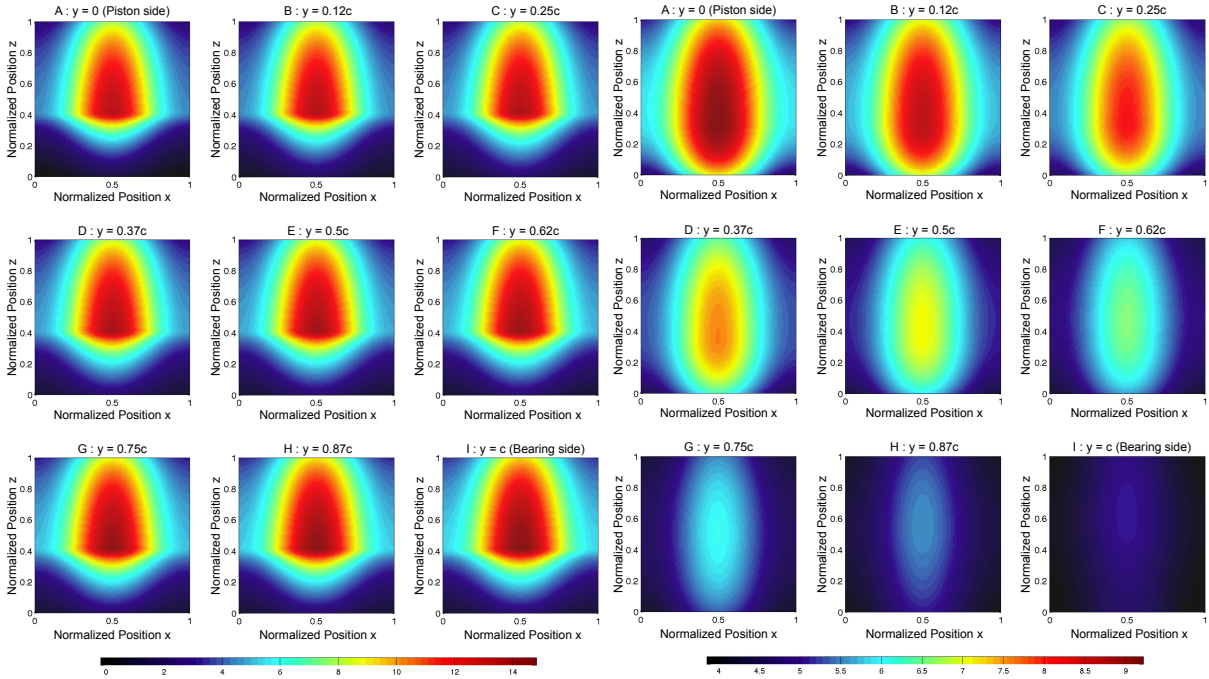

Figure 4.39: Normalized heat flux field across the lubrication gap (grease).

Figure 4.40: Normalized temperature field $\overline{\theta}$ across the lubrication gap (grease).

However, as the heat at the lower bearing diffuses radially and quickly through the structure, the heat does not diffuse significantly in the circumferential direction (narrow temperature band). Unexplained uneven damage has been reported on both surfaces. An asymmetrically distributed temperature field is likely responsible for the reported damage. All structural and fluid quantities are normalized with the same factors. The normalized structural heat flux vector field is shown in Fig. 4.41. By displaying the heat flux as a vector field instead of only the scalar component as in Fig. 4.39, the insulating properties of the plug space are visible. In addition, the heat flux is present around the entire circumference, contrary to the Hertzian contact theory, where only a small contact area over which the generated frictional heat is input exists, as shown in Fig. 2.21. For completeness, the structural temperature field of the piston (more specifically the chrome layer) is shown in Fig. 4.42, which suggests that the phenomenon is very localized and indicates a similar axial thermal behavior as shown in Fig. 2.20.

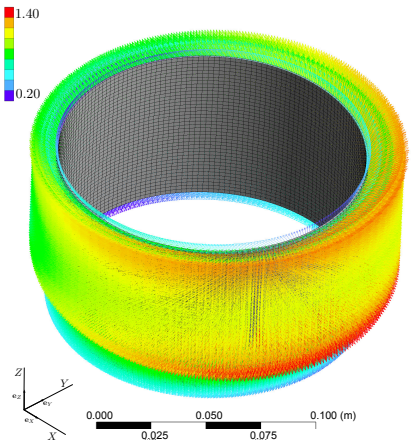

Figure 4.41: Normalized structural heat flux field at the lower bearing.

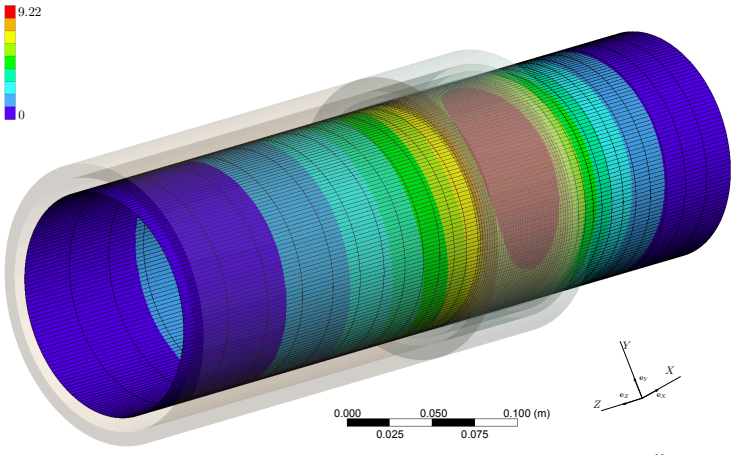

Figure 4.42: Normalized structural temperature field at the piston.

The normalized temperature field of the lower bearing inset is shown in Fig. 4.43. The temperature field is highest at the aft portion of the bearing (positive X direction), as the applied hydrodynamic pressure is highest at this point. The normalized shear stress field $\overline{\tau}_{r\phi}$ is a result of the generated friction forces and the applied fluid pressure, and is shown in Fig. 4.44. The shear stress is lowest for negative ϕ and highest for positive ϕ, which is an indication of the lubricant *escaping* the high pressure zone.

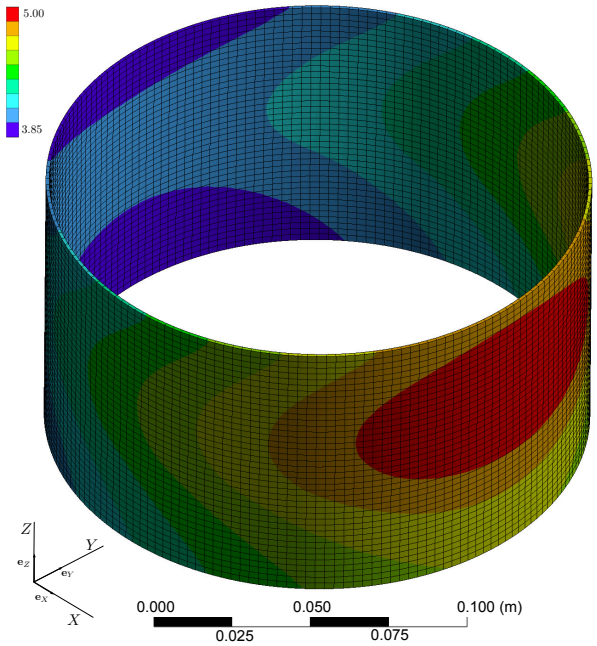

Figure 4.43: Normalized structural temperature field at the lower bearing.

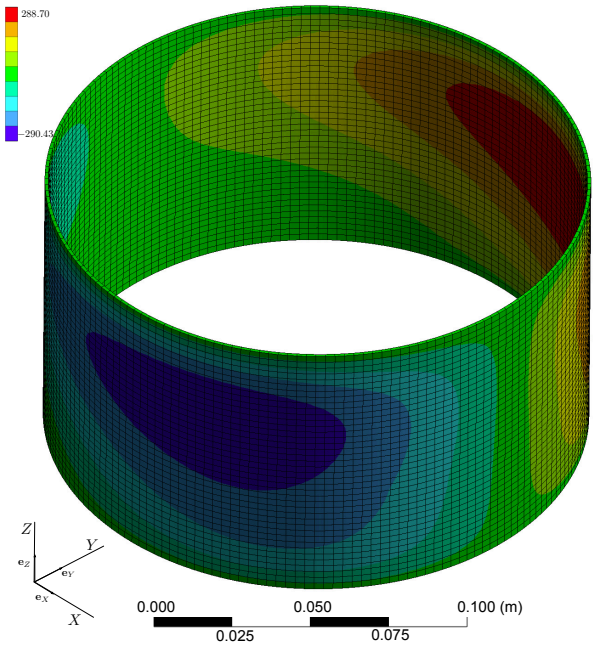

Figure 4.44: Normalized structural shear stress field $\tau_{\phi z}$ at the lower bearing.

The shear stress, however, vanishes at the aft and fore portions of the lower bearing, which is an indication of high and low pressure zones. The structural deformation plays an important role in the performance of the lubrication mechanism, as the clearance c between the piston and the

bearing is a driving parameter in the TEHD solution. The maximum of the total displacement $u = \sqrt{u_r^2 + u_\phi^2 + u_Z^2}$ occurs at the aft portion of the bearing, as shown in Fig. 4.45d. All displacement components of the lower bearing inset are normalized by $\max(u)$. The normalized radial displacement $\overline{u}_r$ of Fig. 4.45a indicates that the aft portion of the bearing is deformed more than the fore portion, but the largest radial displacement occurs at the lower end of the bearing. The normalized circumferential displacement $\overline{u}_\phi$ is positive in the $Y-$ direction and negative in the $Y+$ direction, which indicates an ovalization of the lower bearing inset (not taken into account in Chapter 2). The normalized vertical displacement $\overline{u}_Z$, although not as high as $\overline{u}_r$ or $\overline{u}_\phi$, indicates that the bearing is squeezed vertically, which is a consequence of the shearing of the lubricant. The impact of the displacement field on the clearance and behavior of the lubricant is shown in Section 4.7.4.

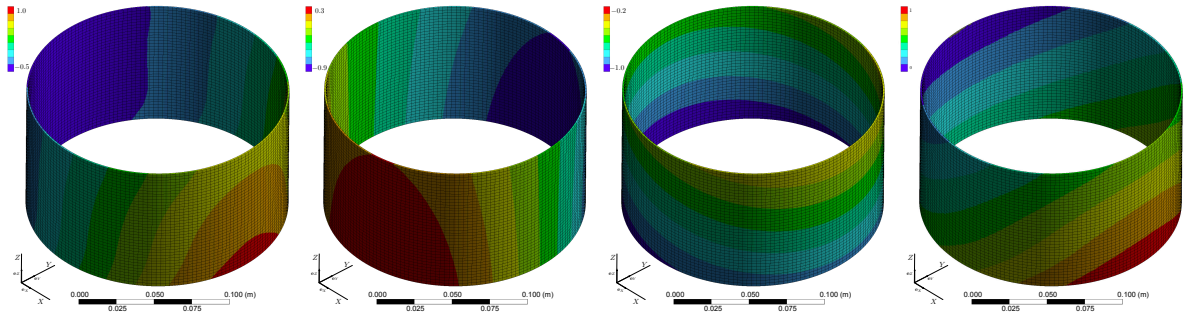

(a) Radial $\overline{u}_r$. (b) Circumfer. $\overline{u}_\phi$. (c) Vertical $\overline{u}_Z$. (d) Total $\overline{u}$.

Figure 4.45: Normalized displacement field of the lower bearing inset.

4.7.4 Comparison Cases

In order to study the impact of the structural behavior as well as the impact of a different lubricant, two comparison studies are performed.

The first study aims to compare the behavior of the lubricant (hydrodynamic pressure and shear stress) when surrounded by a flexible and nonisothermal structure to the behavior of the lubricant in a rigid and isothermal bearing assembly. This comparison study is important for understanding the effect of the structure (especially the deformation) on the lubrication mechanism. The goal of the second study is to understand the impact of the type of lubricant (oil or grease) for both rigid (and isothermal) and flexible (and nonisothermal) structures. This comparison study demonstrates that the TTT developed in Chapter 3 is key to the fundamental understanding of the lubrication mechanism, especially with the presence of a plug space.

Several solution sets from Section 4.7.1 are compared, and the normalized absolute difference of two sets is shown. For example, any physical quantity f (but not the clearance) of solution sets a and b are denoted as $f^{[a]}$ and $f^{[b]}$ respectively. The normalized absolute difference is: $\delta\overline{f}^{[b-a]} = \frac{f^{[b]} - f^{[a]}}{\hat{f}^{[a]}}$, where $\hat{f}^{[a]}$ is the normalizing value of $f^{[a]}$. For the clearance, the relative difference of $c^{[b]}$ to the undeformed clearance $c^{[a]}$ is equivalent to the Cauchy strain, and is defined as $\varepsilon^{[b-a]} = \frac{c^{[b]} - c^{[a]}}{c^{[a]}}$, expressed as a percentage.

Rigid, Isothermal Structure versus Flexible, Nonisothermal Structure

In order to draw a conclusion on the difference between the behavior of the fluid surrounded by a rigid and isothermal structure and that surrounded by a flexible and nonisothermal structure for both oil [7-5] and grease [8-6], the normalized absolute difference of the hydrodynamic pressure $\delta\overline{p}$ governing the fluid flow and the resulting mechanical strain ε are shown in Fig. 4.46. In both cases, the lubricants are nonisoviscous and nonisothermal, and $\delta\overline{p}$ is negative, which indicates a reduction of the hydrodynamic pressure compared to the respective reference case. For both comparison cases, the maximum relative strain occurs at $(\overline{x_e}, \overline{z_0})$, which is the location of the highest pressure. An interesting observation is that the relative shear strain is predominantly positive for $\overline{z} > \overline{z_0}$ and predominantly negative for $\overline{z} < \overline{z_0}$, which is an indication of the nonuniform displacement that is a result of the applied hydrodynamic pressure.

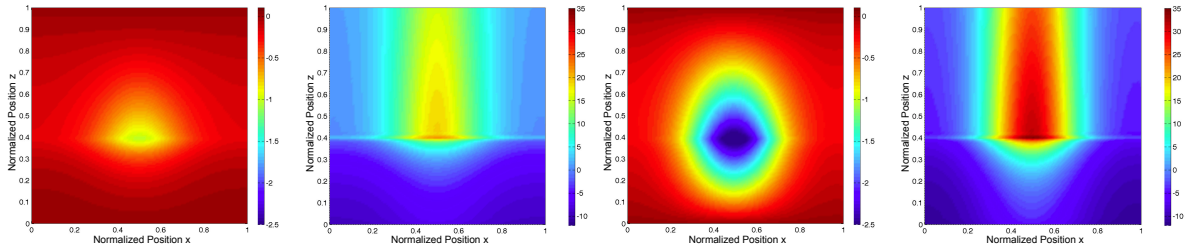

(a) $\delta\overline{p}^{[7-5]}$ (b) $\varepsilon^{[7-5]}$ (c) $\delta\overline{p}^{[8-6]}$ (d) $\varepsilon^{[8-6]}$

Figure 4.46: Comparison of $\delta\overline{p}$ and ε for various solution sets.

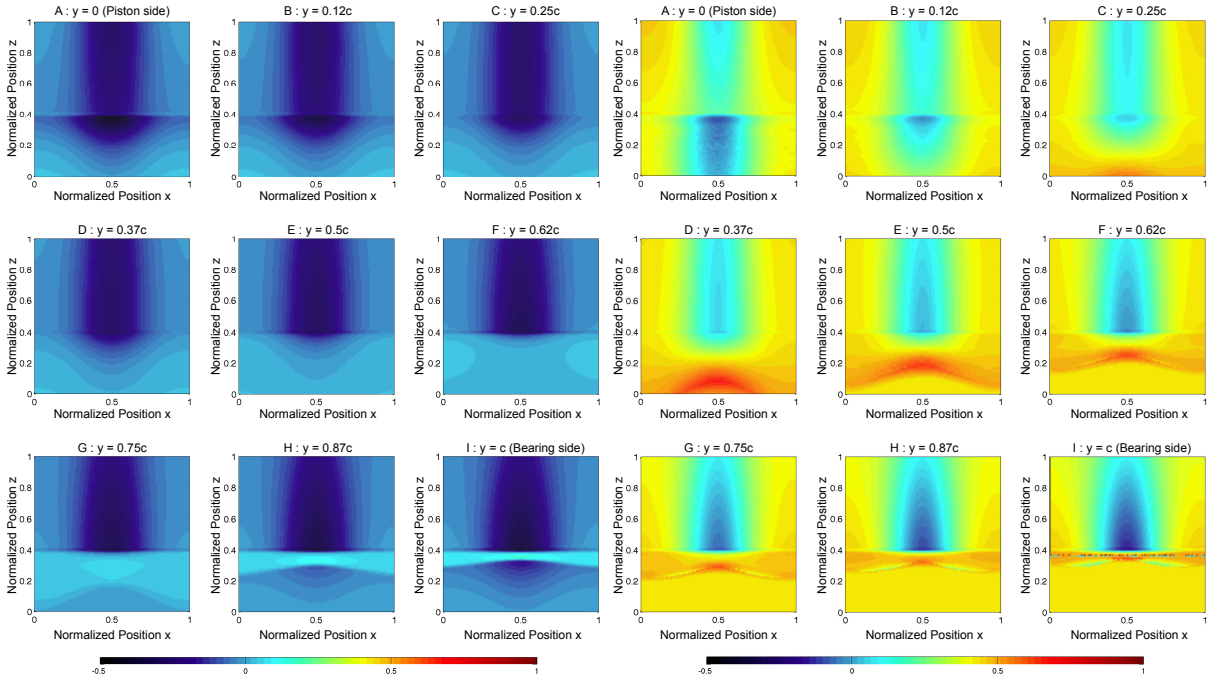

Figure 4.47: Normalized shear stress difference $\delta\overline{\tau}^{[7-5]}$ for an oil-lubricated bearing.

Figure 4.48: Normalized shear stress difference $\delta\overline{\tau}^{[8-6]}$ for a grease-lubricated bearing.

The bearing surface, under applied pressure, deforms and opens up the lubrication gap, which leads to a significant decrease in pressure, especially for grease. The maximum mechanical strain is high for both cases, but especially for grease, which confirms the need for taking into

account the elastic structural deformation. In addition, a particularly critical observation is that the structural deformation is higher for grease than for oil. This observation is studied in more detail in the subsequent comparison case. The normalized shear stress difference for the case of an oil-lubricated bearing is shown in Fig. 4.47, and for the case of a grease-lubricated bearing in Fig. 4.48. For both cases, the shear stress is mostly lower for $\overline{z} > \overline{z_0}$ and greater for $\overline{z} < \overline{z_0}$, which is a consequence of the nonuniform pressure gradient. Nevertheless, the $\delta\overline{\tau}$ is higher for grease than for oil, which is primarily due to the presence of a plug space. In addition, for the case of grease, $\delta\overline{\tau}$ is constant for $\overline{z} < \overline{z_0}$ and $y \geq 0.5c$, and negative for $\overline{z} < \overline{z_0}$ and closer to the piston, which is a direct consequence of the presence of a plug space. As the shear stress is proportional to the heat generation, Fig. 4.48 confirms that an elastic structure has to be taken into account (especially for grease), in order to correctly quantify the heat generation.

Oil- and Grease-lubricated Bearing

As stated previously, the structural deformation is very different for an oil-lubricated bearing than for a grease-lubricated bearing. In order to quantify the differences of the hydrodynamic pressure, the shear stress, and the temperature field for both lubricants, Cases 5 (oil) and 6 (grease) for a rigid and isothermal structure are compared, as well as Cases 7 (oil) and 8 (grease) for a flexible and nonisothermal structure.

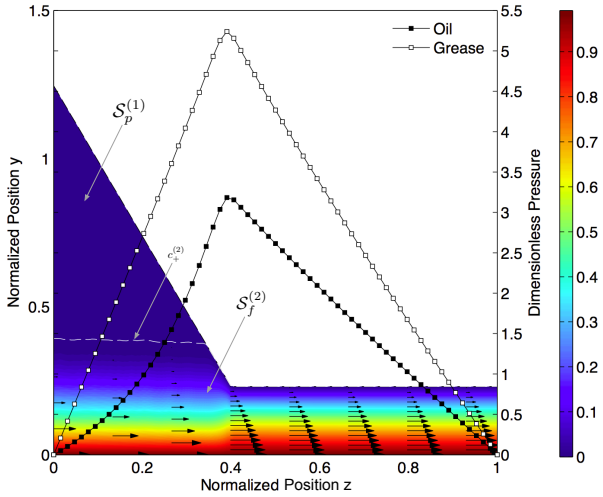

Figure 4.49: Normalized pressure difference $\delta\overline{p}^{[6-5]}$ and grease velocity field (rigid, isothermal, $\overline{x} = \overline{x_e}$).

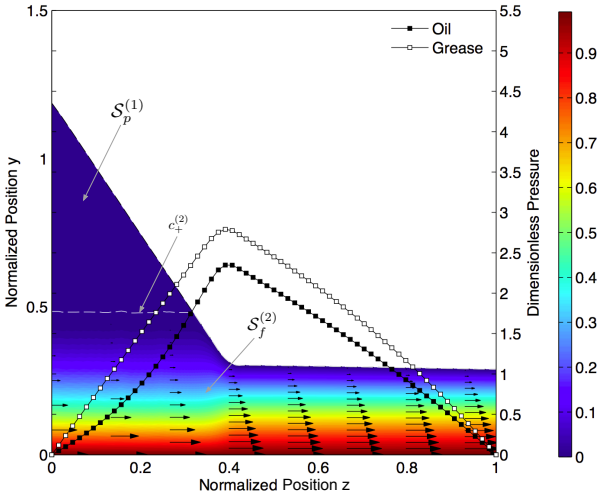

Figure 4.50: Normalized pressure difference $\delta\overline{p}^{[8-7]}$ and grease velocity field (flexible, nonisothermal, $\overline{x} = \overline{x_e}$).

The hydrodynamic pressure fields at $\overline{x} = \overline{x_e} = 0.5$ are shown in Fig. 4.49 and Fig. 4.50. In addition, the velocity field for grease is shown in each figure. The detected plug $\mathcal{S}_p^{(1)}$ and fluid $\mathcal{S}_f^{(2)}$ spaces are indicated, as well as the shell that delimits both spaces, denoted as $c_+^{(2)}$. For each case, the pressure for grease is higher than for oil, and for the cases with a flexible structure, the reduction in the hydrodynamic pressure field can be seen. In addition, $c_+^{(2)}$ is also affected by the deformation of the structure. The plug reduces the clearance between both contacting surfaces, and a notable observation is that the difference in pressure is reduced once the structural deformation is taken into account. The normalized shear stress difference $\delta\overline{\tau}$

between grease and oil for a rigid and isothermal structure is shown in Fig. 4.51, and for a flexible and nonisothermal structure in Fig. 4.52. The shear stress difference $\delta\overline{\tau}$ is highest on the piston side, and is positive for $\overline{z} > \overline{z_0}$.

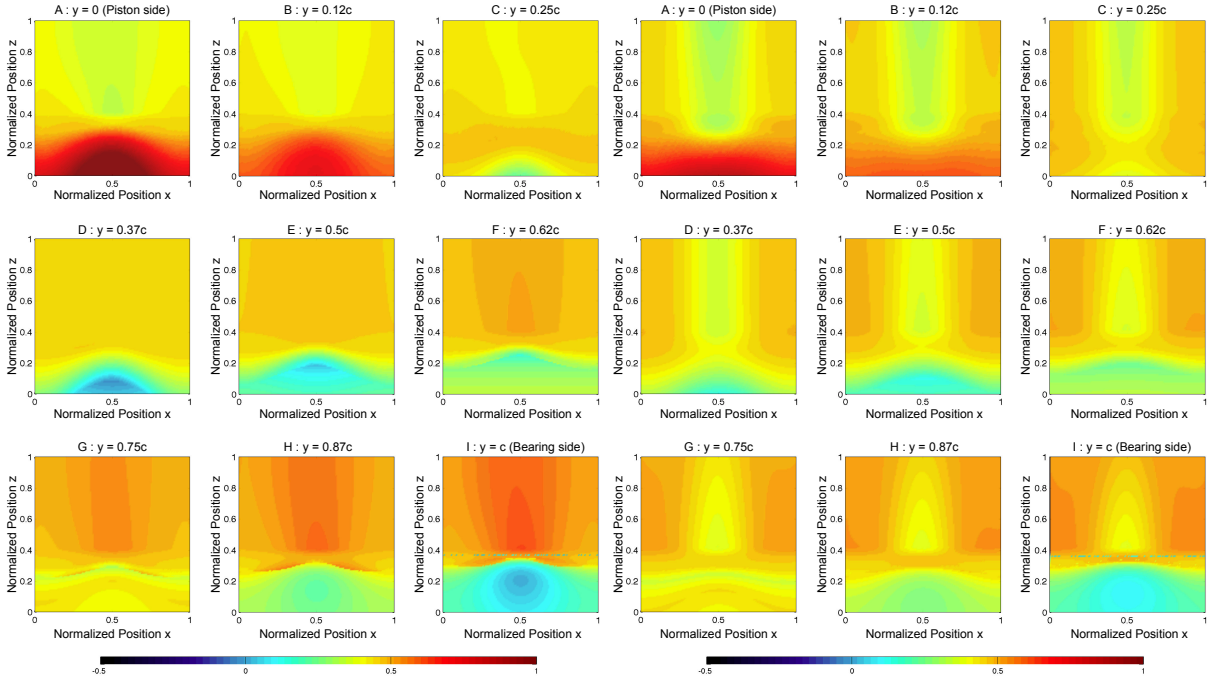

Figure 4.51: Normalized shear stress difference $\delta\overline{\tau}^{[6-5]}$ (rigid, isothermal).

Figure 4.52: Normalized shear stress difference $\delta\overline{\tau}^{[8-7]}$ (flexible, nonisothermal).

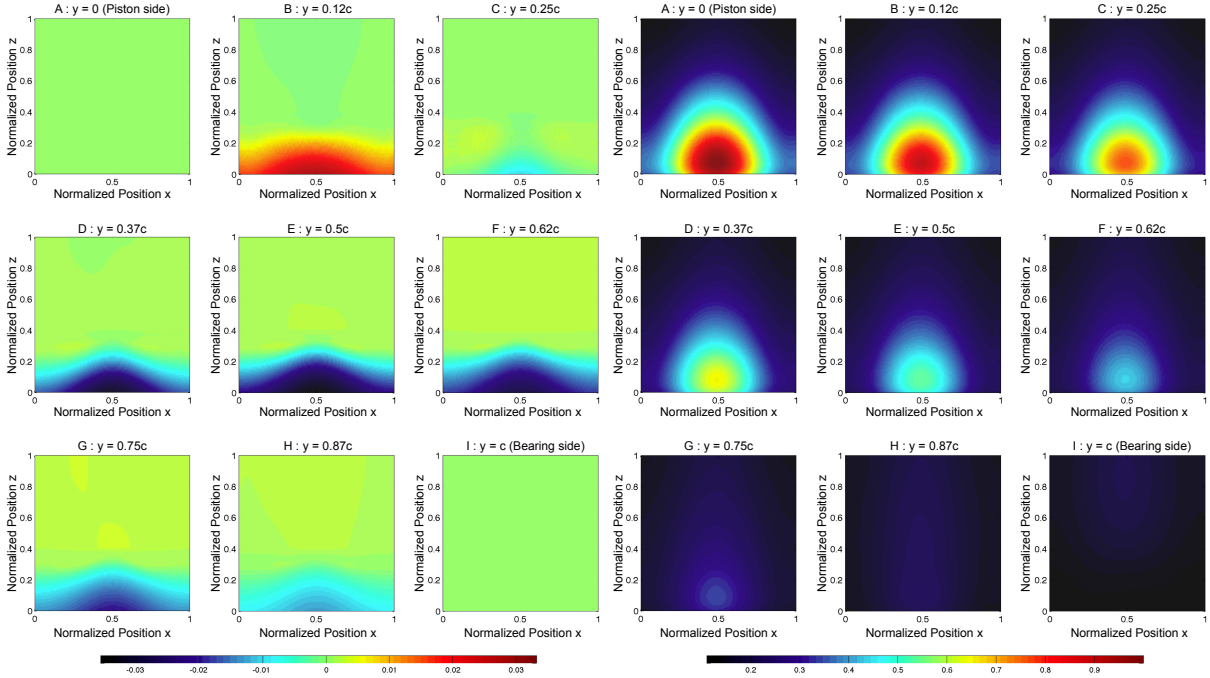

Figure 4.53: Normalized temperature difference $\delta\overline{\theta}^{[6-5]}$ (rigid, isothermal).

Figure 4.54: Normalized temperature difference $\delta\overline{\theta}^{[8-7]}$ (flexible, nonisothermal).

In addition, the shear stress difference $\delta\overline{\tau}$ varies the most for $\overline{z} < \overline{z_0}$. A similar trend is observed if the flexibility of the structure is considered, but the difference, although mostly positive, is less pronounced and more homogeneous. In other words, the shear stress is higher for grease than for oil, which is equivalent to more heat being generated in a grease-lubricated bearing. The heat generation is overpredicted by omitting the structural deformation, especially for a grease-lubricated bearing.

The normalized temperature difference $\delta\overline{\theta}$ is shown in Fig. 4.53 and Fig. 4.54. For the case of a rigid and isothermal structure, the temperature is lower for grease than for oil for $y > 0.25c$, which is attributed to the presence of the plug space. The largest absolute difference, for both cases (rigid and flexible structure), occurs at the thrust portion. Although $\delta\overline{\theta}$ is negative or positive for the case of a rigid and isothermal structure, $\delta\overline{\theta}$ is strictly positive for the case of a flexible and nonisothermal structure. In particular, the temperature is highest at the thrust portion on the piston side. In other words, the temperature is higher for the case of a grease-lubricated bearing than for an oil-lubricated bearing.

4.7.5 Transient Results

The transient results are shown for an oil-lubricated, rigid and isothermal bearing. In previous sections, the results for a steady state regime were highlighted. Although a rigid structure is considered, transient results of a flexible structure would not provide any additional insight to the lubrication mechanism and how to formulate a solution to the reported overheating problems. As stated in Section 4.2, the omission of the inertia of the lubricant allows the consideration of the transient case as a sequence of *instantaneous steady states*, as shown in Fig. 4.55.

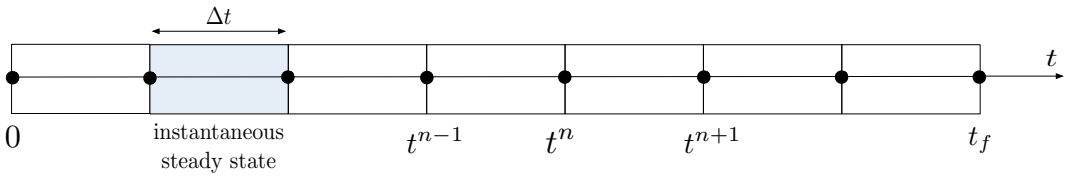

Figure 4.55: Transient regime - sequence of instantaneous steady states.

Each instantaneous steady state converges after the boundary conditions have been applied from the previous converged steady state. As the chosen numerical discretization scheme is implicit (as shown in Section 4.4.3), no conditions on numerical stability have to be considered. For illustration purposes only and in preparation of Chapter 5, the numerical results are shown for a simplified compression/extension movement. For convenience, the motion of the piston is vertical only and is performed during $\hat{t} = 1s$, such that $\overline{U_z}_P = \sin(2\pi t)$, as shown in Fig. 4.56a.

This motion is sufficient and appropriate for studying the behavior of the lubricant and the transient heat generation mechanism. As can be seen in Fig. 4.56b, no hydrodynamic pressure is generated during the extension of the SA (negative $\overline{U_z}_P$). For repetitive sliding motion, this lack of hydrodynamic pressure can be considered as the primary cause of the break-down of the lubrication mechanism, which causes high heat generation. In general, the SA experiences fast

compression and slow extension, as shown in Section 2.9, for which case a single thrust portion is appropriate. Nevertheless, for the maneuvers on rough runways, a single thrust portion is not sufficient. This observation will be further discussed in Section 5.3.

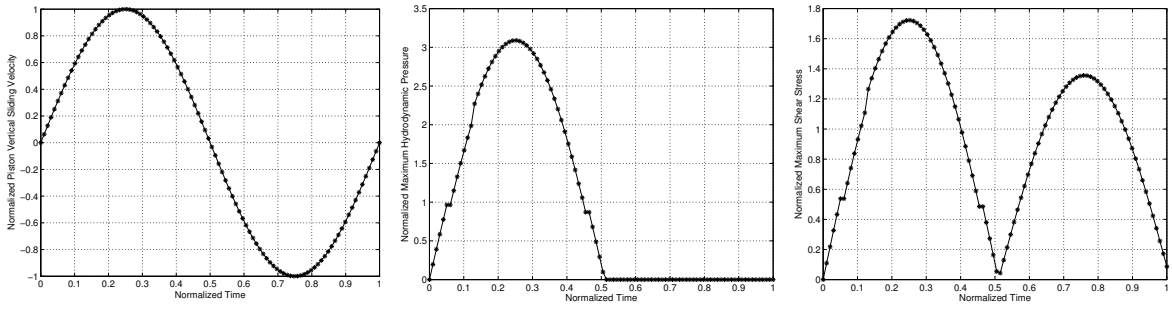

(a) $\overline{U_z}_P$ (b) $\overline{p}$ (c) $\overline{\tau}$

Figure 4.56: Illustration of transient piston motion.

The transient temperature field (or heat flux field) is not shown, as the temperature field is highly dependent on the surrounding structure, as shown in Section 4.7.4. Instead, the evolution of the shear stress (proportional to the generated frictional heat) is highlighted in Fig. 4.56c. The heat generation is almost zero during stiction (very low sliding velocity). As the transient motion is implemented as a sequence of instantaneous steady states, the eventual numerical problems that result from a discontinuity of the friction force as experienced in Chapter 2 are avoided. For zero hydrodynamic pressure, the heat generation is reduced, and the flow regime is classified as Couette flow.

Although the transient results are shown for oil, the transient results for grease can be obtained in a similar way. For grease, the transient hydrodynamic pressure behaves in a similar manner to the hydrodynamic pressure generated in an oil-lubricated bearing. A study of the transient *birth* and *death* of TT spaces is however not relevant to the study of the break-down of the lubrication mechanism during extension. For the current bearing design, $c_{,z} \leq 0$. In other words, the previously mentioned break-down is primarily governed by the clearance c, and is not dependent on the type of lubricant. However, similar to the previous findings of the steady state difference between an oil- and grease-lubricated bearing, the transient structural thermal behavior for a grease-lubricated bearing is different than for oil and is dependent on the lubrication mechanism.

4.8 Summary and Conclusions

The development of a comprehensive model for studying the TEHD behavior of both a rigid (and isothermal) and flexible (nonisothermal) oil- and grease-lubricated aircraft LG lower bearing is shown. The TTT developed in Chapter 3 is applied, for which both the fluid and structural governing equations are solved. In both cases, the physics are coupled through an FSI mapping technique.

The algorithm governing the TEHD-FSI simulation is detailed, and the characteristic

staggered convergence procedure is highlighted. Particular attention is placed on the development of the hybrid numerical solver that is based on the high performance MG method. In addition to the detailed discretization of the governing equations of the TTT using the FD method, the numerical inclusion of the boundary conditions is described, in particular how to include periodicity conditions into a MG solver. The numerical performance of the hybrid numerical solver is demonstrated for various grid sizes and simulation cases, and an ideal mesh size is determined from a mesh convergence study. In addition, the Topology Detection Algorithm (TDA) that is responsible for detecting the shells is shown. The Topology Adjustment Algorithm (TAA) is developed to guarantee convergence of the detected shells.

The 3D model is used to quantitatively investigate the reported heat damage, with the goal of understanding the lubrication mechanism and to determine a solution strategy to improve the performance of a LG lower bearing design. Relevant field variables such as the hydrodynamic pressure, shear stress, heat flux and temperature fields are plotted for a typical aircraft LG lower bearing assembly with an eccentric piston.

From a numerical point of view, the simulations of a grease-lubricated bearing need more global iterations than the simulations of an oil-lubricated bearing, as the presence of TT spaces make the problem highly nonlinear. As a consequence, the solution times for grease are longer than for oil. The solution times are also greatly increased by taking into account the structural behavior, which is a bottleneck in the coupled FSI simulation.

Major findings include that the maximum temperature is not at the mid-plane of the lubrication gap, and that, if grease was used as a lubricant, a plug space is likely to form at the thrust portion (low shear stress region) for the LG bearing. If the plug space formation is not taken into account, invalid conclusions regarding the bearing performance are likely to be drawn. It has also been found that the temperature is higher for the case of a grease-lubricated bearing than for an oil-lubricated bearing. Contrary to the Hertzian contact theory, the heat flux is present around the entire circumference and modified significantly by the presence of a plug space (insulator).

The numerical code is validated against existing analytical solutions for the case of a vertically moving piston and is validated against experimental data for the case of a rotating piston. Nonetheless, the comprehensive model is limited as it is not (yet) validated against experimental data for an existing LG slider bearing.

Four conclusions can be drawn from this chapter:

Conclusion 1: Full FSI must be considered in order correctly quantify the heat generation, as the deformation of the lubrication gap yields different pressure and temperature fields. The structural deformation is higher for a grease- than for an oil-lubricated bearing, and although the clearance is reduced by the presence of a plug space, the structure deforms such that the hydrodynamic pressure is reduced more for a grease- than for an oil-lubricated bearing.

Conclusion 2: Due to the presence of a plug space, the friction coefficient is very different for oil- and grease-lubricated bearings. For future LG dynamic simulations, performing simulations for a grease-lubricated bearing is advised in order to correctly determine the friction coefficient.

Conclusion 3: The temperature field at the surface of the piston is noticeably different from the temperature field at the bearing surface. The heat stagnates on the piston, whereas the heat diffuses radially and quickly on the bearing side. This asymmetrically distributed temperature field is likely responsible for the reported uneven heat damage. The calculated thermal response confirms that the phenomenon of overheating at the lower bearing is a very localized phenomenon.

Conclusion 4: The transient response is calculated as a sequence of instantaneous steady states, which is an efficient means of performing transient simulations (inertia of lubricant omitted) and avoids any numerical difficulties for modeling stiction. For the current bearing design, no hydrodynamic pressure is generated during extension of the SA, and the lubrication mechanism breaks down.

The results of the present chapter will be used in Chapter 5 to conceptualize a solution. Preserving a TEHD lubrication regime during extension and avoiding the escape of the lubricant from the high pressure zone must be taken into account in a novel bearing design.

■

Chapter 5

Conceptualization and Development of Solution Strategy

Ideas shape the course of history.

John Maynard Keynes, economist (1883 - 1946)

5.1 Landing Gear Systemic Analysis

In previous chapters, a comprehensive transient TEHD-FSI model of a greased LG lower bearing that relies on a novel TTT has been given. In order to formulate a solution strategy to remedy the reported overheating issue, a systemic analysis of the LG system is necessary to determine the driving factor(s) of the TTM model in a dynamic simulation of the LG. As the computation times for simulating grease in a coupled dynamic setting are long, the underlying idea is to use the TEHD-FSI model offline in order to determine the temperature variation and the change of the BFC under general loads and speeds for a particular bearing configuration and to generate a response surface (response space). The calculated response of the modified BFC can then be used to efficiently perform online dynamic simulations without the need of a very costly online TEHD-FSI simulation.

This approach satisfies the need for efficient aircraft LG dynamic simulations that include frictional heat generation. The main benefit of this particular approach (offline TEHD-FSI) is shorter computation times compared to online TEHD-FSI simulations. The systemic analysis aims to outline the required steps, but does not aim to demonstrate practically the setup of an offline TEHD-FSI simulation. As shown in [115], a common model of the friction coefficient is a function solely of the sliding speed: $\mu = \mathcal{F}_0(\dot{s})$. This friction model closely follows the laws postulated by Coulomb and is often used to model mechanical systems, as illustrated in Fig. 5.1. The LG dynamic simulations are generally performed in a multibody software package (labeled with ■) that makes use of an isothermal and empirical BFC.

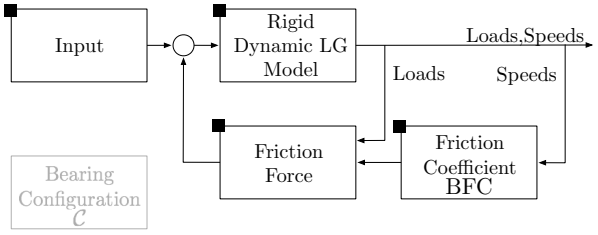

Figure 5.1: Block-diagram of the nonlinear dynamic LG SA model [32].

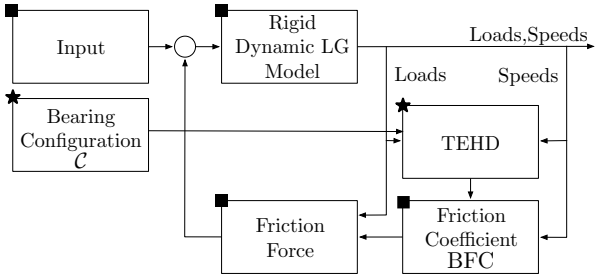

Figure 5.2: On-line TEHD-FSI in a LG dynamic simulation [32].

In Fig. 5.1, the BFC is independent of the LG bearing configuration $\mathcal{C}$ and the loads $\mathbf{f}$. For simplified LG dynamic simulations (such as shown in Chapter 2) for which the LG components are all considered rigid, an equivalent lubricated contact can be modeled through an empirical formulation using a temperature dependency θ of the BFC, cut-off at the dropping point of grease $\hat{\theta}$: $\mu = \mathcal{F}_1(\dot{s}, \theta)$. In this case, the structural deformations are such that $\mathbf{u} = 0$ and the loads $\mathbf{f}$ are determined using a simplified beam submodel, which allows the determination of the dry frictional heat fluxes. These are proportional to an empirical BFC. Lubrication of the LG bearings is modeled indirectly through this empirical BFC. Following [39], the temperature at the interface can be calculated as being directly proportional to the heat flux: $\dot{\theta} \sim \mathcal{F}_2(\mu, \dot{s}, \mathbf{f})$.

As concluded in Chapter 2, a simplified model is not sufficient to accurately capture the frictional heat energy generation at the lower bearing sliding interface. In Chapter 4, it has been demonstrated how to capture local effects and the accurate fluid film behavior, which is achieved by applying the TTT shown in Chapter 3. For the case of dry friction (no lubricant), a dry BFC that is known for the pair of materials is used. As concluded in Chapter 4, the advantage of a full TEHD simulation is that the BFC is *calculated* for a specific bearing configuration, and specific loads and speeds.

The block-diagram of the integration of the online TEHD-FSI simulation (comprehensive model of Chapter 4) into a LG dynamic simulation is shown in Fig. 5.2. In general, the TEHD simulation is a computationally expensive and strongly coupled (or staggered) FSI simulation. The comprehensive model is generally solved in a different software package or in different in-house code (labeled with ★) than the overall dynamic model, which is usually solved by a multibody dynamics solver (labeled with ■). As highlighted previously, the BFC is impacted the most by the lubricant's viscosity, which is dependent on temperature θ, on pressure p (hence on load $\mathbf{f}$) and on the shear rate $\dot{\gamma}$: $\eta = \mathcal{N}(\theta, \mathbf{f}, \dot{\gamma}(\dot{s}))$. The results shown in Chapter 4 indicate that the BFC is determined as a function of the operating conditions (structural deformation $\mathbf{u}$ and sliding speed $\dot{s}$) and the resulting temperature θ, as well as of the configuration $\mathcal{C}$ (materials and geometry). For elastic and homogeneous materials, the structural deformation $\mathbf{u}$ is proportional to the loads $\mathbf{f}$. The modified BFC generally can be defined as:

$$\mu = \mathcal{F}_3(\dot{s}, \theta, \mathbf{u}(\mathbf{f}), \mathcal{C}, \dot{\gamma}) = \mathcal{F}_4(\dot{s}, \eta, \mathcal{C}) \tag{5.1}$$

In Chapter 4, the separate transient TEHD-FSI simulation (comprehensive model) yields results for the BFC as a function of the operating conditions. A block-diagram showing the input and output of the TEHD-FSI simulation is shown in Fig. 5.3.

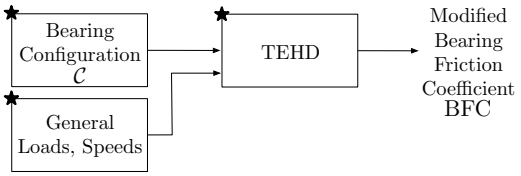

Figure 5.3: Off-line TEHD-FSI numerical simulation (Comprehensive model) [32].

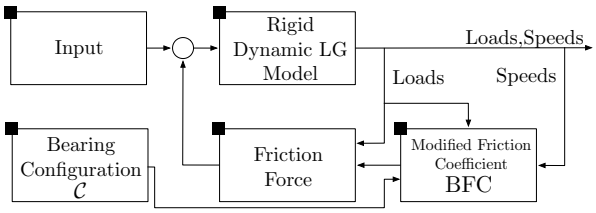

Figure 5.4: Block-diagram of the LG dynamic simulation with a modified BFC [32].

As concluded in Chapter 4, the interface temperature is dependent on the sliding speed $\dot{s}$ and the deformation $\mathbf{u}$ for a particular bearing configuration $\mathcal{C}$:

$$\theta = \mathcal{F}_5(\dot{s}, \mathbf{u}(\mathbf{f}), \mathcal{C}) \tag{5.2}$$

Consequently, Eq. (5.2) yields the change of the BFC as a function of the operating conditions only. By combining the rheological model, Eq. (5.1) and Eq. (5.2), we have:

$$\mu = \mathcal{F}_6(\dot{s}, \mathbf{f}, \mathcal{C}) = \mu^\star \tag{5.3}$$

The temperature is *implicit* and can be determined offline for general operating conditions and a particular bearing configuration. A different reasoning leads to the same results. The law of shearing for a Bingham fluid combined with Eq. (5.2), is given as:

$$\mu = \mathcal{F}_7(\dot{s}, \mathcal{N}(\theta, \mathbf{f}, \dot{\gamma}(\dot{s}))) = \mathcal{F}_7(\dot{s}, \eta) = \mu^\star \tag{5.4}$$

Eq. (5.4) is hence qualitatively the same as Eq. (5.3). The modified BFC $\mu^\star$ is a functional $\mathcal{L}$ of the sliding speed $\dot{s}$ and the loads $\mathbf{f}$. The block-diagram of the dynamic LG simulation can be reduced using the modified BFC (shown in Fig. 5.4) defined by $\mu^\star = \mathcal{L}(\dot{s}, \mathbf{f}, \mathcal{C})$. The goal of the TEHD-FSI simulation is to calculate $\mathcal{F}_4$, which in combination with Eq. (5.2), implies that the temperature depends on the geometry only (the lubrication mechanism, gap or clearance). In this model, the geometry is given by: $\mathcal{C} : c = c(x, z)$. It is critical to mention that an optimal configuration $\mathcal{C}$ can be found such that the temperature at the sliding interface is minimal.

Various solution strategies are discussed in Section 5.2 for the present application of a LG lower bearing. The systemic analysis, which helped to identify the modified BFC as a function of the driving factors (see Eq. (5.4)), is shown to be beneficial for determining a promising solution strategy.

5.2 Solution Strategies

In order to remedy and avoid the reported problems, the following solution strategies can be adopted:

1. *Allow* the heat generation, but focus on improving the heat evacuation.
2. *Withstand* the heat generation by improving the material characteristics.
3. *Reduce* the heat generation by reducing the BFC, loads or sliding speed.

Strategy 1: The heat generated and the hydrodynamic pressure depend primarily on the clearance between the contacting surfaces. In order to address the issues of excessive heat generation at the lower bearing, several strategies can be considered. Heat can be *tolerated* and *evacuated* from the lower bearing interfaces. This strategy, often used in brake cooling, might not lead to a significant improvement as the heat generated at the interface is local and, as shown in Chapter 4, only slowly leaves the TZI. Although materials with higher thermal conductivity and eventual external cooling could lead to heat evacuation, the structural characteristics of the system might be changed and the weight of the LG increased. Neither of these two drawbacks is desired.

Strategy 2: Another strategy is to *withstand* the heat generation and change the materials of the contacting surfaces. Although lubricant-free (sometimes referred to as self-lubricating) bearings might be promising, appropriate materials that tolerate high contact pressures and withstand excessive heat are not known to be used in aircraft LG lower bearings. They are, however, used more frequently in other LG joints. This strategy is impractical for the application of a LG lower bearing, but is sometimes applied in applications using ceramic materials, where high amplitude shock-loads (rapidly varying pressure) are rare.

Strategy 3: The last and preferred solution strategy is to *reduce* the heat generation. In a TEHD lubrication regime, the heat generation is mainly influenced by the clearance between the contacting surfaces. In the present application, as shown by the systemic analysis in Section 5.1, the configuration $\mathcal{C}$ dominates the design, as the input speeds and loads cannot be changed for a given rough runway. The configuration $\mathcal{C}$ of a bearing is defined by the materials and the geometry, whereas the materials are generally defined by aerospace standards. Consequently, the following sections concentrate on changing the geometry in $\mathcal{C}$ (in this context, equivalent to the clearance c), which can be designed for optimal bearing performance.

The practice of *optimizing* the bearing surface is often referred to as the design of the lubrication mechanism, which is a highly complex task. The lubrication mechanism is critical to the design of high efficiency fluid film bearings and is highly application dependent. Unfortunately, in practice, the lubrication mechanism design is often neglected, not only because of time constraints, but mainly because of the longer engineering time, which has a detrimental effect on unit production cost. As the most promising solution strategy is the optimization of the lubrication mechanism, the desired lubrication mechanism characteristics need to be formulated first, before an optimization problem can be mathematically formulated.

5.3 Desired Lubrication Mechanism Characteristics

As explained in Section 5.2, the preferred solution strategy is to optimize the lubrication mechanism. As shown in Chapter 4, the hydrodynamic pressure profile is similar for both oil- and grease-lubricated bearings, but the maximum value is different. In order to simplify the discussion, the hydrodynamic pressure profile for an isoviscous, oil-lubricated, rigid and isothermal bearing is shown in Fig. 5.5 (solution Set 3 from Section 4.7.1). As can be seen in Fig. 5.6, the actual pressure profile has a single pressure peak along the circumference, positioned at the normalized eccentricity position $\overline{x_e}$. The lubricant escapes from this high pressure zone, which causes a low clearance (film, thickness) that barely supports the load, and hence leads to excessive heat generation (as shown in Chapter 4). The underlying idea is to separate the pressure peak into two distinct peaks, such that the desired pressure profile hinders the lubricant from escaping the high pressure zone. In order to further analyze the fluid flow behavior in the lubrication gap, the normalized components of the pressure gradient $\boldsymbol{\nabla} p$, which governs the fluid flow, are shown in Fig. 5.7a and Fig. 5.7b respectively.

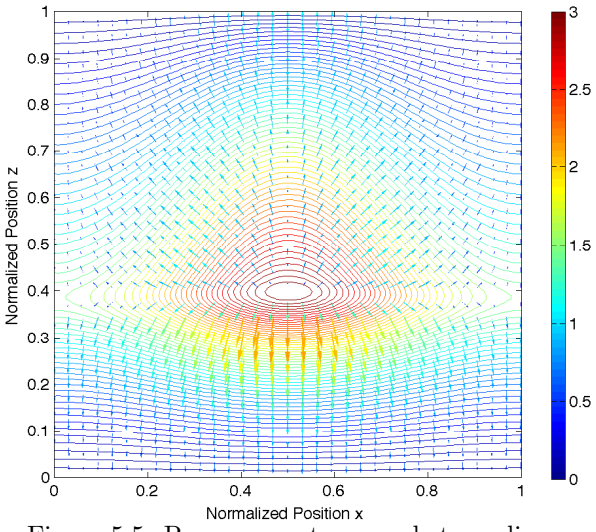

Figure 5.5: Pressure contours and streamlines.

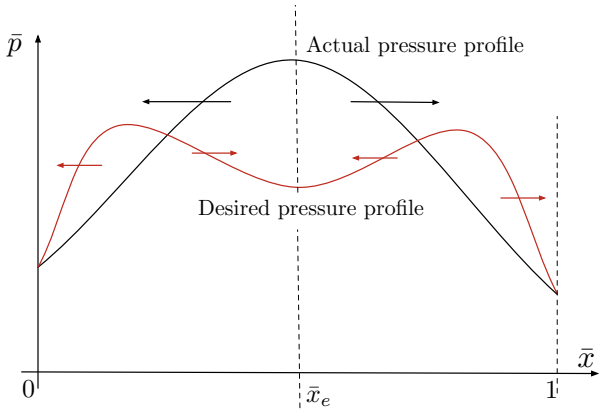

Figure 5.6: Actual and desired profile of $\overline{p}$ ($\overline{z} = \overline{z_0}$).

The circumferential pressure component $\overline{p}_{,\overline{x}}$ is negative for decreasing values of $\overline{x}$ and positive for increasing values of x, which indicates that the lubricant is escaping circumferentially. In addition, $\overline{p}_{,\overline{x}}$ is zero around $\overline{x_e}$, which indicates a circumferential stagnation line. The vertical pressure component $\overline{p}_{,\overline{z}}$ indicates that the pressure gradient acts against the fluid flow for $\overline{z} < \overline{z_0}$, but forces the fluid flow to escape vertically for $\overline{z} > \overline{z_0}$. This driving force vanishes for $\overline{z} \simeq \overline{z_0}$. The norm of the pressure gradient is shown in Fig. 5.7c, and indicates a localized region of high pressure force for $\overline{z} < \overline{z_0}$. In addition, the norm of the pressure gradient changes rapidly around $(\overline{x_e}, \overline{z_0})$, which suggests a saddle point of the pressure gradient.

A saddle point is a stagnation point of the fluid flow, and this saddle point can be found using the Laplacian of the hydrodynamic pressure, shown in Fig. 5.7d. The Laplacian is defined

as the divergence of the pressure gradient field such that $\nabla^2 p = \nabla \cdot \nabla p$, and yields the spatial variations of the hydraulic force (peaks of forces). The sinks and sources of the pressure gradient are distributed around the saddle point.

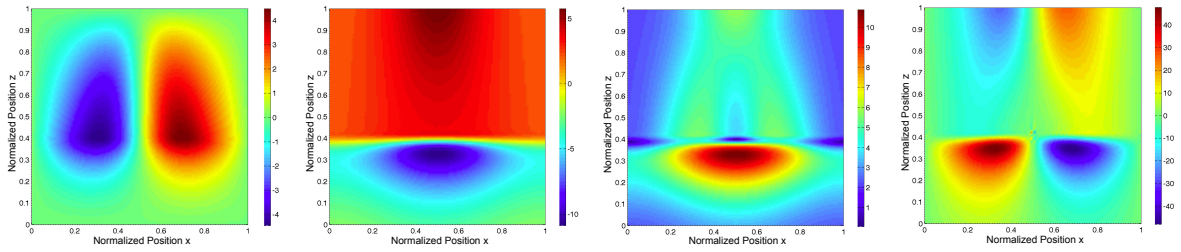

(a) $\overline{p}_{,\overline{x}}$ (b) $\overline{p}_{,\overline{z}}$ (c) $|\nabla \overline{p}|$ (d) $\nabla^2 \overline{p}$

Figure 5.7: Pressure gradient and Laplacian (oil, solution Set 3).

In order to reduce the heat generation, the aim is not to increase the hydrodynamic pressure, but to *reduce the pressure gradient*, as ∇p is directly proportional to the heat source term. In other words, less heat is generated with a lower pressure gradient.

The strategy of optimizing the lubrication mechanism has been applied successfully in [116], but their design is based on a novel wave bearing design for rotational motion, and their numerical model is 2D, hence not making the findings applicable to the LG lower bearing. In [117], a similar study for optimizing the lubrication mechanism has been performed, but the study only includes multilobe, pressure dam and tilting pad bearings. The results are provided for rotating machinery only, and are not applicable to the current configuration of a LG slider bearing.

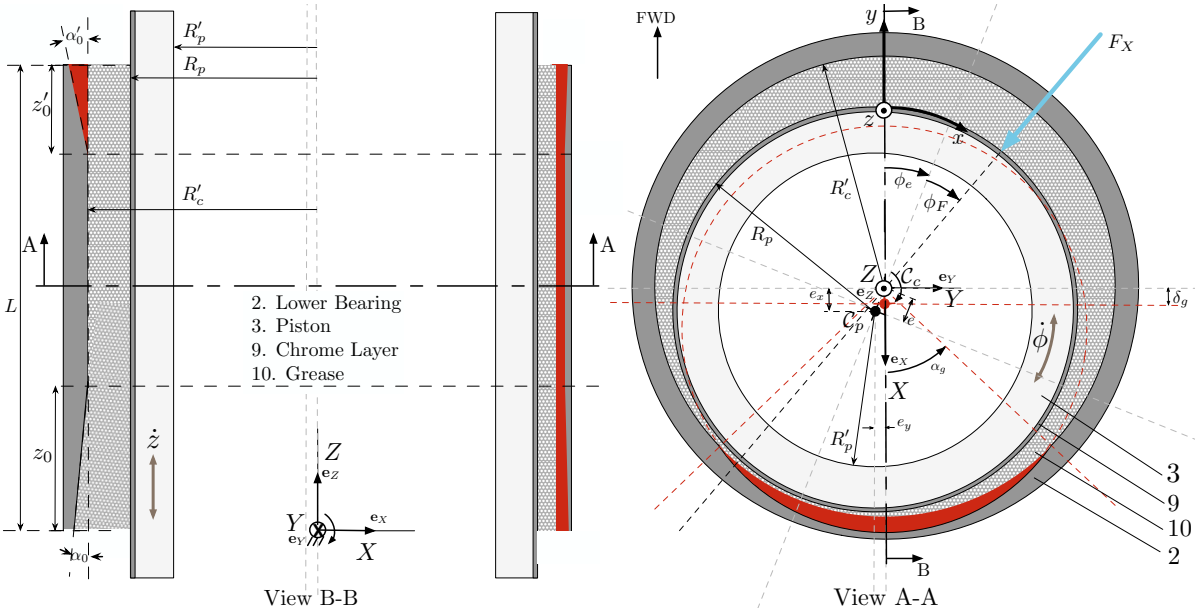

Figure 5.8: Parametric bearing shape (highlighted areas represent physical removal of material).

As shown in Fig. 5.6 and confirmed by the shape of ∇p and $\nabla^2 p$, the solution strategy (Strategy 3) is achieved by separating the pressure peaks and preserving the lubricant in a

pocket, allowing for a *cushion* of grease to form, as shown in Fig. 5.8. Grease in pockets is not sheared enough to flow, and remains stationary in a pocket, preserving a lubricated contact. Similarly, oil is trapped inside a pocket, only escaping under increased pressure. The cushion is positioned opposite to the forward motion of the aircraft where the reported damage occurred (around $\overline{x_e}$).

In addition to the cushion design, the optimized bearing design includes a secondary thrust portion, as is suggested in Section 4.7.5. In the current configuration and as shown in Fig. 4.56b, a hydrodynamic pressure is generated only during compression, and not during extension. Although the bearing is likely to partially cavitate with the presence of a second thrust portion, it is this second thrust portion that allows for the generation of a hydrodynamic pressure during extension. In the current configuration, the fluid film is likely to break down during extension. Although the sliding speed during extension is lower than during compression (because of the SA damping), the lubrication regime changes from hydrodynamic to mixed. By introducing a secondary thrust portion, a full TEHD lubrication regime can be preserved in both compression and extension, hence reducing the heat generated.

Although this engineering design problem may be solved using a reverse solution technique to obtain the lubrication mechanism for a given pressure profile, it is the fact that multiple objectives need to be satisfied that defines the lubrication mechanism design problem as a multi-objective optimization problem. This optimization study with the objectives of a maximized bearing load capability and minimized heat generation is given in Section 5.5 for a rigid, isothermal and oil-lubricated bearing.

5.4 Analytical Film Thickness (Cushion Thickness)

The clearance of the novel bearing design discussed in Section 5.3 can be seen as a physical removal of material along the circumference. Analytically, the clearance is determined from the intersection of two circles. The undeformed, nonmodified clearance is given in Section 4.3.2. The modified film thickness is given as:

$$c(x,z) = \breve{c}_z(z) + e \cdot \cos(\phi + \phi_e) + c_g(\delta_g, \alpha_g) \tag{5.5}$$

where $c_g(\delta_g, \alpha_g)$ is the cushion thickness and $\breve{c}_z(z)$ the vertical bearing profile that includes the second thrust portion. The analytical expression of c_g is derived as:

$$c_g(\delta_g, \alpha_g) = \begin{cases} \delta_g \cdot \cos\left(\frac{\pi}{2\alpha_g}\phi\right) & -\alpha_g \leq \phi \leq \alpha_g \\ 0 & \text{elsewhere} \end{cases} \tag{5.6}$$

where $\phi = xR_P^{-1}$. The half-angle of the cushion α_g is given by:

$$\alpha_g = \tan^{-1}\left(u'^{-1}\sqrt{4u_X^2 R_c'^2 - u'^2}\right) \tag{5.7}$$

where $u' = u_X^2 - R_P^2 + R_c'^2$, R_c' is the inner radius of the bearing, R_P the radius of the piston

and $u_{X|Y}$ the displacement of the virtual cushion circle in X and Y directions respectively. For the engineering design optimization shown in Section 5.5, $u_Y = e_y = 0$ and $u_X = \delta_g + c_0 + e_x$.

5.5 Engineering Design Optimization

Several parameters shown in Table 5.1 are studied to find a higher performing lower bearing profile. The parameters R_P, R'_c and L are considered to be fixed for an existing bearing, as their sensitivities have been extensively studied in the literature [114].

$0 < \overline{z_0}, \overline{z'_0} < 0.4$	Normalized primary and secondary thrust position
$0 < \overline{\alpha_0}, \overline{\alpha'_0} \leq 1$	Normalized primary and secondary cushion thrust angles
$0 \leq \overline{\delta_g} \leq 0.362$	Normalized cushion thickness

Table 5.1: Independent parameters for novel lubrication mechanism.

For the present engineering optimization study, a single normalizing parameter is defined as $\varsigma = z_0 \cdot \tan\alpha_0$. For a vertically symmetric geometry case (i.e., for similar compression/extension speeds of the SA), $\overline{z_0} \simeq \overline{z'_0}$ and $\overline{\alpha_0} \simeq \overline{\alpha'_0}$. Consequently, only three independent parameters have to be studied: $\overline{z_0}$, $\overline{\alpha_0}$ and $\overline{\delta_g}$. In Chapter 4, the differences between an oil- and grease-lubricated bearing have been investigated, and it has been found that eventual TT spaces within grease can be predicted by studying an oil-lubricated bearing; therefore, the engineering optimization study is performed for an oil-lubricated bearing only (isothermal and rigid structure). It has been found that a plug space is likely to form for large cushion thicknesses. The performance of an oil-lubricated (nonisothermal, flexible structure) bearing is evaluated in Section 5.6.1.

In order to determine the most appropriate cushion thickness for the novel bearing design presented in Section 5.3, the load w_y as well as the shear stress τ (proportional to the heat generation) are studied for the novel bearing lubrication mechanism. Consequently, the engineering optimization study can be seen as multi-objective, and a Pareto analysis is performed under constraints. Both multi-objective functions are normalized by their respective maximum for the case of a bearing without a cushion ($\delta_g = 0$) such that:

$$\Xi_w = -\,w_y|_{\delta_g} \cdot \max^{-1}\left(w_y|_{\delta_g=0}\right) \quad , \quad \Xi_\tau = \tau|_{\delta_g} \cdot \max^{-1}\left(\tau|_{\delta_g=0}\right) \tag{5.8}$$

As the main goal is to obtain a maximized load capability and a minimized heat generation, and in order to define a minimization problem, the ratio Ξ_w is defined negatively. The optimal bearing configuration with the highest load capability and lowest heat generation is obtained by the minimization of both normalized multi-objective functions:

$$\overline{\Xi}^* = \min_{\overline{z}_0, \overline{\alpha_0}, \overline{\delta_g}} \begin{bmatrix} \overline{\Xi_w} & \overline{\Xi_\tau} \end{bmatrix} \qquad \text{s.t. } 0 < \overline{z_0} \leq 0.4 \text{ and } 0 < \overline{\alpha_0} \leq 1 \text{ and } 0 \leq \overline{\delta_g} \leq 0.362 \tag{5.9}$$

The multi-objective optimization problem is solved with a popular Evolutionary Algorithm (EA) in order to obtain a set of Pareto optimal solutions, as given in Section 5.5.1. The engineering optimization study is performed for two different gap configurations: a clearance with a cushion and one thrust portion (Gap 1), and a clearance with a cushion and a second

thrust portion (Gap 2). The normalized objective vector components are given for various values of $\overline{\delta_g}$. For both gaps, the normalized load values $\overline{\Xi_w}$ are shown in Fig. 5.9 and Fig. 5.10 as a function of $\overline{z_0}$ and $\overline{\alpha_0}$. Similarly, for both gaps, the normalized shear stress values $\overline{\Xi_\tau}$ are shown in Fig. 5.11 and Fig. 5.12. The shape of the optimization functions is convex, suggesting that a scalar and weighted optimization function is very difficult to define.

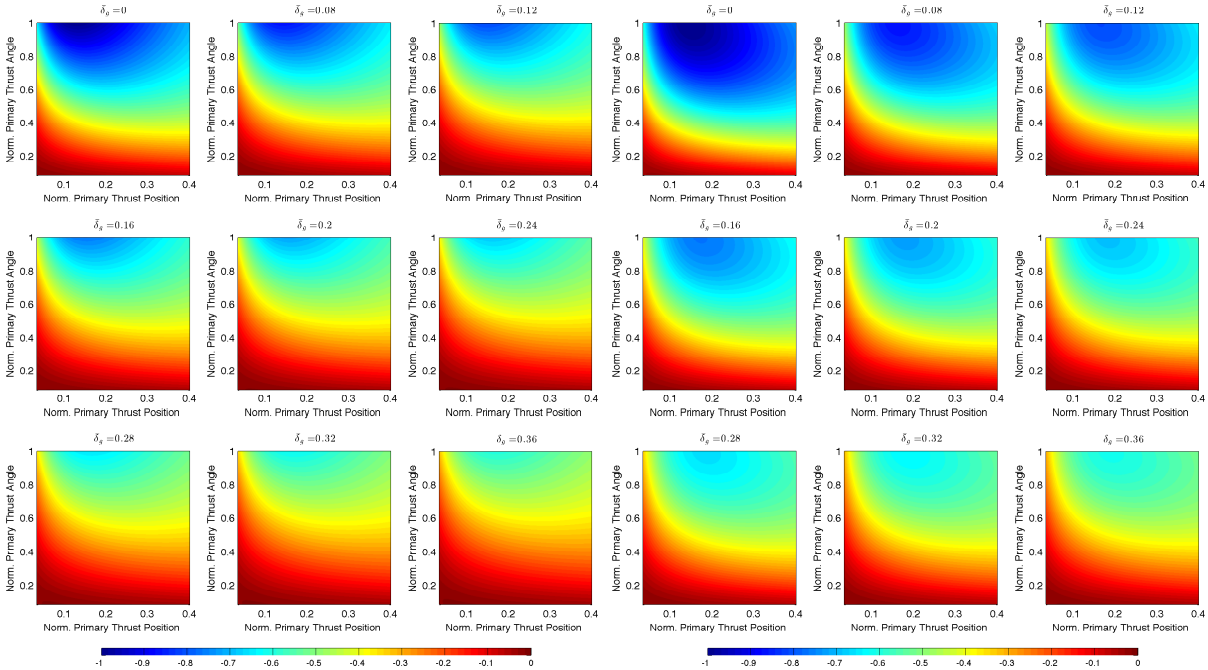

Figure 5.9: Normalized multi-objective function $\overline{\Xi_w}$ (Gap 1).

Figure 5.10: Normalized multi-objective function $\overline{\Xi_w}$ (Gap 2).

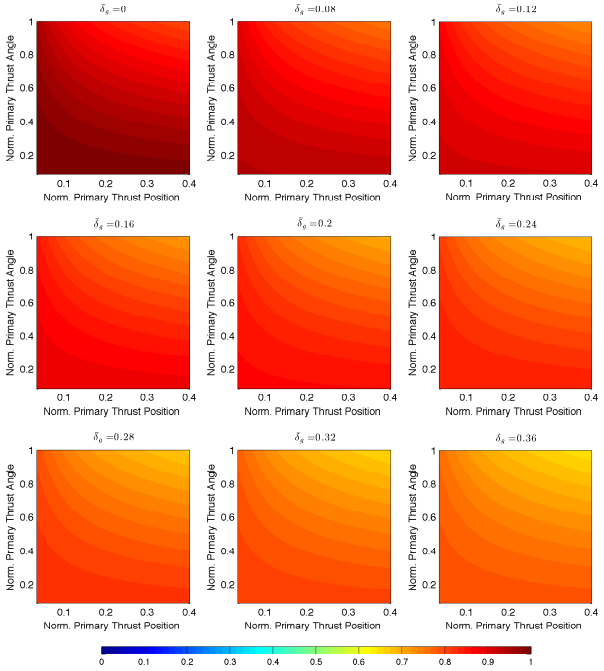

Figure 5.11: Normalized multi-objective function $\overline{\Xi_\tau}$ (Gap 1).

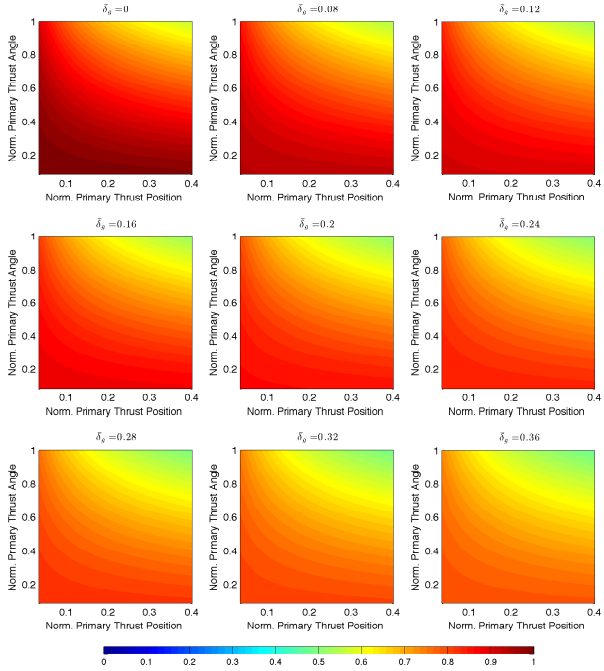

Figure 5.12: Normalized multi-objective function $\overline{\Xi_\tau}$ (Gap 2).

5.5.1 Pareto Analysis and Genetic Algorithm

The goal of the Pareto Analysis is to determine a Pareto optimal solution set such that both objectives are in optimal equilibrium, that is, that neither of the two objectives can be improved without degrading the other. As the two objectives of the engineering optimization problem are different, the chosen method is to use the commonly used Non-dominated Sorting Genetic Algorithm-II (NSGA-II).

The present optimization study has been performed using the *gamultiobj* function within MATLAB, which is an implementation of a variant of the NSGA-II algorithm. This variant is classified as a controlled elitist algorithm [118], which not only attributes a higher *fitness value* to better solutions, but also favors individual solutions that increase the diversity of the solutions set, which helps the convergence of the algorithm to an optimal Pareto set.

Although the speed of the optimization algorithm is low, the chosen algorithm serves the purpose of determining a Pareto solution set in a reasonable time. The default parameter settings of the implementation within MATLAB have been chosen. As the NSGA-II algorithm is a stochastic algorithm, and in order to obtain a representative Pareto solution set, the algorithm is run 20 times consecutively.

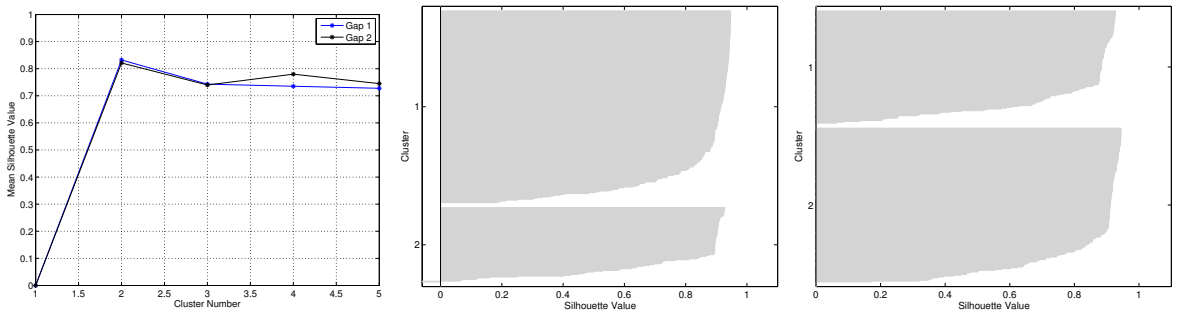

(a) Mean silhouette value as a function of k.

(b) Silhouette values for Gap 1 ($k = 2$)

(c) Silhouette values for Gap 2 ($k = 2$)

Figure 5.13: Mean silhouette values and silhouette plots.

The most challenging stage of a multi-objective optimization is the decision stage for determining the *best* Pareto solution [119]. Several techniques exist, but for the engineering optimization study at hand, the data clustering method is performed on the Pareto solution set. As shown in [120], the clusters are calculated with the well-known *k-means++* partitioning algorithm, which is used to minimize the Euclidean distance to the center of the cluster k. Based on the mean silhouette value as a function of k for both gaps, the optimal cluster configuration is $k = 2$ (see Fig. 5.13a). The higher the silhouette value, the tighter the data are grouped around the center of the cluster and the better the cluster separation. In other words, the quality of the cluster is given by the silhouette value. The silhouette plots, which are used to determine the appropriate number of clusters, are shown in Fig. 5.13b and Fig. 5.13c.

5.5.2 Post-Pareto Analysis and Optimal Configuration

For each gap, the cluster plot is shown in Fig. 5.14 and Fig. 5.15 respectively. It has been found that the optimal configurations are all such that $\overline{\alpha_0} \simeq 1$. In addition to the cluster data points (Pareto optimal solution set), the centers of the clusters are shown. The advantage of grouping the Pareto solution set into clusters is that the decision of the optimal configuration can then be made among a few distinct solutions.

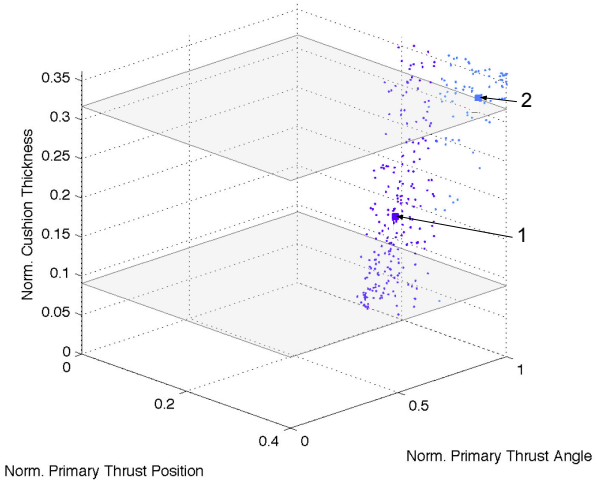

Figure 5.14: Pareto optimal solution set and clusters (Gap 1).

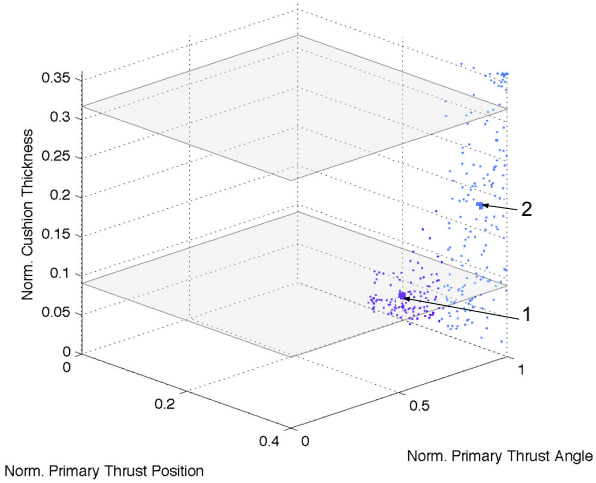

Figure 5.15: Pareto optimal solution set and clusters (Gap 2).

Although the calculated solutions are Pareto optimal, they are not necessarily optimal from an engineering point of view.

	k	$\overline{z}_0$	$\overline{\alpha_0}$	$\overline{\delta_g}$	N_k
Gap 1 : One thrust portion	**1**	0.190	0.992	**0.130**	232
	2	0.348	0.992	0.319	90
Gap 2 : Two thrust portions	**1**	0.351	0.986	**0.182**	185
	2	0.204	0.986	0.032	135

Table 5.2: Pareto optimal configurations.

The normalized clearance $c_0/\varsigma = 0.317$ as well as the normalized eccentricity $e/\varsigma = 0.09$ are shown in Fig. 5.14 and Fig. 5.15, which form the engineering physical limits the feasibility of the solutions. Although $\overline{\delta_g}$ can be smaller than the eccentricity of the piston, the clearance between the bearing and the piston would be extremely low, and a full TEHD regime would not be guaranteed. If $\overline{\delta_g}$ was larger than c_0/ς, the clearance would be larger than the mechanical tolerances of the lower bearing assembly. The normalized coordinates of the centers of the clusters are shown in Table 5.2, where N_k is the number of Pareto solutions in cluster k. In addition, the optimal solution, which is the center of the cluster and found within the engineering limits, is identified.

5.6 Novel Lubrication Mechanism Analysis

5.6.1 Thermo-Tribomechanical Performance Study

The engineering optimization study shown in Section 5.5 provides an optimal solution for reducing the heat generation and maximizing the load capability of the bearing, but in order to confirm the optimal solution, a performance analysis of the novel bearing design is done. The performance analysis is shown for an oil-lubricated bearing (nonisothermal and flexible structure) for the two considered clearances (Gap 1 and Gap 2), and compared to the existing design shown in Section 4.7.1 (solution Set 3, denoted as the reference case).

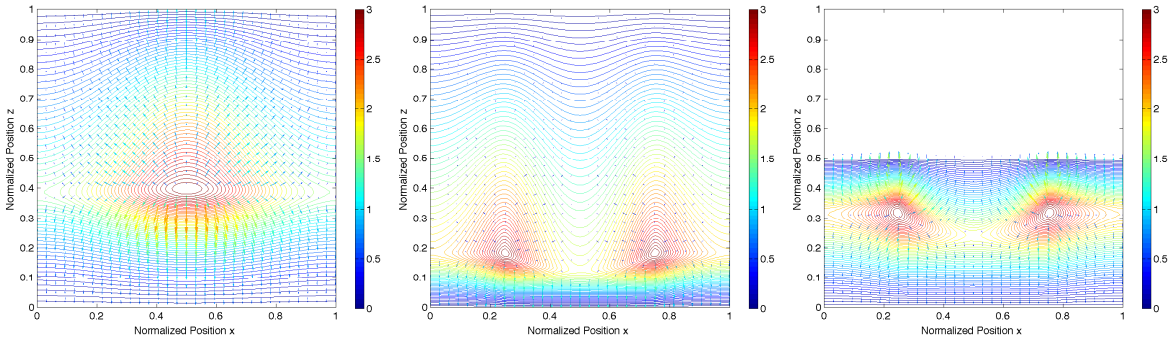

(a) $\overline{p}$ (ref.) (b) $\overline{p}$ (Gap 1) (c) $\overline{p}$ (Gap 2)

Figure 5.16: Hydrodynamic pressure contours and streamlines.

The hydrodynamic pressure contours and streamlines are shown in Fig. 5.16, and the reference pressure is shown in Fig. 5.16a. One primary pressure peak as mentioned in Chapter 4 is clearly identifiable. For both cases (Gap 1 and Gap 2), two pressure peaks exist in the hydrodynamic pressure field, and are separated from the eccentricity position $\overline{x_e}$ by the angle of the cushion $2\overline{\alpha_g}$. Although the total load is reduced, it is the separation of the pressure peaks that is of interest in order to avoid the fluid escape from the high pressure zone noted in Section 5.3. A similar pressure peak separation is shown in Fig. 5.16c. However, the bearing cavitates for $\overline{z} > \overline{z_0}$. Cavitation is not desirable, and is a direct consequence of a second thrust portion. In order to avoid cavitation, the bearing length should be increased for a second thrust portion.

In order to understand the lubrication mechanism of the optimized bearing design, the normalized components of the pressure gradient shown in Fig. 5.17 are compared to the reference bearing shown in Fig. 5.17a and Fig. 5.17d. With the separation of the pressure peak, the pressure gradient changes significantly. As desired, the circumferential pressure gradient component $\overline{p}_{,\overline{x}}$ shown in Fig. 5.17b indicates that the lubricant is contained within the cushion and is hindered (opposite $\overline{p}_{,\overline{x}}$ to the direction of fluid flow) from escaping. A similar cushion effect is observed when a second thrust portion is present, as shown in Fig. 5.17c.

The normalized vertical pressure gradient components are shown in Fig. 5.17e and Fig. 5.17f. The separation of the pressure peaks has a significant effect on $\overline{p}_{,\overline{z}}$, which is reduced for Gap 1. Due to the encountered cavitation for Gap 2, $\overline{p}_{,\overline{z}}$ is higher. The net effect of the thrust portion

and the separation of the pressure gradient on the fluid behavior can be understood by analyzing the norm of the pressure gradient and the Laplacian of the pressure, which are shown in Fig. 5.18. Compared to the reference case, $\boldsymbol{\nabla}^2\overline{p}$ is lower at the thrust portion for Gap 1 and Gap 2, which indicates that the cushion thickness has a significant effect on the driving force $\boldsymbol{\nabla}^2\overline{p}$.

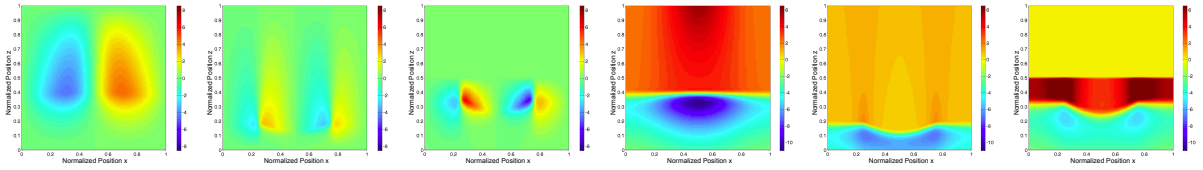

(a) $\overline{p}_{\overline{x}}$ (ref.) (b) $\overline{p}_{\overline{x}}$ (Gap 1) (c) $\overline{p}_{\overline{x}}$ (Gap 2) (d) $\overline{p}_{\overline{z}}$ (ref.) (e) $\overline{p}_{\overline{z}}$ (Gap 1) (f) $\overline{p}_{\overline{z}}$ (Gap 2)

Figure 5.17: Normalized components of the hydrodynamic pressure gradient $\boldsymbol{\nabla}\overline{p}$.

For the reference case, the Laplacian indicates one saddle point, whereas for Gap 1 and Gap 2, two saddle points appear and the Laplacian is significantly increased, indicating a higher variation of $\boldsymbol{\nabla}\overline{p}$.

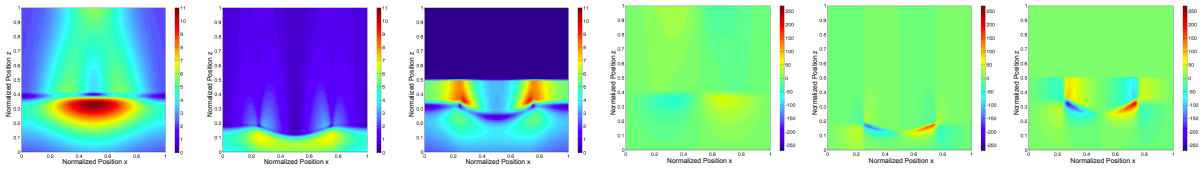

(a) $|\boldsymbol{\nabla}\overline{p}|$ (ref.) (b)$|\boldsymbol{\nabla}\overline{p}|$(Gap 1) (c) $|\boldsymbol{\nabla}\overline{p}|$(Gap 2) (d) $\boldsymbol{\nabla}^2\overline{p}$ (ref.) (e) $\boldsymbol{\nabla}^2\overline{p}$ (Gap 1) (f) $\boldsymbol{\nabla}^2\overline{p}$ (Gap 2)

Figure 5.18: Norm of the pressure gradient $|\boldsymbol{\nabla}\overline{p}|$ and Laplacian $\boldsymbol{\nabla}^2\overline{p}$.

The velocity field in the lubrication gap is shown in Fig. 5.19 for the compression of the SA. The recirculation zone occurs at the primary thrust portion for the reference case as well as for Gap 1 (see Fig. 5.19a and Fig. 5.19b). However, for Gap 2 as shown in Fig. 5.19c, the recirculation zone is not present at the secondary thrust portion, because the bearing cavitates. Instead, the velocity profile is similar to Couette flow.

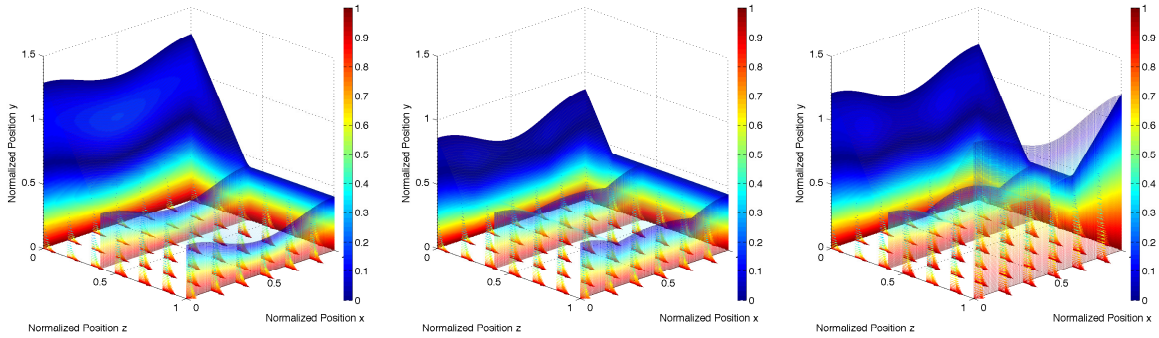

(a) $\overline{\mathbf{v}}$ (ref.) (b) $\overline{\mathbf{v}}$ (Gap 1) (c) $\overline{\mathbf{v}}$ (Gap 2)

Figure 5.19: Normalized velocity field $\overline{\mathbf{v}}$.

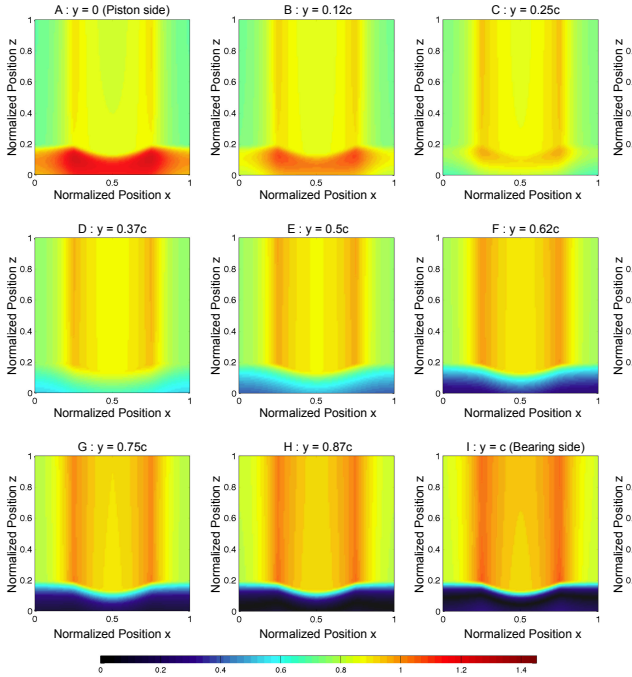

Figure 5.20: Normalized shear stress field $\overline{\tau}$ (Gap 1).

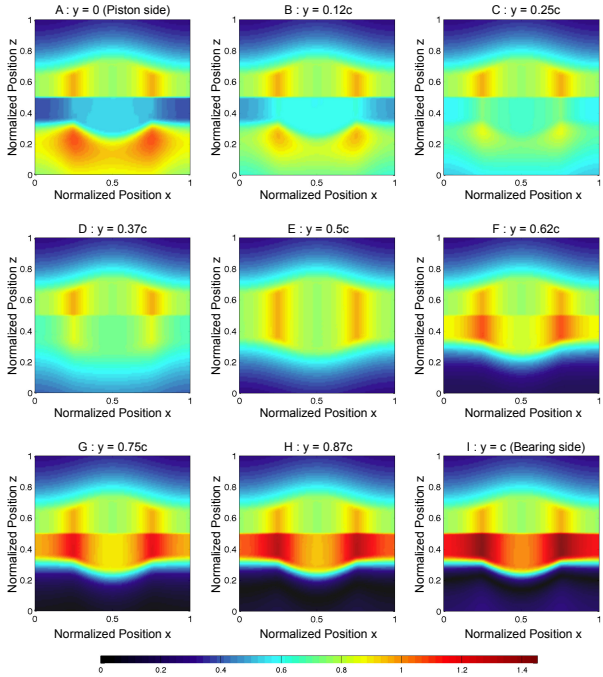

Figure 5.21: Normalized shear stress field $\overline{\tau}$ (Gap 2).

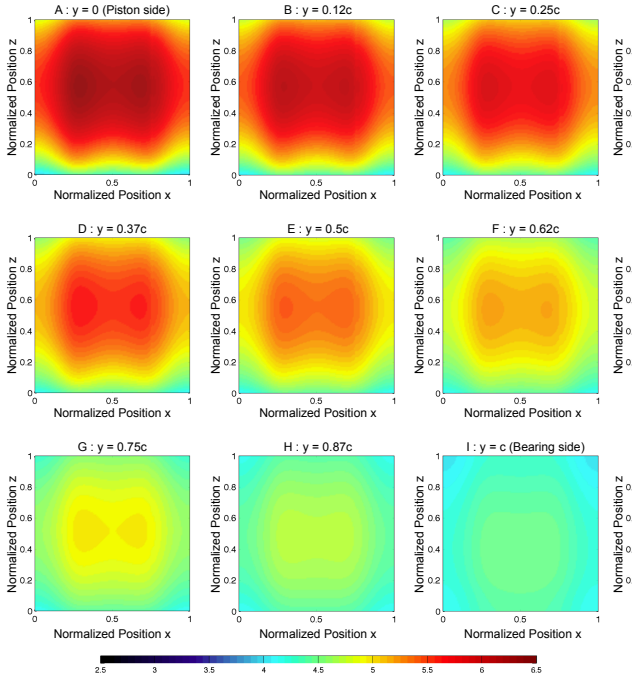

Figure 5.22: Normalized temperature field $\overline{\theta}$ (Gap 1).

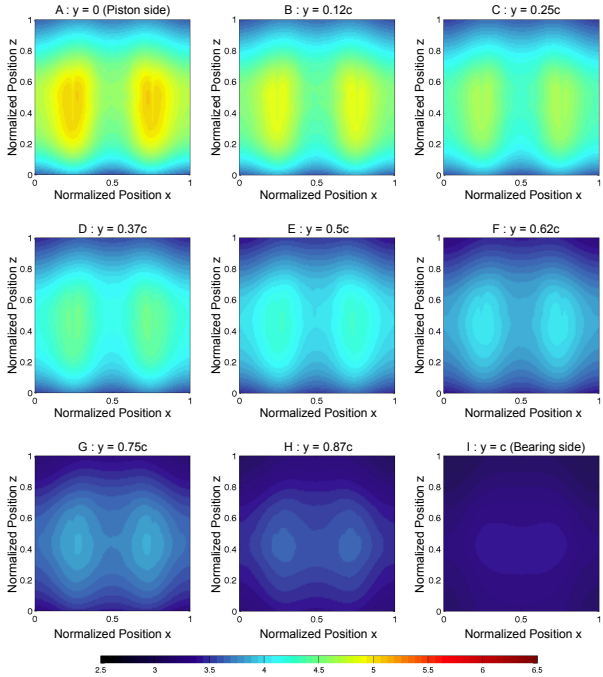

Figure 5.23: Normalized temperature field $\overline{\theta}$ (Gap 2).

In addition to $\overline{\mathbf{v}}$, the clearance profile can be seen in Fig. 5.19. The cushion effect is clearly visible, as the defined cushion thickness 'eliminates' the eccentricity of the piston. The normalized shear stress field $\overline{\tau}$ is shown in Fig. 5.20 for Gap 1 and in Fig. 5.21 for Gap 2. Although the shear stress for both cases is low at the thrust portion, where a plug space is likely to form (as

described in Section 4.7.2), the overall $\overline{\tau}$ (proportional to the heat generation) is lower for Gap 2 than for Gap 1, but locally higher for Gap 2.

The shape of $\overline{\theta}$ is similar for both gaps. The temperature is higher on the piston side than on the bearing side. However, $\overline{\theta}$ is lower for Gap 2 than for Gap 1, which is essentially due to a lower pressure gradient and a cavitating bearing. In order to understand the effect of the heat generation on the temperature field (for the instantaneous steady state), the normalized temperature field $\overline{\theta}$ is shown in Fig. 5.22 and Fig. 5.23 for Gap 1 and Gap 2 respectively. In order to demonstrate the desired effect of a reduced temperature field and shear stress field, the novel lubrication mechanism is compared to the current bearing design in Section 5.6.2.

5.6.2 Comparison to Current Bearing Design

The hydrodynamic pressure difference between Gap 1 and Gap 2 and the current bearing design is shown in Fig. 5.24 and Fig. 5.25 respectively. The normalized difference is negative for both cases, suggesting that the hydrodynamic pressure in the novel bearing design is less than that in the current bearing design (reference case). Although the maximum hydrodynamic pressure is reduced, the load capability is similar to that of the lubrication mechanism of the reference case, as the pressure at both vertical ends of the bearing is higher than for the reference configuration. In addition to a reduced pressure peak, the position of the maximum pressure is different for both Gap 1 and Gap 2, which is an effect of the second thrust portion. In particular, for Gap 2 (shown in Fig. 5.25), the pressure is significantly reduced for $\overline{z} \simeq 0.5$, which is the vertical position of cavitation.

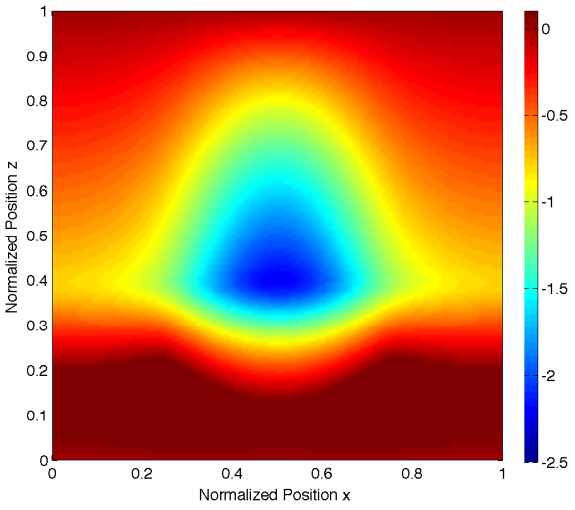

Figure 5.24: Normalized hydrodynamic pressure difference (Gap 1 - ref.).

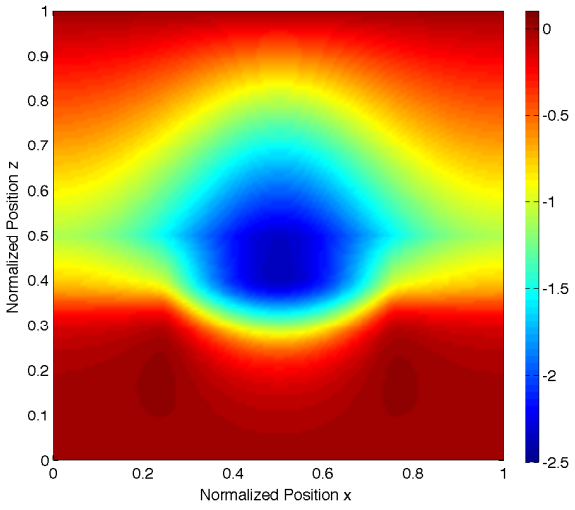

Figure 5.25: Normalized hydrodynamic pressure difference (Gap 2 - ref.).

The normalized shear stress difference (proportional to the heat generation) between the novel bearing designs and the reference case is shown in Fig. 5.26 and Fig. 5.27. For both lubrication mechanisms, the shear stress is reduced on the piston side, and slightly but locally increased on the bearing side. In particular for Gap 2, the heat generation is significantly

reduced under the second thrust portion, which is a consequence of the vanishing pressure. Although the shear stress is reduced, it is the temperature field difference that is of particular interest, because it confirms that the novel lubrication mechanism has a significant effect on reducing the temperature.

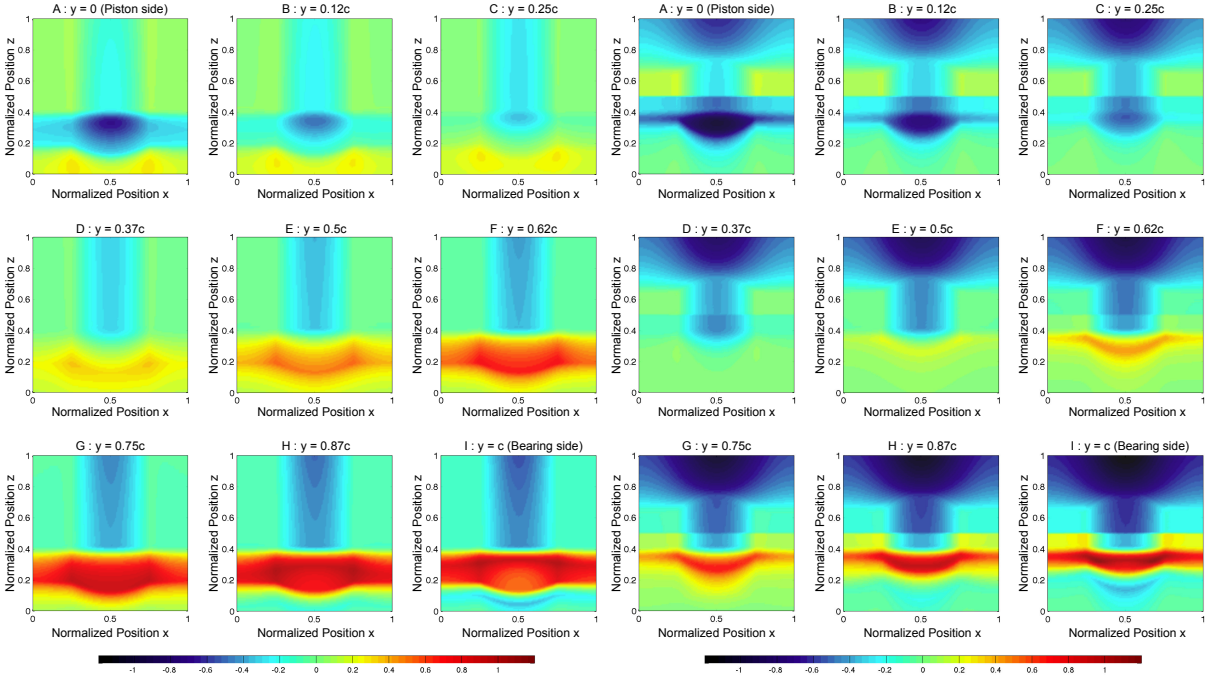

Figure 5.26: Normalized shear stress difference (Gap 1 - ref.).

Figure 5.27: Normalized shear stress difference (Gap 2 - ref.).

The temperature difference between Gap 1 and Gap 2 and the reference case is shown in Fig. 5.28 and Fig. 5.29 respectively. For both cases, the temperature difference is negative, which indicates a reduction in temperature, especially on the piston side. Most significantly, the temperature difference is higher and negative for Gap 2. Although the temperature on the bearing side is only slightly reduced, it is the significant reduction of the temperature on the piston side that is particularly important, because the reported heat damage occurs predominantly on that side.

The reduced temperature in the novel bearing design is shown for the instantaneous steady state. The temperature field at the lower bearing assembly after an aircraft ground maneuver on a rough runway is significantly reduced with the novel bearing design, as the transient temperature rise is an additive sequence of instantaneous steady states. The results are for oil, as the differences between oil and grease are similar in the new bearing design as shown in Chapter 4. For thick cushions (e.g., $\overline{\delta_g} > 0.25$), a plug space is likely to form within the cushion space. This *storage* of semisolid grease restricts the clearance, which has a similar effect as the plug space at the primary thrust portion identified in Chapter 4. The optimization results could change if other engineering design and manufacturing factors, such as production costs, are included in the optimization study. Further investigations would determine the importance of these other factors.

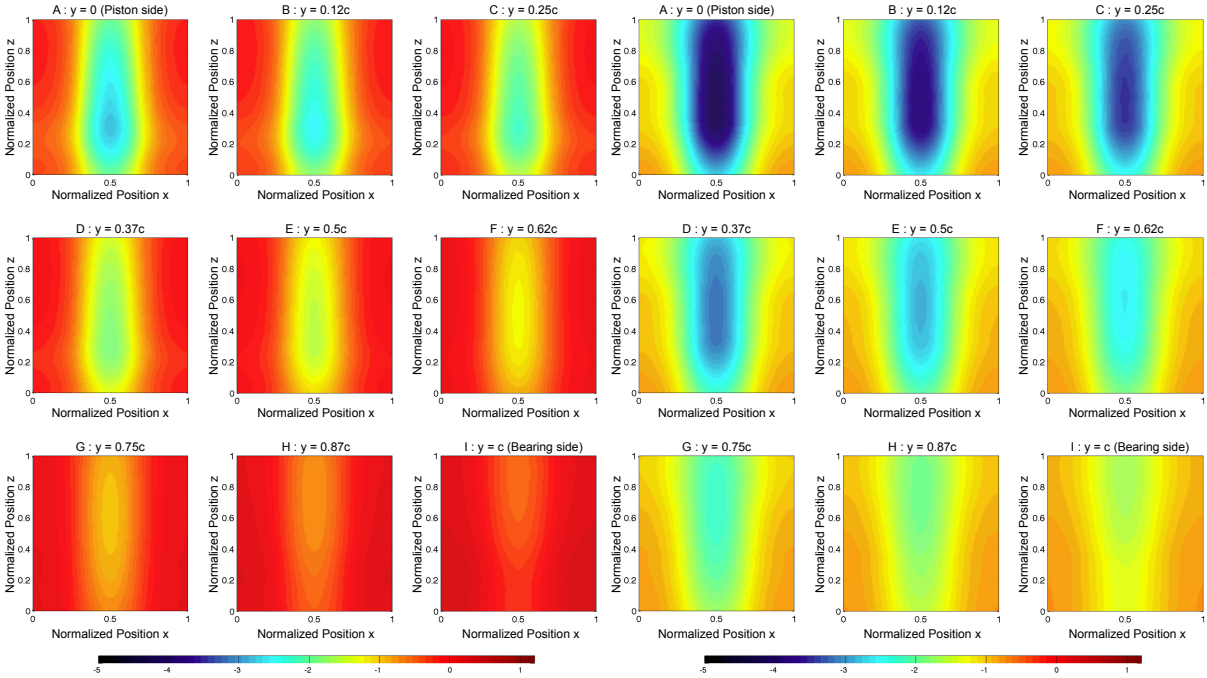

Figure 5.28: Normalized temperature difference (Gap 1 - ref.).

Figure 5.29: Normalized temperature difference (Gap 2 - ref.).

5.7 Summary and Conclusions

In this chapter, a conceptualized solution strategy is developed for efficiently including frictional heat generation and thermal effects in aircraft LG dynamic simulations (e.g., for landing and taxiing) without the need for online and costly thermal simulations. A methodological framework is developed using block-diagrams and functional analysis.

The systemic analysis led to the identification of a functional that yields the BFC as a function of the operating conditions and bearing configuration. The temperature at the lower bearing interface is found to be implicit and can be determined offline for a particular bearing configuration. As the bearing materials are defined by aerospace standards, the bearing configuration can be seen as equivalent to the clearance (or lubrication mechanism) between the lower bearing and the piston.

In order to conceptualize a solution to the reported overheating issues, three relevant solution strategies are considered: *allow*, *withstand* or *reduce* the heat generation. For a LG, reducing the heat generation by modifying the lubrication mechanism is the most promising strategy.

The novel lubrication mechanism includes a second thrust portion to guarantee a TEHD regime for both the compression and extension of the LG SA. In addition, the novel lubrication mechanism includes a cushion to eliminate the eccentricity of the piston (caused either through manufacturing or through the application of the external load) and avoid the escape of the lubricant from a high pressure zone.

As multiple goals must be satisfied to determine the optimal design parameters of the novel lubrication mechanism, a Pareto analysis is used to determine, by using the NSGA-II algorithm, a set of Pareto optimal solutions. These solutions are then grouped into clusters using the *k-means++* algorithm in order to determine the best Pareto optimal solution. Once the optimal solution has been determined under the practical constraints as shown in Section 5.5.2, the results of a TTM performance analysis are shown for a flexible and nonisothermal oil-lubricated bearing. Three major findings are:

Finding 1: The shear stress, which is proportional to the heat generation, is significantly reduced for the novel lubrication mechanism compared to the current mechanism.

Finding 2: Cavitation occurs for a second thrust portion. In order to avoid cavitation, the bearing length should be increased for a second thrust portion. This is necessary in order to guarantee a TEHD regime during transient motion.

Finding 3: For the novel lubrication mechanism that includes a cushion, the hydrodynamic pressure is reduced, but the total generated load is preserved. The pressure peak identified in the current bearing design is split into two pressure peaks, hindering the lubricant from escaping the region of highest pressure.

Based on these findings and the attained goal of reducing the heat generation and lowering the temperature, the proposed novel bearing design is promising for engineering higher performing aircraft LG lower bearings in the future. Nevertheless, a more detailed engineering analysis is needed in order to practically implement the proposed design.

■

Chapter 6

Conclusions and Recommendations

> Now this is not the end. It is not even the beginning of the end. But it is, perhaps, the end of the beginning.
>
> Winston Churchill, politician (1874 - 1965)

6.1 Summary and Conclusions

A TTM model of an aircraft LG is developed to fundamentally understand the thermal behavior of the LG SA. When maneuvering, landing or taking-off on rough runways, a commercial aircraft typically encounters high piston sliding velocities and, in combination with high drag loads, excessive heat generation at the bearing sliding interface leads to damaged chrome coating on the piston and thermal damage on the bearing surface. Commercial airlines have reported severe issues on the MLG, such as piston cracks and SA oil and lubricant loss. Previous studies have postulated the root cause to be the overheating of the lower bearing due to frictional heating; quantitative investigations have not delivered plausible results or sufficient explanations of *how* and *why* excessive heat generation occurred.

While overheating problems have been studied and solved for machine elements such as rotational bearings or components of automobiles, no studies have satisfactorily considered aircraft LG overheating. In addition, although the LG system is counted among the most critical components of an aircraft, extensive thermal (or TTM) studies of the LG SA are usually not performed as part of the engineering process. The LG is designed to withstand high loads and perform when maneuvering, landing or taking-off on smooth runways, but is not designed to perform well on rough runways. Two goals address the reported heat damage. The first goal is to understand the overall thermal behavior of a LG SA, and in particular, the transient heat generation process in a grease-lubricated LG SA bearing. A numerical model is essential for theoretical understanding, but is not sufficient for formulating strategies to solve the reported overheating problems; consequently, the second goal is to conceptualize and develop a solution strategy.

To the best of the author's knowledge, this thesis is the first comprehensive study in the area of LG TTM. Eight contributions to the research in the area of TTM modeling are:

1. Understanding of the overall TTM behavior of the LG SA

Although the root cause of the reported overheating is postulated to be at the lower bearing, the overall thermal behavior of a LG SA was unknown. Therefore, it is essential to understand the location and magnitude of the heat sources and sinks within the LG from a global point of view. The TTM model is defined and subdivided into three parts (thermo-, tribo- and mechanical-subsystems). The complete system must be considered in a transient regime, as the dynamic and thermal responses are closely related. The overheating occurs in a localized region, called the TZI, which confirms the root-cause theoretically and also confirms the need for a comprehensive model of the lower bearing interface.

2. Determination of critical parameters in the TTM model

A sensitivity study shows that the maximum heat flux is not sensitive to a change in WOG. Contrary to common belief, the contact pressures are higher for a higher WOG, but as the stiffness of the LG SA is nonlinear, the piston sliding speed is reduced; consequently, the heat flux (product of the contact pressure and the piston sliding speed) is also reduced. In addition, the heat flux at the lower bearing is most impacted by the runway amplitude, and not the runway bump wavelength.

3. Development of a novel tribotopological theory

As the LG SA overheating must be modeled in a transient regime and as the lubricant is multiphasic and non-Newtonian, one of the only known numerical methods is full CFD that solves the transient Navier-Stokes equations. However, the computational cost is so high for non-Newtonian transient lubrication simulations that it is impractical to obtain a solution for the case of an aircraft maneuvering on a rough runway. Other theories, including the classical lubrication theory, are based on the Reynolds equation, which is only applicable for a uniphasic and Newtonian lubricant. The TTT, falling between the classical lubrication theory and the Navier-Stokes equations solved with the CFD method, modifies the classical lubrication theory by deriving a modified Reynolds (TTR) equation, and takes into account the advantages of CFD (such as cavitation and a multiphasic lubricant). The TTT is not only essential for understanding the heat generation within the lubricated lower bearing, but is necessary for determining the transient TTM behavior of a grease-lubricated LG lower bearing.

4. Definition of tribotopologies for high numerical performance

The TTT is based on tribotopologies derived from a scalar threshold value. The defined TT spaces are surrounded by shells that englobe the various physical phases of the lubricant. For example, the semisolid phase is denoted as a plug space, and the disintegrated phase (or dry phase) is denoted as a dry space. The virtual tribotopologies have a huge positive impact on the computational speed of the velocity profile and the hydrodynamic pressure. In combination with

high-performing numerical methods, they provide a unique method for solving the governing equations derived from conservation laws. It has been demonstrated that the TTT is an extension of existing theories.

5. Development of a hybrid solver for the governing equations of the TTT

As the TTR equation is a 2D parabolic PDE with variable and nonlinear coefficients (circumferential and vertical directions), the only known iterative method that allows for fast solution times is the MG method. Similarly, the energy equation is reduced to a 1D parabolic PDE (radial direction). As the dimensionality of both governing equations is different, a hybrid solver based on the MG method is developed and implemented. A performance analysis shows that the numerical method provides results efficiently for both oil- and grease-lubricated bearings. The code has been verified and validated against analytical solutions and existing test data.

6. Integration of the TEHD-FSI code into a commercial FE package (ANSYS)

The detection and convergence of the tribotopologies is a critical algorithm and is kept as simple as possible to avoid affecting the speed of the overall convergence of the numerical code. The numerical simulation is the result of a unique TEHD-FSI integration. The TEHD code is tightly integrated into commercial FE code, and the FSI algorithm relies on shared memory, contrary to conventional co- or coupled simulations. This allows for very efficient fluid-structure data mapping and the exchange of data between the TEHD code and ANSYS.

7. Development of a comprehensive transient model of the lower bearing interface

The comprehensive model is a detailed numerical model of the lower bearing slider interface and relies on the TTT. The model assumptions allow the transient simulation to be seen as a sequence of instantaneous steady states, which is an efficient means of performing transient TEHD-FSI simulations; consequently, the focus is on the steady state results. A plug space forms at the thrust portion, significantly affecting the friction coefficient. In addition, full FSI must be considered in order to correctly quantify the heat generation. Although application dependent, the temperature on the piston side is higher than on the bearing side, which explains the reported unevenly and asymmetrically distributed heat damage.

8. Development of a novel lubrication mechanism

The comprehensive model based on the TTT is a powerful tool that allows for the conceptualization and development of a solution strategy. Several solution strategies are considered, and a simple yet efficient way of *reducing* the heat generation is to modify the clearance between the piston and the lower bearing by introducing a cushion, allowing for the retention of the lubricant in a pocket and hindering it from escaping. In addition, in order to avoid a break-down of the TEHD regime, a second thrust portion is added, preserving the TEHD regime during compression and extension of the SA. A multi-objective optimization study shows that the proposed modifications of the lubrication mechanism have a beneficial effect on the reduction of the temperature in the TZI.

The TTM model can be integrated into existing LG dynamic simulations in order to design higher-performing future aircraft LG. The proposed solution to the overheating problem - the novel lubrication mechanism - alters the TTM behavior of the LG such that the reported heat damage is unlikely to occur when operating on rough runways.

6.2 General Applicability

Although this thesis focuses on developing a TTM model for aircraft LG, and in particular on explaining phenomena only occurring while operating on rough runways, some concepts and methods are intentionally kept as general as possible to be of use for other research communities. Several new methods described in this thesis might be of use to modeling, in a more general sense, any mechanical systems, especially grease-lubricated systems, that undergo rapid transient translational or rotational motion with high loads and load variations. For instance, such systems can be found in the sector of heavy machinery and energy generation installations.

The *analytical method* of defining the system and identifying the response of complex mechanical systems such as the LG can be applied to other mechanical systems that are dominated by all three subsystems or any combination of a mechanical, tribological and thermal subsystem. Such systems can be found in any branch of engineering and can be of any scale.

The *tribotopological theory* has been derived for grease in general, and can be applied to any other grease-like lubricant. As the number of physical phases of the lubricant is not limited, the TTT can be applied to any other lubricant or thin film exhibiting electro- or magneto-rheological phases. This can be particularly interesting for the development of *smart* lubricants. The concept of tribotopologies is not specific to lubrication problems. For instance, the concept might well be applied to analyze live traffic, as outlined in Chapter 3.

The *numerical approach* has been detailed in a general way, and can be applied to solve governing equations of the same type as those of the TTT. The numerical approach relies on coupling multiple fields of physics together in an efficient way, in particular to achieve convergence in a staggered manner. The hybrid solver based on the MG method is applicable for determining a solution to lubrication problems. The memory is shared between the fluid and structural code, which might be of particular interest for the development of FE/CFD software in order to accurately and efficiently simulate multiphasic thin films in a transient way.

6.3 Limitations and Recommendations for Future Research

Although the model development steps are extensive, there are some limitations. The TTM model development only sets the stage for further research. The novel TTT is derived for the general case of an oil- and grease-lubricated bearing and has been applied to the slider bearing of a specific aircraft LG, but is more widely applicable and has been prepared to be applied to other non-Newtonian or smart lubricants. Although it has been demonstrated that the TTT is an extension of the classical lubrication theory, eventual recirculation effects are not included (zero velocity gradient across the lubrication gap), and may need to be considered if deep groves were

included in the lubrication mechanism. Future research in the following areas is recommended:

1. Advanced Numerical Development

The results retrieved from the comprehensive model are valid only for a slider bearing. Although the TTT has been validated for journal bearings, no results have been retrieved for this configuration and setup, and some numerical adaptations may be necessary (e.g., convergence relaxation parameters).

The convergence procedures as well as the TTT have been developed in order to overcome the challenge of TEHD simulation being a bottleneck in a transient TTM model. The current TDA relies on a basic root finding algorithm and is appropriate for the application at hand, but might not be for studying different applications. Under different operating conditions, the current TDA might eventually become numerically unstable, with convergence of the tribotopologies not achieved, limiting the applicability of the TEHD-FSI software. A different isosurface detection algorithm based on the Marching Cubes algorithm would likely provide higher robustness, reliability and stability of the numerical code.

In this thesis, the computational grid used for solving the governing fluid equations is uniform. Nonuniform grid generation methods shown in [121] would likely help to achieve faster convergence, especially when TT spaces are present. The mesh is currently globally refined in order to accurately capture the TT spaces. Adaptive grids with local refinements at the shells (mesh squeezing) are a promising way of reducing the total number of nodes, and speeding up convergence. During the simulations, the structural solver is a bottleneck due to the fact that serial code dictates the number of processors used (in this case, the TEHD code). The TEHD-FSI code could be parallelized to take advantage of multiple cores and speed up the process. Parallelization can initially be achieved by forcing the TEHD code to run on a single processor, and the FE code on multiple processors.

2. Birth, Growth and Death of Overlapping Tribotopologies

In the TTT, multiple spaces could co-exist and overlap each other. After long transient runs, there is a possibility for dry spaces to be born and grow. The birth of dry spaces marks a local disintegration of the lubricant. The growth of dry spaces is not relevant for the understanding of the heat generation mechanism, but might contribute to the explanation of heat damage. As the disintegration of the lubricant is an irreversible process, the death of dry spaces (equivalent to the regeneration of the lubricant), contrary to the death of plug and fluid spaces, would never occur. In addition, the tribotopologies might be overlapping, for example, with the dry spaces dominating a plug space. The growth and death of various TT spaces would allow for the study of the mechanism of grease disintegration ('burning' of the lubricant), providing valuable insight into the limits of operation. These simulations would be application specific.

3. Experimental Validation of the Numerical Model

The numerical model is validated against existing experimental test data for rotational motion and oil and against existing analytical solutions for slider bearings. However, as experimental data

of a LG slider bearing are not available, the model development consists of a partially validated theoretical framework, and an experimental validation of the numerical code is important and needed. A validated numerical code would pave the way for the integration of the numerical TEHD-FSI code into an industrial environment.

4. Additional Real-life Applications

The TTM model is a representation of a specific LG lower bearing. Several assumptions of the model allowed for the development of numerical code that can be used to study real-life applications. Several other factors may have an effect on the TEHD solution. For instance, the roughness of the surfaces in contact could be included to obtain similarly-shaped, but closer-to-reality solutions. Grooves that are usually present in bearings could also be included to simulate the spread of the lubricant within the bearing. Sealing elements such as rubber seals that preserve the oil within the LG SA and prevent external dust from entering the lubrication mechanism have been omitted, as the sealing material behaves fundamentally differently than the surrounding structure. The seals contribute to the overall friction force and could be included. In the comprehensive model, the applied external HTC is constant. For an aircraft accelerating (or decelerating) during take-off and landing, the application of a position- and time-varying HTC from a full CFD simulation would be necessary for capturing the external heat removal more accurately by taking into account the eventual turbulence around the LG SA.

In the current model, the loads are applied from a simplified dynamic model of the LG. In order to take into account the structural deformations under real-life loads, a multibody simulation would be required. In particular, the method for running an offline TEHD simulation and performing dynamic multibody simulations with an implicit temperature could be implemented.

5. Active Control of Lubrication Mechanism

The novel lubrication mechanism takes into account a fixed cushion thickness. As the eccentricity of the piston changes as a function of time for a real-life LG application, the optimal cushion thickness is not preserved during a typical ground maneuver. The thrust portion might not be at the right position and angle throughout a transient maneuver. Instead of *passively* controlling the lubrication mechanism, and in order to maintain an optimal solution, the design parameters of the lubrication mechanism could be *actively* controlled. This implementation could be a promising avenue of future research. An actively controlled lubrication mechanism might be theoretically feasible, but it could prove difficult in practice. Another possibility would be to replace the lubricant with an electro- or magnetorheological fluid used to control the stiffness of the bearing and derive the TT spaces from a magnetic or electric field.

The TTM model is developed to determine an optimal lubrication mechanism and improve the TTM performance of existing LG. Once validated against LG-specific experimental data, the numerical model would be ready for use in an engineering design process to determine the pre-service TTM performance of the LG. This would allow the maintenance costs of the operator to be kept at a minimum. ■

Bibliography

[1] K.J. DeBord. Runway roughness measurement, quantification, and application - The Boeing method. Technical Report D6-81746, Boeing Commercial Airplane Group - Airport Technology Organization (B-B210), 1995.

[2] L. Heirendt, H.H.T. Liu and P. Wang. Aircraft landing gear thermo-tribo-mechanical model and sensitivity study. *Journal Of Aircraft*, 52(2):511–519, 2014.

[3] J.Y. Jang and M.M. Khonsari. On the thermohydrodynamic analysis of a Bingham fluid in slider bearings. *Acta Mechanica*, 148:165–185, 2001.

[4] SAE Aerospace. Landing gear schock strut heat damage. Technical Report SAE AIR 5913, SAE International, 2011.

[5] N.S. Currey. *Aircraft Landing Gear Design: Principles and Practices*. AIAA Education Series, 4 edition, 1988.

[6] A.W. Hall. Three-track runway and taxiway profiles measured at international airports C and D. Technical Report NASA TN D-5703, NASA, 1970.

[7] J. Pritchard. Overview of landing gear dynamics. *Journal of Aircraft*, 38(1):130–137, 2001.

[8] Z.H. Zhu, M. Larosa and J. Ma. Fatigue life estimation of helicopter landing probe based on dynamic simulation. *Journal of Aircraft*, 46(5):1533–1543, 2009.

[9] J. García de Jalón and E. Bayo. *Kinematic and Dynamic Simulation of Multibody Systems*. Springer Verlag, New York, 1994.

[10] G. Vanheers. Simulation and optimisation of helicopter oleo strut behaviour at touchdown. Master's thesis, Departement Industriële Wetenschappen en Technologie, 2009.

[11] E.W. Turner and J.T. Riechers. An assessment of the B-747's capability to operate on rough surfaces. Technical Report WL-TM-92-313-FIBE, Flight Dynamics Directorate Wright Laboratory, Ohio, May 1992.

[12] H. Wang, J.T. Xing, W.G. Price and W. Li. An investigation of an active landing gear system to reduce aircraft vibrations caused by landing impacts and runway excitations. *Journal of Sound and Vibration*, 317: 50–66, 2008.

[13] R. Lernbeiss and M. Plöchl. Simulation model of an aircraft landing gear considering elastic properties of the shock absorber. *Proceedings of the Institution of Mechanical Engineers, Part K: Journal of Multi-body Dynamics*, 221(1):77–86, 2007.

[14] Prashant Khapane. *Simulation of Landing Gear Dynamics and Brake-Gear Interaction*. PhD thesis, Universität Carolo-Wilhelmina zu Braunschweig, August 2006.

[15] I.J.M. Besselink. *Shimmy of Aircraft Main Landing Gears*. PhD thesis, Mechanical Maritime and Materials Engineering, Delft University of Technology, Delft, The Netherlands, 2000.

[16] J.N. Daniels. A method for landing gear modeling and simulation with experimental validation. Technical report, George Washington University and NASA Langley Research Center, June 1996.

[17] R. Dragani and M. Sarra. Etude d'un amortisseur avec des butées et du frottement non-linéaire. *Mechanics Research Communications*, 8(1):23–28, 1981.

[18] J.D. Byerlee. The mechanics of stick-slip. *Tectonophysics*, 9:475–486, 1969.

[19] W. Krüger. *Integrated Design Process for The Development of Semi-Active Landing Gears For Transport Aircraft*. PhD thesis, Universität Stuttgart, December 2000.

[20] W. Karam and J.C. Mare. Advanced model development and validation of landing gear shock struts.

Journal of Aerospace Engineering, 224:575–586, 2009.

[21] A. Lion and S. Loose. A thermomechanically coupled model for automotive shock absorbers: Theory, experiments and vehicle simulations on test tracks. *Vehicle System Dynamics*, 37(4):241–261, 2002.

[22] J.C. Ramos, A. Rivas, J. Biera, G. Sacramento and J.A. Sala. Development of a thermal model for automotive twin-tube shock absorbers. *Applied Thermal Engineering*, 25:1836–1853, 2005.

[23] S.M. Cormie and T.A. Stolarski. The influence of friction in the guide bearing on the damping characteristic of a suspension system. *Tribology International*, 19(6):318–323, December 1986.

[24] R. C. Redfield. Thermal modeling in mountain bike air shocks. *Procedia Engineering*, 2:2625–2630, 2010.

[25] M. Mansouri and M.M. Khonsari. Surface temperature in oscillating sliding interfaces. *Journal of Tribology*, 127:1–9, 2005.

[26] B. Wikiel and J.M. Hill. Stick-slip motion for two coupled masses with side friction. *International Journal Of Non-Linear Mechanics*, 35:953–962, 2000.

[27] Z.S. Olesiak and Y.A. Pyryev. A nonlinear, nonstationary problem of frictional contact with inertia and heat generation taken into account. *Acta Mechanica*, 143:67–78, 2000.

[28] J. Awrejcewicz, Y. Pyryev. Dynamics of a two-degrees-of-freedom system with friction and heat generation. *Communications in Nonlinear Science and Numerical Simulation*, 11:635–645, 2006.

[29] H. Olsson, K.J. Aström, C. Canudas de Wit, M. Gäfvert and P. Lischinsky. Friction models and friction compensation. Technical report, Lund University, 1997.

[30] W. Krüger, I. Besselink, D. Cowling, D.B. Doan, W. Kortüm, and W. Krabacher. Aircraft landing gear dynamics: Simulation and control. *Vehicle System Dynamics*, 28:119–158, 1997.

[31] L. Heirendt, H.H.T. Liu and P. Wang. Characteristic aircraft landing gear thermo-tribo-mechanical model. In *Proceedings of the ASME 2012 International Mechanical Engineering Congress & Exposition, IMECE 2012*, volume 3: Design, Materials and Manufacturing, Parts A, B, and C, pages 1743–1748, 2012.

[32] L. Heirendt, H.H.T. Liu and P. Wang. Modified bearing friction coefficient in aircraft landing gear dynamic simulations. In *Proceedings of the Canadian Congress of Applied Mechanics 2013*, 2013.

[33] E.R. Booser, editor. *Handbook Of Lubrication and Tribology. Monitoring, Materials, Synthetic Lubricants, and Applications*, volume 3. CRC Press Inc., 1994.

[34] J.F. Archard. The temperature of rubbing surfaces. *Wear*, 2:438–455, 1958.

[35] B. Bhushan. Temperature and friction of sliding surfaces. Master's thesis, Massachusetts Institute of Technology, August 1970.

[36] J.R. Barber. Distribution of heat between sliding surfaces. *Journal Mechanical Engineering Science*, 9(5), 1967.

[37] J.R. Barber. The conduction of heat from sliding solids. *Int. J. of Heat Mass Transfer*, 13:857–869, 1969.

[38] H. A. Abdel-Aal. On the interdependence between kinetics of friction-released thermal energy and the transition in wear mechanisms during sliding of metallic pairs. *Wear*, 254:884–900, 2003.

[39] E. Rabinowicz. *Friction and wear of materials.* John Wiley & Sons Inc., New York, 2nd edition, 1995.

[40] D.V. Grilitskii and P.P. Krasnyuk. Steady-state vertical thermoelastic oscillations in a system of two plane-parallel layers with friction heat generation. *Journal of Engineering Physics and Thermophysics*, 70 (4):691–695, 1997.

[41] A.Z. Szeri. *Fluid film lubrication.* Cambridge University Press, New York, 2nd edition, 2011.

[42] E. Pollmann and D. Schüler. Reibungswärme und Temperaturen in einem Schmierspalt mit konstanter Dicke. *Wear*, 64:205–229, 1980.

[43] E. C. Sekharan and G. Ramanaiah. Unsteady flow between two oscillating plates. *Defence Science Journal*, 32(2):99–104, 1982.

[44] R. S. Paranjpe and T. Han. A study of the thermohydrodynamic performance of steadily loaded journal bearings. *Tribology Transactions*, 37(4):679–690, 1994.

[45] Q. Liu. *Friction in Mixed and Elastohydrodynamic Lubricated Contacts including Thermal Effects.* PhD thesis, Universiteit Twente, 2002.

[46] J. Mitsui. A study of thermohydrodynamic lubrication in a circular journal bearing. *Tribology International*, 20(6):331–341, 1987.

[47] N.M. Bujurke, N.B. Naduvinamani and S.S. Benchalli. Secant-shaped porous slider bearing lubricated with couplestress fluids. *Industrial Lubrication and Tribology*, 57(4):155–160, 2005.

[48] T. Ciconea, M.D. Pascovici and A. Minculescu. A simplified thermoelastohydrodynamic model for a parallel surface slider. *Tribology International*, 41:947–953, 2008.

[49] M. Pelosi and M. Ivantysynova. Heat transfer and thermal elastic deformation analysis on the piston cylinder interface of axial piston machines. *Journal of Tribology*, 134:1–15, 2012.

[50] L. Heirendt, H.H.T. Liu and P. Wang. Thermo-hydrodynamic analysis of a rigid and oil-lubricated aircraft landing gear lower bearing. In *Proceedings of The Canadian Society for Mechanical Engineering International Congress 2014*, 2014.

[51] L. Heirendt, H.H.T. Liu and P. Wang. Aircraft landing gear greased slider bearing steady-state thermo-elastohydrodynamic concept model. *Tribology International*, 82(B):453–463, 2015.

[52] J. Bouyer and M. Fillon. Relevance of the thermoelastohydrodynamic model in the analysis of a plain journal bearing subjected to severe operating conditions. In *Proceedings of the Institution of Mechanical Engineers, Part J: Journal of Engineering Tribology*, volume 218, pages 365–377, 2004.

[53] X. Jiang, J. Wang and J. Fang. Thermal elastohydrodynamic lubrication analysis of tilting pad thrust bearings. In *Proceedings of the Institution of Mechanical Engineers, Part J: Journal of Engineering Tribology*, volume 225, 2011.

[54] P. Yang, Z.M. Jin, F. Liu and D. Dowson. Line contact thermal elastohydrodynamic lubrication subjected to longitudinal vibration. *Transient Processes in Tribology*, pages 759–767, 2004.

[55] A. Fatu, M. Hajjam and D. Bonneau. A new model of thermoelastohydrodynamic lubrication in dynamically loaded journal bearings. *Journal Of Tribology*, 128:85–95, 2006.

[56] D. Piffeteau, D. Souchet and D. Bonneau. Influence of thermal and elastic deformations on connecting-rod big end bearing lubrication under dynamic loading. *Journal Of Tribology*, 122:181–191, 2000.

[57] R.A.J. van Ostayen and A. van Beek. Thermal modelling of the lemon-bore hydrodynamic bearing. *Tribology International*, 42:23–32, 2009.

[58] B.T. Paulsen, S. Morosi, and I.F. Santos. Static, dynamic, and thermal properties of compressible fluid film journal bearings. *Tribology Transactions*, 52(2):252–299, 2011.

[59] Y. Wang and B. Yang. An investigation into grease behavior in thermal EHL circular contacts. *Tribology Transactions*, 49:449–453, 2006.

[60] S. Wada, H. Hayashi and K. Haga. Behavior of a Bingham solid in hydrodynamic lubrication (Part 3, Application to Journal Bearing). In *Bulletin of the JSME (Japan Society of Mechanical Engineers)*, volume 17, pages 1182–1191, 1974.

[61] J.J. Kauzlarich and J.A. Greenwood. Elastohydrodynamic lubrication with Herschel-Bulkley model greases. In *ASLE Transactions*, volume 15, pages 169–277, 1972.

[62] B.K. Karthikeyan, M. Teodorescu, H. Rahnejat and S.J. Rothberg. Thermoelastohydrodynamics of grease-lubricated concentrated point contacts. *Proceedings of the Institution of Mechanical Engineers, Part C: Journal of Mechanical Engineering Science*, 224:683–694, 2010.

[63] J.Y. Jang and M.M. Khonsari. Performance analysis of grease-lubricated journal bearings including thermal effects. *Journal of Tribology*, 119(4):859–868, 1997.

[64] S-M. Ju and C-I. Weng. Thermohydrodynamic analysis of finite-width journal bearings with non-Newtonian lubricants. *Wear*, 171:41–49, 1994.

[65] J.H. Kim and A.A. Seireg. Thermohydrodynamic lubrication analysis incorporating Bingham rheological model. *Journal Of Tribology*, 122:137–46, January 2000.

[66] J.A. Tichy. Hydrodynamic lubrication theory for the Bingham plastic flow model. *Journal of Rheology*, 35 (4):477–496, 1991.

[67] M.M. Khonsari and D.Y. Hua. Generalized non-Newtonian elastohydrodynamic lubrication. *Tribology International*, 26(6):405–411, 1993.

[68] Y. Peiran and W. Shizhu. A generalized Reynolds equation based on non-Newtonian flow in lubrication mechanics. *Acta Mechanica Sinica*, 6(4):289–295, December 1990.

[69] H.S. Carslaw and J.C. Jaeger. *Conduction of Heat in Solids*. Oxford at the Clarendon Press, 2nd edition, 1959.

[70] D. Sfyris and A. Chasealevris. An exact analytical solution of the Renyolds equation for the finite journal bearing lubrication. *Triboloy International*, 55:46–58, 2012.

[71] J. Durany, J. Pereira and F. Varas. Numerical solution to steady and transient problems in thermohydrodynamic lubrication using a combination of finite element, finite volume and boundary element methods. *Finite Elements in Analysis and Design*, 44:686–695, 2008.

[72] K. Kphno, S. Takahashi and K. Saki. Elasto-hydrodynamic lubrication analysis of journal bearings with combined use of boundary elements and finite elements. *Engineering Analysis with Boundary Elements*, 13: 273–281, 1994.

[73] M. Attia Hili, S. Bouaziz, M. Maatar, T. Fakhfakh and M. Haddar. Hydrodynamic and elastohydrodynamic studies of a cylindrical journal bearing. *Journal of Hydrodynamics*, 22(2):155–163, 2010.

[74] M. He, C.H. Cloud and J.M. Byrne. Fundamentals of fluid film journal bearing operation and modeling. In *Proceedings Of The Thirty-Fourth Turbomachinery Symposium*, 2005.

[75] E. A. Zargari. Computational analysis of integral and differential formulations of the elastohydrodynamic lubrication film thickness equation. Master's thesis, University of Leeds, May 2007.

[76] C.H. Venner, A.A. Lubrecht. *Multilevel Methods in Lubrication.* Elsevier, July 200.

[77] M. Lieb. A full multigrid implementation on staggered adaptive cartesian grids for the pressure Poisson equation in computational fluid dynamics. Master's thesis, Technische Universität München, 2008.

[78] Q. Chen and D.Y. Li. A computational study of frictional heating and energy conversion during sliding processes. *Wear*, 259:1382–1391, 2005.

[79] V. Oancea and A. Laursen. A finite element formulation of thermomechanical rate-dependent frictional sliding. *International Journal for Numerical Methods in Engineering*, 40:4275–4311, 1997.

[80] P. Brajdic-Mitidieri. *Advanced Modelling of Elastohydrodynamic Lubrication.* PhD thesis, Imperial College London, 2005.

[81] P.G. Tucker and P.S. Keogh. A generalized computational fluid dynamics approach for journal bearing performance prediction. In *Proceedings of the Institution of Mechanical Part J: Journal of Engineering Tribology*, volume 209, pages 99–108, 1995.

[82] K.P. Gertzos, P.G. Nikolakopoulos, C.A. Papadopoulos. CFD analysis of journal bearing hydrodynamic lubrication by Bingham lubricant. *Tribology International*, 41:1190–1204, 2008.

[83] B.S. Shenoy, R.S. Pai, D.S. Rao, and R. Pai. Elasto-hydrodynamic lubrication analysis of full 360° journal bearing using CFD and FSI techniques. *World Journal of Modelling and Simulation*, 5(4):315–320, 2009.

[84] M. Hartinger, M Dumont, S. Ioannides, D. Gosman and H. Spikes. CFD modeling of a thermal and shear-thinning elastohydrodynamic line contact. *Journal Of Tribology*, 130:1–16, 2008.

[85] V. Bruyere, N. Fillot, G.E. Morales-Espejel, P. Vergne. Computational fluid dynamics and full elasticity model for sliding line thermal elastohydrodynamic contacts. *Tribology International*, 46:3–13, 2012.

[86] H. Liu, H. Xu, P. J. Ellison and Z. Jin. Application of computational fluid dynamics and fluid - structure interaction method to the lubrication study of a rotor–bearing system. *Tribology Letters*, 38:325–336, 2010.

[87] M. Hartinger. *CFD Modelling of Elastohydrodynamic Lubrication.* PhD thesis, Department of Mechanical Engineering, Imperial College London, London, November 2007.

[88] Sutthinan Srirattayawong. *CFD Study of Surface Roughness Effects on the Thermo- Elastohydrodynamic Lubrication Line Contact Problem.* PhD thesis, Engineering Department, University of Leicester, Leicester, United Kingdom, 2014.

[89] T. Almqvist, A. Almqvist and R. Larsson. A comparison between computational fluid dynamic and Reynolds approaches for simulating transient EHL line contacts. *Tribology International*, 37:61–69, 2004.

[90] J.C. Dixon. *The Shock Absorber Handbook.* John Wiley & Sons, Inc. and Professional Engineering Publishing Ltd., 2nd edition, 2007.

[91] J.H. Lienhard IV and J.H. Lienhard V. *A Heat Transfer Textbook.* Phlogiston Press, 3rd edition, 2008.

[92] The Engineering Society For Advanced Mobility Land Sea Air and Space. Aerospace hydraulic fluids physical properties. Aerospace Information Report AIR1362, SAE International, 2000.

[93] D. Knežević, V. Savić. Mathematical modeling of changing of dynamic viscosity, as a function of temperature and pressure, of mineral oils for hydraulic systems. *Facta Universitatis. Series: Mechanical Engineering*, 4 (1):27–34, 2006.

[94] Verein Deutscher Ingenieure. *VDI Heat Atlas.* Springer Verlag, Berlin/Heidelberg, 2nd edition, 2010.

[95] K. Siik and J. Vuorinen. The influence of shear thinning behavior on lubricating grease consistency and its

effect on oil separation. In *Annual Transactions of the Nordic Rheology Society*, volume 13, 2005.

[96] AeroShell. *The Aeroshell Book*. 18th edition, 2003.

[97] R.F. Smiley and W.B. Horne. Mechanical properties of pneumatic tires with special reference to modern aircraft tires. Technical Report R-64, Langley Research Center, Langley Field, Va., 1960.

[98] M. Meier. *Dimensionieren I*. WS 2003-04. ETH, Eidgenössische Technische Hochschule Zürich, Zentrum für Produkt Entwicklung, 2003.

[99] R.I. Leine. *Bifurcations in Discontinuous Mechanical Systems of Filippov-Type*. PhD thesis, Mechanical Engineering, Technische Universiteit Eindhoven, Eindhoven, The Netherlands, 2000.

[100] L. Borel and D. Favrat. *Thermodynamique et énergétique*, volume 1: De l'énergie à l'exergie. Presses Polytechniques et Universitaires Romandes, 2nd edition, 2005.

[101] R.K. Sleeper, R.C. Dreher. Tire Stiffness and Damping Determined From Static and Free-Vibration Tests. NASA Technical Paper 1671, National Aeronautics and Space Administration, 1980.

[102] U.S. Environmental Protection Agency. Sensitivity analysis: How do we know what's important? In *Process for Conducting Probabilistic Risk Assessment*, volume 3 (RAGS), 2001.

[103] J. Botsis, M. Deville. *Mécanique des milieux continus: Une introduction*. Presses Polytechniques et Universitaires Romandes, 1st edition, 2006.

[104] R. Gohar. *Elastohydrodynamics*. Imperial College Press, 2nd edition, 2001.

[105] K.R. Rajagopal and A.Z. Szeri. On an inconsistency in the derivation of the equations of elastohydrodynamic lubrication. In *Proceedings of the Royal Society A*, volume 459, pages 2771–2786, 2003.

[106] W.C. Young and R. G. Budynas. *Roark's Formulas for Stress and Strain*. McGraw-Hill, 7th edition, 2002.

[107] I. Yavneh. Why multigrid methods are so efficient. *Computing In Science and Engineering*, 8(6):12–22, 2006.

[108] W.L. Briggs, H. Van Emden and S.F. McCormick. *A multigrid tutorial*. Society for Industrial and Applied Math, 2nd edition, 2000.

[109] W. Hörmann and G. Derflinger. A portable uniform random number generator well suited for the rejection method. *ACM Transactions on Mathematical Software*, 19(4):489–495, 1993.

[110] K. Morken and M. Reimers. An unconditionally convergent method for computing zeros of splines and polynomials. *Mathematics of Computation*, 76(258):846–865, April 2007.

[111] W.H. Press, S.A. Teukolsky, W.T. Vetterling and B.P. Flannery. *Numerical recipes in Fortran 77. The art of scientific computing*, volume 1. Cambridge University Press, Cambridge/New York/Melbourne, 2nd edition, 1992.

[112] G. Hou, J. Wang and A. Layton. Numerical methods for fluid-structure interaction. *Communications in Computational Physics*, 12(2):337–377, 2012.

[113] H. Akima. A method of bivariate interpolation and smooth surface fitting for values given at irregularly distributed points. OT Report 75-70, U.S. Department of Commerce, 1975.

[114] B.J. Hamrock, S.R. Schmid, and B.O. Jacobson. *Fundamentals of Fluid Film Lubrication*. Marcel Dekker, Inc., 2nd edition, 2004.

[115] D.P. Hess. Modelling lubricated friction for dynamic contact systems. *Tribtotest Journal*, 5(2):121–133, 1998.

[116] F. Dimofte. Wave journal bearing with compressible lubricant - Part I: The wave bearing concept and a comparison to the plain circular bearing. *Tribology Transactions*, 38(1):153–160, 1995.

[117] P.E. Allaire and R.D. Flack. Design of journal bearings for rotating machinery. In *Proceedings Of The Tenth Turbomachinery Symposium*, pages 25–45. Turbomachinery Laboratories, Texas A&M University, December 1981.

[118] K. Deb, A. Pratab, S. Agarwal, and T. Meyarivan. A fast and elitist multiobjective genetic algorithm: Nsga-ii. *IEEE Transactions On Evolutionary Computation*, 6(2), 2002.

[119] P. K. Malladi, D. Puvvula, A. Nagalla. Reliable pareto solutions for multiple objective scheduling problems. *International Journal of Computer Science and Information Technologies*, 3(3):4331–4338, 2012.

[120] H. Taboada, D. Coit. Post-pareto optimality analysis to efficiently identify promising solutions for multi-objective problems. Working Paper 05-15, Rutgers University ISE, 2005.

[121] V.D. Liseikin. *Grid Generation Methods*. Scientific Computation. Springer Science+Business Media LLC, 2nd edition, 2010.